

Énergie, Matériaux et Télécommunications

Pt-Based and Graphene-based Electrocatalysts for Oxygen Reduction Reaction

Par
Xin Tong

Thèse présenté(e) pour l'obtention du grade de
Philosophiae Doctor (Ph.D.)
en sciences de l'énergie et des matériaux

Jury d'évaluation

Président du jury et examineur interne	Prof. Luca Razzari INRS-EMT
Examineur externe	Prof. Gessie Brisard Université de Sherbrooke
Examineur interne	Prof. John Oh Concordia University
Directeur de recherche	Prof. Shuhui Sun INRS-EMT
Codirecteur de recherche	Prof. Jerome P. Claverie Université de Sherbrooke

ABSTRACT

Climate change caused by the use of fossil fuels has become an urgent challenge on a daily basis all over the world. Practical and environmentally sustainable energy sources to replace the traditional fossil fuels are thus desperately needed. Fuel cell, in particular, the proton exchange membrane fuel cell (PEMFC), is regarded as one of the most promising candidates, which could efficiently convert chemical energy directly into usable electric power through the electrochemical process. Theoretically, the output performance of fuel cells is decided by the kinetics of hydrogen oxidation reaction (HOR) on anode and oxygen reduction reaction (ORR) on the cathode. Notably, the kinetics of ORR on the cathode is five orders of magnitude slower than HOR on the anode. Therefore, developing highly efficient electrocatalysts to facilitate sluggish cathodic ORR is a key issue. So far, Platinum (Pt) is still the most widely used ORR electrocatalyst. However, the high cost and inadequate long term operational stability of Pt/C catalysts inhibit their commercialization. Thus far a lot of researches have been devoted to dealing with the aforementioned problems through two main directions including (i) improving Pt/C catalyst via either the modification of Pt particle approach, replacing conventional support, or surface engineering by modifying the coating of the Pt nanoparticle; and (ii) replacing Pt-based catalysts with nonprecious metal catalyst and metal-free catalysts.

In this work, two kinds of material (Pt based materials and graphene base materials) are developed with the ultimate objective of enhance the ORR activity and extending the lifetime without considerably increasing its cost. For Pt based material, novel supporting materials such as carbon nanotubes and graphene are used and high active Pt nanoparticles are stabilized by carbon coating method. For graphene based material, heteroatom doped graphene material are both used as the supporting material of Pt nanoparticles and metal-free catalysts.

First, we synthesized electro-catalysts composed of Pt NPs supported on carbon nanotubes (CNTs), which were further covered by an ultra-thin layer of graphitic carbon. Such hybrid ORR catalysts were obtained by an *in situ* polymer encapsulation–graphitization method on the interfaces, where a glucose-containing polymer was grown directly on the surface of Pt/CNTs. The thickness of the carbon coating layer can be precisely tuned between 0.5 and several nanometers by simply programming the polymer growth on Pt/CNTs. The resulting Pt/CNTs@C with a carbon layer thickness of ~0.8 nm (corresponding to ~2-3 graphene layers) showed high activity and excellent durability with no noticeable activity loss, even after 20000 cycles of ADT test. This ultrathin carbon coating not only acts as a protective layer to prevent aggregation of Pt NPs but also leads to a better sample dispersion in the solvent which is devoid of

aggregates resulting in a better Pt utilization. We believe that this polymeric nanoencapsulation strategy is a promising technique for the production of highly active and stable ORR catalysts for fuel cells and metal-air batteries.

Second, we used three different kinds of graphene materials including pristine graphene, nitrogen-doped graphene (N-graphene) and nitrogen phosphorus co-doped graphene (N, P-graphene) as supporting materials to anchor platinum clusters. Then a comprehensive study of the interaction effect between support and Pt clusters was discussed. The N, P graphene not only reduces the Pt size and facilitates the homogeneous distribution on the surface but also affects the Pt electronic structure that promotes the ORR activity. The Pt/N, P-graphene not only shows a high ORR activity, low Tafel slope, and 4-electron ORR pathway with low H₂O₂ yield but also excellent durability.

In addition, on the basis of the research about the doped graphene, we synthesized nitrogen and phosphorus co-doped graphene dots supported on nitrogen-doped three-dimensional graphene (N, P-GDs/N-3DG) by a facile freeze-annealing process. The as-obtained N, P-GDs are uniformly dispersed on the surface of the interconnected 3D porous network. The metal-free N, P-GDs/N-3DG composite exhibits excellent electrocatalytic activity for the ORR comparable to the commercial Pt/C catalyst. Moreover, it shows a higher tolerance to methanol and better stability than the Pt/C. This enhanced electrocatalytic performance can be ascribed to the synergetic effect of abundant functional groups and the edge defects.

Keywords: PEMFCs, ORR, Pt, carbon coating, CNTs, graphene, N, P doped, 3D graphene

RÉSUMÉ

Les changements climatiques à cause de la consommation des combustibles fossiles sont actuellement un défi urgent dans le monde entier. Les sources d'énergie pratiques et écologiquement durables pour remplacer les combustibles fossiles traditionnels sont indispensables. La pile à combustible, en particulier la pile à combustible à membrane échangeuse de protons (en anglais : PEMFC), est considérée comme l'un des candidats les plus prometteurs, car elle pourrait convertir directement l'énergie chimique en énergie électrique utilisant par la méthode électrochimique. Théoriquement, la performance du rendement des piles à combustible est déterminée par la cinétique de la réaction d'oxydation de l'hydrogène (en anglais : HOR) sur l'anode et par la réaction de réduction de l'oxygène (en anglais : ORR) sur la cathode. Pratiquement, la cinétique de l'ORR sur la cathode est inférieure à cinq ordres de grandeur ($\sim \times 10^5$) à celle du HOR sur l'anode. La mise au point d'électrocatalyseurs très efficaces pour faciliter l'ORR cathodique très lente est un souci très important. À présent, le platine (Pt) est toujours un électrocatalyseur d'ORR le plus utilisé dans l'industrie. Cependant, l'électrocatalyseur de Pt/C est difficile à commercialiser dans l'industrie en raison du coût élevé et la stabilité opérationnelle à long terme inadéquate. Jusqu'à maintenant, un grand nombre de recherches ont été contribuées à la résolution des problèmes susmentionnés et ces stratégies peuvent être divisées en deux parties: (i) Le catalyseur de Pt/C sera amélioré soit par la méthode de modification de particule de Pt en remplaçant le support conventionnel; soit par l'ingénierie de surface par la modification du revêtement des nanoparticules (en anglais : NPs) de Pt;

(ii) Des catalyseurs à base de Pt seront remplacés par des catalyseurs à base de métaux non-précieux et des catalyseurs sans métaux.

Tout d'abord, nous avons synthétisé des électrocatalyseurs composés des NPs de Pt avec le support des nanotubes de carbone (en anglais : CNTs) et recouverts d'une couche ultramince de carbone graphitique. Ces catalyseurs d'ORR hybrides ont été obtenus par la méthode d'encapsulation-graphitisation de polymère *in situ* interfaciale, dans lequel un polymère contenant du glucose a été croit directement à la surface de Pt/CNTs. L'épaisseur de la couche de revêtement de carbone peut être réglée d'entre 0,5 et plusieurs nanomètres en programmant simplement la croissance du polymère sur Pt/CNTs. Les résultats sur Pt/CNTs@C avec l'épaisseur de couche de carbone d'environ de 0,8 nm (correspondant au graphène en 2-3 couches) ont montré l'activité élevée et une excellente durabilité sans perte d'activité notable, même après 20000 cycles du test ADT. Ce revêtement de carbone ultramince s'agit non seulement comme une couche protectrice pour empêcher l'agrégation des NPs de Pt, mais conduit également à une meilleure dispersion de l'échantillon dans un solvant dépourvu d'agrégats, ce qui entraîne une meilleure utilisation de Pt. Nous

croyons que cette stratégie de nano-encapsulation polymère constitue une technique prometteuse pour la production de catalyseurs d'ORR actifs et stables pour les piles à combustible et les batteries du métal-air.

Ensuite, nous avons développé trois types de graphène différents: le graphène non modifié, le graphène dopé à l'azote (N-graphène) et le graphène co-dopé aux phosphore et azote (i.e., N, P-graphène) en s'agitant des supports pour ancrer les amas de Pt. Après, l'étude complète de l'effet d'interaction du support sur les amas de Pt a été discutée. Le N, P-graphène réduit non seulement la taille du Pt et facilite la distribution homogène à la surface, mais influence également la structure électronique du Pt qui favorise l'activité d'ORR. Le Pt/N, P-graphène présente non seulement l'activité élevée d'ORR, la pente basse de Tafel et le voie d'ORR à 4-électron avec le rendement faible en H_2O_2 mais une excellente durabilité.

En fin, à base de recherche sur le graphène dopé, nous avons synthétisé des points de graphène co-dopés aux phosphore et azote en soutenant sur le graphène 3-D dopé à l'azote (i.e., N, P-GDs/N-3DG) par une simple méthode sur le recuit par congélation. Les N, P-GDs sont uniformément dispersés à la surface du réseau poreux 3-D interconnecté. Le composite N, P-GDs/N-3DG sans métal montre une performance électrocatalytique très élevée sur l'ORR comparable au catalyseur commercial de Pt/C. De plus, il présente la tolérance au méthanol plus élevée et la stabilité meilleure au Pt/C. La performance électrocatalytique peut être améliorée par l'effet synergique d'entre les groupes fonctionnels abondants et les défauts du bord.

Mots-clés:

PEMFCs, ORR, Pt, revêtement de carbone, CNTs, graphène, dopé aux N, P, et graphène 3-D

ACKNOWLEDGEMENTS

Firstly, I would like to thank Prof. Shuhui Sun for giving me the opportunity to study at INRS-EMT. Thanks to his patient guidance and consistent support during my Ph.D. study. Under his supervision, I not only made progress in the academic field but also developed and polished my personality. Also, I would like to express my very great appreciation to my co-supervisor Prof. Jerome P. Claverie for providing me precious advice and direction throughout my Ph.D. study. His willingness to give his time so generously has been very much appreciated.

I would like to offer my special thanks to Dr. Gaixia Zhang for her great help and valuable comments on my research and thesis writing.

I would like also to thank all the group members named below: Dr. Qiliang Wei, Nathan Komba, Xiaohua Yang, Yanqing Fu, Mingjie Wu, Zhangsen Chen, Fan Yu, Jun Zhang, Dr. Erhu Yan, Dr. Lei Du, Dr. Zonghua Pu, Dr. Zhankun Jiang and so on. I am very honor to be part of such a supportive, hardworking, and inspiring group. Many thanks to Dr. Lei Du for revising my thesis.

I would like to thank the jury members, Prof. Luca Razzari, Prof. Gessie Brisard, and Prof. John Oh for agreeing to be the reviewers and thanks in advance for the comments. Thanks to Prof. Ana Tavares and Prof. Fiorenzo Vetrone, their advice given on my doctoral examination has been a great help in later research.

I would like to thank all my collaborators for their assistance with the collection of my data. I also thank the departmental and technical staff at INRS-EMT.

I would like to express my very great appreciation to my friends and family. I am particularly grateful for my parents, and my parents in law for their love and support during my life. Thanks for my daughter Xiaotong, the best gift for me from heaven. Special thanks to my wife Xinxing, she made me feel like the luckiest man in the world every single day. I'd like to take this opportunity to tell them, I love you.

TABLE OF CONTENTS

ABSTRACT	III
RÉSUMÉ	V
ACKNOWLEDGEMENTS	VII
TABLE OF CONTENTS	VIII
LIST OF FIGURES	XI
LIST OF TABLES	XIII
LIST OF CHEMICAL COMPOUNDS	XV
LIST OF ABBREVIATIONS	XVI
1 INTRODUCTION	1
1.1 PROTON EXCHANGE MEMBRANE FUEL CELLS	2
1.1.1 <i>Work Fundamentals</i>	2
1.1.2 <i>Fuel Cell Thermodynamics</i>	3
1.1.3 <i>Fuel Cell Reaction Kinetics</i>	4
1.2 OXYGEN REDUCTION REACTION	8
1.2.1 <i>Oxygen Reduction in Acidic Media</i>	9
1.2.2 <i>Oxygen Reduction in Alkaline Media</i>	10
1.3 CATALYSTS FOR ORR	12
1.3.1 <i>Pt-based material</i>	12
1.3.2 <i>Non-precious metal catalysts</i>	13
1.3.3 <i>Metal-free catalysts</i>	14
1.4 PT-BASED ORR CATALYSTS	16
1.4.1 <i>The modification of Pt particle</i>	17
1.4.2 <i>Surface engineering</i>	19
1.4.3 <i>Replacing conventional support</i>	21
1.5 GRAPHENE-BASED METAL-FREE CATALYST	22
1.5.1 <i>Chemically modified graphene</i>	22
1.5.2 <i>Dimension-tailored graphene</i>	24
1.5.3 <i>Graphene-based supporting material</i>	27
1.6 OBJECTIVES OF THE WORK	27
1.7 THESIS ORGANIZATION	28
2 EXPERIMENTAL	31
2.1 CHEMICAL AND MATERIALS	31
2.2 MATERIAL SYNTHESIS	31
2.2.1 <i>Carbon-coated Pt/CNTs catalyst</i>	31

2.2.2	<i>Pt/N, P-graphene catalyst</i>	32
2.2.3	<i>N, P-graphene dots/N-3DG catalyst</i>	33
2.3	PHYSICAL CHARACTERIZATIONS	33
2.4	ELECTROCHEMICAL CHARACTERIZATIONS	34
2.4.1	<i>Cyclic voltammetry</i>	35
2.4.2	<i>ORR polarization curve</i>	37
2.4.3	<i>ORR durability screening technique based on RDE</i>	39
3	ULTRA-THIN CARBON COATED PT/CNTS CATALYST	40
4	PLATINUM SUPPORTED ON DOPED GRAPHENE	69
5	GRAPHENE BASED METAL FREE CATALYST	95
6	CONCLUSIONS AND PERSPECTIVES	122
6.1	CONCLUSIONS.....	122
6.2	PERSPECTIVES	123
7	BIBLIOGRAPHY	125
	LIST OF PUBLICATIONS	138
	SOMMAIRE RÉCAPITULATIF	140

LIST OF FIGURES

Figure 1.1.	A Schematic diagram of PEMFCs. ¹¹	2
Figure 1.2.	Gibbs Energy change for an electrochemical reaction. An activation barrier (E_a) impedes the conversion of reactants to products. A catalyzed reaction has lower activation energy barrier (E_a^*). ¹²	4
Figure 1.3.	At equilibrium, the chemical free-energy difference (a) across a reaction interface is balanced by an electrical potential difference (b), resulting in a zero net reaction rate (c). ¹²	5
Figure 1.4.	With an external bias, η , the forward reaction is favoured over the reverse reaction. While the (a) of the chemical energy is the same as before, The external bias changes the electrical potential (b) upsets the balance between the forward and reverse activation barriers (c). ¹²	7
Figure 1.5.	(a) Different configurations of O_2 adsorption on catalyst surfaces and (b) Reaction scheme of an associative mechanism and a dissociative mechanism for ORR. ^{25, 26}	10
Figure 1.6.	Schematic illustration of the double-layer structure during ORR in acidic (left) and alkaline (right) conditions. ²⁸	11
Figure 1.7.	Trends in oxygen reduction activity plotted as a function of the oxygen binding energy. ²²	12
Figure 1.8.	Possible mechanisms for ORR on (a) precious metal and (b) Me-N-C catalysts. RDS is shown in red. ⁴²	14
Figure 1.9.	Carbon nanomaterials: (A) graphite, (B) diamond, (C) buckminsterfullerene C60, (D) single-wall carbon nanotube, (E) graphene, (F) heteroatom-doping of graphitic carbon structure, and (G) charge-transfer doping of graphitic carbon structure by electron donor (n-doping) or electron acceptor (p-doping) and the associated bandgap structures. ⁴⁸	15
Figure 1.10.	Simplified representation of suggested degradation mechanisms for platinum particles on carbon support in fuel cells. ⁶⁹	16
Figure 1.11.	Recent important advances in new active and durable Pt-based nanostructures for improved ORR catalysis. ⁷⁷	18
Figure 1.12.	Schematic of the stable mechanism of ultrathin carbon layer (UTCL) coated Pt/C catalysts in terms of UTCL on Pt NPs. (A) Mitigating dissolution-growth of Pt NPs; (B) inhibiting Pt NPs from detachment (left) and migration (right). ¹¹³	20
Figure 1.13.	Schematic representation of different types of N atoms (graphitic, pyridinic and pyrrolic N). ¹⁴⁷	23
Figure 1.14.	(a) The TEM image of graphene quantum dots (GQDs). ¹⁵² (b) The TEM image of graphene nanoribbons (GNRs). (c) SEM images of 3D-Graphene (3D-G). A digital photo of 3D-G is presented in the inset. ¹⁵³	24
Figure 1.15.	A guide illustrating the arrangement of this thesis.	28
Figure 2.1.	Photo and schematic Illustration of the freezing process of N, P-GDs/N-3DG.	33
Figure 2.2.	Schematic of an RRDE setup in a three-electrode electrochemical cell. ²⁰²	35
Figure 2.3.	The typical CV of the commercial Pt/C catalyst at a sweep rate of 50 mV s^{-1} in N_2 -saturated 0.1 M HClO_4 between 0.02 to 1.2 V vs. RHE.	36
Figure 2.4.	Typical ORR polarization curve.....	37
Figure 3.1.	TEM images of Pt/CNTs (a, b), PSAGA encapsulated Pt/CNTs before (c, d) and after (e, f) graphitization. Inset of (f) shows the HR-TEM image of Pt/CNTs@C. (g) Corresponding Pt NP size variation of all nanohybrids at different synthetic steps. The size distributions of Pt were analyzed by randomly selecting 100 NPs to measure their diameters.	46
Figure 3.2.	TEM images of Pt/CNTs@C samples prepared using different amount of monomers. (a-d) correspond to the Pt/CNTs@C-1 to 4, respectively, listed in Table 1. Insets show the HR-TEM images.	48

Figure 3.3.	TGA curves of Pt/CNTs and Pt/CNTs@C with a carbon coating of ~ 0.8 nm (Pt/CNTs@C-2 in Table 1)	48
Figure 3.4.	XRD patterns (a) and XPS spectra (b) of Pt/CNTs and Pt/CNTs@C.	50
Figure 3.5.	CV curves of different cycles on Pt/CNTs (a), Pt/CNTs@C-1 (b), Pt/CNTs@C-2 (c), Pt/CNTs@C-3 (d) and Pt/CNTs@C-4 (e). (f) CVs of the 1st cycle for all samples. CVs were recorded in N ₂ -saturated 0.1 M HClO ₄ . (50 mV s ⁻¹ , room temperature).	51
Figure 3.6.	ECSA as a function of reaction cycles for Pt/CNTs and Pt/CNTs@C-(1-4). The values of ECSA were calculated from the H _{ads} /H _{des} charge in CVs.	52
Figure 3.7.	LSVs on Pt/CNTs (a), Pt/CNTs@C-1 (b), Pt/CNTs@C-2(c), Pt/CNTs@C-3 (d) and Pt/CNTs@C-4 (e) (before and after ADT test, 3000cycles) (f) Pt/CNTs and Pt/CNTs@C-2 in the presence of 0.5M methanol. LVs were recorded in O ₂ -saturated 0.1 M HClO ₄ . (10 mV s ⁻¹ , room temperature)	54
Figure 3.8.	The TEM images and the size distribution of Pt NPs of Pt/CNTs (a), Pt/CNTs@C-2 (b) after ADT.	55
Figure 3.9.	Long-term performance on CV curves of Pt/CNTs@C-2 (a) and Pt/CNTs (c). ECSA as a function of reaction cycles for Pt/CNTs@C-2 (b) and Pt/CNTs (d). CVs were recorded in N ₂ -saturated 0.1 M HClO ₄ .	56
Figure 4.1.	Schematic Illustration of the Fabrication Process of Pt supporting on RGO, N-Graphene and N, P-Graphene.	72
Figure 4.2.	TEM and HRTEM images of (a, b) Pt/N, P-Graphene, (c, d) Pt/N-Graphene and (e, f) Pt/RGO.	73
Figure 4.3.	(a) XPS survey spectra and (b) high-resolution XPS spectra of Pt 4f of Pt/RGO, Pt/N-Graphene and Pt/N, P-Graphene.	75
Figure 4.4.	Electrochemical characterization of commercial Pt/C (20%), Pt/N, P-Graphene, Pt/N-Graphene, and Pt/RGO (a) LSV curves on RRDE in O ₂ -saturated 0.1 M HClO ₄ at a scan rate of 10 mV s ⁻¹ (rotation speed: 1600 rpm), room temperature. (b) Tafel region of ORR measurement. (c) H ₂ O ₂ yields and Electron transfer numbers. (d) Chronoamperometric responses in an O ₂ -saturated aqueous solution of 0.1 M HClO ₄ .	76
Figure 4.5.	Schematic Illustration of the assembly mechanism of Pt supported on doped graphene.	78
Figure 5.1.	TEM images of N, P-GDs/N-3DG. (a, b) Inset: corresponding size distribution histogram of N, P-GDs/N-3DG. Elemental mapping images of N, P-GDs/N-3DG. (c) Dark-field TEM image, elemental mapping of C, N, O, P and the mixed elements with the dark-field image.	101
Figure 5.2.	(a) High resolution N1s XPS spectra of N-3DG (a) and N, P-GDs/N-3DG (b). (b) High resolution P2p XPS spectra of P-GDs/3DG (c) and N, P-GDs/N-3DG (d). Normalized concentrations of (e) N1s binding configurations for N-3DG, N, P-GDs/N-3DG and (f) P2p binding configurations for P-3DG, N, P-GDs/N-3DG.	102
Figure 5.3.	(a) CVs of four samples named as 3D graphene, N-3DG, P-GDs/3DG and N, P-GDs/N-3DG in N ₂ -saturated 0.1 M KOH at a scan rate of 100 mV s ⁻¹ . (b) RDE polarization curves of the as-prepared materials and Pt/C 20% in O ₂ -saturated 0.1 M KOH at a scan rate of 10 mV s ⁻¹ (rotation speed: 1600 rpm). (c) Hydrogen peroxide yields and (d) electron transfer numbers of 3D graphene, N-3DG, P-3DG and N, P-GDs/N-3DG as the function of the electrode potential.	103
Figure 5.4.	Optimized structures of the lowest O ₂ adsorption energy configurations on different bond structures in N, P-GDs/N-3DG: (a, b) P-N bond structure, (c, d) P-C, N-C bond structure. (a, c) Side-on direction, (b, d) Head-on direction. The gray, yellow, blue and red colors represent carbon, phosphorus, nitrogen, and oxygen atom, respectively.	106

LIST OF TABLES

Table 1.1	The main types of fuel cell.....	1
Table 1.2	Summary of some typical work of 3D-G based material on ORR.....	25
Table 2.1	The recipe of the catalyst ink.....	35
Table 3.1	Recipe for the synthesis of carbon coated Pt supported on CNTs with different thickness.....	47

LIST OF CHEMICAL COMPOUNDS

C	carbon
Pt	platinum
N	nitrogen
B	boron
S	sulfur
P	phosphorus
Ar	argon
CO	carbon monoxide
H ₂	hydrogen
N ₂	nitrogen gas
NH ₃	ammonia
O ₂	oxygen
HClO ₄	perchloric acid
HCl	hydrochloric acid
H ₂ SO ₄	sulfuric acid
H ₂ PtCl ₆	chloroplatinic acid
HCOOH	formic acid
Ph ₃ P	triphenylphosphine
HNO ₃	nitric acid
H ₂ O ₂	hydrogen peroxide
KOH	potassium hydroxide
KMnO ₄	potassium permanganate
SDS	sodium lauryl sulfate
AGA	N-acryloyl-D-glucosamine

LIST OF ABBREVIATIONS

3D-G	three dimensional graphene
ADT	accelerated durability test
AFC	alkaline fuel cell
BE	binding energy
CNTs	carbon naotubes
CV	cyclic voltammetry
DFT	density functional theory
ECSA	electrochemical active surface area
EDS	energy dispersive spectroscopy
FC	fuel cell
FCC	face-centered cubic
HRTEM	high-resolution transmission electron microscope
GC	glassy carbon
HOR	hydrogen oxidation reaction
LSV	linear sweeping voltammetry
MA	mass activity
NPs	nanoparticles
N-G	nitrogen doped graphene
N-3DG	nitrogen doped three dimensional graphene
N, P-G	nitrogen and phosphorus co doped graphene
N, P-GDs	nitrogen and phosphorus co doped graphene dots
N, P-GDs/N-3DG	nitrogen and phosphorus co doped graphene dots on nitrogen doped three dimensional graphene
OCV	open circuit voltage

ORR	oxygen reduction reaction
PEMFC	polymer electrolyte membrane/proton exchange membrane fuel cell
P-GDs	phosphorus doped graphene dots
P-GDs/3DG	phosphorus doped graphene dots supported on three dimensional graphene
Pt/C	platinum supported on carbon black
Pt/CNTs	platinum supported on carbon nanotubes
Pt/CNTs@C	carbon coated platinum supported on carbon nanotubes
Pt/3DG	platinum supported on three dimensional graphene
Pt/P-G	platinum supported on phosphorus doped graphene
Pt/N-G	platinum supported on nitrogen doped graphene
Pt/P, N-G	platinum supported on nitrogen and phosphorus co doped graphene
RHE	reversible hydrogen electrode
RPM	revolutions per minute
RRDE	rotating ring-disk electrode
RGO	reduced graphene oxide
SAC	single-atom catalysts
SCE	saturated calomel electrode
SEM	Scanning Electron Microscopy
SHE	standard hydrogen electrode
TEM	transmission electron microscope
TPP	triphenylphosphine
XPS	X-ray photoelectron spectroscopy
XRD	X-ray diffraction

1 INTRODUCTION

Climate change caused by the use of fossil fuels has become an urgent and worldwide challenge on a daily basis. Besides, with rising global population and the development of human society, there will be continuously increased energy demands (more than a quarter to 2040 predicted by International Energy Agency) as well as rapid depletion of world's limited fossil fuel sources. Energy crisis and environmental pollution are highlighted to be one of the major global problems. Therefore, the search for clean energy generation and utilization technologies has become one of the greatest challenges to ensure the world's sustainable development. Fuel cells are one of the most promising clean energy devices offering high energy densities and energy efficiencies.¹⁻⁴

Over the last few decades, five major categories of fuel cells have been developed as shown in Table 1.1. Among various fuel cells, the proton exchange membrane fuel cells (PEMFCs), which use a solid phase proton conducting membrane (typically Nafion) as an electrolyte, show many advantages such as low operating temperature, fast startup, and high power density. It has been attracting significant attention and receiving intense research efforts for portable electronic and transportation applications, which are already used in the commercial fuel cell vehicles such as Mirai, Clarity and Tucson FCEV.⁵⁻¹⁰

Table 1.1 The main types of fuel cell.

Fuel Cell Type	Proton exchange membrane fuel cells(PEMFC)	Alkaline fuel cell (AFC)	Phosphoric acid fuel cell (PAFC)	Molten carbonate fuel cell (MCFC)	Solid oxide fuel cell (SOFC)
Fuel	H ₂	H ₂	H ₂	H ₂ /CO/reformate	CO,H ₂
Oxidizer	O ₂ , air	O ₂ , air	O ₂ , air	CO ₂ , O ₂ , air	O ₂ , air
Electrolyte	Solid polymer film	Alkaline solution	Phosphoric acid	Molten carbonate	Ceramic oxide
Operating temperature	50-100 °C	50-120 °C	150-220 °C	600-700 °C	600-1000 °C
Efficiency	60%	60%	40%	50-60%	50-60%
Application	Backup power, Portable power, Distributed generation, Transportation	Military, Space	Distributed generation	Electric utility, Distributed generation	Electric utility, Distributed generation
Challenge	Expensive catalyst, sensitive to fuel impurities	Membrane, electrolyte management	Long start up time	High temperature corrosion and breakdown of cell components, Long start up time	High temperature corrosion and breakdown of cell components

1.1 Proton Exchange Membrane Fuel Cells

1.1.1 Work Fundamentals

A PEMFC is an electrochemical cell which directly converts the chemical energy of a fuel (typically hydrogen, methanol, etc.) into electrical energy, heat, and water. The structure of PEMFCs is shown in Figure 1.1. A polymer electrolyte membrane is sandwiched between a cathode (or positive electrode) and an anode (or negative electrode). The hydrogen molecules on the anode could be catalytically split into protons and electrons through hydrogen oxidation reaction (HOR). The electrons go through an external circuit to the cathode side, producing direct current electricity. The protons are drawn through the polymer electrolyte membrane to the cathode, reacting with one oxygen molecule and desired four electrons to form two water molecules. Although the reaction is thermodynamically spontaneous, under fuel cell operating condition, the hydrogen and oxygen gas are kinetically stable. The catalysts on both electrode sides are thus essential to lower the activation energy and ensure the reaction proceeds by alternative pathways.

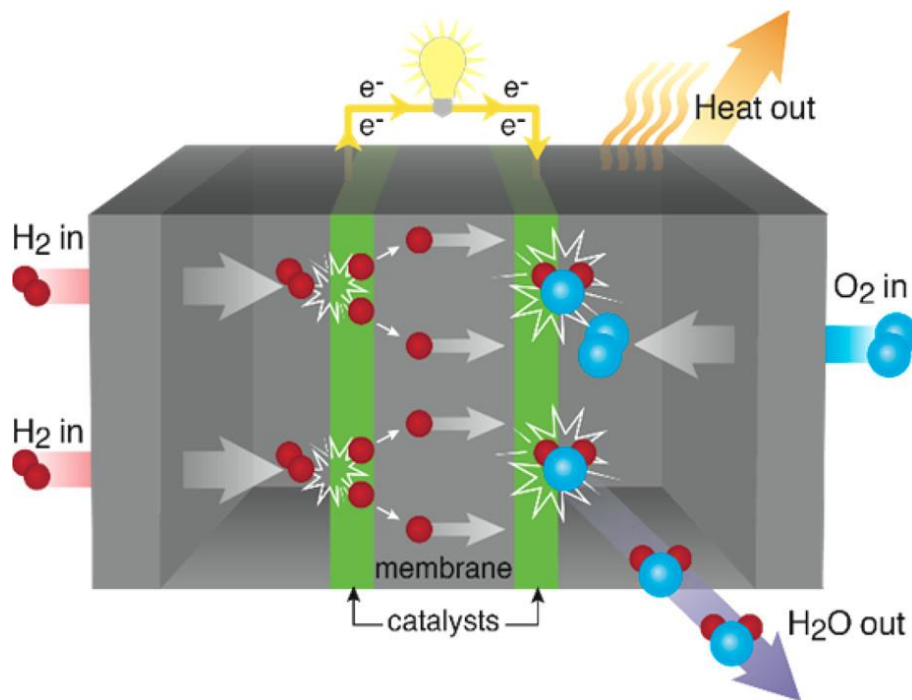
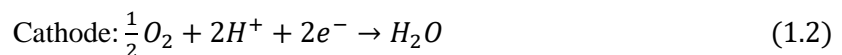


Figure 1.1. A Schematic diagram of PEMFCs.¹¹

Different from the direct chemical reaction, e.g combustion, the electrochemical reactions in the fuel cell happen simultaneously on anode and cathode. This half-cell reaction is described as follows:



Thus, the overall reaction is:



1.1.2 Fuel Cell Thermodynamics

Fuel cell thermodynamics is crucial to understanding the conversion of chemical energy into electrical energy. The target of a fuel cell is to convert the chemical energy into electrical energy in high efficiency. It's deserved to know the theoretical efficiency, equilibrium potential and other thermodynamic factors of the fuel cell.

By definition, the efficiency η is defined as the ratio between the useful output work of a device and the supplied heat.

$$\eta = \frac{W_{out}}{Q_{in}} \quad (1.4)$$

In a fuel cell, the heat input means the heating value of the fuel, which is the enthalpy of the reaction, that is $Q_{in} = -\Delta H$. The useful output work in fuel cell means theoretical maximum electrical energy output, which is identical to the negative variation in Gibbs free energy.

$$W_{out} = W_{elec} = -\Delta G \quad (1.5)$$

So the efficiency η can be obtained by the following formula,

$$\eta = \frac{\Delta G}{\Delta H} \quad (1.6)$$

Therefore, the efficiency of the fuel cell is not limited by Carnot's rule. For example, under ambient conditions the $\Delta G = -237$ kJ/mol and the $\Delta H = -286$ kJ/mol (producing liquid water). The maximum efficiency at 25 °C would be 83%. In addition, the work done by an internal combustion engine (seemed as ideal heat engine) increases with the increasing temperature while the reverse is true in Fuel cell because the ΔG decreases with increasing temperature. So the FC shows a higher thermodynamic efficiency at low temperature but lower efficiency at high temperature (> 700 °C) than that of heat engine.

In addition, in fuel cell the electrical work can be described by the equation:

$$W_{elec} = nFE \quad (1.7)$$

where the n is the number of electrons exchanged during the reaction (2 for H₂/O₂ fuel cell), F is the faraday constant (96500 C mol⁻¹). So the reversible open circuit voltage can be obtained from Gibbs free energy change of an electrochemical transformation:

$$E^0 = -\frac{\Delta G}{nF} \quad (1.8)$$

So under standard-state conditions, the maximum equilibrium cell potential is 1.229V, as known as open circuit voltage (OCV). According to the Nernst equation, the equilibrium potential of oxygen electrode reactions in nonstandard conditions can be estimated:

$$E = E^0 - \frac{RT}{nF} \ln\left(\frac{a_{H_2O}}{p_{H_2} * p_{O_2}^{\frac{1}{2}}}\right) \quad (1.9)$$

where R is the gas constant, T is the Kelvin temperature, n is the number of electrons transferred, F is the Faraday constant, and p is the pressure of the reactant and product.

The above are all based under thermodynamic balance conditions, where the FC cell is in a state of equilibrium, with no current delivered. In practice, the real efficiency and output voltage are always less than the theoretical value. The low real efficiency of a fuel cell is impacted by fuel utilization loss and voltage loss. The fuel utilization loss means that not all of the fuel participates in the real reaction. The voltage loss accounts for the fact that the output voltage of the fuel cell depends on the current drawn from the fuel cell.

1.1.3 Fuel Cell Reaction Kinetics

Although the Gibbs free energy of the PEMFCs reaction is negative, meaning the PEMFCs reaction is thermodynamically spontaneous, this reaction still needs to be kinetically-activated. That is, the reaction rates are finite under fuel cell operating condition. An energy barrier needs to be overcome for the reaction to occur. Only the reactant in an activated state (at the peak of energy diagram in Figure 1.2.) can be converted into products. The reaction rate is determined by the probability that the reactant species can make it over the activation energy barrier. A catalyst can provide an alternative path that has a lower activation energy barrier. A lower activation energy barrier is expected to result in a faster reaction rate.

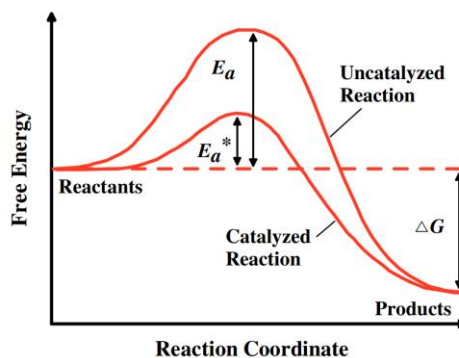


Figure 1.2. Gibbs Energy change for an electrochemical reaction. An activation barrier (E_a) impedes the conversion of reactants to products. A catalyzed reaction has lower activation energy barrier (E_a^*).¹²

Statistical mechanics indicates that the probability of finding a species in an activated state is exponentially dependant on the activation barrier:

$$P = \exp\left(\frac{-\Delta G_1^\ddagger}{RT}\right) \quad (1.10)$$

where P is the probability of finding a reactant species in the activated state, ΔG_1^\ddagger is the energy barrier (energy gap between the reactants and the activated species), R is the universal gas constant and T is the temperature (K). So the reaction rate of forward reaction (r_1) can be written as:

$$r_1 = c_R^* f_1 P = c_R^* f_1 \exp\left(\frac{-\Delta G_1^\ddagger}{RT}\right) \quad (1.11)$$

where c_R^* is the reactant surface concentration, f_1 is the transformation rate from activated state to final products, and ΔG_1^\ddagger is the energy barrier between the reactant and activated states. However, this is still not the net reaction rate, because the reverse reaction is happening too. Corresponding forward (r_1) and reverse (r_2) rates, the net reaction rate is defined as the

$$r = r_1 - r_2 \quad (1.12)$$

In a fuel cell, the reaction rate can be converted into current density (j) by:

$$j = nFr \quad (1.13)$$

where n is the number of electrons transferred. Combining equations (1.11), (1.12) and (1.13), the overall current density of the reaction can be written as:

$$j = nFc_R^* f_1 \exp\left(\frac{-\Delta G_1^\ddagger}{RT}\right) - nFc_P^* f_2 \exp\left(\frac{-\Delta G_2^\ddagger}{RT}\right) \quad (1.14)$$

where subscripts “1” and “2” denote the forward and reverse reactions, respectively. c_p^* is the product surface concentration.

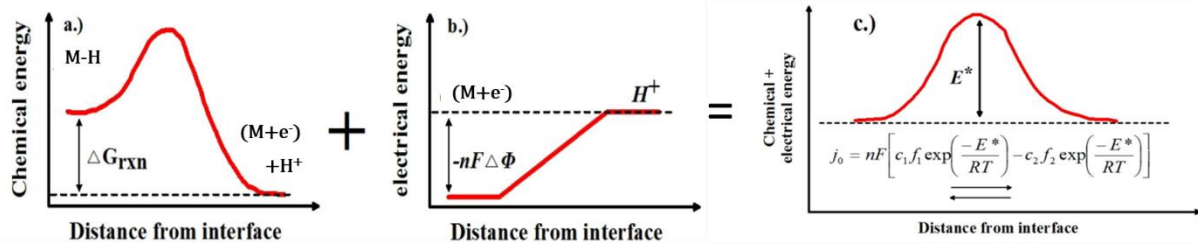


Figure 1.3. At equilibrium, the chemical free-energy difference (a) across a reaction interface is balanced by an electrical potential difference (b), resulting in a zero net reaction rate (c).¹²

Understanding the equilibrium state of a reaction is useful to analyze the energies of the system. At equilibrium, there is no net current density. That is, the forward and reverse current densities must balance. Using the HOR as an example, Figure 1.3(a) shows the free-energy of the reaction state(M-H) is higher than the product state([M+e-]+H⁺). It leads to unequal activation barriers for the forward- versus reverse-

reaction directions and results in a net forward reaction. However, the net forward reaction creates a separation of electrons and ions at opposite sides of the interface (with e^- accumulating in the metal electrode and H^+ accumulating in the electrolyte). As shown in Figure 1.3(b), the separation of charges caused a potential difference ($\Delta\phi$) across the electrode-electrolyte interface. The separation of charges and ions continues until the resultant potential difference ($\Delta\phi$) counterbalances the difference in free energies between the reactant and product state. Figure 1.3(c) shows the combined effect of the chemical and electrical potentials. This balance results in an equal activation barrier (ΔG^*) for the forward and reverse reactions, so the equilibrium current density (also known as the exchange current density, j_0) is defined as:

$$j_0 = nF c_R^* f_1 \exp\left(\frac{-\Delta G^*}{RT}\right) - nF c_P^* f_2 \exp\left(\frac{-\Delta G^*}{RT}\right) \quad (1.15)$$

At the equilibrium condition, the two force (difference in chemical free energy between the reactant and product states; electrical potential difference which is created by charges and ions accumulate at opposite sides of the interface) contributions balance, leading to a dynamic equilibrium with zero net reaction. The electrons are not transferred to an external load and the ions are not consumed in further reactions. Both the anode and cathode have interfacial electrical potential differences. The sum of these interfacial electrical potential differences ($\Delta\phi_{anode} + \Delta\phi_{cathode}$) yields the overall equilibrium voltage for the fuel cell, which is known as the Galvani potential.

A change in cell voltage can affect the magnitude of activation barrier. Charged species are involved in the reaction as either reactants or products. The free energy of a charged species is sensitive to voltage. Therefore, changing the cell voltage changes the free energy of the charged species taking part in a reaction, thus affecting the size of the activation barrier. As shown in Figure 1.4 (using the HOR as an example), if the electrical potential is decreased by η due to an external bias, the free-energy for the forward and reverse reactions does not change (compared with Figure 1.4(a)). The change in electrical potential break the balance between the forward and reverse activation barriers. The forward reaction activation barrier is (reduced by $\alpha nF\eta$ and the reverse reaction activation barrier is increased by $(1-\alpha)nF\eta$. Here, α is called the charge transfer coefficient depending on the symmetry of the activation barrier and it denotes how a change in Galvani potential changes the activation barrier for forward and reverse reactions thus producing a net cell current. The change in Galvani potential as a result of an external load or an applied potential (η) is defined as the overpotential. Overpotential is the potential applied to the electrode-electrolyte interface to direct the net reaction away from equilibrium. In the fuel cell, the overpotential reduces the cell potential from the reversible voltage to a lower value.

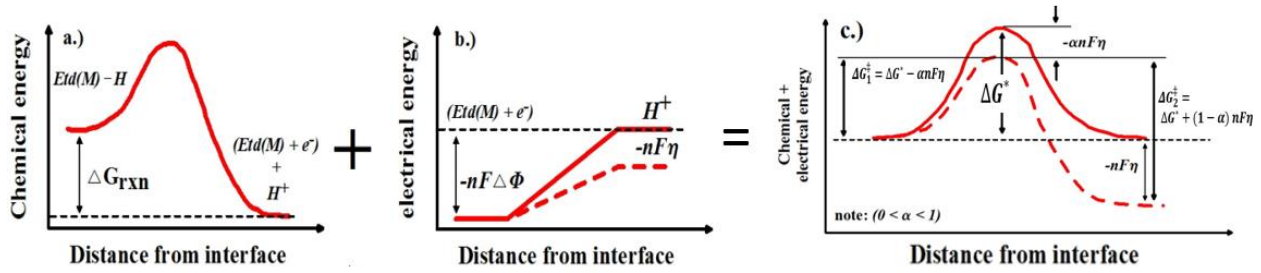


Figure 1.4. With an external bias, η , the forward reaction is favoured over the reverse reaction. While the (a) of the chemical energy is the same as before, The external bias changes the electrical potential (b) upsets the balance between the forward and reverse activation barriers (c).¹²

Combining the current density of the reaction counting formula in equation (1.14) and Figure 1.4, the relationship between the current density and activation overpotential can be described as

$$j = j_0 \exp\left(\frac{\alpha n F \eta}{RT}\right) - j_0 \exp\left(\frac{-(1-\alpha) n F \eta}{RT}\right) \quad (1.16)$$

Where j is electrode current density, j_0 is exchanged current density, α is the charge transfer coefficient (between 0-1), η is activation overpotential.

This equation is called as Butler–Volmer equation, which is broadly used as an excellent approximation for most electrochemical reactions. The Butler–Volmer equation basically states that the current produced by an electrochemical reaction increases exponentially with overpotential. In other words, if there are more current output from the fuel cell, there will be increases in voltage loss.

In reality, a fuel cell typically operates at a voltage far away from equilibrium. Particularly when the $\eta > 50\text{-}100$ mV at room temperature, only the forward reaction rate contributes significantly to current density. So the Butler–Volmer equation can be simplified to

$$j = j_0 \exp\left(\frac{\alpha n F \eta}{RT}\right) \quad (1.17)$$

Solving for η yields

$$\eta = \frac{-RT}{\alpha n F} \ln(j_0) + \frac{RT}{\alpha n F} \ln(j) \quad (1.18)$$

In a given reaction, the transfer coefficient (α) and the exchange current density (j_0) are both constant. So the equation 1.18 can be further simplified into:

$$\eta = a + b \ln(j) \quad (1.19)$$

It is known as the Tafel equation, and b is called the Tafel slope. We can get the exchange current density (j_0) and exchange current density (α) by fitting the line of η and $\ln(j)$.

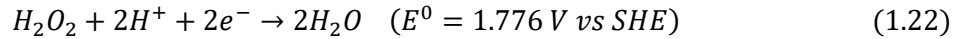
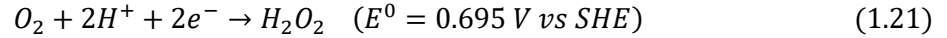
In summary, the kinetic parameters such as α and j_0 seriously affect the electrochemical reactions. Fast reaction kinetics (high α and j_0) results in minor performance loss while sluggish reaction kinetics (low α

and j_o) results in severe performance loss. In PEMFCs, the HOR kinetics on anode is pretty fast, while the ORR on cathode kinetics is greatly slow because of its complicated multi-step reaction. Therefore, most of the activation overvoltage loss takes place at the cathode side. In practice, the kinetics of ORR on the cathode is five orders of magnitude slower than the oxidation reaction on the anode.¹³ Therefore, the ORR at the cathode is the main limiting factor within the overall cell reactions.

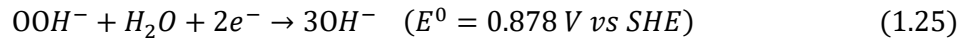
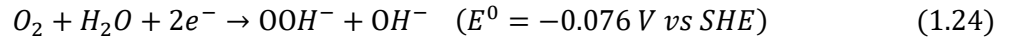
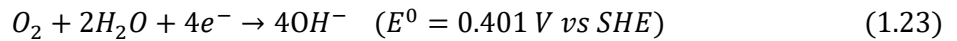
1.2 Oxygen Reduction Reaction

As we mentioned before, the sluggish ORR is the key challenge in high-performance fuel cells as well as metal-air batteries. ORR is an extremely slow reaction because of the high bond energy of oxygen molecules ($\Delta H=498$ kJ/mol). For low-temperature fuel cell, the lack of a sufficiently efficient ORR catalyst seriously limits the overall efficiency of the device. So researchers have put tremendous efforts into discovering and optimizing the ORR catalyst.^{14, 15}

It is generally accepted that ORR proceeds through two different pathways: (i) direct four-electron pathway (ii) indirect two-electron processes. In acidic media, oxygen can either be reduced directly into water molecules or be reduced to hydrogen peroxide as the intermediate species.



Instead of hydrogen peroxide and water as intermediate and product, the ORR generates peroxide anion in the indirect pathway and hydroxide anion as the final product in alkaline media.



Obviously, the four-electron reaction is favored pathway to ensure higher operating potentials and current efficiency. In contrast, the formation of the two-electron reduction product will reduce the effective electron-transfer number of ORR, leading to low energy conversions. Furthermore, the reactive intermediate species can form harmful free radical species that lead to membrane degradation.

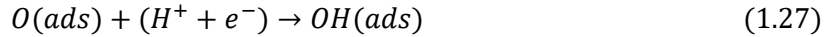
Understanding the role of catalytic active sites and the nature of intermediates involved in the ORR is extremely valuable for four-electron pathway in both theoretical and practical aspects.¹⁶⁻¹⁹ It is important to elucidate those ORR processes at the atomic level, which may help to identify the rate-determining step of the ORR kinetics and the origin of the overpotential. However, the mechanism of ORR is complicated because there are multiple adsorption/desorption, electron transfer processes and reaction steps involving

various oxygen-containing intermediate species. It is easy to be influenced by many experiment parameters such as oxygen partial pressure, temperature, electrolyte pH, potential and surface properties.²⁰ Until now, there is no overwhelming consensus on the ORR mechanism because of the lack of appropriate experimental validation techniques which can precisely identify the composition of the intermediates formed during this reaction.²¹

1.2.1 Oxygen Reduction in Acidic Media

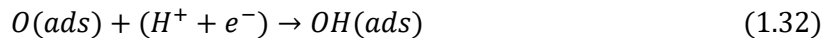
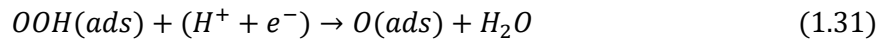
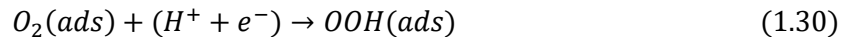
Oxygen reduction in acidic media has been known as an important electrochemical reaction in PEMFCs. Until now, under acidic media Pt-based catalysts remain the mainstay as catalyst materials for ORR. Therefore, we only discussed the ORR mechanism of Pt-based material under acidic media.

In acid, the oxygen can be reduced over different catalysts following two different mechanisms.²² One is the simple dissociative mechanism,

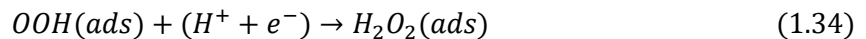


Here, * denotes an active site on the surface, *ads* indicates the corresponding species that are adsorbed on the active site. First, the O=O bond can be broken and then form adsorbed atomic O during the O₂ adsorption process. Then the adsorbed O further gains two electrons and protons to form H₂O in the two consecutive steps.

Another associative mechanism is shown as follow²³.



An alternative to forming water in step 1.33 is to form hydrogen peroxide:



The associative mechanism can also be termed a peroxo mechanism. The first step (Reaction 1.31) represents the adsorption of O₂ on active sites. Obviously, it depends on the number of active sites and the surface properties of the catalyst. Reaction 1.30 represents the first electron transfer of the ORR to form

OOH(ads). After that, a portion of such an intermediate can be further reduced to produce water through reactions 1.33-1.35. The other may be reduced to produce H₂O₂ through Reaction 1.36-1.37. Depending on the catalyst used in ORR, the proportion of two- and four-electron transfer pathways vary, giving an overall electron transfer number of less than four.

The ORR pathway is also believed to be affected by the adsorption and coverage of oxygen on the catalyst surface.²⁴ If there are high oxygen coverage, an associative mechanism is dominant. At low oxygen coverage, ORR occurs via dissociative mechanism without the formation of a HOO (ads) intermediate.²² Moreover, the situation varies on different electrode materials.¹³

1.2.2 Oxygen Reduction in Alkaline Media

ORR in alkaline media is supposed to be a vital electrochemical reaction in alkaline fuel cells and alkaline metal-air batteries. Compared with ORR in acid, it is more facile for both thermodynamic and kinetic reasons.¹⁹ A large number of non-precious-metal (Pt-free) catalysts have shown equivalent or even better electrocatalytic ORR performance than Pt in alkaline electrolytes.

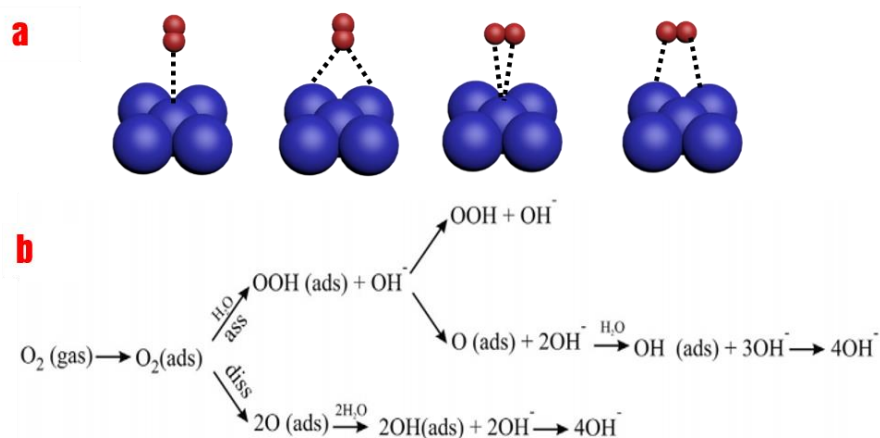


Figure 1.5. (a) Different configurations of O₂ adsorption on catalyst surfaces and (b) Reaction scheme of an associative mechanism and a dissociative mechanism for ORR.^{25, 26}

The ORR pathways and mechanisms can vary with the catalytic materials used. Even for the same catalyst, the ORR behaves as a structure-sensitive reaction, related to the active sites of the catalyst. The first step is the adsorption of O₂ on active sites of the catalyst. Depending on the surface properties and the binding energy, there are four kinds of configurations of O₂ adsorption on catalyst surfaces: top end-on, bridge end-on, bridge side-on one site, and bridge side-on two sites (as shown in Figure 1.5). Then O₂(ads) can accept protons from H₂O and electrons to form OOH(ads) by associative or directly dissociate mechanism to yield two O(ads). If only one oxygen atom is coordinated perpendicularly to the active sites in an end-on manner, one electron transfer is favored, mainly forming OOH(ads) to achieve the reaction by 4e pathway or series

$2 \times 2e$ pathways. In contrast, the O_2 dissociation process is more likely to result in the direct $4e$ ORR pathway while the parallel coordination with two O atoms adsorbed on the surface. Both the above-mentioned pathways may occur concomitantly and compete with each other. It is now generally accepted that $2e$ reduction primarily participates on carbonaceous materials and $4e$ reduction predominates on noble metals, while various ORR pathways exist for other metal and metal oxide.²⁷

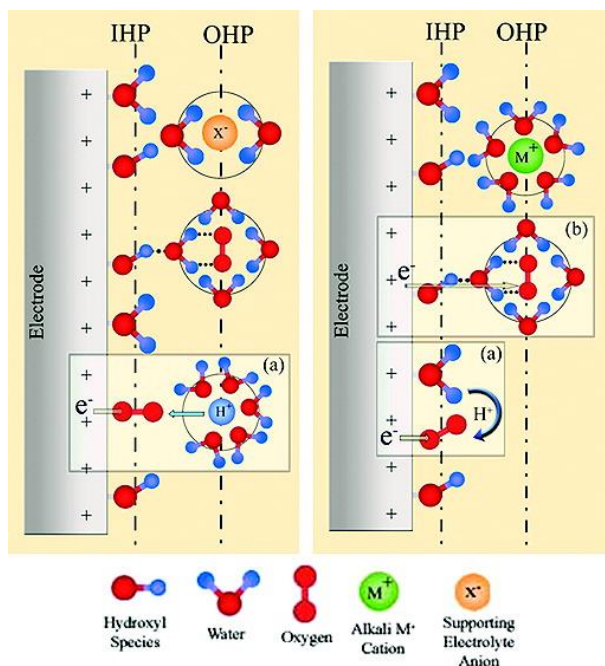


Figure 1.6. Schematic illustration of the double-layer structure during ORR in acidic (left) and alkaline (right) conditions.²⁸

In addition, non-covalent interactions between adsorbed species on the catalyst surface and hydrated alkali-metal cations take great effect on the ORR characteristics.^{25, 27-31} Influence of the inner Helmholtz plane (IHP) and outer Helmholtz plane (OHP) electron transfer mechanisms are proposed. As shown in the double layer structure in Figure 1.6, the IHP is occupied by hydroxyl species, solvent water dipoles and chemisorbed molecular O_2 in both acidic and alkaline media. The inner-sphere ORR mechanism (Figure 1.6 inset (a)) typically involves the chemisorption of molecular oxygen followed by electron transfer. The OHP is populated by solvated O_2 molecules and alkali metal ions in alkaline media or anions in acid media. In alkaline media (Figure 1.6 inset (b)), there are noncovalent interaction between the solvated molecular O_2 and the specifically adsorbed surface hydroxyl groups via a hydrogen bond formation. The H bond formation is just enough to trigger the outer-sphere electron transfer to form superoxide radical anion ($O_2^{\cdot-}$), thus promoting a $2e^-$ reduction pathway forming HO_2^- anion which desorbs into the electrolyte. In acid, this interaction is also presented but the barrier for the electron transfer is high enough to prevent the transfer through this outer sphere electron transfer mechanism. The surface independent outer-sphere electron

transfer mechanism leads to the availability of a variety of metals for ORR in alkaline media. However, this mechanism leads to ORR by inefficient 2 electron transfer process. It is critical to promote the inner-sphere ORR mechanism to increase the faradaic efficiency of the ORR.

In conclusion, because of the high complexity of ORR kinetics, an atomic-level understanding of the ORR mechanism is still a challenging task in many cases.²⁶

1.3 Catalysts for ORR

1.3.1 Pt-based material

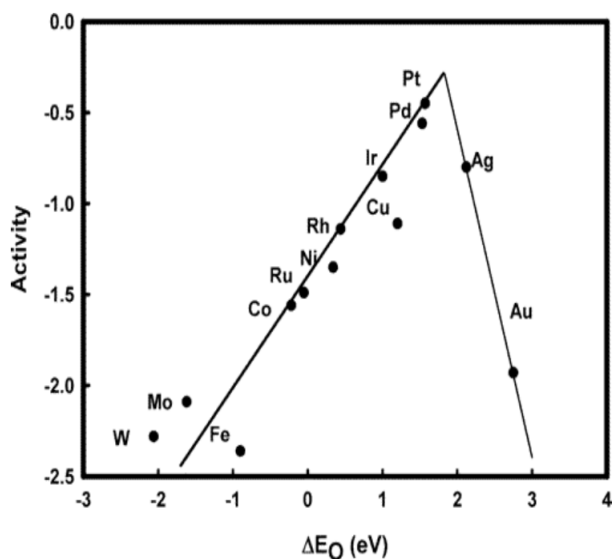


Figure 1.7. Trends in oxygen reduction activity plotted as a function of the oxygen binding energy.²²

Currently, Pt-based catalysts are proved to be the state-of-the-art catalyst for ORR in acid.³² Theoretically, the ORR activity can be described by the binding energy of the oxygenated species on the catalyst surface. An optimal catalyst should have a moderate binding to the intermediates. If the catalysts bind oxygen too strongly, the activity is restricted by the removal of adsorbed O and OH intermediates, which in turn blocks the active site for further oxygen adsorption. If the adsorption on the electrode surface is too weak, the activity is limited by proton and electron transfer to adsorbed oxygen for catalysts.³² In Figure 1.7, a volcano-shaped relationship between the ORR activity and O binding energy has been identified and it shows that Pt is the best catalyst for ORR. In practice, Pt supported on carbon black has been extensively used and considered to be the best catalysts since 1992 when it was firstly reported by Wilson et al.³³

However, there are still many issues that are failed to be addressed before reaching large-scale commercial implementation.³⁴⁻³⁷ On one hand, Pt is a scarce and expensive metal. The high price of Pt accounts for approximately 56% cost of a fuel cell stack.¹³ On the other hand, the poor long-term stability of such Pt

catalyst significantly curtails the lifetime and durability of PEM fuel cells. The lifetime of the state-of-art Pt catalyst maintaining high fuel-cell performance is far less than the 5000 h set as the year 2020 target by the US Department of Energy (DOE). Therefore, how to reduce costs by reducing Pt loadings without loss of activity and durability remains a critical issue in ORR catalyst research.

1.3.2 Non-precious metal catalysts

Non-precious metal-based ORR electrocatalyst has been emerging as promising alternative catalysts to Pt.^{11, 38-41} The non-precious metal catalysts using abundant, inexpensive metal precursor have not only a comparable ORR activity to Pt, but also superior stability and methanol tolerance for ORR than Pt, specifically in alkaline media.

Inorganic NPs, such as metal carbides, metal nitrides, metal oxynitrides, and metal oxides have been employed as highly active and stable precious-metal-free catalysts. Metal carbides such as tungsten carbide (WC) and iron carbide (Fe_3C) are promising alternatives to Pt-based catalysts considering their interesting electronic structure and good electrical conductivity.¹¹ Metal oxides, in particular, manganese and cobalt oxides, have also been investigated for ORR catalysis applications due to their easy preparation, reasonable activity, and considerable stability in an oxidative and alkaline environment.³⁹ In addition to the single-component metal oxides, perovskite-type mixed-metal oxides (ABO_3 , A = La, Ca, Sr, or Ba, and B = Ni, Co, Fe, Mn, or Cr) have attracted growing attention because of their high electrical conductivity and very high chemical stability.⁴⁰ Besides, transition-metal nitrides (MN_x , M = Mo, Co, Ti, Ta, etc.) and oxynitrides are of high interest for oxygen reduction owing to their good electrical conductivities and corrosion resistance.⁴¹ However, these materials usually show superb activity in alkaline conditions, but moderate ORR activity in acidic conditions. Future improvement of their ORR activity and stability via optimizing and controlling their size, phase, and morphology is necessary.

One of the most promising non-precious metal electrocatalysts for ORR is transition metal-nitrogen-carbon (Me-N-C, Me = Fe, Co, Cu, Ni, Mn, etc.) complexes or composites because some of them have exhibited high ORR activity in both acidic and alkaline medium, in part due to the use of new synthetic methods.^{11, 43} The synthesis strategy of the Me-N-C catalysts is similar, containing high-temperature pyrolysis of the precursors of metal salts, nitrogen-containing components on carbon supports. However, despite over 50 years of study, the exact nature of the active site remains unknown due to the complex composition and structure. The prevailing concepts in the literature regarding active-site identity can be summarized mainly as follows: (a) M-N₄ site⁴⁴ resembling the initial porphyrin and phthalocyanine which are retained during pyrolysis and incorporated into the catalyst surface; (b) metallic or carbide nanoparticle-related sites (Me-N_x),⁴⁵⁻⁴⁷ which are formed via aggregation of metal atoms during pyrolysis and protected by layers of

graphitic carbon; and (c) activated C/N sites, which are formed by defects or heteroatom doping that influences the electronic properties of the catalyst surface. Further investigations of the ORR mechanism of Me-N-C have been done to boost the ORR performance of this group of catalyst. As shown in Figure 1.8, proton transfer plays an important role in determining the activity and selectivity of Me-N-C catalysts, while for Pt and Pd no effect of proton transfer was observed.⁴²

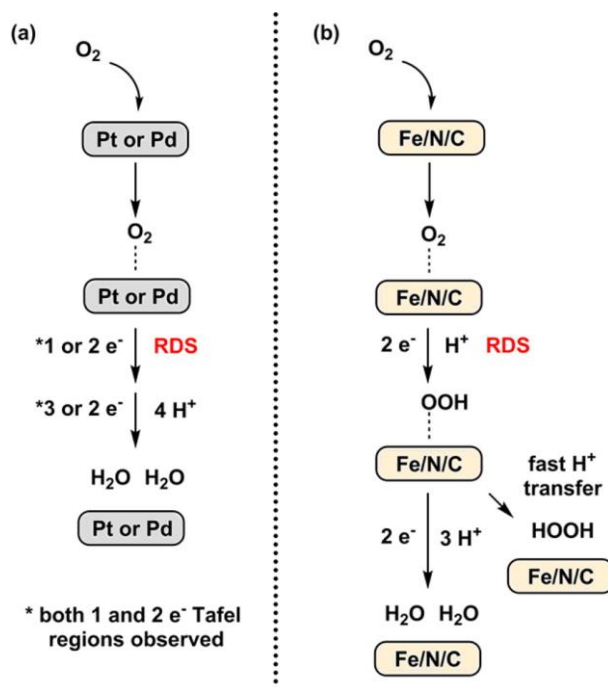


Figure 1.8. Possible mechanisms for ORR on (a) precious metal and (b) Me-N-C catalysts. RDS is shown in red.⁴² However, there is still a big gap in ORR activity between non-precious nanomaterials and commercial Pt. This drawback can be partially resolved by considering adding more non-precious catalysts at the cathode for providing more active catalytic sites for ORR. Yet problems arise with the introduction of more catalyst into fuel cells, such as a severe technical problem with regard to mass-transport property.

1.3.3 Metal-free catalysts

Apart from metal-containing catalysts, metal-free ORR catalysts have been intensively studied as substitutes for Pt/carbon materials have been widely used as active catalysts for ORR in metal-air batteries and fuel cells originating from their general advantages, such as excellent conductivity, superior chemical stability, and low cost.⁴⁸⁻⁶² As shown in Figure 1.9, the carbon family consists of diamond, amorphous carbon, graphite, fullerene (C₆₀), carbon nanotubes (CNT), and graphene. Among the carbon materials, One-dimensional (1D) carbon nanotubes (CNTs) and two dimensional (2D) graphene have attracted great attention for ORR due to their unique structural characteristics and outstanding physicochemical properties

such as large surface area, high mechanical property, good electrical conductivity, and excellent chemical stability.

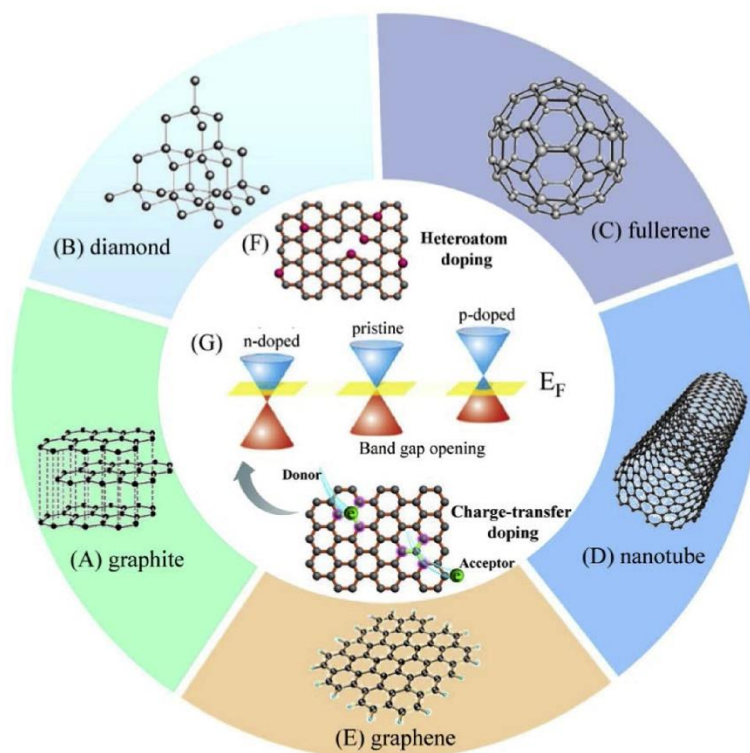


Figure 1.9. Carbon nanomaterials: (A) graphite, (B) diamond, (C) buckminsterfullereneC60, (D) single-wall carbon nanotube, (E) graphene, (F) heteroatom-doping of graphitic carbon structure, and (G) charge-transfer doping of graphitic carbon structure by electron donor (n-doping) or electron acceptor (p-doping) and the associated bandgap structures.⁴⁸

CNTs and graphene are constructed of sp^2 -bonded carbon atoms with abundant free-flowing π -electrons. However, these π -electrons in pristine carbon materials are too inert to trigger the sluggish ORR. With heteroatom (N, B, P, S) -doping, i.e. chemically attaching or incorporating them into the backbone of the respective carbon material, carbon π -electrons have shown activity due to the broke of electroneutrality and the spine density of sp^2 carbon. Also, the electronic properties, surface structure, and electrochemical properties of the carbon materials can be tuned efficiently by heteroatom-doping. When the electronegativity of the dopants is larger than that of C (e.g. nitrogen), the active sites are the positively charged C atoms through conjugation with lone-pair electrons from N dopants. When the electronegativity of the dopants is smaller than that of C (eg. boron), the paired covalent electrons will be slightly polarized towards the C atoms, forming local positive charge density on the B atoms, which could be taken as active sites for ORR. Co-doped carbon-based metal-free catalysts with different heteroatoms were found to be an efficient material solution to further improve the electrocatalytic activity of the ORR, as exemplified by B,N-CNTs⁶³, S,N-graphene⁶⁴ P,N-graphene.⁶⁵

Intermolecular charge-transfer has also been reported to create good ORR electrocatalytic activities, as exemplified by certain polyelectrolyte (e.g., PDDA) adsorbed CNTs or graphene.⁶⁶ Intermolecular charge-transfer can also be achieved by charge-transfer doping carbon nanomaterials with small electron acceptor(s) or donor(s) (Figure 1.9. (G)), though the importance of charge-transfer doping to ORR has not been fully recognized.

Compare with the metal-based (noble or nonprecious metal) ORR catalysts that have been extensively researched and developed for more than 50 years, however, the field of carbon-based metal-free electrocatalysis for renewable energy technologies is still very young since the publication of the seminal paper in 2009.⁶⁷ In-depth understanding of the type of active sites toward ORR and unambiguous identifying of different types of active configurations is imperative for developing advanced metal-free catalysts in terms of rationally selecting synthesis methods and precursors.

1.4 Pt-Based ORR Catalysts

In fuel cells, the ORR catalyst operates under harsh conditions (highly positive potentials and strongly acidic media), where the electrochemical surface area (ECA) of Pt is rapidly lost during cycling.⁶⁸ As shown in Figure 1.10, different degradation mechanisms of Pt/C are summarized.⁶⁹

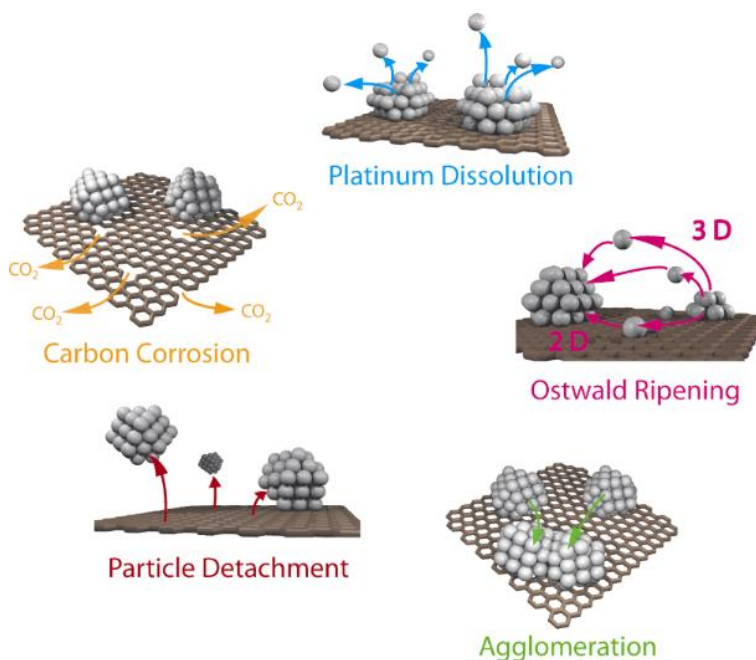


Figure 1.10. Simplified representation of suggested degradation mechanisms for platinum particles on carbon support in fuel cells.⁶⁹

The degradation of catalysts includes the two aspects of Pt metal and carbon support, which influence each other. During operation, platinum dissolution can occur in PEMFCs as dissolved platinum in the water

stream because the presence of Pt species in the membrane was detected. If the dissolved platinum is redeposited on other platinum particles, significant particle growth can occur and the according degradation mechanism is called 3D Ostwald ripening. If the dissolved platinum travel on the carbon support, it is as called 2D Ostwald ripening. Another possible mechanism for the growth of Pt is the coalescence of Pt nanoparticles via migration on the carbon support. Because of the high specific surface energy of the nanometer-sized Pt-based catalyst which is generally used in PEMFC, these nanoparticles inherently show a strong tendency to agglomerate. Meanwhile, the Pt can catalyze the oxidation of carbon and result in severe electrochemical corrosion of the carbon surface, which leads to changes in the surface chemistry of the carbon. The presence of oxygen-containing groups on carbon support can both decrease the conductivity and increase the hydrophilicity for the catalyst. Thus it can enhance flooding effects that can hamper the transport of oxygen to platinum within the catalyst layer and thus lead to a decline in performance. It is also assumed that the formation of excessive oxygenated functional groups at the carbon surface can weaken the interactions between platinum particles and support. Then the movement of surrounding Pt particle will be accelerated, resulting in the detachment of whole platinum particles from the support.

Thus far, a great number of researches have been devoted to dealing with the aforementioned problems and these strategies can be divided into three main categories: (i) The modification of Pt particle itself with precise controls of size, shape, composition, structure, and architecture;(ii) Surface engineering by modifying the coating of the Pt nanoparticle; (iii) Replacing conventional support with another appropriate catalyst support with high corrosion resistance and with strong interactions with Pt.

1.4.1 The modification of Pt particle

In this section, as shown in Figure 1.11, we will briefly review the recent literature on the modification of Pt particle itself for enhanced ORR activity such as shape controlling, alloying, building NPs, hollow and core/shell structure.^{20, 70-76}



Figure 1.11. Recent important advances in new active and durable Pt-based nanostructures for improved ORR catalysis.⁷⁷

ORR is structure-sensitive and heavily relies on the crystallographic orientation of the Pt surface.⁷⁸ Platinum has a face-centered cubic (FCC) crystal structure, which typically has Pt (111), (100), and (110) index planes. Commercial Pt/C catalysts are usually bounded by low-index facets such as (100) and (111). It was found that the activity of ORR in a weakly adsorbed electrolyte, such as HClO₄ solution, followed the order of Pt (100) \ll Pt (111) \approx Pt (110).⁷⁹ Furthermore, attempts to synthesize high index facets Pt nanocrystals have been taken. Pt nanocrystals with high index facets exhibit higher activities than Pt (111) because of their high densities of atomic steps, edges, and corners that act as active sites. Inspired from the ORR activity trend obtained on Pt single crystals, that is, high index planes $>$ (111) $>$ (100), efforts have been taken to synthesize shape-controlled nanostructures to optimize the structure effect. Different shape platinum catalysts have been developed, such as nanowires, nanotubes, thin film, branched nanoflower and nano dendrite. These materials exhibit improved catalytic performance because of the presence of low-coordinated atoms situated on edges, steps, and kinks. The main issue with the shape-controlled Pt nanoparticles is their stability under ORR condition as they tend to evolve to thermodynamically equilibrated state.

Size is also an important factor when optimizing a catalyst. Of course, the surface area increases with particle size. This gives rise to more sites where catalysis can take place. Therefore, a small Pt particle size has been preferred for a long time as the finely dispersed Pt on porous supports can maximize the

electrochemically active surface area (ECSA) and mass activity (MA). Shao et al. found the maximum ORR mass activity on 2.2 nm Pt NPs in HClO₄ solutions by investigating Pt particles in the range of 1–5 nm.⁸⁰ However, the underlying Pt particle size effect on ORR activity is a long-standing problem that has not yet been well solved due to the complicated mechanisms of ORR performance, related to size distribution, shape, and inter-particle distance.⁸¹⁻⁸⁴ As the size of a nanometal cluster is further decreased to the sub-nanometre scale and ultimately to an atomic level (Single-atom catalysts (SACs)), the unique selectivity shows up, which is distinct from nanoparticle catalysts.^{71-73, 85-88} Atomically dispersed Pt catalysts exhibited excellent ORR catalytic performance and relatively low cost owing to the maximum atom efficiency of Pt.⁸⁹⁻⁹⁵ Remaining challenges include tuning the active site structure to anchor Pt single atoms are further required to be addressed to ensure excellent activity and durability.

Alloying Pt with low-cost transition metals can lead to significant improvements in atomic and electronic structure as well as the available surface sites, benefiting for tuning the binding strength of adsorbed species (reactants, products, spectator ions) with Pt. Great effects have been devoted to investigate the ORR properties of PtM alloys (M = Ni, Co, Fe, Cu, Pd, Rh, Ti, V, Cr, Mo, W etc.).⁹⁶⁻¹⁰⁴ It has been known that the activity enhancement on Pt alloys depends on their crystalline orientations. To tune the structural effect of the Pt alloys, one may is to synthesize shape-controlled Pt alloy NPs with only (111) facets exposed.^{105, 106} Furthermore, recent advances in chemical synthetic methods have led to the formation of Pt-based core-shell and hollow structure.^{70, 107} The reasonable selection of the alloy metals and the precise control of the size, compositions, and structures of this Pt-based system can boost the final performance.

1.4.2 Surface engineering

ORR is very sensitive to the surface electronic properties and surface atomic arrangement or coordination of the catalyst. Hence, engineering the surface properties, which means modifying Pt nanoparticles surfaces with metal clusters, molecules, ions, organic or inorganic compounds, and protective layer can also lead to effectively tuned catalytic properties of Pt catalyst, enabling enhancement in terms of both activity and durability.^{108,109}

Decorating Pt NP surfaces with carbon or a silica layer can suppress the agglomeration, dissolution, migration, and detachment of Pt NPs and result in excellent stabilities.¹¹⁰⁻¹²⁰ As shown in Figure 1.12, during operation PtNPs in the commercial Pt/C can be dissolved into small species and reprecipitated onto surfaces of larger particles or recrystallized at other positions, causing an increase of Pt NP size through diffusion. Also, Pt NPs could migrate on carbon supports and aggregate when the carbon below Pt NPs is oxidized. For ultrathin carbon layer (UTCL) coated Pt/C, the protective layer can hinder the migration, agglomeration, and detachment of Pt NPs from supports as well as mitigates the dissolution-growth process

of Pt NPs. So this method can offer a persuasive approach towards increasing the lifetime of catalysts. However, the ORR activity of these catalysts is highly dependent on the thickness of the protective layer.¹¹⁵ Too thin carbon coating layers are not efficiently protecting the Pt NPs while too thick ones prevent the facial diffusion of the reactants onto Pt active sites.

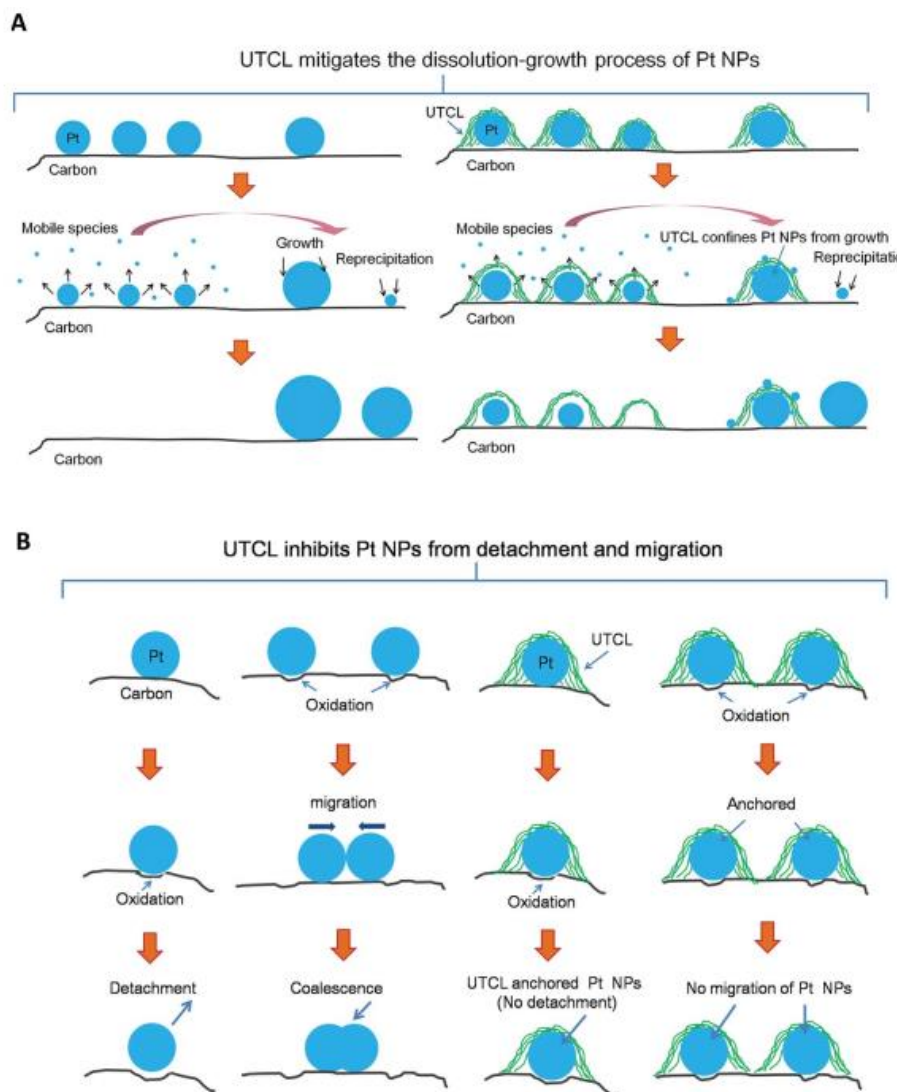


Figure 1.12. Schematic of the stable mechanism of ultrathin carbon layer (UTCL) coated Pt/C catalysts in terms of UTCL on Pt NPs. (A) Mitigating dissolution-growth of Pt NPs; (B) inhibiting Pt NPs from detachment (left) and migration (right).¹¹³

Chemical functionalization of the metal surface is used for the rational design and improvement of Pt catalysts.^{121,122} This is based on the modification of the Pt surface by non-metallic molecules or compounds that can block the adsorption of poisoning species or influence the hydrophilicity and electronic property. Markovic's group used cyanide to modify platinum surfaces and develop new concepts for designing ORR catalysts. On the cyanide functionalized Pt(111) surface, activities of the ORR can change from a 25-/10-fold increase in the presence of sulfuric/phosphoric acid anions to no effect in the presence of perchloric

acid anions, to a 50-fold decrease in alkaline solutions. This is because Pt surfaces with adsorbates can efficiently block the sites for adsorption of spectator anions while the oxygen reduction reaction proceeds unhindered.¹²¹

The approach to modify the Pt NP surface with elaborately selected foreign species will open a new approach for the further evolution of Pt-based catalysts.

1.4.3 Replacing conventional support

As we mentioned before, the commonly used support of the Pt/C is carbon black because of its high surface area, excellent electronic conductivity, and chemical stability. However, the weak interactions between Pt NPs and the carbon support cannot anchor Pt tightly, leading to migration and aggregation of supported Pt NPs and a consequent decrease in the active surface area with the long-term operation. Carbon black also suffers from corrosion, especially under conditions such as start-up and fuel starvation in fuel cell operation. Carbon corrosion may result in separation of Pt particles from the carbon support and consequent performance loss. Appropriate catalyst support with high corrosion resistance and with strong interactions with the supported metallic catalyst should be introduced to improve ORR catalysts.^{123, 124}

Ideal support should possess satisfactory catalyst-support interaction, large surface area, excellent electrical conductivity, good corrosion resistance, ability to maximize the triple phase boundary, and satisfying water management capability to avoid flooding. Among them, new carbon support material such as carbon nanotubes, mesoporous carbon, carbon nanofibers, and graphene have attracted interest due to their better conductivities, corrosion resistance, and mechanical/electrochemical properties compared with commonly used carbon blacks. There are abundant π electrons on these graphitized carbon surface. Therefore, the Pt–C interactions are partially covalent, due to the electron delocalization between the carbon π sites and the Pt d-orbital, and also partially ionic due to the electron transfer from Pt to carbon. These strong metal-support interactions may help to inhibit Pt oxidation and dissolution during potential cycling. Furthermore, appropriate doping and functionalization can offer the possibility of controlling and improving several properties at the same time. For example, N-doped CNTs were used as excellent supports because the N doping can create electrochemically active defects on the CNT surface while preserving its electrical conductivity. Sun's group demonstrated that uniform Pt nanoparticles with smaller size and better ORR activity were obtained from NCNTs than pure CNTs.^{125,126} Also, graphene and its derivatives have emerged as promising platinum electrocatalyst supports. This part will be discussed in details in the next chapter.

Besides, non-carbonaceous materials such as metal oxides are considered to be promising support materials because of their extremely high corrosion resistance,¹²⁷⁻¹²⁹ and strong interactions between metal nanoparticles and the metal oxide support induced by electron transfer from the metal oxide to Pt.

The electronic structure of the Pt nanoparticles can be modified by charge transfer, thereby affecting the activity of the catalyst. Also, long-term durability was much enhanced. This extremely high stability was attributed to tightly bounded Pt, which could suppress Pt dissolution and migration.¹³⁰

1.5 Graphene-based metal-free catalyst

In recent years, 2D graphene-based materials have been applied as electrochemical catalysts because of their excellent conductivity and strength, high specific surface area (SSA) and tailorable surface chemistry, as seen in previous reviews.^{62, 131-133} Although the large SSA and high electrical conductivity of pristine graphene are supposed to be useful for the electrocatalysis process, in practice, with the strong van der Waals interactions and π - π stacking between graphene layers, the 2D graphene nanosheets could easily restack and aggregate, which significantly diminish the SSA and hinder the rapid electron transport consequently limit their utilization. Moreover, a limited number of reactive sites of the pristine graphene is unacceptable to deploy them in practical use. Therefore, the center and forefront of this research area have moved into the exploration of chemically modified graphene (CMG) such as functionalized or heteroatoms doped graphene, and dimension-tailored graphene nanostructure.¹³³⁻¹³⁷

1.5.1 Chemically modified graphene

As mentioned above, pristine graphene is inert for ORR due to a low adsorption energy and a limited number of active sites. With doping, the electronic properties, surface structure, and electrochemical properties of the graphene can be changed efficiently. It is the most widely applied and most effective approaches for inducing intramolecular charge transfer in graphene frameworks and enhancing electrocatalytic activity. The neighbor elements of carbon such as B, N, and P are chemically relatively easy to be doped into graphene.^{49,138,139} These kinds of electrocatalysts can usually be prepared by annealing GO with the appropriate heteroatom containing precursor at high temperatures (> 900 °C). It is known that doping graphene with heteroatoms of either higher or lower electronegativities than carbon ($\chi = 2.55$), such as N ($\chi = 3.04$), B ($\chi = 2.04$), and P ($\chi = 2.19$), can induce electrocatalytic ORR activity through intramolecular charge transfer in the graphene matrix.

N-graphene is the most studied graphene-based electrocatalyst due to its simple synthesis process and relatively good electrocatalytic performance. Nitrogen (N) is of similar atomic size (65 pm) to carbon (70 pm), and its electronegativity is larger than that of C. The incorporation of N atom into graphene lattice plane could modulate the local electronic properties, as it could form strong bonds with carbon atoms because of its comparable atomic size with carbon and therefore could generate a delocalized conjugated system between the graphene π -system and the lone pair of electrons from N atom. The introduction of N

into carbon nanomaterials could improve both the reactivity and electrocatalytic performance, so the N-doped carbon materials have been intensively studied among all the available heteroatoms for doping.¹⁴⁰⁻¹⁴⁵ The ORR mechanism on N-graphene has been extensively investigated from both experimental and theoretical perspectives. As schematically illustrated in Figure 1.13, three common bonding configurations of N atoms in graphene is demonstrated, including pyrrolic, pyridinic, and graphitic (or quaternary) N.¹⁴⁶ Graphitic (or quaternary) N refers to the N atoms that replace the carbon atoms in the graphene plane. Pyridinic N atoms locate at the edges of graphene planes and each N atom is bonded to two C atoms and donates one p electron to the π system. While in the case of pyrrolic N atoms, they are incorporated into the heterocyclic rings and each N atom is bonded to two C atoms, contributing two p electrons to the π system. However, there are the controversial conclusion to whether the pyridinic N configuration or the graphitic N configuration determines the ORR activity.⁵⁶

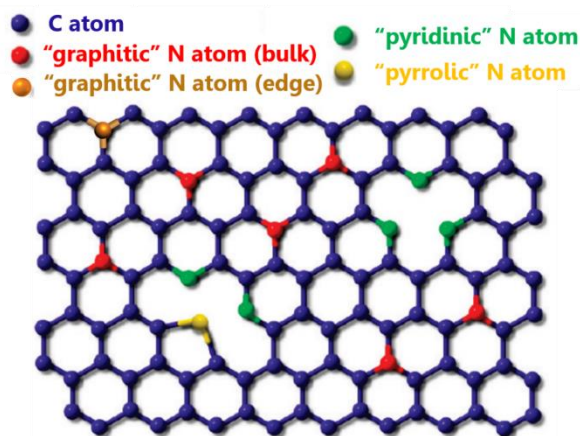


Figure 1.13. Schematic representation of different types of N atoms (graphitic, pyridinic and pyrrolic N).¹⁴⁷

Compared to the single-doped graphene, co-doped graphene have also been studied and show significantly enhanced ORR activity. It is suggested that two or more active centers could act synergistically in ORR to jointly promote catalytic activity. Typical examples are N,P-graphene,¹⁴⁸ N,S-graphene,¹⁴⁹ B,N-graphene¹⁵⁰ and N,S,P-graphene.¹⁵¹ However, the studies of the co-doping effect are very preliminary. Extensive investigations are needed to understand the exact formats and concentrations of the co-doped elements on the surface of the graphene, as well as their influence for the catalytic properties.

1.5.2 Dimension-tailored graphene

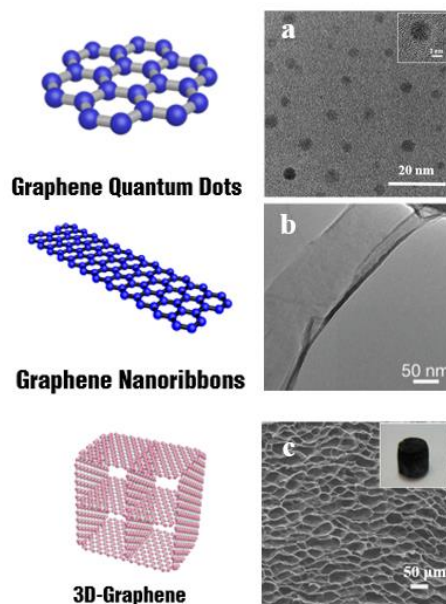


Figure 1.14. (a) The TEM image of graphene quantum dots (GQDs).¹⁵² (b) The TEM image of graphene nanoribbons (GNRs). (c) SEM images of 3D-Graphene (3D-G). A digital photo of 3D-G is presented in the inset.¹⁵³

The slow mass transport in cathode is the major barrier for available power output of fuel cell. Nanostructured graphene materials have been identified as some of the most promising materials due to their high chemical stabilities, high electric conductivities and improved mass transport capabilities.¹⁵³ The 2D graphene can be a building block for a series of novel graphene-based nanostructures.¹⁵⁴ As shown in Figure 1.14, graphene can be cut into small pieces: graphene quantum dots (GQDs), split into small slices: graphene nanoribbons (GNR) and scaffold into 3D graphene architectures: 3D-G. Since the intrinsic properties of graphene are almost maintained in these structures, they are defined as graphene family materials. Further, the graphene family materials also possess some fancy electrochemical performances compared with the pristine graphene.

As shown in Figure 1.14(a), in terms of lateral length (usually <100 nm) and the thickness (in single and few layers (<10 nm)), GQDs are all nanometer-sized; the edge effects and properties associated with the quantum confinement are found in numerous papers.¹⁵⁵⁻¹⁵⁷ Tremendous attempts have been conducted to investigate the electrocatalytic activity of GQDs.¹⁵⁸⁻¹⁶³ Those results show that the existence of GQDs can drastically facilitate ORR performance through altering electronic characteristics and offering more active sites. Moreover, doping with heteroatoms in GQDs can offer more active sites and tune their electronic characteristics, thus improve the ORR performance. The GQDs can be used to build composite materials since their small dimension and easy tunability with heteroatoms doping.

The thin elongated morphology of GNRs is shown in Figure 1.14(b). The GNRs can be regarded as quasi-1D material since a much shorter dimension than the other one in the plane. Because of their unique structure, the GNRs possess some exclusive features such as abundant edges, non-zero band gaps, high length-to-width ratio, and numerous activate sites, which make them extremely attractive to enhance the ORR activity.¹⁶⁴⁻¹⁷⁵ Due to the exposed edges along with the inherent size and high length-to-width ratio of GNRs, the ORR activity is promoted because of the significant reduction in the activation barriers for the first electron transfer and the oxygen adsorption on active edges.

In Figure 1.14(c), an interconnected 3D porous structure was constructed by physical cross-linking of randomly oriented wrinkled paper-like graphene sheets; the pore sizes could range from several hundred nanometers to several micrometers. In a macroscopic view, the 3D-G shows a certain shape morphology (cylindrical structure in most papers) with mechanical strength. All these 3D networks present similar properties such as high SSA, low density, strong mechanical strength, flexibility, high conductivity, and fast mass and electron transport kinetics. Obviously, these porous 3D-G structures could prevent the aggregation of graphene nanosheets, guarantee electron and mass rapid transport, and supply enough activate sites to promote the catalytic reaction, thus enhancing their performances in applications. Table 1.2 lists a part of recent reports about the summary of some typical work of 3D-G based material on ORR.

Table 1.2 Summary of some typical work of 3D-G based material on ORR

The catalyst	Electro-Catalytic Performance	Onset potential	Electron Transfer Number	Ref
3D-S, N-G	Excellent catalytic activity including highly positive onset potential and high kinetic limiting current	-0.06 V vs. Ag/AgCl	3.3–3.6	176
3D-N-G	Lower onset potential than that of Pt/C, higher diffusion current density	0.18 V vs. Ag/AgCl	3.7	142
N-macro-mesoporous carbon/3D-G	Excellent ORR activity, complete tolerance to methanol cross-over effect and excellent long term durability	-0.05 V vs. Ag/AgCl	-	177
3D-N-G	One of the best performed NGs for ORR electrocatalysis and is superior to other scalable preparation methods	-0.2 V vs. Ag/AgCl	3.8–3.9	178
3D-N-G	Large kinetic-limiting current density, long-term stability and good tolerance to methanol crossover	-0.2 V vs. Ag/AgCl	3.8–3.9	179
3D-B, N-G	A higher current generation capability, better stability, and superior tolerance to the methanol crossover effect	-0.16 V vs. SCE	3.4-3.8	180
3D-S-G	A much enhanced ORR catalytic activity as well as an especially high electrochemical stability	-	-	181

The catalyst	Electro-Catalytic Performance	Onset potential	Electron Transfer Number	Ref
3D-N-G	A truly metal-free electrocatalyst material for the oxygen reduction reaction in acid medium	0.83 V vs.RHE	2.6-3.5	182
3D-G	Multilayer 3D graphene exhibits higher electrocatalytic activity	-0.252 V vs.Ag/AgCl	-	183
3D-N-S-Graphene nanomesh	Excellent electrocatalytic activity for ORR better than most of the graphene-based catalysts reported	0.04 V vs.Ag/AgCl	3.6	184
3D-N-G	Comparable electrocatalytic performance with the commercial Pt/C in alkaline	-0.05 V vs.Ag/AgCl	3.79	185
3D-N-B-G	The onset potential and current density of N and B co-doped 3D-G are comparable to those of the commercial Pt (30%)/C catalyst	-0.04 V vs.Ag/AgCl	3.8	186
3D-N-B-G	The onset potential, halfwave potential and limiting current density were comparable to or even better than those in previous reports	-0.07 V vs.SCE	3.9	187
3D-N-G	A high diffusion-limited current, superior durability and better immunity towards methanol crossover in alkaline solution	0.9 V vs.RHE	4.2-4.6	188
3D-N-G	Remarkable ORR activity and long term stability in both alkaline and acidic solutions	0.83 V vs.RHE	3.9	189
3D-B-G	Comparable to Pt/C (20 wt.%) catalyst, in addition to their superior durability and resistance to the crossover effect.	-0.05 V vs.Ag/AgCl	4.16	190
GQDs/3D-G	Enhanced electrocatalytic activity, good durability in alkaline solution	-0.13 V vs.Ag/AgCl	3.2-4.0	163
3D-N-S-G	Higher electrocatalytic activity and diffusion-limiting current density, better stability and methanol tolerance	-0.12 V vs. SCE	3.5	191
3D-N-G	high specific surface area, porous structure, and free-stacking properties, and exhibit enhanced ORR performance	-0.03v vs.Ag/AgCl	~4	192
3D-N-G	An excellent electrocatalytic activity toward the ORR with an efficient four-electron-dominated pathway and high durability in alkaline media.	0.93v vs.RHE	~3.94	193
3D-N-G	comparable electrocatalytic activity, higher selectivity and outstanding durability compared to commercial Pt/C in the alkaline media	~0.9v vs.RHE	3.7	194

Although there are various forms in the graphene family materials, they share some common properties. The large specific area, high accessibility, and superior electrical conductivity render these materials ideal candidates for the application in ORR. Especially 3D-G is the most promising ORR catalyst because of its easy preparation, high economical and efficiency, as seen in a large number of the latest excellent articles. The 3D open structure could suppress the stacking and aggregation of graphene layers and therefore provide a good conducting network. Moreover, the 3D-G could not only supply abundant active sites but also endow the material the features of fast reactants diffusion. In addition, these graphene family materials can easily be doped with heteroatoms and intrinsically alter electronic characteristics and facilitate ORR performance.

1.5.3 Graphene-based supporting material

Although most of the heteroatom-doped graphene, dimension-tailored graphene nanostructure metal-free catalyst mentioned showed very promising electrocatalytic activities which were comparable to Pt/C in alkaline media. PEMFCs that operate with acidic electrolytes are still far more commercially viable and are based on more mature infrastructure. Until now, there are rare graphene-based electrocatalysts reported for the acidic ORR. Fortunately, with the high conductivity, enormous surface area, abundant structural variety, and tailorable surface chemistry, the graphene is an excellent supporting material to allow the utilization of the unique features in acid.

Graphene, with its sp²-hybridized honeycomb structure, enhances mass transport and electron transfer, and the synergetic coupling between metal catalysts and graphene supports prevents the occurrence of particle dissolution and aggregation. Metal NPs grown on graphene have uniform particle size distribution relative to unsupported counterparts due to the strong interactions between metal NPs and graphene.¹⁹⁵

Doped graphene and dimension-tailored nanostructural graphene are also used as supporting materials. Typically, heteroatom-doping could introduce anchoring sites for metal nanoparticle deposition. doped graphene is thus proposed to be able to stabilize the noble metal nanoparticles and improve the durability of the catalysts.¹⁹⁶⁻¹⁹⁸ For doped 3D graphene, the 3D structure can provide multi-dimensional interconnected pores that facilitate electrons/reactants transport and maximize the triple-phase boundary for ORR. The high specific surface area enables the preparation of highly dispersed metal particles, while the doped heteroatoms can change the growth behavior of the subsequently deposited catalyst particles, resulting in catalyst-support interactions to increase the activity and durability of the Pt catalyst.¹⁹⁹⁻²⁰¹

1.6 Objectives of the work

This Ph.D. project aims at designing and realizing a high performance, extremely durable, and low cost Pt-based ORR catalyst and graphene-based ORR catalysts for fuel cell application.

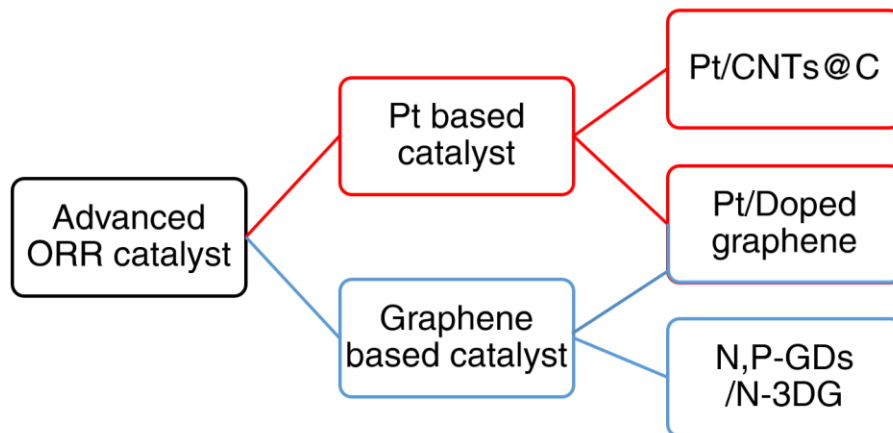


Figure1.15. A guide illustrating the arrangement of this thesis.

As shown in Figure 1.15, the main objectives of this thesis are as follows:

- I. To build Pt NPs encapsulated within carbon layers supporting on CNTs (Pt/CNTs@C) with precisely controllable thickness structure.
- II. To synthesis platinum clusters anchored on doped graphene supports (Pt/Doped graphene) and discuss the support interaction effect.
- III. To prepare nitrogen and phosphorus co-doped graphene dots supported on nitrogen-doped three-dimensional graphene (N, P-GDs/N-3DG) metal-free catalyst with enhanced performance towards ORR.

1.7 Thesis organization

This doctoral thesis is composed of 6 parts and organized as follows:

Chapter 1: Introduction: This chapter briefly introduces the background and fundamental knowledge of ORR in the fuel cell. Then the progress of ORR catalysts is presented in detail, in particular, Pt-based catalyst and graphene-based catalyst.

Chapter 2: Experimental: This chapter is about the details of used chemicals, materials synthesis, the physical and electrochemical characterizations involved in this thesis.

The Results parts are divided into three chapters.

Chapter 3: Ultra-thin carbon coated Pt/CNTs: a highly durable electrocatalyst for oxygen reduction

Chapter 4: Support interaction effect of platinum clusters anchoring on doped graphene supports for the oxygen reduction reaction

Chapter 5: N, P co-doped graphene dots supported on N-doped 3D graphene as metal-free catalyst for oxygen reduction

Chapter 6: Conclusion and Perspective: This chapter summarizes the main conclusions of this work and discusses the prospects in this field.

2 EXPERIMENTAL

In this chapter, the detailed synthesis process, physical and electrochemical characterizations are introduced.

2.1 Chemical and Materials

CNTs (multiwall, several hundred nm in length and 15–30 nm in diameter) were purchased from Bayer. Pt/C (20%) was purchased from E-TEK. Triphenylphosphine (TPP, 99%), formic acid (HCOOH, 98%), hexachloroplatinic acid ($\text{H}_2\text{PtCl}_6 \cdot 6 \text{H}_2\text{O}$, 99.95%), 4, 4'-azobis (4-cyanovaleric acid) (ABV, >75%), sodium lauryl sulfate (SDS), styrene (99.9%), hydrogen peroxide solution (H_2O_2 , 30%wt in H_2O) and potassium permanganate (KMnO_4 , 97%) were all purchased from Sigma-Aldrich. Sulfuric acid (H_2SO_4 , 95.0–98.0%), nitric acid (HNO_3 , 86%), hydrochloric acid (HCl, 32% in H_2O), perchloric acid (HClO_4 , 70%) graphite (graphite flake, natural, 325mesh, 99.8%) and potassium hydroxide (KOH, 87.1%), were bought from Fisher Scientific. Reversible addition-fragmentation chain transfer (RAFT) polymerization agent poly(acrylic acid)(butyl acrylate) (PABA) was synthesized previously in our laboratory.

2.2 Material Synthesis

2.2.1 Carbon-coated Pt/CNTs catalyst

The synthesis of N-acryloyl-D-glucosamine (AGA) and of the RAFT agent PABA containing 10 acrylic acid units and 5 butyl acrylate units were reported previously.³⁵⁻³⁷ The polymer encapsulation of Pt/CNTs was achieved as follows: typically, 40 mg of Pt/CNTs and 20 mg of PABA were dispersed into 8 mL of water and sonicated with 30% amplitude for 5 min (Fisher scientific sonic dismembrator 500, 400W) to yield a black stable Pt/CNTs@PABA suspension. Then 10 mg of ABV initiator was added to the above solution. Meanwhile, 300 mg of AGA, 200 mg of styrene and 10 mg of SDS were added to 8 mL of water, and the resulting emulsion was degassed with N_2 for 30 min. Then a syringe (50 mL) was filled with the emulsion and fixed to a syringe pump connected to the Pt/CNTs@PABA dispersion. The Pt/CNTs@PABA dispersion was heated at 80 °C under magnetic stirring and the monomers were added in under N_2 atmosphere over a period of 5 h. Then, the dispersion was kept at 80 °C for another 2 h to complete the polymerization. The encapsulated Pt/CNTs was collected by centrifugation and dried in a vacuum oven. The product was then heated under N_2 atmosphere at 550°C for 3 h.

2.2.2 Pt/N, P-graphene catalyst

GO was synthesized by an improved Hummers' method using natural graphite flake. The general method is: firstly, 1 g graphite powders were poured into the mixture of 92 mL concentrated sulfuric acid and 24 mL nitric acid in a 500 mL flask (immersed in an ice bath). After the suspended solution was strongly stirred at 0 °C for 15 min, 6 g of KMnO_4 was gradually added in the above mixture solution. The suspended solution was stirred continuously for 1 h. This process was named low-temperature oxidation. Subsequently, in order to increase the oxidation degree of the graphite, the mixture was heated to 80 °C and maintained for 30 min, and then 92 mL of deionized water was slowly added in. The suspension was stirred at 80 °C for 30 min again. After that, 5 mL H_2O_2 (30%) was added into the solution to reduce the residual permanganate. On completion of the reaction, the mixture was washed with 5% solution of HCl and water until sulfate could not be detected with BaCl_2 . Finally, the GO powders were dried at 80 °C for 24 h.

For N, P-graphene synthesis, GO was dispersed in DI water, followed by the addition of triphenylphosphine (Ph_3P) ether solution in a weight ratio of 1:5. Then the mixture was under ultra-sonication for 4 h and stirred for another 4 h at room temperature. This precursor solution was vacuum dried on 60°C for at least 24 h. Subsequently, the powders were heated at 200 °C for 1 h under an argon atmosphere, and then the temperature was raised to 950 °C and kept for 15 min while feeding Ar (100 sccm) and NH_3 (100 sccm) at room pressure. The preparation of N-Graphene follows similar procedures, without the Ph_3P mixing process. For reduced graphene oxide (RGO), similar annealing process was achieved under inert argon atmosphere.

Pt nanoparticles loaded on graphene material (include RGO, N-Graphene and N, P-Graphene) were synthesized by a traditional wet impregnation method. First, graphene material was added into water and sonicated for 2 h, followed by adding an aqueous $\text{H}_2\text{PtCl}_6 \cdot 6\text{H}_2\text{O}$ solution (5 wt%). After 2-hour strong magnetic stirring, the products were washed with water and freeze-dried for 12 h. Then, the mild heat treatment of the powder was performed at 450°C for 2 h under inert argon atmosphere with a flow rate of 100 mL min^{-1} .

2.2.3 N, P-graphene dots/N-3DG catalyst

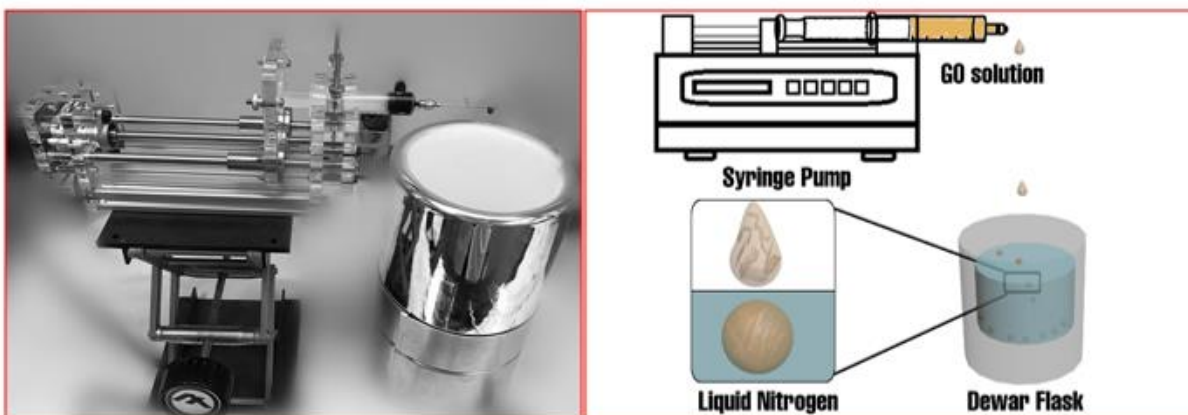


Figure 2.1. Photo and schematic illustration of the freezing process of N, P-GDs/N-3DG.

N, P-GDs/N-3DG was prepared by freeze-annealing approach. Briefly, 20 ml GO solution (10 mg/ml) was mixed with 1 g triphenylphosphine (Ph_3P) (dissolved in ether) by ultrasonic treatment for 2 h. The mixture was then transferred into syringe and was fixed to a syringe pump connected to the liquid nitrogen, which was stored in a thermal insulation container (as shown in Figure 2.1). Once the GO solution contacted with the liquid nitrogen, a small ball was formed and sank in the liquid nitrogen. The flow velocity was 1 ml/min. The GO balls were kept in the liquid nitrogen at least 30 min. The obtained composite hydrogel was freeze-dried for 1 day. After that, the hydrogel was annealed under ammonia at 950 °C for 10 min. For the production of 3DG, the GO balls without adding TPP were annealed under argon at 300 °C for 1 h. For the N-3DG, the GO balls without adding TPP were annealed ammonia at 950 °C for 10 min. For P-GDs/3DG, the GO balls with TPP were annealed under argon at 950 °C for 10 min.

2.3 Physical Characterizations

Various characterization techniques were used in order to characterize the structure and chemical composition of the materials. The technique used is listed and introduced briefly below:

The scanning electron microscope (SEM) is a powerful magnification technique to get the 3D image with information about the morphology and composition on sample surfaces. The powder samples were mounted on the holders using double-sided conductive carbon tapes. Then the images and energy dispersive spectroscopy (EDS) were achieved by Tescan Vega3 LMH.

Transmission electron microscopy (TEM) is used to directly observe the morphologic, compositional and crystallographic information of the samples. The samples were firstly ultrasonic in ethanol solution and then dropped onto a Cu grid and excess solution was wicked away by a filter paper. The observations were

conducted with a JEOL JEM-2100F (École Polytechnique de Montréal, Montréal, Canada). Meanwhile, the EDS spectras were measured at different locations on the sample. The sizes of the nanoparticles were estimated by counting at least 100 nanoparticles with Nano measurer free software.

X-ray diffraction (XRD) is a technique used for determining the atomic and molecular structure of a crystal. The powder samples were packed to a flat surface onto a sample holder and then tested with Bruker D8 Advance with Cu K α as an X-ray source.

Thermogravimetric analysis (TGA) is a method of thermal analysis in which the mass of a sample is measured over time as the temperature changes. The samples were loaded into the crucible and performed under air atmosphere with a heating rate of 4 °C/min on an MS coupled Thermogravimetric Analyzer (TA Instruments TGA Q500 / MS Discovery, NanoQAM).

X-ray photoelectron spectroscopy (XPS) is a surface-sensitive quantitative spectroscopic technique that measures the elemental composition, chemical state and electronic state of the elements that exist within a material. The samples were mounted on the holders using double-sided conductive carbon tapes and then were measured with a VG Escalab 220i-XL using Mg K α line as an excitation source. All the spectras were calibrated by placing the C 1s principle peak at 284.6 eV. The XPS data were analyzed with the Casa software.

Inductively Coupled Plasma / Optical emission spectrometry (ICP-OES) is an analytical technique used for the detection of chemical elements. After acid digestion and fusion by nitric acid and hydrochloric acid, the samples were dissolved and characterized by Agilent Technologie, 5100(NanoQAM, Montreal).

2.4 Electrochemical Characterizations

To evaluate the ORR performance of catalysts, a practical fuel cell by using membrane electrode assembly (MEA) is needed, intend to compare the perfoemce of the catalyst to the state-of-the-art Pt/C catalyst. In most cases, this approach is impractical because it is difficult to exclude the influence from electrode structure and the mass-transport effects in the complicated MEA fabrication and test, which require a special procedure, equipment, and abundant materials. Moreover, this type of measurement shows the overall performance of the tested catalyst, but gives no insight into the underlying reaction mechanism on the catalyst surface. Therefore, the thin-film rotating disk electrode (RDE) and rotating ring-disk electrode (RRDE) which are the most widely used technique were mainly employed in this thesis to characterize the electrochemical behaviors of newly developed materials at the lab scale. A typical three-electrode cell used in an RRDE technique is shown below in Figure 2.2.

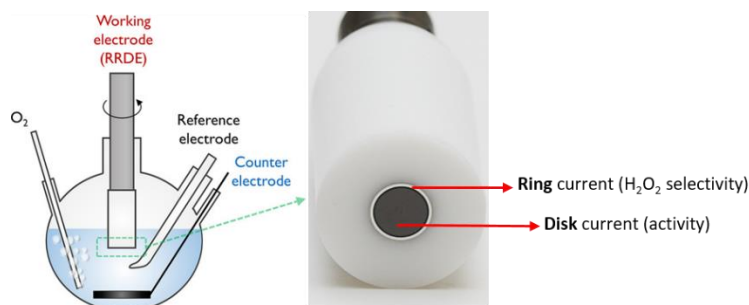


Figure 2.2. Schematic of an RRDE setup in a three-electrode electrochemical cell. ²⁰²

In this thesis, a Pt wire or the graphite rod were used as counter electrode. A saturated calomel electrode (SCE) or mercury-mercury oxide electrode (Hg/HgO) was used as reference electrodes, in acid and alkaline media, respectively. The RRDE with a Pt ring and a GC disk (Φ 5.61 mm, 0.245cm²) was used as the substrate for the working electrodes. Before using, the RRDE were polished using aqueous alumina suspension on felt polishing pads. The catalyst ink is prepared as the following tables. Firstly, the catalyst was mixed with the solvent followed by sonication and agitation in a vortex mixer, which were then repeated for 3 times. Then the catalyst suspension was pipetted onto the polished GC (Pine Research Instrument) and wait for air-dry.

Table 2.1 The recipe of the catalyst ink.

	catalyst	deionized Water	ethanol	Nafion(5wt%)	Drop on disk	Loading
Pt based material	5mg	85 μ L	1650 μ L	50 μ L	9 μ L	100 μ g/cm ² _{catalyst}
Non-noble	10mg	-	350 μ L	95 μ L	9 μ L	802 μ g/cm ² _{catalyst}

2.4.1 Cyclic voltammetry

Cyclic voltammetry (CV) is a potentiostatic electrochemical technique used to examine the electrochemical properties of electrodes. In cyclic voltammetry (CV), the applied potential of the working electrode is varied linearly with a constant rate between two potential limits, and the corresponding current between the working electrode and the counter electrode is measured accordingly. A typical CV of Pt/C (20%) at a sweep rate of 50 mV s⁻¹ in N₂-saturated 0.1 M HClO₄ between 0.02 to 1.2 V vs. RHE is shown in Figure 2.3. Positive current corresponds to anodic current and negative current represents the cathodic current. The CV can be divided into three regions:

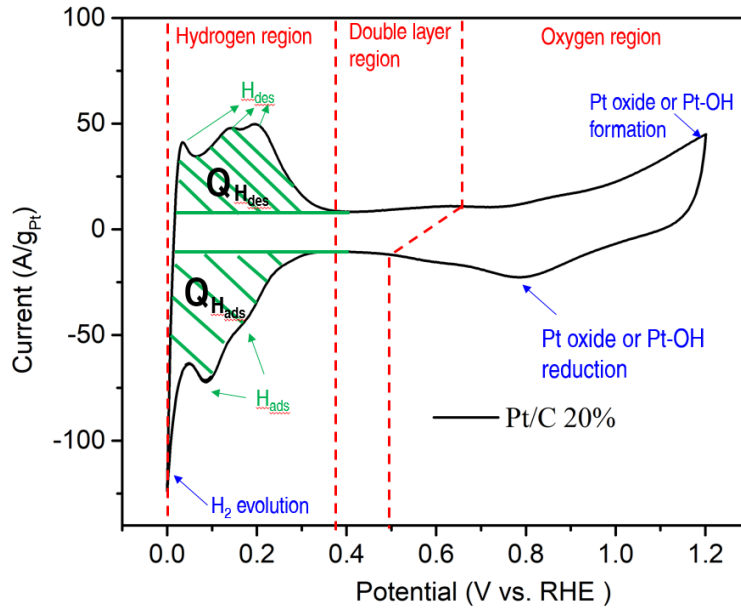


Figure 2.3. The typical CV of the commercial Pt/C catalyst at a sweep rate of 50 mV s^{-1} in N_2 -saturated 0.1 M HClO_4 between 0.02 to 1.2 V vs. RHE .

(i) **H region** (~ 0.03 to 0.4 V vs. RHE), which is related to the molecular hydrogen re-oxidation/evolution and the atomic hydrogen adsorption/desorption (H_{ads} and H_{des}). When the potential increases from ~ 0.02 to 0.4 V vs. RHE (forward scan), the pre-adsorbed H atoms on Pt surface are oxidized to form protons which desorb from the Pt surface and then diffuses into the electrolyte. When the potential decreases from ~ 0.4 to 0.02 V vs. RHE (backward scan), the protons in the electrolyte adsorb on the Pt surface and are reduced via H underpotential deposition. The multiple peaks originated from different crystalline facets of Pt. The charge associated with H adsorption or desorption is integrated to determine the number of hydrogen atoms adsorbed in a monolayer of coverage of the electrode surface, which can be used to determine the real electrochemical surface area (ECSA) of Pt and some Pt-based catalyst by the following formula.

$$\text{ECSA} = \frac{Q_H}{m_{\text{Pt}} q_H} \quad (2.1)$$

where Q_H is the charge for hydrogen adsorption region, m_{Pt} is the weight of Pt (mg) on the working electrode and q_H is constant (0.21 mC cm^{-2}) corresponding to the theoretical charge required for monolayer adsorption of hydrogen on Pt surface.

(ii) **Double layer region** (~ 0.4 to 0.7 V vs. RHE), related to the double layer charging/discharging. The current measured in this region is not associated with a faradaic process and is just associated with capacitive effects due to the contribution from the large surface area carbon support and anionic adsorption of the electrolyte.

(iii) **Oxide region** (above 0.7 V vs. RHE), related to the Pt oxides formation/reduction. By the adsorption and dissociation of H₂O molecules, the Pt can be oxidized into Pt-OH or Pt-oxide. During the backward scan, there is a peak related to the reduction of Pt-OH or Pt-oxide.

In this thesis, the electrochemical measurements were all conducted at room temperature. Initially, 50 potential cycles between 0.04 and 1.2 V (scan rate=100 mV s⁻¹) were completed to make sure that the surface of the working electrode was clean. CVs of the all the catalysts were measured between 0.04 and 1.2 V (scan rate=50 mV s⁻¹) in an N₂-saturated HClO₄ (0.1 M) solution.

2.4.2 ORR polarization curve

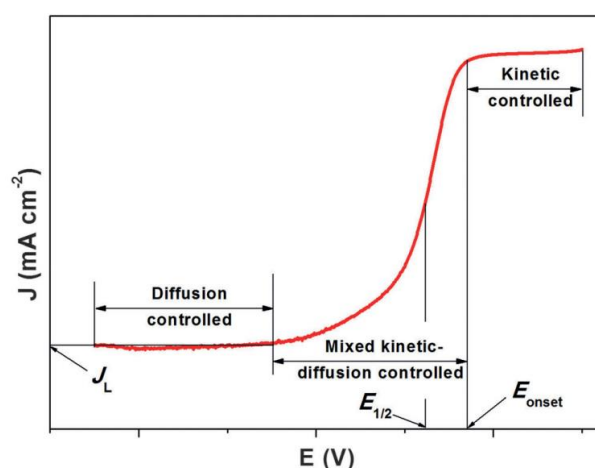


Figure 2.4. Typical ORR polarization curve.

In this thesis, the polarization curves for the ORR on the samples were performed between 0.04 and 1.2 V (scan rate=10 mV s⁻¹) in an O₂- or N₂-saturated HClO₄ (0.1 M) with an electrode rotation rate of 1600 rpm. Then, the net Faradic current was obtained by subtracting the voltammogram recorded under N₂ from the one recorded under O₂.

As shown in Figure 2.4, the typical ORR polarization curve can be divided into three parts in which ORR kinetics are controlled in different ways. (i) Kinetic-controlled region. The rate of ORR is quite low due to the insufficient overpotential to drive the ORR forward and the current density increases slightly as the potential decreases. (ii) Mixed controlled region. Both ORR kinetics and O₂ mass transport affect the overall rate, where the reaction is accelerated as the potential drops, reflecting in a remarkable increase of the current density. (iii) Diffusion-controlled region. The rate-limiting step is the transport of oxygen to the catalyst surface and the current density reaches a platform at a certain rotating speed (i_d).

Besides, there are two parameters including onset potential (E_{onset}) and half-wave potential ($E_{1/2}$), which are usually used to verify the activities of catalysts qualitatively. The onset potential is defined as the potential

when the current density exceeds 0.1 mA cm^{-2} . The half-wave potential is a potential at which the current is equal to one half of diffusion current (i_d). The more positive is the potential value, the more active is the catalyst.

Kinetic current density (i_k) is another important parameter in evaluating the intrinsic activity of ORR catalysts. It can be calculated by the following Levich-Koutechky equation,

$$\frac{1}{i} = \frac{1}{i_k} + \frac{1}{i_d} \quad (2.2)$$

$$i_d = 0.620nFC_{O_2}D_{O_2}^{2/3}\nu^{-1/6}\omega^{1/2} \quad (2.3)$$

where, n is the number of moles of electrons transferred in the half-reaction (number), F is the Faraday constant (96500C/mol), C_{O_2} is the concentration of dissolved O_2 (mol/cm^3), D_{O_2} is the diffusion coefficient of O_2 (cm^2/s), ν is the kinematic viscosity of the electrolyte solution (cm^2/s), ω is the rotation rate represented by the angular rotation rate (rad/s).

Furthermore, the Tafel slope is also a criterion related to the surface mechanism. When the current is small in the high potential region, the Tafel plots can be drawn by the formula 1.19 ($\eta = a + \text{bln}(i_k)$).

The Tafel slope tells how much one has to increase the overpotential to increase the reaction rate by a factor ten. The value of the Tafel slope can tell us which step is the rate-determining step.

As the RRDE protocol shown in Figure 2.2, oxygen reduction takes place at the disk electrode to produce H_2O_2 or H_2O . H_2O_2 produced at the disk electrode is radially transferred to the concentric platinum ring electrode by the forced convection caused by the rotating motion of the electrode. Subsequently, H_2O_2 is oxidized back to O_2 at the ring electrode. So the electron transfer number (n) and H_2O_2 intermediate production can be determined from RRDE by the following formula.

$$H_2O_2\% = \frac{200 I_r/N}{I_d + I_r/N} \quad (2.4)$$

$$n = \frac{4 I_d}{I_d + I_r/N} \quad (2.5)$$

where I_d is the disk current and I_r is the ring current. The collection efficiency of the RRDE was calibrated as $N = 0.37$.

2.4.3 ORR durability screening technique based on RDE

2.4.3.1 ADT test

A highly durable catalyst is crucial for the commercialization of fuel cells. The RRDE set-up can be used to conduct accelerated degradation testing (ADT) to investigate the durability of the catalyst materials. The ADT test of Pt/CNTs@C was carried out by potential cycling between 0.6 and 1.2 V in N₂-purged 0.1 M HClO₄ (scan rate=200 mV s⁻¹). After the cycles with certain numbers, the CV was conducted and ECSA was estimated. Through the ECSA loss before and after ADT test, we can compare the stability of the catalyst

2.4.3.2 Chronoamperometry

Chronoamperometry is an electrochemical technique in which the potential of the working electrode is stepped and the resulting current from faradaic processes occurring at the electrode (caused by the potential step) is monitored as a function of time. A promising electrocatalyst should maintain a high steady-state current density with time. The chronoamperometric (CA) measurement was achieved at a constant potential of 0.8 V versus RHE using the carbon rod as a counter electrode.

3 ULTRA-THIN CARBON COATED Pt/CNTS CATALYST

Ultra-thin carbon coated Pt/CNTs: a highly durable electro-catalyst for oxygen reduction

Titre de l'article: Ultra-minces revêtus de carbone Pt/CNTs: un électrocatalyseur très durable pour la réduction de l'oxygène

Authors: Xin Tong, Jianming Zhang, Gaixia Zhang, Qiliang Wei, Régis Chenitz, Jerome P. Claverie, and Shuhui Sun

Title of the journal: Chemistry of Materials, Publication Date: October 17, 2017

DOI: 10.1021/acs.chemmater.7b04221

Link between the following articles:

In this article, we synthesized electro-catalysts composed of Pt NPs supported on carbon nanotubes (CNTs) and covered with an ultra-thin layer of graphitic carbon. Such hybrid ORR catalysts were obtained by an interfacial *in situ* polymer encapsulation–graphitization method, where a glucose-containing polymer was grown directly on the surface of Pt/CNTs. The thickness of the carbon coating layer can be precisely tuned between 0.5 and several nanometers by simply programming the polymer growth on Pt/CNTs. The resulting Pt/CNTs@C with a carbon layer thickness of ~0.8 nm (corresponding to ~2-3 graphene layers) showed high activity and excellent durability with no noticeable activity loss, even after 20000 cycles of ADT test. This ultrathin carbon coating not only acts as a protective layer to prevent aggregation of Pt NPs but they also lead to a better sample dispersion in the solvent which is devoid of aggregates resulting in a better Pt utilization.

We found that there are metal–support interactions between the supporting material CNTs and Pt. This metal–support interaction is believed to be the key to stabilize catalyst and modulate the electronic structure, thereby affecting the stability and activity of the catalyst. So we will use doped graphene which is more favored to be doped to study the support interaction effect.

Ultra-thin carbon coated Pt/CNTs: a highly durable electro-catalyst for oxygen reduction

Xin Tong,^{†,‡} Jianming Zhang,^{‡, *} Gaixia Zhang,[†] Qiliang Wei,[†] Régis Chenitz,[†] Jerome P. Claverie^{§,*} and Shuhui Sun^{†,*}

[†] Institut National de la Recherche Scientifique-Énergie Matériaux et Télécommunications, Varennes, QC, Canada J3X 1S2.

[‡] School of Chemistry and Chemical Engineering, Jiangsu University, Zhenjiang, China, 212013.

[§] Department of Chemistry, Université de Sherbrooke, Sherbrooke, QC, Canada J1K 2R1.

[‡]School of Chemistry and Material Science, Guizhou Normal University, Guiyang, China, 550001.

ABSTRACT: Nanostructures constituted of Pt nanoparticles (NPs) supported on carbon materials are considered to be among the most active oxygen reduction reaction (ORR) catalysts for fuel cells. However, in practice, the usage of such ORR catalysts is limited by their insufficient durability caused by the low physical and chemical stability of Pt NPs during the reaction. We herein present a strategy to synthesize highly durable and active electro-catalysts composed of Pt NPs supported on carbon nanotubes (CNTs) and covered with an ultra-thin layer of graphitic carbon. Such hybrid ORR catalysts were obtained by an interfacial in situ polymer encapsulation–graphitization method, where a glucose-containing polymer was grown directly on the surface of Pt/CNTs. The thickness of the carbon coating layer can be precisely tuned between 0.5 and several nanometers by simply programming the polymer growth on Pt/CNTs. The resulting Pt/CNTs@C with a carbon layer thickness of ~0.8 nm (corresponding to ~2-3 graphene layers) showed high activity, and excellent durability, with no noticeable activity loss, even after 20000 cycles of ADT test. These ultrathin carbon coating not only act as a protective layer to prevent aggregation of Pt NPs but they also lead to better sample dispersion in solvent which are devoid of aggregates resulting in a better utilization of Pt. We envision that this polymeric nanoencapsulation strategy is a promising technique for the production of highly active and stable ORR catalysts for fuel cells and metal-air batteries.

Introduction

Proton exchange membrane (PEM) fuel cells are one of the most promising clean energy devices to convert chemical energy into electricity via a sustainable process.¹⁻⁴ However, their performance is highly dependent on the sluggish kinetics of the cathodic oxygen reduction reaction (ORR) process, which itself is determined by the efficiency of the electrocatalyst.⁵⁻⁷ Platinum (Pt) nanoparticles (NPs) dispersed on carbon materials are currently considered as the best ORR catalysts.^{8,9} Despite their popularity, there are

still many issues that are yet to be addressed before reaching large-scale commercial implementation. Notably, the insufficient stability of such Pt catalyst significantly curtails the lifetime and durability of PEM fuel cells. On the other hand, in direct methanol fuel cells (DMFCs), methanol can diffuse from anode to cathode through the membrane, which can lead to cathode depolarization and thus to a significant reduction of the overall cell potential due to the methanol oxidation reaction on Pt.^{10,11} Thus, extending the lifetime and enhancing methanol tolerance of the cathode catalyst without reducing its activity and without considerably increasing its cost remains a critical issue in the development of PEM fuel cells.

In PEM fuel cells, the ORR catalyst operates under harsh conditions (highly positive potentials and strongly acidic media) and the electrochemical surface area (ECSA) of Pt is lost during cycling, due to Ostwald ripening, dissolution and aggregation of the Pt NPs, as well as the corrosion and oxidation of the carbon support.¹² One of the effective strategies to improve the durability of Pt catalysts is to employ novel supporting materials.¹³ For example, hollow core–mesoporous shell carbon,¹⁴ mesoporous carbon,¹⁵ ordered hierarchical nanostructured carbon,¹⁶ colloid-imprinted carbon supports,¹⁷ graphene,^{9, 18} carbon nanotubes (CNTs)¹⁹⁻²¹ have been examined as alternatives to Vulcan XC-72, a commercial carbon black which is often used as benchmark support.²² Among those, CNTs have shown encouraging results that have been correlated with their high conductivity, high surface area and excellent chemical resistance.^{19, 21}

Another successful strategy consists in protecting the Pt NPs in a shell.^{11,23-33} With the help of this protective layer, the Pt NPs are less prone to agglomerate or to detach from the support under highly oxidizing conditions. Among those, carbon shells have shown to prolong the catalyst lifetime,^{11,24,26,28,29,33,34} but with highly variable results which can be explained by the fact that too thin carbon coating layers are not efficiently protecting the Pt NPs while too thick ones are blocking the effective active surface of Pt.²⁸ In this report, we designed a highly durable and active ORR catalyst by combining the excellent properties endowed by CNTs as support and the protective action of ultra-thin graphitic carbon layers with controlled thickness. Thus, Pt NPs supported on CNTs and encapsulated in carbon layers (Pt/CNTs@C) were prepared by a facile *in-situ* polymeric encapsulation-graphitization method which allowed a precise control over carbon thickness as well as a solid anchoring of the Pt NPs at the surface of the CNTs (Scheme 1). Electrochemical evaluations indicate that the electrocatalytic activity strongly depends on the thickness of the carbon coating layers. Once optimized, the thin coating around Pt/CNTs effectively inhibits the Pt catalyst aggregation or dissolution during cycling, while maximizing reagent mass-transport. Thus, the Pt/CNTs@C composite combines high durability and catalytic activity in ORR. It also shows a high methanol tolerance, overcoming the loss of ORR activity of Pt/CNTs in the presence of methanol.

EXPERIMENTAL SECTION

Materials. CNTs (multiwall, several hundred nm in length and 15–30 nm in diameter) were purchased from Bayer. Formic acid (HCOOH, 98 %), hexachloroplatinic acid (H₂PtCl₆·6 H₂O, 99.95 %), 4,4'-azobis (4-cyanovaleric acid) (ABV, >75%), sodium lauryl sulfate (SDS) and styrene (99.9%) were all purchased from Sigma-Aldrich. Reversible addition-fragmentation chain transfer (RAFT) polymerization agent poly(acrylic acid)(butyl acrylate) (PABA) was synthesized previously in our laboratory.³⁵⁻³⁷

Synthesis of Pt NPs supported on carbon nanotubes (Pt/CNTs). Pt/CNTs were obtained by the chemical reduction of Pt precursor with formic acid (as shown in Scheme 1).³⁷ Typically, 10 mg of CNTs were dispersed in 4 mL of H₂O and mixed ultrasonically for ~1 h. Then 0.5 mL of formic acid and 2 mL of hexachloroplatinic acid solution (1 mg_{Pt} mL⁻¹) were added to the above suspension. The mixture was stirred at 80 °C for 30 min until the solution turned from golden-orange to colorless transparent. The as-prepared product was washed 3 times with water and collected by centrifugation. Then the Pt/CNTs (Pt: 17 wt. %) were dried in a vacuum oven at 60 °C for 12h.

Synthesis of Pt/CNTs coated with carbon layer (Pt/CNTs@C). The synthesis of N-acryloyl-D-glucosamine (AGA) and of the RAFT agent PABA containing 10 acrylic acid units and 5 butyl acrylate units were reported previously.³⁵⁻³⁷ The polymer encapsulation of Pt/CNTs was achieved as follows: typically, 40 mg of Pt/CNTs and 20 mg of PABA were dispersed into 8 mL of water and sonicated with 30% amplitude for 5 min (Fisher scientific sonic dismembrator 500, 400W) to yield a black stable Pt/CNTs@PABA suspension. Then 10 mg of ABV initiator was added to the above solution. Meanwhile, 300 mg of AGA, 200 mg of styrene and 10 mg of SDS were added to 8 mL of water, and the resulting emulsion was degassed with N₂ for 30 min. Then a syringe (50 mL) was filled with the emulsion and fixed to a syringe pump connected to the Pt/CNTs@PABA dispersion. The Pt/CNTs@PABA dispersion was heated at 80 °C under magnetic stirring and the monomers were added in under N₂ atmosphere over a period of 5h. Then, the dispersion was kept at 80 °C for another 2h to complete the polymerization. The encapsulated Pt/CNTs was collected by centrifugation and dried in a vacuum oven. The product was then heated under a N₂ atmosphere at 550°C for 3h.

Characterizations.

Transmission electron microscopy (TEM) observations were conducted with a JEOL JEM-2100F microscope equipped with a field emission gun running at 200 kV. X-ray diffraction (XRD) patterns were recorded with Bruker D8 Advance with Cu K α as an X-ray source. Thermogravimetric analysis (TGA) was performed under air atmosphere with a heating rate of 4°C min⁻¹ on a MS coupled Thermogravimetric Analyzer (TA Instruments TGA Q500 / MS Discovery). X-ray photoelectron spectroscopy (XPS) was measured with a VG Escalab 220i-XL using Mg K α line as an excitation source.

Electrochemical characterizations. An Autolab electrochemical system (Model, PGSTAT-302, Ecochemie, Brinkman Instruments) was used to characterize the electrochemical properties of the corresponding samples. In a three-electrode system, a glassy carbon rotating disk electrode (RDE) was used as the working electrode, a Pt wire was used as the counter electrode, and a saturated calomel electrode (SCE) was used as the reference electrode. All potentials in this study were referred to reversible hydrogen electrode (RHE). The catalyst ink was prepared as follows, 5 mg of catalyst was mixed with 50 μL deionized water, 1650 μL ethanol and 85 μL of 5 wt% Nafion Solution (in lower aliphatic alcohols and water) followed by 30 min ultrasonication. Then 7 μL of the catalyst suspension was pipetted onto the polished GC (Pine Research Instrument, \varnothing 5 mm, 0.196 cm^2), to maintain a Pt loading of about 20 $\mu\text{g}_{\text{Pt}} \text{cm}^{-2}$ for all tests. Then the working electrode was dried at ambient conditions before being immersed in a 0.1M HClO_4 solution. The electrochemical measurements were all conducted at room temperature. Initially, 50 potential cycles between 0.04 and 1.2 V (scan rate=100 mV s^{-1}) were completed to make sure that the surface of the working electrode was clean. CVs of the all the catalysts were measured between 0.04 and 1.2 V (scan rate=50 mV s^{-1}) in a N_2 -saturated HClO_4 (0.1 M) solution. The polarization curves for the ORR on the samples were performed between 0.04 and 1.2 V (scan rate=10 mV s^{-1}) in an O_2 - or N_2 -saturated HClO_4 (0.1 M) with an electrode rotation rate of 1600 rpm. Then, the net Faradic current was obtained by subtracting the voltammogram recorded under N_2 from the one recorded under O_2 . Accelerated durability tests (ADT) was carried out by potential cycling in a square wave between 0.6 and 1.2 V in N_2 -purged 0.1 M HClO_4 (scan rate=200 mV s^{-1}). To calculate the ECSA of Pt, the following equation was used:

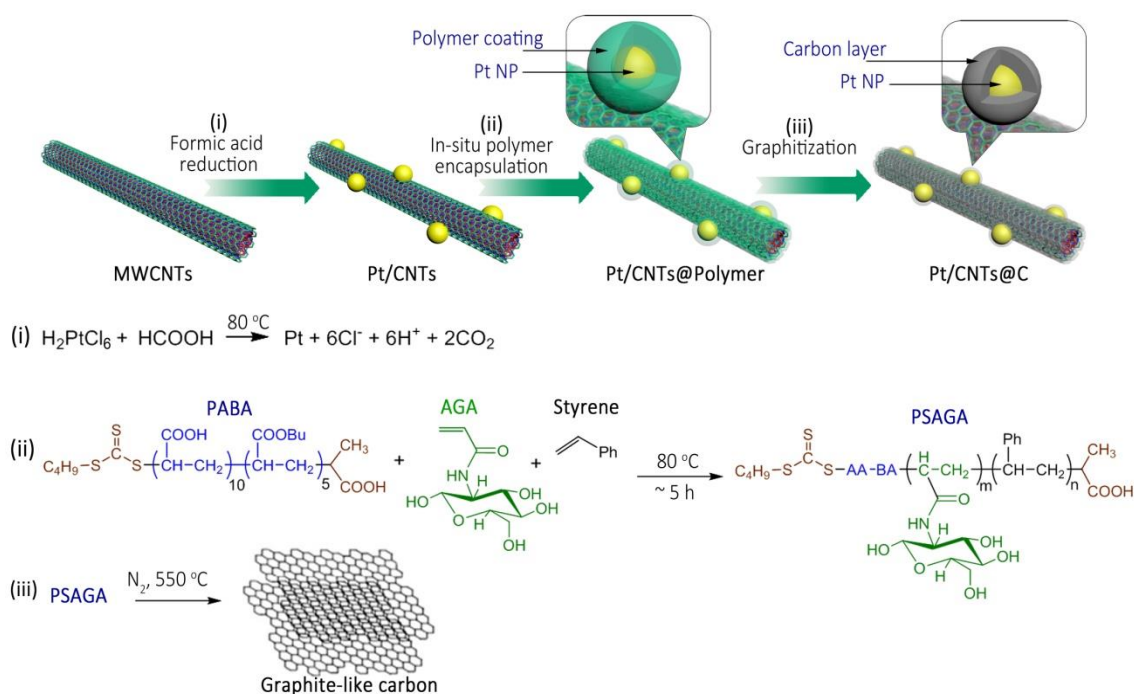
$$\text{ECSA} = \frac{Q_{\text{H}}}{m_{\text{Pt}} q_{\text{H}}}$$

Where Q_{H} is the charge for hydrogen adsorption region, m_{Pt} is the weight of Pt (mg) on the working electrode and q_{H} is constant (0.21 mC cm^{-2}) corresponding to the charge required for monolayer adsorption of hydrogen on Pt surface.³⁸

RESULTS AND DISCUSSION

Preparation of Pt/CNTs@C Composite. The Pt/CNTs@C nanostructures were synthesized via an *in situ* polymer nano-encapsulation method, followed by a graphitization process. As presented in Scheme 1, Pt NPs are first formed at the surface of the CNTs through the reduction of H_2PtCl_6 by HCOOH (Step i). The encapsulation of Pt/CNTs begins with the adsorption of the PABA RAFT dispersant constituted of acrylic acid and butyl acrylate units onto the CNTs surface via non-covalent interactions. The PABA molecules adsorbed on Pt/CNTs act as spacers which obstruct the formation of π - π interactions between CNTs, allowing the uniform and stable dispersion of Pt/CNTs in water (see supporting Figure S1 and our previous reports).^{36,37} Afterward, upon the introduction of the monomers, an *in situ* growth of polymer chain occurs

at the Pt/CNT surface via RAFT polymerization (Step ii). As the RAFT process is a so-called controlled polymerization process, the newly formed polymer extends the RAFT dispersant chain, resulting in the formation of a block copolymer. Because the active RAFT dispersant is anchored at the surface of the Pt/CNTs, the hydrophobic block constituted by the newly formed polymer can effectively grow into a continuous polymer shell encapsulating the Pt/CNTs. Since the initial dispersion of Pt/CNTs is devoid of aggregates, the encapsulation occurs in a 1 to 1 fashion, leading to the formation of Pt/CNT@polymer coaxial structures. Herein, a special monomer, N-acryloyl-D-glucosamine (AGA), was used to form the shell as it contains a glucosamine unit which is a carbon source. However, the resulting glucosamine polymer tends to desorb from the CNTs surface as it is water soluble. Therefore, a mixture of AGA and hydrophobic styrene (S) (Step ii) was selected to form the copolymer shell. Since the amount of monomers (S + AGA) is much larger than the RAFT dispersant one, the asymmetric block copolymer is constituted of a long hydrophobic block, PSAGA, and a short surface-active block (the RAFT dispersant). The encapsulation process is exceedingly efficient as every Pt NP and CNT are trapped in a continuous shell of copolymer to form a Pt/CNTs@PSAGA structure (confirmed by TEM, Figure 1, see below). The uniform glucose polymer layer laid the foundations of next step. After being annealed at 550 °C under N₂ atmosphere, the polymer layer was pyrolyzed into a graphitic carbon shell (Step iii).



Scheme 1. Synthetic process of Pt/CNTs@C and the corresponding reaction at each step.

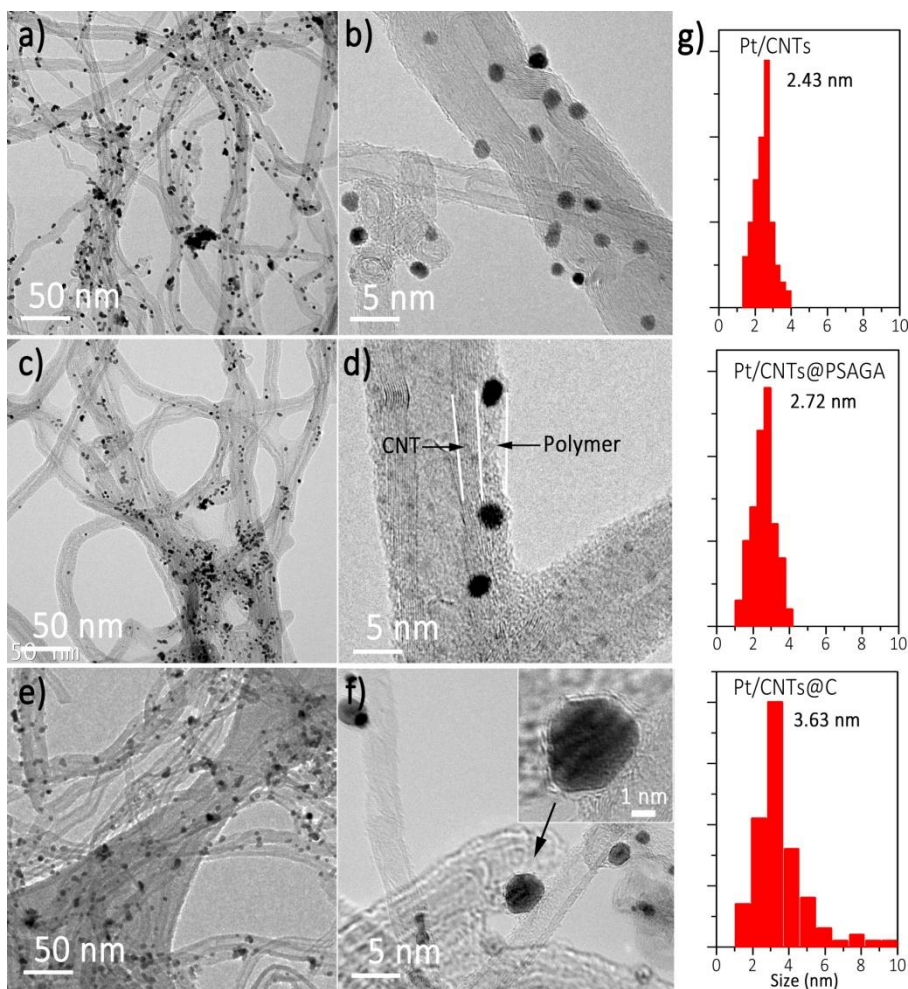


Figure 3.1. TEM images of Pt/CNTs (a, b), PSAGA encapsulated Pt/CNTs before (c, d) and after (e, f) graphitization. Inset of (f) shows the HR-TEM image of Pt/CNTs@C. (g) Corresponding Pt NP size variation of all nanohybrids at different synthetic steps. The size distributions of Pt were analyzed by randomly selecting 100 NPs to measure their diameters.

Structure Characterization. The morphologies of the nanostructures at each synthetic step were investigated by TEM. Figure 3.1-a and b show the TEM images of the Pt/CNTs at different magnifications. Clearly, the Pt NPs are uniformly distributed at the CNTs surface. After polymer encapsulation, as shown in Figure 3.1-c and d, a continuous and uniform polymer coating with a thickness $\sim 5-8$ nm is formed around each CNT, and the well separated Pt NPs are completely embedded in the polymer (Figure 3.1-d), indicating the successful encapsulation. After thermal annealing, the polymer layer is transformed into graphitic carbon layer covering all around the Pt/CNTs (Pt/CNTs@C). As displayed in the TEM images (Figure 3.1-e and f), no significant aggregation of Pt NPs can be observed after annealing. High-resolution TEM (HR-TEM) image (inset of Figure 3.1-f) further shows that each Pt NP is completely covered by a continuous graphene-like carbon coating with a thickness ~ 0.8 nm, corresponding to 2-3 graphene layers. The particle size of the Pt NPs was measured at each synthetic step (Figure 3.1-g). Remarkably, the size of Pt NPs

remains nearly unchanged, with a slight increase from ~ 2.4 nm to 3.6 nm due to the heat-treatment. By contrast, when Pt/CNTs composite (no polymer coating) is annealed under the same conditions, the size of the Pt NPs reaches ~ 6.7 nm (Figure S3). These results indicate that the carbon coating is efficiently protecting the Pt NPs from the coarsening process which is usually associated to a loss of catalytic activity in ORR.

Table 3.1 Recipe for the synthesis of carbon coated Pt supported on CNTs with different thickness.

Sample	Pt/CNTs (g)	PABA (g)	ABV (g)	Styrene (g)	AGA (g)	SDS (g)	C coating thickness (nm)
Pt/CNTs@C-1	0.04	0.02	0.02	0.1	0.15	0.005	~0.5
Pt/CNTs@C-2	0.04	0.02	0.02	0.2	0.3	0.01	~0.8
Pt/CNTs@C-3	0.04	0.02	0.02	0.4	0.6	0.02	~1.5
Pt/CNTs@C-4	0.04	0.02	0.02	0.8	1.2	0.04	>2

As illustrated in Scheme 1, by increasing the amount of monomers, the final copolymer chain becomes longer, resulting in a thicker carbon coating due to a higher content of glucose unit. Thus, the thickness of the carbon coating can be precisely controlled by tuning the amount of added monomer.³⁴ Table 1 lists the composition of the various Pt/CNT@C composites. The samples were analyzed by TEM investigations to assess the thickness of the C coating layer. Figure 3.2 presents the TEM images of the corresponding Pt/CNT@C composites listed in Table 1. The average thickness of the carbon coating gradually increased from 0.5 nm (a), to ~ 0.8 nm (b), ~ 1.5 nm (c) and ~ 2 nm (d) as the monomer amount increased, which is consistent with the controlled nature of the RAFT polymerization. Observations by HR-TEM indicate that the carbon coating is composed of distorted graphite-like carbon segments containing between a single (a) to ~ 5 graphene layers (d). However, for Pt/CNTs@C-1 (a), the carbon coverage is not complete, and bare Pt surface can be observed occasionally (arrows in Figure 3.2a). In this case, the size of the Pt NPs is augmented during annealing (~ 4.5 nm in diameter, see Figure S2), which is consistent with the insufficient polymer protection.

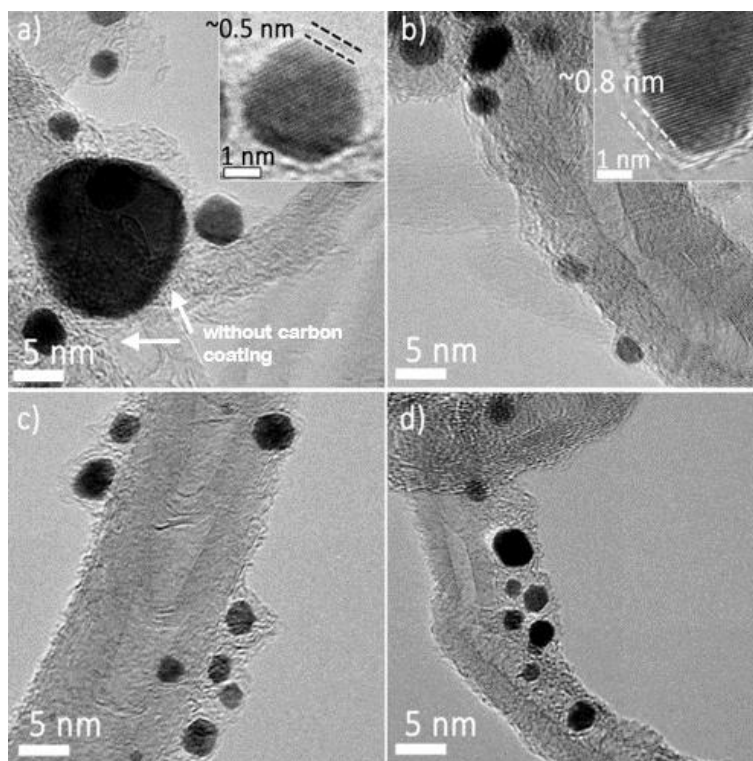


Figure 3.2. TEM images of Pt/CNTs@C samples prepared using different amount of monomers. (a-d) correspond to the Pt/CNTs@C-1 to 4, respectively, listed in Table 1. Insets show the HR-TEM images.

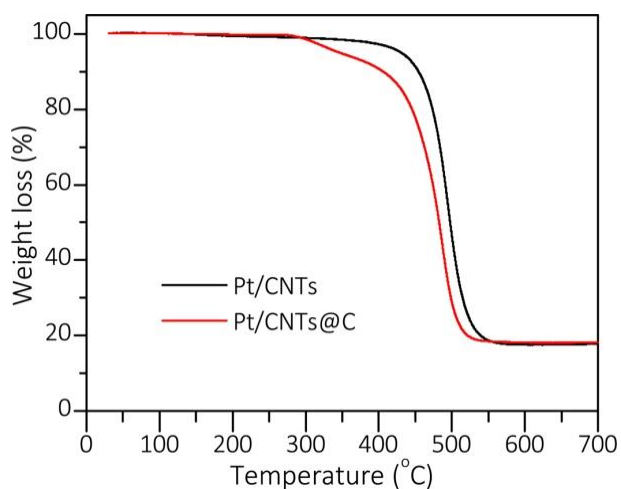


Figure 3.3. TGA curves of Pt/CNTs and Pt/CNTs@C with a carbon coating of ~ 0.8 nm (Pt/CNTs@C-2 in Table 1) Thermogravimetric analysis (TGA) further confirms the content of carbon coating on Pt/CNTs@C sample. Figure 3.3 shows the TGA curves of the Pt/CNT sample with (red) and without (black) carbon coating (~ 0.8 nm of thickness, Pt/CNTs@C-2). As reported, different oxidation behaviors can be observed in different structural forms of carbon,⁴⁰ and a less ordered carbon form tends to be oxidized at a lower temperature, whereas a well graphitized structure is more stable.³⁹ For both samples, a sharp weight loss occurred from

~450 up to 500°C which could be assigned to the oxidation of CNTs.³⁹ For Pt/CNTs@C sample, an additional weight loss of ~ 6.5 % appeared at the lower temperature region between 300°C and 400°C, which corresponds to the oxidation of the disordered graphene-like carbon coating. This relatively high weight loss indicates that the carbon layer not only covers the Pt NPs but also the CNTs (such layer is not visible by TEM because it is carbon over carbon).

The crystallinity of Pt/CNTs and Pt/CNTs@C was assessed by XRD. As shown in Figure 3.4 (a), both Pt/CNTs and Pt/CNTs@C composites show a well-crystallized Pt and graphitic carbon structure. The four major diffraction peaks at ~39.8°, 46.3°, 67.5°, and 81.4° correspond to the (111), (200), (220), and (311) planes of the face-centered cubic (fcc) Pt (JCPDS No.04-0802).²⁹ The peak at ~25.5° can be assigned to the (002) diffraction of the graphitic carbon in CNTs.⁴¹ After carbon coating (red), the Pt peaks become more narrow, indicating an increase of crystallinity. A decrease of the peak intensity ratio of the graphite (002) to Pt (111) is also observed, perhaps due to the less ordered structure of carbon coating compared to CNTs, which is consistent with the TGA analysis.

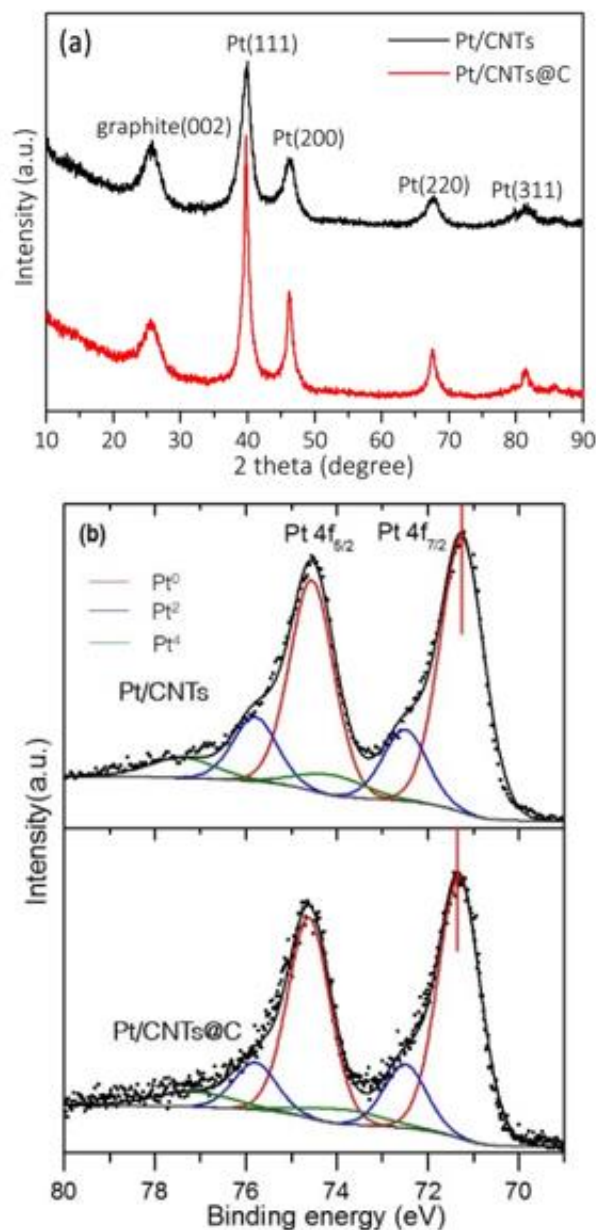


Figure 3.4. XRD patterns (a) and XPS spectra (b) of Pt/CNTs and Pt/CNTs@C.

Surface chemistry variations of the Pt/CNTs samples with and without a carbon coating were examined using XPS. Figure 3.4 (b) shows the Pt 4f spectra of the samples before and after carbon coating. Both samples show the two typical peaks at high and low binding energy respectively corresponding to Pt 4f_{5/2} and Pt 4f_{7/2}. The Pt 4f signals can be deconvoluted into three doublets which can be assigned to the Pt⁰ state (red line), Pt²⁺ state (blue line) and Pt⁴⁺ state (green line).^{25, 28} The abundance of the three oxidation states is not affected by the presence of the carbon coating, indicating that Pt remains unchanged during the coating process. However, a slight shift of ~ 0.2 eV of Pt to higher binding energy (BE) is detected in Pt/CNTs@C compared to Pt/CNTs. The increase in Pt BE in Pt/CNTs@C may result in slightly weaker Pt-

O binding in comparison to Pt/CNT samples, an effect which has been reported to lead to an improvement of ORR rates by inhibiting the formation of surface Pt oxides.^{42, 43}

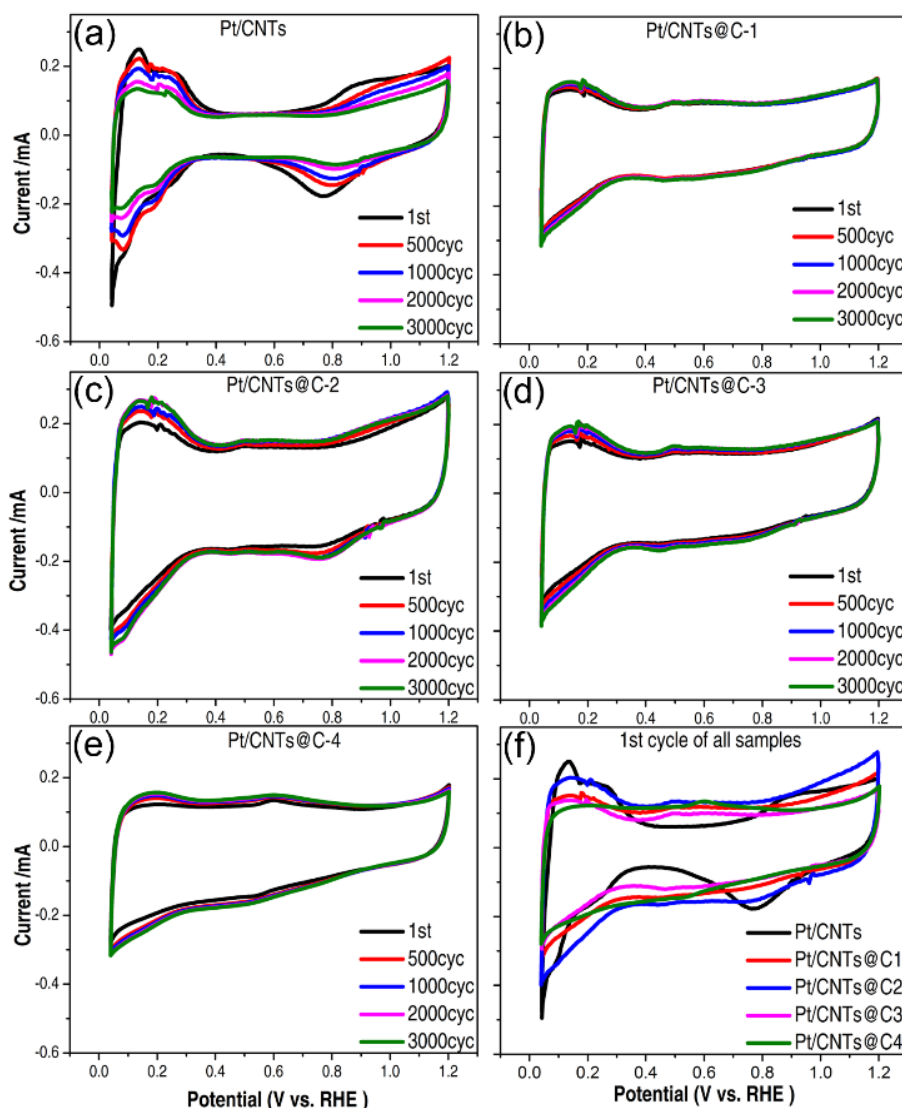


Figure 3.5. CV curves of different cycles on Pt/CNTs (a), Pt/CNTs@C-1 (b), Pt/CNTs@C-2 (c), Pt/CNTs@C-3 (d) and Pt/CNTs@C-4 (e). (f) CVs of the 1st cycle for all samples. CVs were recorded in N_2 -saturated 0.1 M $HClO_4$. (50 mV s^{-1} , room temperature).

Electrochemical Properties. Cyclic voltammetry (CV) experiments were conducted to estimate the electrochemical performance of as-prepared material and the effects of the carbon layer on the catalytic performance. During the preparation of catalyst ink, the dispersion of Pt/CNTs in water is not colloidal stable, leading to non-uniform electrodes. However, after carbon coating, a uniform dispersion of Pt/CNTs@C was readily obtained (Figure S4) which likely originates from the fact that the samples are prepared by carbonization of well-dispersed Pt/CNTs@polymer sample. As shown in Figure 3.5, the CV curves of all catalysts present the typical characteristic features of the monolayer hydrogen adsorption (H_{ads})

and desorption (H_{des}) on Pt surface and of the formation/reduction of Pt-OH and Pt-O groups. However, for the samples with carbon coating (b-e), the peaks of H_{ads}/H_{des} are generally much lower in height and less well-defined compared with those of pure Pt/CNTs (a). With the increase of carbon coating layer thickness (samples listed in Table 1), the intensity of the peak of H_{des} and H_{ads} is decreased (f). For Pt/CNTs@C-1, the lower activity can be ascribed to the larger Pt particle size.⁴⁴ For Pt/CNTs@C-4, the H_{des} and H_{ads} almost disappeared, indicating that the carbon layer is too thick and hinders the ORR and cause more sluggish kinetics. Besides, the Pt oxides reduction peak around 0.8 V has also nearly disappeared. By contrast, the Pt/CNTs@C-2 shows a more obvious H_{des}/H_{ads} and Pt oxidation/reduction peaks compared with other carbon coated materials, revealing a higher exposed Pt surface.

The accelerated durability test (ADT) is a convenient method to evaluate the stability of the electrocatalysts in an accelerated fashion.³⁸ In Figure 3.5-a, the catalytic performance of Pt/CNTs is deteriorated during the test, as shown by the obvious ECSA loss after 3000 cycles. In contrast, the performance of Pt/CNTs@C (b-e) is more stable. The ECSAs in the first cycles are always the smallest, which may be due to the prolonged time necessary to activate the catalyst. Once activated, the CV curves of the catalysts do not show significant change over time, suggesting that the carbon layer protects the Pt NPs during ADTs. Thus, the carbon coatings exert two antagonistic effects on the ORR as it can improve the stability, but also reduce the catalytic activity more or less, depending on the layer thickness. Therefore, precisely controlling and optimizing the carbon coating thickness is highly desirable, yet, remains great challenge.

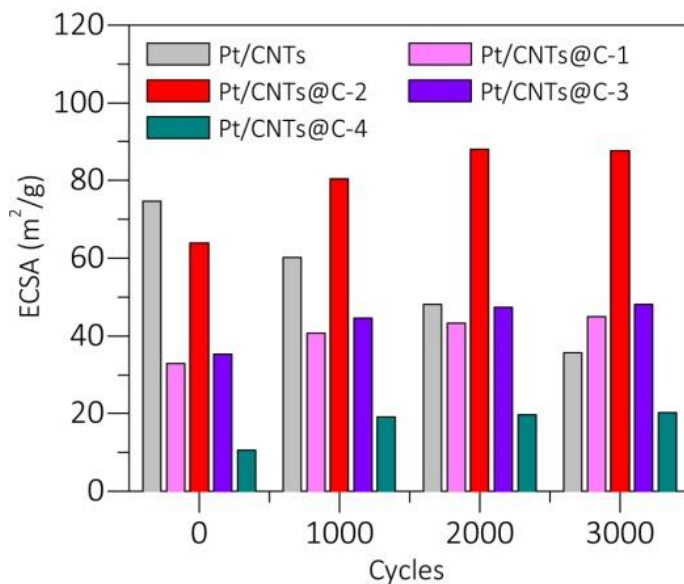


Figure 3.6. ECSA as a function of reaction cycles for Pt/CNTs and Pt/CNTs@C-(1-4). The values of ECSA were calculated from the H_{ads}/H_{des} charge in CVs.

The accelerated durability test (ADT) is a convenient method to evaluate the stability of the electrocatalysts in an accelerated fashion.³⁸ In Figure 3.5-a, the catalytic performance of Pt/CNTs is deteriorated during the

test, as shown by the obvious ECSA loss after 3000 cycles. In contrast, the performance of Pt/CNTs@C (b-e) is more stable. The ECSAs in the first cycles are always the smallest, which may be due to the prolonged time necessary to activate the catalyst. Once activated, the CV curves of the catalysts do not show significant change over time, suggesting that the carbon layer protects the Pt NPs during ADTs. Thus, the carbon coatings exert two antagonistic effects on the ORR as it can improve the stability, but also reduce the catalytic activity more or less, depending on the layer thickness. Therefore, precisely controlling and optimizing the carbon coating thickness is highly desirable, yet, remains great challenge.

By integrating the charge in the hydrogen adsorption region ($0 \leq V \leq 0.3$ V), ECSA can be estimated to evaluate the catalyst properties. After the 1st cycle (Figure 3.5-f, also see Table S1), the ECSA of Pt/CNTs and Pt/CNTs@C-(1-4) are found to be 75, 33, 64, 35 and 11 m²/g, respectively. Except for Pt/CNTs@C-1, the ECSA decreases with the increase of carbon coating thickness, since the carbon layer acts as an obstacle for the catalysis reaction. The ECSA value of Pt/CNTs@C-2 is comparable to that of Pt/CNTs, suggesting that the hindrance caused by the carbon layer in this catalyst is minimized. The low ECSA value for Pt/CNTs@C-1 is mainly attributed to the larger size of Pt NPs caused by the annealing process at 550 °C but without sufficient carbon layer protection.

The alteration of ECSA as a function of cycle numbers is summarized in Figure 3.6. For Pt/CNTs, a sharp drop of ECSA takes place after 3000 cycles, with only 50% of the initial ECSA remaining. By contrast, for Pt/CNTs@C samples, no obvious changes (except for the 1st cycle as mentioned above) occurred after 3000 cycles ADT. Impressively, after 1000 cycles ADT, the ECSA of Pt/CNTs@C-2 is significantly larger (2 to 4 times) than those of pristine Pt/CNTs and other carbon coated samples. The increase in ECSA over time for all carbon coated samples can be attributed to the slight corrosion of the carbon layer, leading to a gradual exposition of fresh Pt surface.²⁸ Thus, a carbon coating thickness of ~ 0.8 nm (Pt/CNTs@C-2, Figure 3.5-c) offers the optimal compromise between activity and durability.

Figure 3.7 shows the typical ORR linear sweep voltammeteries (LSVs) for all samples under identical experimental conditions. The best catalyst should exhibit the highest possible value of half-wave potential ($E_{1/2}$) and current values at 0.80 V (vs. RHE) (see Table S2 for details). The sample Pt/CNTs@C-4 shows the lowest values before and after ADT testing, indicative that the carbon layer is too thick. Initially (before ADT testing), the “best” catalyst (based on $E_{1/2}$, and current value at 0.80 V) is the Pt/CNTs catalyst. However, after 3000 cycles, the trend is clearly reversed, compared to Pt/CNTs, the Pt/CNTs@C-2 shows much higher $E_{1/2}$ potential (0.84V vs 0.76V) and current density at 0.80V (3.1 vs 1.4 mA/cm²). The activity of Pt/CNTs@C-2 catalyst after 3000 ADT is still lower than the initial activity of the state-of-the-art Pt/C catalyst⁴⁵⁻⁴⁸, and more work is underway to improve the activity of this highly stable catalyst. Remarkably, the $E_{1/2}$ potential and current values of Pt/CNTs@C have increased during ADT testing, whereas those of

Pt/CNTs decrease (by more than 50% for the current density), clearly indicating the protective role of the carbon coating. These results confirm that the Pt/CNTs@C-2 catalyst has a much better lifetime performance. In addition, the ORR performance of Pt/CNTs and Pt/CNTs@C-2 catalysts in the presence of CH₃OH are shown in Figure 3.7(f). In the presence of methanol, there are obvious anodic peaks for methanol oxidation reaction (MOR) at around 0.8 V (vs. RHE) in the ORR polarization curves for all samples. Therefore, there are competitions between the ORR and MOR for all catalysts.¹⁰ Interestingly, Pt/CNTs@C-2 shows much smaller current density for MOR than that for Pt/CNTs, indicating the much better methanol tolerance of the former catalyst. This is because that the carbon shell could reduce/block the adsorption of methanol on the Pt surface.

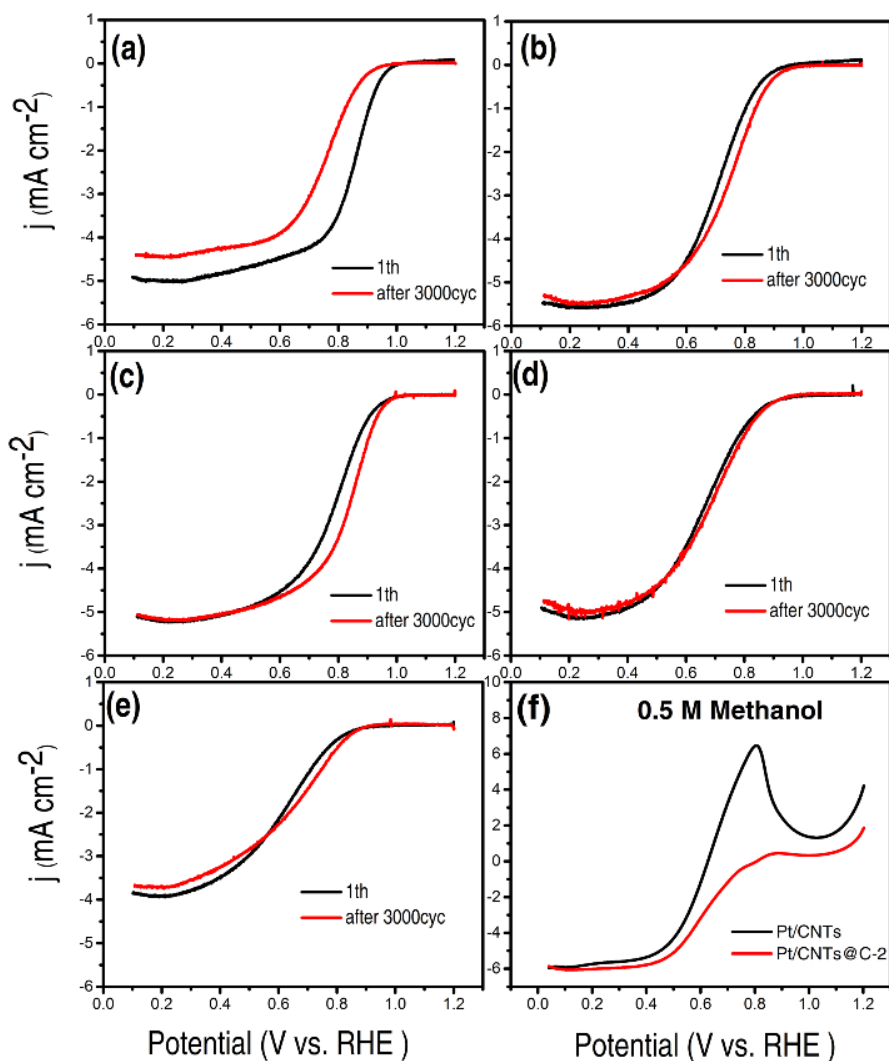


Figure 3.7. LSVs on Pt/CNTs (a), Pt/CNTs@C-1 (b), Pt/CNTs@C-2(c), Pt/CNTs@C-3 (d) and Pt/CNTs@C-4 (e) (before and after ADT test, 3000cycles) (f) Pt/CNTs and Pt/CNTs@C-2 in the presence of 0.5M methanol. LVs were recorded in O₂-saturated 0.1 M HClO₄. (10 mV s⁻¹, room temperature)

TEM analyses were conducted for samples after 3000 cycles of ADT. Figure 3.8 (a) shows that Pt NPs in Pt/CNTs (initial size 2.4 nm) agglomerated into irregular larger NPs of size ~ 11.5 nm. By stark contrast, no obvious aggregation is observed for Pt NPs in Pt/CNTs@C-2 (Figure 3.8-b, 3.9 nm after ADT vs. 3.6 nm before ADT). This observation is consistent with all electrochemical tests, and confirms that the Pt/CNTs@C-2 is more electrochemically stable than the unmodified Pt/CNTs catalyst. The TEM images (Figure 3.8) also indicate that Pt/CNTs@C is less aggregated (better dispersion in solvent) than Pt/CNTs without carbon coating. Indeed, during the polymer nanoencapsulation step, the carbon nanotubes are dispersed in water, forming a stable, homogeneous and aggregate free dispersion.²¹

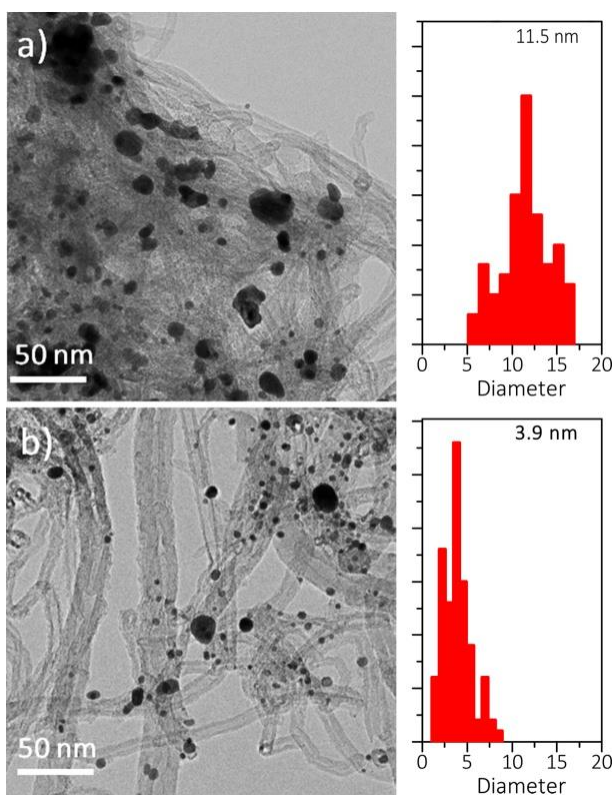


Figure 3.8. The TEM images and the size distribution of Pt NPs of Pt/CNTs (a), Pt/CNTs@C-2 (b) after ADT.

Furthermore, we evaluated the stability of Pt/CNTs@C-2 catalyst by a continuous 20000 potential cycling ADT test. As shown in Fig. 3.9(a,b), with cycling, the ECSA of Pt/CNTs@C-2 catalyst gradually increases due to the corrosion of the carbon coating and increased exposure active sites of Pt NPs. Interestingly, the ECSA reaches a plateau (~ 85 m²/g) at 2000 cycle and it remains stable for 10000 cycles, indicating the important role of carbon layer in preventing the aggregation of PtNPs. Even after extended 20000 cycles, the ECSA is still ~ 64 m²/g which is close to the initial ECSA, and represents only a 25% loss compared to the plateau value. In sharp contrast, the ECSA of Pt/CNTs decreases continuously over time, as shown in Figure. 3.9 (c,d). Moreover, after 10000 cycles, the ECSA of Pt/CNTs is only 27 m²/g, which indicates a

~64% loss of its initial ECSA. In this test, Pt/CNTs@C-2 clearly demonstrates extremely high durability due to carbon coating.

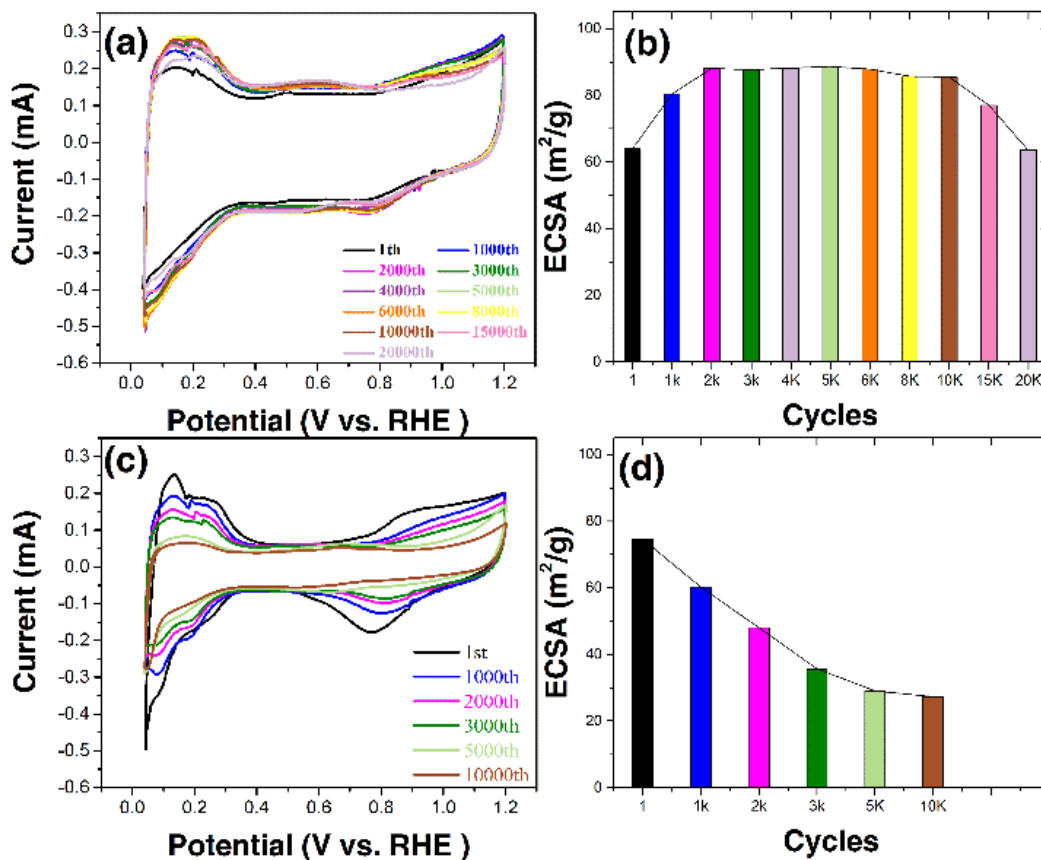
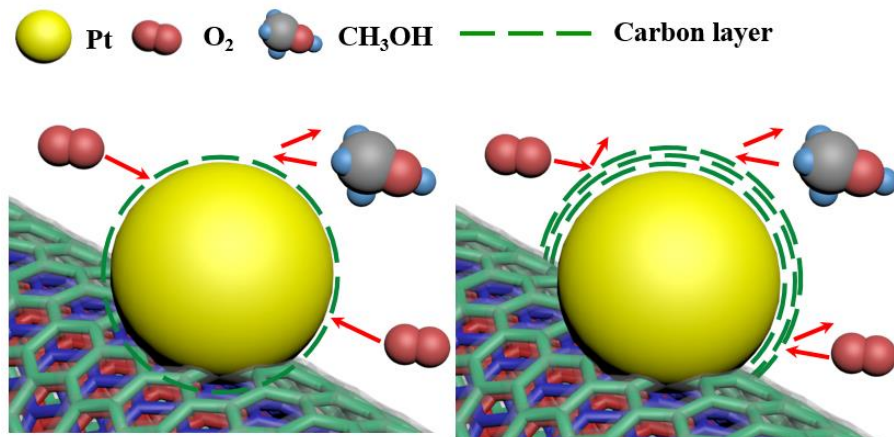


Figure 3.9. Long-term performance on CV curves of Pt/CNTs@C-2 (a) and Pt/CNTs (c). ECSA as a function of reaction cycles for Pt/CNTs@C-2 (b) and Pt/CNTs (d). CVs were recorded in N_2 -saturated 0.1 M $HClO_4$.



Scheme 2. ORR reaction taking place on Pt/CNTs@C samples with different carbon coating layers.

Based on the above results, a possible mechanism for the significantly enhanced durability is proposed. In general, the size increase of the pristine Pt NPs is due to the Ostwald ripening.^{12, 26} The thin carbon layer wrapped on the Pt NPs not only acts as a protective layer but also a barrier between catalytic sites and reactants. The thickness of the disordered graphitic layer of carbon plays a key role to control the electrocatalytic performance.³⁴ A carbon coating of ~ 0.8 nm average thickness (Pt/CNTs@C-2, Scheme 2, left) is permeable to oxygen molecules without hindering the mass transport of molecular oxygen and the contact between oxygen and the catalyst surface. In addition, such carbon coating is sufficiently thick to prevent Pt NP dissolution or detachment from the CNT surface. Furthermore, it can reduce the adsorption of methanol (the methanol molecule is too large) on the Pt surface and shows higher tolerance to methanol. While, when the carbon coating is too thick, as depicted on the right part of Scheme 2, the oxygen molecules cannot easily reach the surface of the catalyst. In this case, the carbon layer mainly works as an obstacle for ORR, therefore, resulting in a lower activity of the catalyst.

CONCLUSIONS

We have developed a facile *in-situ* polymer nanoencapsulation-graphitization method to prepare carbon coated catalysts (Pt/CNTs@C). The thickness of the carbon coating can be precisely controlled by varying the amount of added monomer, and the optimal thickness for ORR catalysis has been explored. This *in-situ* polymeric encapsulation-graphitization method leads to materials which are devoid of macroscopic aggregates (see Figure 3.1 and 3.8), thus overcoming the tendency of CNTs to bundle and to resist homogeneous deposition. Remarkably, after 20000 cycles ADT, the electrocatalytic activity of the Pt/CNTs@C sample with 0.8 nm carbon coating is comparable to the initial ECSA of Pt/CNTs before ADT cycling, demonstrating that proper carbon coating can significantly improve the stability of the Pt-based catalysts. Furthermore, it also shows a high tolerance to methanol after coating with carbon layer. As it is a facile, easily scalable and environmentally benign approach, this polymeric nanoencapsulation strategy is a promising technique for the design of highly active and stable Pt-based catalysts for ORR in fuel cells or to other electro-active devices.

ASSOCIATED CONTENT

Supporting Information. Optical images of catalyst dispersions, TEM images. This material is available free of charge via the Internet at <http://pubs.acs.org>.

AUTHOR INFORMATION

Corresponding Authors

*E-mail: zhangjm@uj.edu.cn (J. Z)

*E-mail: jerome.claverie@usherbrooke.ca (J.C.)

*E-mail: shuhui@emt.inrs.ca (S.S.)

ACKNOWLEDGMENT

The authors would like to acknowledge funding from the Natural Sciences and Engineering Research Council of Canada and Fonds de la Recherche du Québec sur la Nature et les Technologies (FRQNT), Centre Québécois sur les Matériaux Fonctionnels (CQMF), the Canada Research Chair program. J. Z. and Q. W. would like to thank to FRQNT for the fellowship. J. Z. also thanks to the funding support (17JDG008) from Jiangsu University. X.T. and Q. W. are grateful to the CSC scholarship.

REFERENCES

- (1) Zhang, J.; Sasaki, K.; Sutter, E.; Adzic, R. R., Stabilization of Platinum Oxygen-Reduction Electrocatalysts Using Gold Clusters. *Science* **2007**, 315, 220-222.
- (2) Zhang, N.; Guo, S.; Zhu, X.; Guo, J.; Huang, X., Hierarchical Pt/PtxPb Core/Shell Nanowires as Efficient Catalysts for Electrooxidation of Liquid Fuels. *Chemistry of Materials* **2016**, 28, 4447-4452.
- (3) Wang, J.; Li, B.; Yersak, T.; Yang, D.; Xiao, Q.; Zhang, J.; Zhang, C., Recent advances in Pt-based octahedral nanocrystals as high performance fuel cell catalysts. *Journal of Materials Chemistry A* **2016**, 4, 11559-11581.
- (4) Jeon, T.-Y.; Kim, S. K.; Pinna, N.; Sharma, A.; Park, J.; Lee, S. Y.; Lee, H. C.; Kang, S.-W.; Lee, H.-K.; Lee, H. H., Selective Dissolution of Surface Nickel Close to Platinum in PtNi Nanocatalyst toward Oxygen Reduction Reaction. *Chemistry of Materials* **2016**, 28, 1879-1887.
- (5) Debe, M. K., Electrocatalyst approaches and challenges for automotive fuel cells. *Nature* **2012**, 486, 43-51.
- (6) Baldizzone, C.; Mezzavilla, S.; Carvalho, H. W. P.; Meier, J. C.; Schuppert, A. K.; Heggen, M.; Galeano, C.; Grunwaldt, J.-D.; Schüth, F.; Mayrhofer, K. J. J., Confined-Space Alloying of Nanoparticles for the Synthesis of Efficient PtNi Fuel-Cell Catalysts. *Angewandte Chemie International Edition* **2014**, 53, 14250-14254.
- (7) Chung, H. T.; Won, J. H.; Zelenay, P., Active and stable carbon nanotube/nanoparticle composite electrocatalyst for oxygen reduction. *Nat Commun* **2013**, 4, 1922.
- (8) Lim, B.; Jiang, M.; Camargo, P. H. C.; Cho, E. C.; Tao, J.; Lu, X.; Zhu, Y.; Xia, Y., Pd-Pt Bimetallic Nanodendrites with High Activity for Oxygen Reduction. *Science* **2009**, 324, 1302-1305.
- (9) Shao, Y.; Zhang, S.; Wang, C.; Nie, Z.; Liu, J.; Wang, Y.; Lin, Y., Highly durable graphene nanoplatelets supported Pt nanocatalysts for oxygen reduction. *Journal of Power Sources* **2010**, 195, 4600-4605.
- (10) Tan, Y.; Xu, C.; Chen, G.; Zheng, N.; Xie, Q., A graphene-platinum nanoparticles-ionic liquid composite catalyst for methanol-tolerant oxygen reduction reaction. *Energy & Environmental Science* **2012**, 5, 6923-6927.
- (11) Song, W.; Chen, Z.; Yang, C.; Yang, Z.; Tai, J.; Nan, Y.; Lu, H., Carbon-coated, methanol-tolerant platinum/graphene catalysts for oxygen reduction reaction with excellent long-term performance. *Journal of Materials Chemistry A* **2015**, 3, 1049-1057.

- (12) Shao, Y.; Yin, G.; Gao, Y., Understanding and approaches for the durability issues of Pt-based catalysts for PEM fuel cell. *Journal of Power Sources* **2007**, 171, 558-566.
- (13) Nie, Y.; Li, L.; Wei, Z., Recent advancements in Pt and Pt-free catalysts for oxygen reduction reaction. *Chemical Society Reviews* **2015**, 44, 2168-2201.
- (14) Fang, B.; Kim, J. H.; Kim, M.; Kim, M.; Yu, J.-S., Hierarchical nanostructured hollow spherical carbon with mesoporous shell as a unique cathode catalyst support in proton exchange membrane fuel cell. *Physical Chemistry Chemical Physics* **2009**, 11, 1380-1387.
- (15) Viva, F. A.; Bruno, M. M.; Franceschini, E. A.; Thomas, Y. R. J.; Ramos Sanchez, G.; Solorza-Feria, O.; Corti, H. R., Mesoporous carbon as Pt support for PEM fuel cell. *International Journal of Hydrogen Energy* **2014**, 39, 8821-8826.
- (16) Fang, B.; Kim, J. H.; Kim, M.; Yu, J.-S., Ordered Hierarchical Nanostructured Carbon as a Highly Efficient Cathode Catalyst Support in Proton Exchange Membrane Fuel Cell. *Chemistry of Materials* **2009**, 21, 789-796.
- (17) Banham, D.; Feng, F.; Furstenhaupt, T.; Ye, S.; Birss, V., First time investigation of Pt nanocatalysts deposited inside carbon mesopores of controlled length and diameter. *Journal of Materials Chemistry* **2012**, 22, 7164-7171.
- (18) Kou, R.; Shao, Y.; Wang, D.; Engelhard, M. H.; Kwak, J. H.; Wang, J.; Viswanathan, V. V.; Wang, C.; Lin, Y.; Wang, Y.; Aksay, I. A.; Liu, J., Enhanced activity and stability of Pt catalysts on functionalized graphene sheets for electrocatalytic oxygen reduction. *Electrochemistry Communications* **2009**, 11, 954-957.
- (19) Wang, X.; Li, W.; Chen, Z.; Waje, M.; Yan, Y., Durability investigation of carbon nanotube as catalyst support for proton exchange membrane fuel cell. *Journal of Power Sources* **2006**, 158, 154-159.
- (20) Zhang, W.; Chen, J.; Swiegers, G. F.; Ma, Z.-F.; Wallace, G. G., Microwave-assisted synthesis of Pt/CNT nanocomposite electrocatalysts for PEM fuel cells. *Nanoscale* **2010**, 2, 282-286.
- (21) Gupta, C.; Maheshwari, P. H.; Sachdev, D.; Sahu, A. K.; Dhakate, S. R., Highly purified CNTs: an exceedingly efficient catalyst support for PEM fuel cell. *RSC Advances* **2016**, 6, 32258-32271.
- (22) Trogadas, P.; Fuller, T. F.; Strasser, P., Carbon as catalyst and support for electrochemical energy conversion. *Carbon* **2014**, 75, 5-42.
- (23) Choi, C. H.; Kwon, H. C.; Yook, S.; Shin, H.; Kim, H.; Choi, M., Hydrogen Peroxide Synthesis via Enhanced Two-Electron Oxygen Reduction Pathway on Carbon-Coated Pt Surface. *The Journal of Physical Chemistry C* **2014**, 118, 30063-30070.
- (24) Nie, Y.; Chen, S.; Ding, W.; Xie, X.; Zhang, Y.; Wei, Z., Pt/C trapped in activated graphitic carbon layers as a highly durable electrocatalyst for the oxygen reduction reaction. *Chemical Communications* **2014**, 50, 15431-15434.
- (25) Takenaka, S.; Miyamoto, H.; Utsunomiya, Y.; Matsune, H.; Kishida, M., Catalytic Activity of Highly Durable Pt/CNT Catalysts Covered with Hydrophobic Silica Layers for the Oxygen Reduction Reaction in PEFCs. *The Journal of Physical Chemistry C* **2014**, 118, 774-783.
- (26) Cheng, K.; Kou, Z. K.; Zhang, J.; Jiang, M.; Wu, H.; Hu, L.; Yang, X. Y.; Pan, M.; Mu, S., Ultrathin carbon layer stabilized metal catalysts towards oxygen reduction. *Journal of Materials Chemistry A* **2015**, 3, 14007-14014.
- (27) Cheng, N.; Banis, M. N.; Liu, J.; Riese, A.; Li, X.; Li, R.; Ye, S.; Knights, S.; Sun, X., Extremely Stable Platinum Nanoparticles Encapsulated in a Zirconia Nanocage by Area-Selective Atomic Layer Deposition for the Oxygen Reduction Reaction. *Advanced Materials* **2015**, 27, 277-281.

- (28) Chung, D. Y.; Jun, S. W.; Yoon, G.; Kwon, S. G.; Shin, D. Y.; Seo, P.; Yoo, J. M.; Shin, H.; Chung, Y.-H.; Kim, H.; Mun, B. S.; Lee, K.-S.; Lee, N.-S.; Yoo, S. J.; Lim, D.-H.; Kang, K.; Sung, Y.-E.; Hyeon, T., Highly Durable and Active PtFe Nanocatalyst for Electrochemical Oxygen Reduction Reaction. *Journal of the American Chemical Society* **2015**, *137*, 15478-15485.
- (29) Guo, L.; Jiang, W.-J.; Zhang, Y.; Hu, J.-S.; Wei, Z.-D.; Wan, L.-J., Embedding Pt Nanocrystals in N-Doped Porous Carbon/Carbon Nanotubes toward Highly Stable Electrocatalysts for the Oxygen Reduction Reaction. *ACS Catalysis* **2015**, *5*, 2903-2909.
- (30) Shen, L.; Sun, T.; Zhuo, O.; Che, R.; Li, D.; Ji, Y.; Bu, Y.; Wu, Q.; Yang, L.; Chen, Q.; Wang, X.; Hu, Z., Alcohol-Tolerant Platinum Electrocatalyst for Oxygen Reduction by Encapsulating Platinum Nanoparticles inside Nitrogen-Doped Carbon Nanocages. *ACS Applied Materials & Interfaces* **2016**, *8*, 16664-16669.
- (31) Chen, S.; Wei, Z.; Qi, X.; Dong, L.; Guo, Y.-G.; Wan, L.; Shao, Z.; Li, L., Nanostructured Polyaniline-Decorated Pt/C@PANI Core - Shell Catalyst with Enhanced Durability and Activity. *Journal of the American Chemical Society* **2012**, *134*, 13252-13255.
- (32) Galeano, C.; Meier, J. C.; Peinecke, V.; Bongard, H.; Katsounaros, I.; Topalov, A. A.; Lu, A.; Mayrhofer, K. J. J.; Schüth, F., Toward Highly Stable Electrocatalysts via Nanoparticle Pore Confinement. *Journal of the American Chemical Society* **2012**, *134*, 20457-20465.
- (33) Wu, Z.; Lv, Y.; Xia, Y.; Webley, P. A.; Zhao, D., Ordered Mesoporous Platinum@Graphitic Carbon Embedded Nanophase as a Highly Active, Stable, and Methanol-Tolerant Oxygen Reduction Electrocatalyst. *Journal of the American Chemical Society* **2012**, *134*, 2236-2245.
- (34) Zhao, H.; Li, Y.; Xiang, Q.; Shen, J.; Xu, J., High Efficiency Graphitized Carbon Coated Pt Composite for Hydrogen Electro-Oxidation and Hydrogen Storage. *Integrated Ferroelectrics* **2011**, *129*, 133-138.
- (35) Zhang, J.; Vasei, M.; Sang, Y.; Liu, H.; Claverie, J. P., TiO₂@Carbon Photocatalysts: The Effect of Carbon Thickness on Catalysis. *ACS Applied Materials & Interfaces* **2016**, *8*, 1903-1912.
- (36) Zhong, W.; Zeuna, J. N.; Claverie, J. P., A versatile encapsulation method of noncovalently modified carbon nanotubes by RAFT polymerization. *Journal of Polymer Science Part A: Polymer Chemistry* **2012**, *50*, 4403-4407.
- (37) Zhong, W.; Claverie, J. P., Probing the carbon nanotube-surfactant interaction for the preparation of composites. *Carbon* **2013**, *51*, 72-84.
- (38) Sun, S.; Zhang, G.; Geng, D.; Chen, Y.; Li, R.; Cai, M.; Sun, X., A Highly Durable Platinum Nanocatalyst for Proton Exchange Membrane Fuel Cells: Multiarmed Starlike Nanowire Single Crystal. *Angewandte Chemie International Edition* **2011**, *50*, 422-426.
- (39) Mathur, R. B.; Chatterjee, S.; Singh, B. P., Growth of carbon nanotubes on carbon fibre substrates to produce hybrid/phenolic composites with improved mechanical properties. *Composites Science and Technology* **2008**, *68*, 1608-1615.
- (40) Mathur, R. B.; Seth, S.; Lal, C.; Rao, R.; Singh, B. P.; Dhami, T. L.; Rao, A. M., Co-synthesis, purification and characterization of single- and multi-walled carbon nanotubes using the electric arc method. *Carbon* **2007**, *45*, 132-140.
- (41) Li, W.; Wang, X.; Chen, Z.; Waje, M.; Yan, Y., Carbon nanotube film by filtration as cathode catalyst support for proton-exchange membrane fuel cell. *Langmuir* **2005**, *21*, 9386-9389.
- (42) Nørskov, J. K.; Rossmeisl, J.; Logadottir, A.; Lindqvist, L.; Kitchin, J. R.; Bligaard, T.; Jónsson, H., Origin of the Overpotential for Oxygen Reduction at a Fuel-Cell Cathode. *The Journal of Physical Chemistry B* **2004**, *108*, 17886-17892.

- (43) Greeley J.; Stephens, I. E. L.; Bondarenko, A. S.; Johansson, T. P.; Hansen, H. A.; Jaramillo, T. F.; Rossmeisl J.; Chorkendorff I.; Nørskov, J. K., Alloys of platinum and early transition metals as oxygen reduction electrocatalysts. *Nat Chem* **2009**, 1, 552-556.
- (44) Chen, Y.; Wang, J.; Liu, H.; Banis, M. N.; Li, R.; Sun, X.; Sham, T.-K.; Ye, S.; Knights, S., Nitrogen doping effects on carbon nanotubes and the origin of the enhanced electrocatalytic activity of supported Pt for proton-exchange membrane fuel cells. *The Journal of Physical Chemistry C* **2011**, 115, 3769-3776.
- (45) Gasteiger, H. A.; Kocha, S. S.; Sompalli, B.; Wagner, F. T., Activity benchmarks and requirements for Pt, Pt-alloy, and non-Pt oxygen reduction catalysts for PEMFCs. *Applied Catalysis B: Environmental* **2005**, 56, 9-35.
- (46) Garsany, Y.; Baturina, O. A.; Swider-Lyons, K. E.; Kocha, S. S., Experimental Methods for Quantifying the Activity of Platinum Electrocatalysts for the Oxygen Reduction Reaction. *Analytical Chemistry* **2010**, 82, 6321-6328.
- (47) Nesselberger, M.; Ashton, S.; Meier, J. C.; Katsounaros, I.; Mayrhofer, K. J.; Arenz, M., The particle size effect on the oxygen reduction reaction activity of Pt catalysts: influence of electrolyte and relation to single crystal models. *Journal of the American Chemical Society* **2011**, 133, 17428-17433.
- (48) Garsany, Y.; Ge, J.; St-Pierre, J.; Rocheleau, R.; Swider-Lyons, K. E., Analytical procedure for accurate comparison of rotating disk electrode results for the oxygen reduction activity of Pt/C. *Journal of The Electrochemical Society* **2014**, 161, F628-F640.

Supporting information for
Ultra-thin carbon coated Pt/CNTs: a highly durable electro-catalyst
for oxygen reduction

Xin Tong,^{†,‡} Jianming Zhang,^{‡,*} Gaixia Zhang,[†] Qiliang Wei,[†] Régis Chenitz,[†] Jerome P. Claverie^{§,*} and Shuhui Sun^{†,*}

[†] Institut National de la Recherche Scientifique-Énergie Matériaux et Télécommunications, Varennes, QC, Canada J3X 1S2.

[‡] School of Chemistry and Chemical Engineering, Jiangsu University, Zhenjiang, China, 212013.

[§] Department of Chemistry, Université de Sherbrooke, Sherbrooke, QC, Canada J1K 2R1.

[‡]School of Chemistry and Material Science, Guizhou Normal University, Guiyang, China, 550001.

E-mail: zhangjm@ujs.edu.cn; jerome.claverie@usherbrooke.ca; shuhui@emt.inrs.ca;

Supplementary Figures&Tables

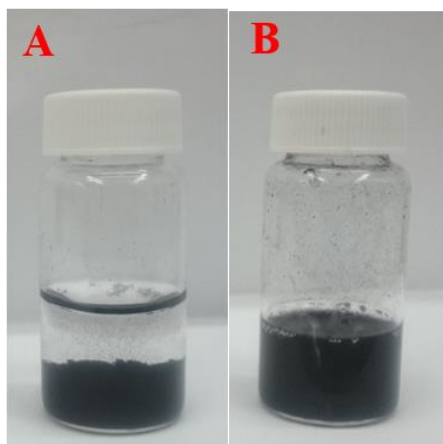


Figure S1. The digital image of Pt/CNTs(A) and Pt/CNTs encapsulated with PABA(B).

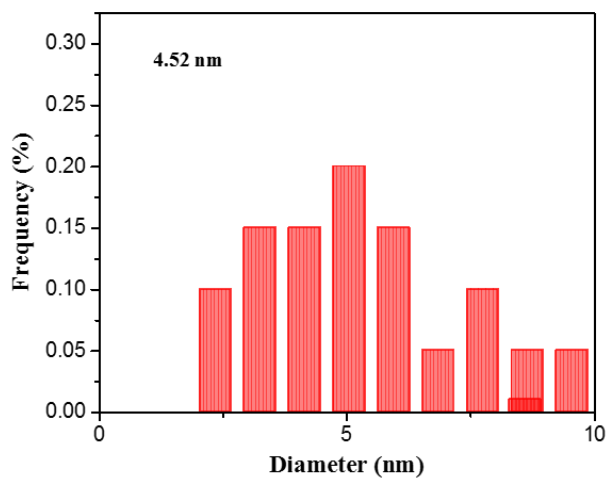


Figure S2. The size distribution of Pt nanocrystals in Pt/CNTs@C 1.

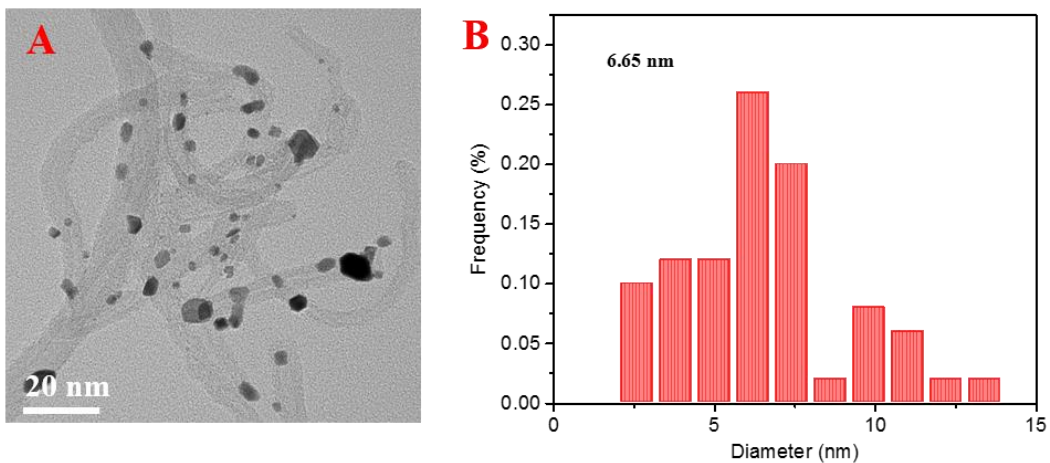


Figure S3. The TEM image Pt/CNTs after annealing process (A) and the size distribution of Pt nanocrystals in Pt/CNTs (B). Without encapsulation process, the Pt/CNTs was annealed under 550 °C for 2h directly (the same condition with the normal graphitization process).

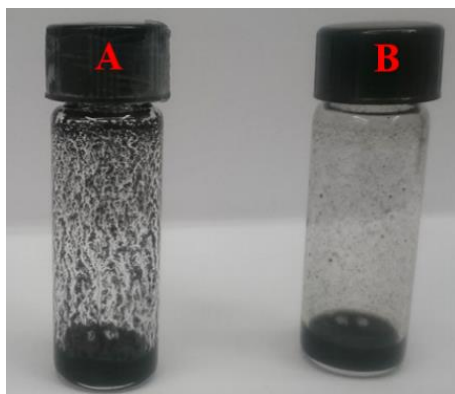


Figure S4. The digital image of Pt/CNTs ink (A) and Pt/CNTs@C S2 ink (B) for the electrochemical test.

Table S1. The electrochemical surface areas on Pt/CNTs(20%), Pt/CNTs@C-1, Pt/CNTs@C-2, Pt/CNTs@C-3 and Pt/CNTs@C-4.

CYCLES	PT/CNTS	PT/CNTS@C-1	PT/CNTS@C-2	PT/CNTS@C-3	PT/CNTS@C-4
1	74.59	32.94	63.92	35.29	10.64
500	71.17	36.09	76.38	41.68	17.78
1000	60.21	40.59	80.48	44.52	19.21
2000	48.04	43.36	88.04	47.43	19.67
3000	35.68	45.01	87.65	48.04	20.16

Table S2. A comparison of the catalytic activity before and after ADT test. Data were obtained from the Figure8.

SAMPLES	FRESH SAMPLES				AFTER ADT TEST			
	Onset potential (v)	Half-wave potential (v)	The current @ 0.8v (mA cm ⁻²)	The current @ 0.9v (mA cm ⁻²)	Onset potential (v)	Half-wave potential (v)	The current @ 0.8v (mA cm ⁻²)	The current @ 0.9v (mA cm ⁻²)
PT/CNTS	0.99	0.85	3.4	1.1	0.94	0.76	1.4	0.23
PT/CNTS@C-1	0.96	0.70	1.1	0.14	0.97	0.74	1.5	0.30
PT/CNTS@C-2	0.99	0.78	2.2	0.57	0.99	0.84	3.1	1.1
PT/CNTS@C-3	0.94	0.67	0.75	0.17	0.94	0.69	0.92	0.17
PT/CNTS@C-4	0.89	0.63	0.30	0.04	0.89	0.65	0.53	0.04

Support interaction effect of platinum clusters anchoring on doped graphene supports for the oxygen reduction reaction

Titre de l'article: Effet d'interaction des amas de platine sur les supports en graphène dopé pour la réaction de réduction de l'oxygène

Authors: Xin Tong, Gaixia Zhang, Jerome P. Claverie, and Shuhui Sun

Title of the journal: To be submitted

Link between the previous articles:

Based on previous research, metal–support interactions are supposed to be the key to stabilize catalyst and modulate the electronic structure, thereby affecting the stability and activity of the catalyst. Therefore, a fundamental understanding of metal–support interactions is extremely desirable to realize the rational design of efficient catalyst.

In this article, we used three different kinds of graphene materials including unmodified graphene, nitrogen-doped graphene (N-graphene) and nitrogen phosphorus co-doped graphene (N, P-graphene) as supporting materials to anchor platinum clusters. Then a comprehensive study of the support interaction effect to Pt clusters was discussed. The N, P graphene not only reduces the Pt size and facilitate the homogeneous distribution on the surface but also affects the Pt electronic structure that promotes the ORR activity. The Pt/N, P-graphene not only shows a high ORR activity, low Tafel slope, and 4-electron ORR pathway with low H₂O₂ yield but also excellent durability.

Support interaction effect of platinum clusters anchoring on doped graphene supports for the oxygen reduction reaction

Xin Tong,^{†,‡} Gaixia Zhang,[†] Jerome P. Claverie^{§,*} and Shuhui Sun^{†,*}

[†] Institut National de la Recherche Scientifique-Énergie Matériaux et Télécommunications, Varennes, QC, Canada J3X 1S2.

[‡] School of Chemistry and Material Science, Guizhou Normal University, Guiyang, China, 550001.

[§] Department of Chemistry, Université de Sherbrooke, Sherbrooke, QC, Canada J1K 2R1.

Abstract

Increase the platinum utilization in oxygen reduction reaction (ORR) is especially attractive for large-scale application of Pt catalyst in Proton exchange membrane fuel cells (PEMFCs). However, the carbon support which is mostly used cannot stabilize highly-active Pt cluster or single atom effectively. Here three different kinds of graphene material- unmodified graphene, nitrogen-doped graphene (N-graphene) and nitrogen phosphorus co-doped graphene (N, P-graphene) were used as supporting material to anchor platinum. Then a comprehensive study of the support interaction effect on Pt supported on graphene material was discussed. The N, P graphene can not only reduce the Pt size and facilitate the homogeneous distribution on the surface but also affect the Pt electronic structure that promotes ORR activity. The Pt/N, P-graphene shows high ORR activity, low Tafel slope, 4-electron ORR pathway with low H₂O₂ yield and excellent durability.

Introduction

Proton exchange membrane fuel cells (PEMFCs), which can directly convert hydrogen energy into usable electric power, have been regarded as hopeful candidates for efficient and clean energy conversion.¹⁻⁵ Though active catalysts are required to lower overpotential and to obtain higher voltage output on both anode and cathode sides, there is more demand for the cathodic oxygen reduction reaction (ORR) because of its sluggish kinetics (5 orders of magnitude slower than the hydrogen oxidation reaction at the anode). So far, Platinum (Pt) is still the most widely used ORR electrocatalysts with high activity and durability in acid.⁶ Owing to the scarcity and high price of Pt, the target of United States Department of Energy (DOE) is set to reduce the total Pt loading to 0.125 mg_{Pt} cm⁻² from more than 0.4 mg_{Pt} cm⁻² used on cathodes now.^{7, 8}

Numerous effects have concentrated on reducing the Pt loading without sacrificing the performance by downsizing Pt particle into nanoscale even single atom,⁹⁻¹² structure/shape control,¹³ alloying and composition tuning,¹⁴⁻¹⁶ and surface engineering.¹⁷ However, these Pt-based nanoparticles (Pt NPs) are extremely unstable and prone to agglomeration because of the high surface energy. The loss of active surfaces of Pt due to Ostwald ripening, migration and aggregation as well as their non-uniform dispersion are main barriers to reduce the performance of Pt-based catalysts. Different substrates are used to immobilize the Pt NPs.¹⁸⁻²¹ Carbon-based materials demonstrate excellent stability, large surface area, and high electric conductivity, making it an excellent supporting material for precious metal catalysts.^{22, 23} Unfortunately, the carbon show inert characteristics and provide weak metal–support interaction. So surface modifications and heteroatom doping are desired to stabilize metal clusters through a strong metal-support interaction. Furthermore, the metal–support interactions can modulate the electronic structure of metal catalysts, thereby affect the activity and stability of the catalyst. Therefore, a fundamental understanding of metal–support interactions is extremely desirable to realize the rational design of efficient catalyst.

However, it is complicated to study this metal–support interaction because it is susceptible to interference by the tiny difference of the surface morphology and chemical properties of the support. Graphene, a two-dimensional carbon structure, can be seemed as a model supporting material that allows direct observation of Pt NPs morphology and further research of the metal-support interactions.²⁴ In this study, Pt catalysts were anchoring on three different graphene supports. Unmodified graphene (reduced graphene oxide, RGO) was synthesized by thermal reduction of graphene oxide(GO) according to a modified Hummers method.²⁵ Nitrogen-doped graphene (N-graphene) and Nitrogen phosphorus co-doped graphene (N, P-graphene) was obtained by pyrolysis under ammonia using GO or the mixture of GO and Triphenylphosphine (Ph₃P). Then the Pt catalysts are loaded on these different graphene supports by wet impregnation method. The morphological changes and electron delocalization induced by Pt–graphene support interaction of the Pt nanoparticles on different supports was discussed, thus obtained the effect on ORR activity. An assembly mechanism Pt supported on doped graphene and are proposed.

Results and discussion

As shown in Figure 4.1, three different kinds of graphene were used as supporting material. Firstly, GO was obtained after the modified Hummers' oxidation process. Wet chemical method synthesized from GO was an efficient and regular route to get doped graphene because of its abundant oxygen-containing functional groups. Also, Triphenylphosphine (Ph₃P) was used as a phosphorus source to produce N, P-graphene. During thermal treatment, inert Argon atmosphere was used to get reduced graphene oxide (RGO) while ammonia was employed to nitrogen doping and reduction of GO simultaneously for the

production of N-graphene and N, P-graphene. Subsequently, Pt catalyst was loaded on graphene material (include RGO, N-Graphene, and N, P-Graphene) by traditional wet impregnation method followed by annealing under 450 °C. Pt loadings of RGO, N-Graphene, and N, P-Graphene were found to be 4.88 wt%, 5.03 wt% and 5.22 wt% by Inductively Coupled Plasma / Optical emission spectrometry (ICP-OES), respectively.

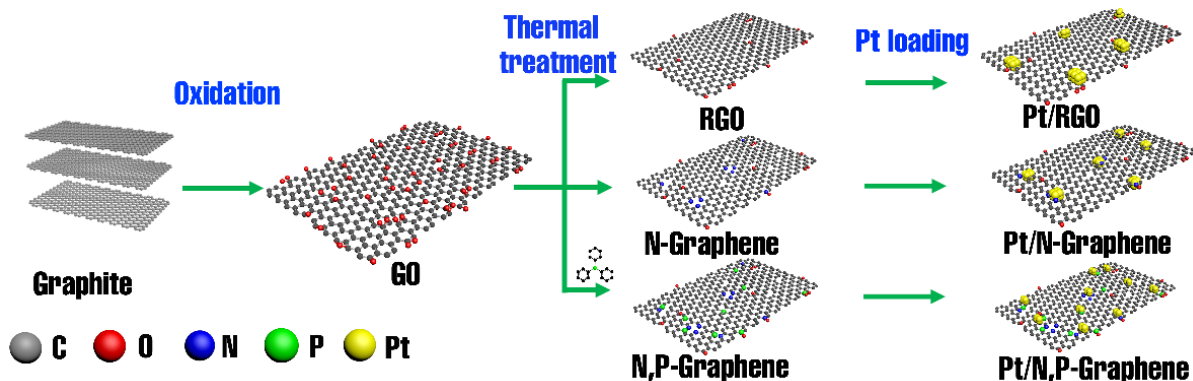


Figure 4.1. Schematic Illustration of the Fabrication Process of Pt supporting on RGO, N-Graphene and N, P-Graphene.

The surface morphology of RGO, N-Graphene, and N, P-Graphene was probed with transmission electron microscopy (TEM). In low magnification TEM in Figure S1 (Supporting Information) these graphene material all show thin wrinkled and folded morphology with the presence of the Pt cluster responded as black dots. It seems like that the nanosheets in N, P-graphene are more crumpled than those in RGO and N-Graphene. The wrinkles and folded on the surface which means lots of open edge sites might originate from the structural distortion caused by the decrease of bond angles and increase of bond length during incorporation of P atoms.²⁶ As seen in Figure 4.2(a, b), Pt nanoclusters are anchored and homogeneously distributed on the surface of the N, P-graphene materials. TEM images in (Figure 4.2c, d) show that larger Pt clusters are dispersed in N-graphene. There are large Pt particles with a limited number are found in Pt/RGO in Figure 4.1(e, f). The Pt particle size distributions (Figure S2) show an average particle size of 0.76 nm, 2.7 nm and 4.43 nm for N, P-Graphene, N-Graphene, and RGO, respectively. The surface properties play vital roles in the Pt nucleation mechanism for the growth of Pt on the graphene surface. The N, P-Graphene support shows the highest abundance of surface nucleation sites for Pt attachment with the smallest cluster, and therefore reduce the size and facilitate the homogeneous distribution on the surface. To further investigate the compositional distribution of N, P-graphene, the EDX Elemental mapping was conducting and shown in Figure S3. Uniform and dense N, P and Pt signals were found all over the graphene support, implying success co-doping of P and N into graphene and homogeneously distributed Pt cluster.

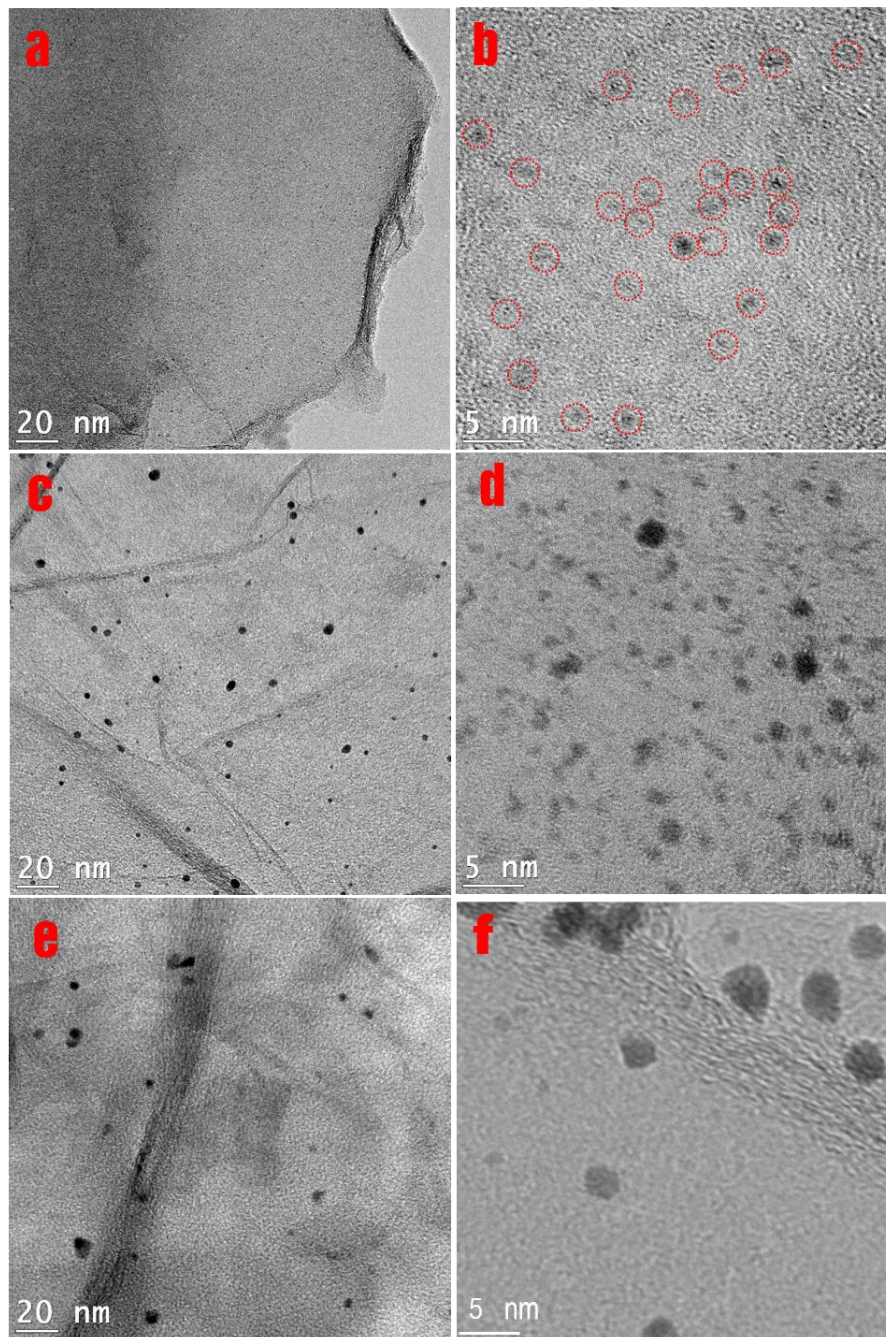


Figure 4.2. TEM and HRTEM images of (a, b) Pt/N, P-Graphene, (c, d) Pt/N-Graphene and (e, f) Pt/RGO.

X-ray photoelectron spectroscopy (XPS) was employed to characterize the surface composition and valence state information of RGO, N-Graphene and N, P-Graphene. The XPS survey spectra in Figure 4.3a display that N 1s and Pt 4f, N1s, P 2p, and Pt4f appear on N-Graphene and N, P-Graphene, respectively, which indicates the successful heteroatoms doping and Pt deposition. As seen in Table S.1 (Supporting Information), the oxygen content of N-Graphene and N, P-Graphene was much lower than in RGO, indicating a more effective reduction from the thermal annealing treatment in NH₃ vs. Ar. Despite the greater oxygen-containing surface groups for

RGO, oxygen groups are be found not efficient to anchor Pt NPs in the previous study.²⁷The nitrogen content of Pt/N-Graphene and Pt/N, P-Graphene are 3.13 wt. % and 3.31 wt. %, respectively. The high-resolution N 1s XPS spectra (Figure S4) of Pt/N-graphene and Pt/N, P-graphene reveal the presence of pyridinic type N (398.1 eV), pyrrolic type N (399.5 eV), and graphitic type N (401.5 eV) as well as N–O species (403.5 eV). New P-N peaks can be found in the Pt/N, P-graphene around 400.8 eV.²⁸ As shown in Table S.2, more than 30% of pyridinic N is observed in both Pt/N-graphene and Pt/N, P-graphene. Besides, the P content in Pt/N, P-graphene is ~1%. In Figure S5, the high-resolution P2p XPS spectra of Pt/N, P-graphene were deconvoluted into three doublet components (2p_{1/2} and 2p_{3/2}, $\Delta E=0.84$ eV) due to the spin-orbit splitting.²⁹ The three components in 2p_{3/2} can be assigned to P-C bonding (131.6 eV), P-N bonding(133.0 eV) and P-O bonding(134.5 eV), respectively. The presence of P-N peak re-confirms that the existence of P-N bonded structure. In figure 4.3b, the Pt 4f signals can be deconvoluted into three doublets (Pt 4f_{5/2} and Pt 4f_{7/2}, $\Delta E=3.33$ eV) which can be assigned to the Pt⁰ state (71.5 eV), Pt²⁺state (72.6 eV) and Pt⁴⁺ state (74.5 eV). For Pt/RGO, the metallic Pt⁰ state content is 72% (Figure S6). It means that most of the Pt atoms boned with Pt atoms which is consistent with the large Pt particles in TEM images. In Pt/N-graphene, the high content of Pt²⁺ ions imply the presence of square-planar-type Pt–N₄ configuration.^{9, 30}In contrast, the percentage (98%) of Pt^{δ+} in Pt/N, P-graphene is much higher than that of Pt/RGO (28%) and Pt/N-graphene (79%) due to the improved Pt dispersion with few particles on N, P-graphene.¹¹ Besides, the positive shift of Pt peaks are following the trend of Pt/N, P-graphene > Pt/N-graphene > RGO, illustrating there is an enhanced interaction between the Pt and graphene substrate in N, P-Graphene.

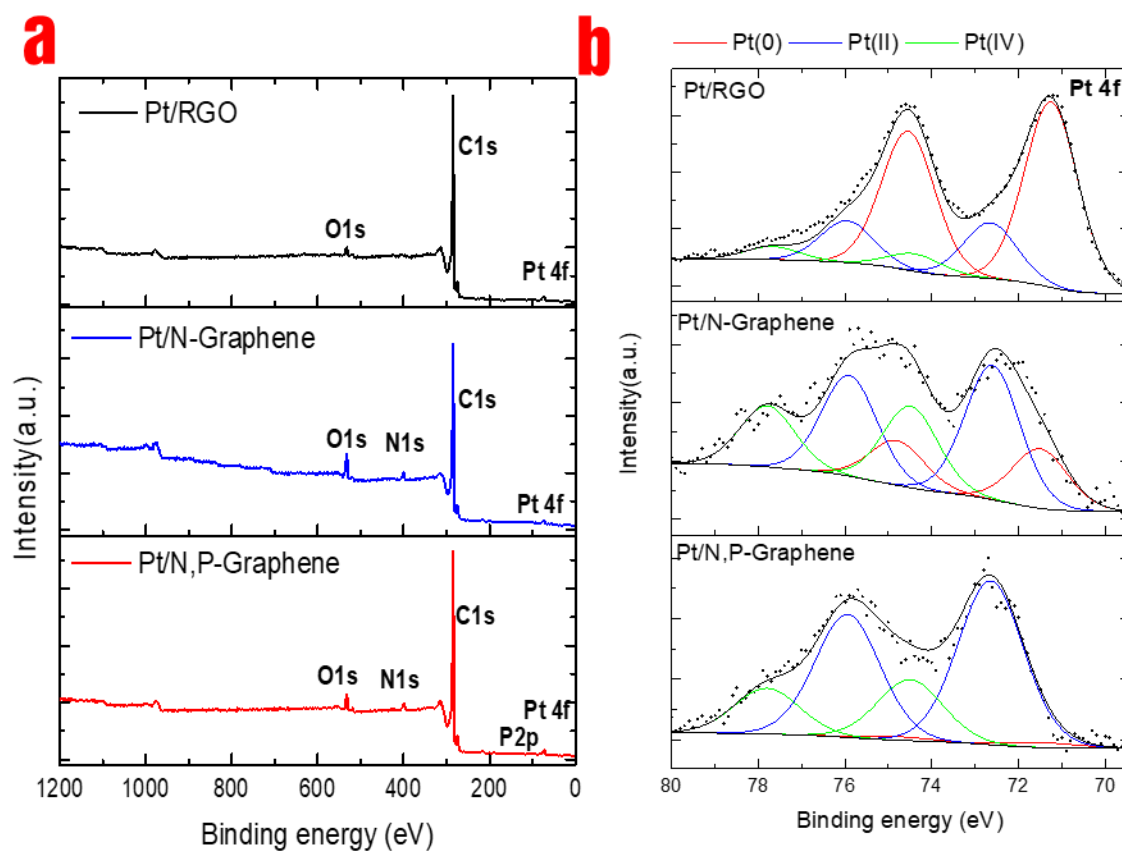


Figure 4.3. (a) XPS survey spectra and (b) high-resolution XPS spectra of Pt 4f of Pt/RGO, Pt/N-Graphene and Pt/N, P-Graphene.

Figure 4.4a shows the rotating ring-disk electrode (RRDE) Linear sweep voltammetry (LSV) curve of commercial Pt/C (20 wt.%), Pt/N, P-Graphene, Pt/N-Graphene, and Pt/RGO in O₂-saturated 0.1 M HClO₄. The onset potential and half-wave potential ($E_{1/2}$) of Pt/N, P-Graphene are 1.06 V and 0.88 V versus reversible hydrogen electrode (RHE), respectively, which are positive than those of Pt/C (0.95 and 0.83 V versus RHE), Pt/N-Graphene (0.90 and 0.73 V versus RHE) and Pt/RGO (0.85 and 0.58 V versus RHE). Therefore, the Pt/N, P-Graphene catalysts display superior activity towards ORR among the series. Compared with pristine graphene supporting material in Figure S7, anchoring Pt onto graphene significantly increase the ORR activity. Without Pt, the graphene materials show low ORR activity in acid solution. Compared to the ORR polarization curves of N-graphene and N, P-graphene, the values of onset potential and half-wave potential are very close. It hints that there is a synergistic effect to dramatically enhance ORR activity when deposited Pt cluster onto N, P-graphene, compared with Pt/N-Graphene. In other word, the ORR activity is promoted by the combining use of Pt cluster and N,P-graphene.

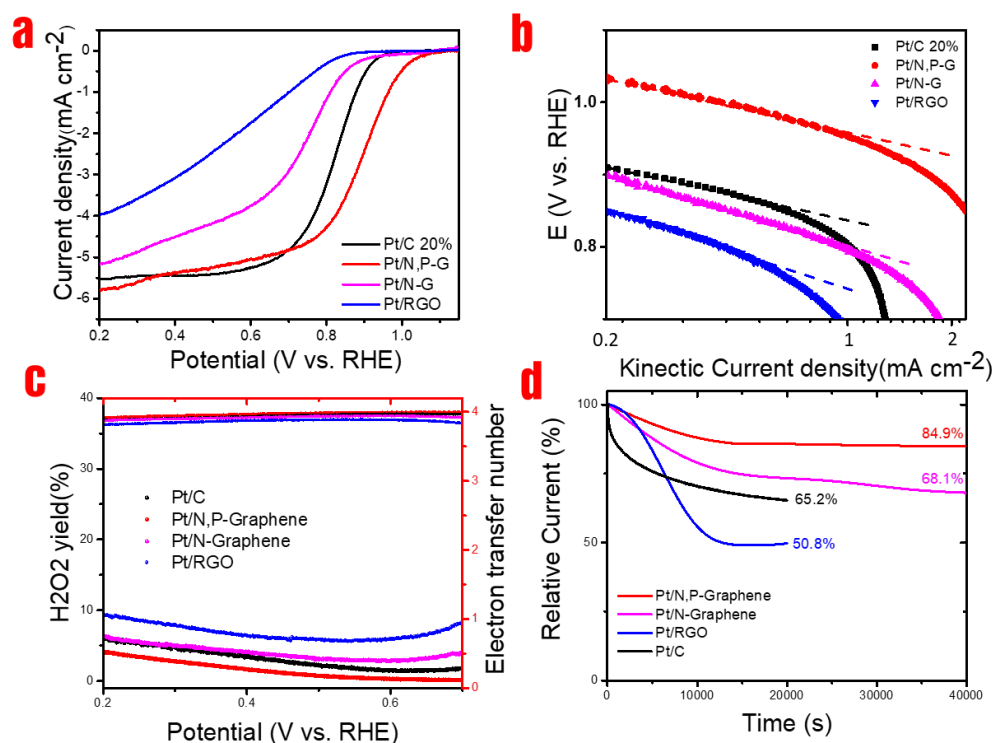


Figure 4.4. Electrochemical characterization of commercial Pt/C (20%), Pt/N, P-Graphene, Pt/N-Graphene, and Pt/RGO (a) LSV curves on RRDE in O₂-saturated 0.1 M HClO₄ at a scan rate of 10 mV s⁻¹ (rotation speed: 1600 rpm), room temperature. (b) Tafel region of ORR measurement. (c) H₂O₂ yields and Electron transfer numbers. (d) Chronoamperometric responses in an O₂-saturated aqueous solution of 0.1 M HClO₄.

The mass-transport corrected Tafel plots were calculated through Koutecky–Levich equation to figure out the reaction kinetics. As shown in Figure 4.4b, the Tafel slope of the Pt/N, P-Graphene catalyst is 60.5 mV dec⁻¹, which is lower than that of Pt/C (67.8 mV dec⁻¹), revealing a faster ORR kinetics derived from the synergistic catalytic effect of high activated Pt cluster and N, P-co-doped graphene matrix. Tafel slope of 93.6 and 96.4 mV dec⁻¹ is obtained for Pt/N-Graphene and Pt/RGO, implying that the rate determine step is first electron-transfer in the ORR mechanism.³¹ The kinetic mass activity (J_m) at 0.90 V, which was normalized by the Pt loading, is used to evaluate the activity. As shown in Figure S8, the kinetic mass activity of Pt/N, P-Graphene catalyst is 170 mA mg⁻¹_{Pt}, which is ~6-times greater than that of the commercial Pt/C (21.8 mA mg⁻¹_{Pt}). It reveals that the small Pt cluster which is supported on N, P-graphene can noticeably increase the utilization of Pt, thus improving ORR performance and lowering the cost at the same time.

To deeply understand the ORR mechanism, the amount of hydrogen peroxide generated from the Pt ring in the electrode, and electrotransfer number during the ORR process were calculated from the disk and ring currents in RRDE measurements (Figure 4.4c). The electronic transfer numbers of the Pt/C (20 wt.%), Pt/N, P-Graphene, Pt/N-Graphene, and Pt/RGO catalysts in the potential from 0.2 to 0.7v were found to be in the

range of 3.88-3.97, 3.91–4.00, 3.87-3.94, and 3.81-3.87, respectively, revealing a nearly 4-electron ORR pathway. The peroxide yield results exhibit that Pt/N, P-Graphene has the best selectivity with low H₂O₂ yield (~4% in high overpotentials and ~0.2% in low overpotentials) over the whole potential range, whereas that of commercial Pt/C is ~6% and ~1.5%. The low yield of H₂O₂ is expected because the intermediate H₂O₂ can cause corrosion of membranes and catalysts thus hinder fuel cell performance. The H₂O₂ yield of Pt/RGO is around 10%, implying insufficient activate sites for this sample which can be attributed to the relatively-big particle size and low loading of Pt and the adverse effects for the residual oxygen-containing groups.

To evaluate the stability of these catalysts for ORR, chronoamperometric (CA) measurement was carried out at a constant potential of 0.8v versus RHE. As shown in figure 4.4d, Pt/N, P-Graphene could keep ~85.7% of initial activity after 20k seconds whereas commercial Pt/C exhibited ~34.8 % current loss over the same period, illustrating excellent stability of Pt/N, P-Graphene for ORR. By comparison, the current of Pt/RGO catalyst is drastically reduced, with a half current wastage after 20000 s. Longer time CA tests were performed with Pt/N, P-Graphene and Pt/N-Graphene. The Pt/N, P-graphene and Pt/N-graphene show slow current decay even after 40000s, and relatively high currents of 84.9% and 68.1%, respectively. It can be attributed to the strengthened interaction between Pt particle and functional groups on doped graphene.²⁴ The aggregation, dissolution and Ostwald ripening of the Pt particles and carbon support corrosion under harsh fuel cell operation condition can be avoided using the doped graphene as supporting material.

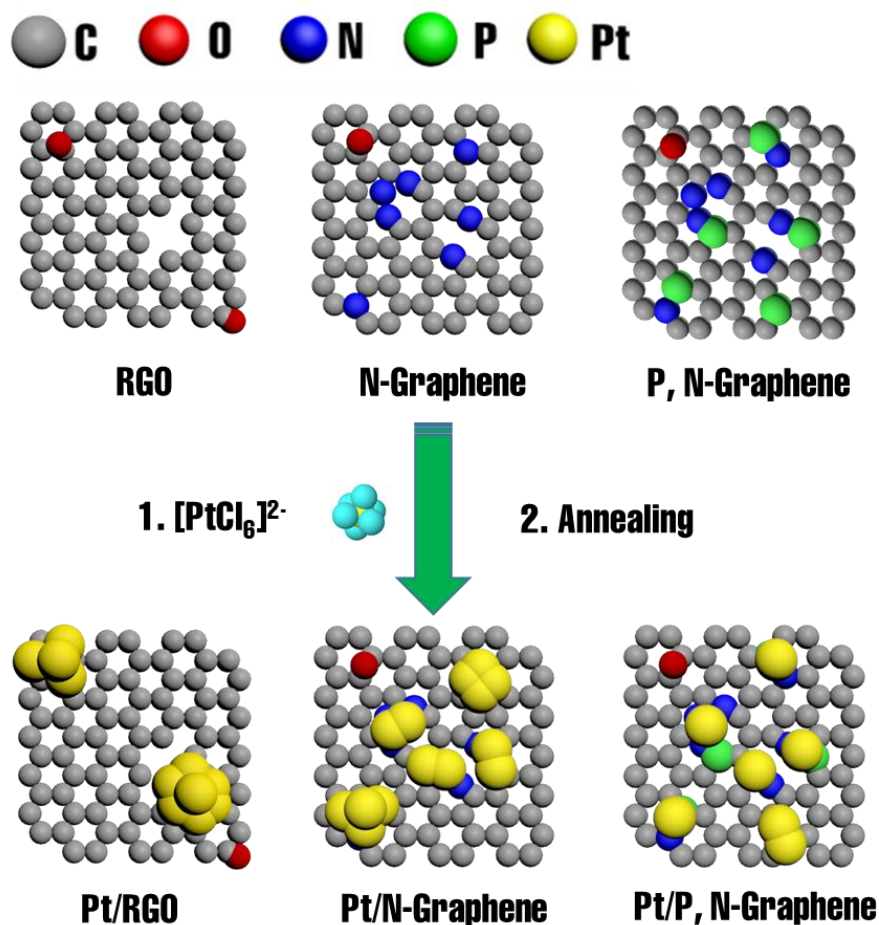


Figure 4.5. Schematic Illustration of the assembly mechanism of Pt supported on doped graphene.

The assembly mechanism of Pt supported by doped graphene is discussed. In aqueous solution, the Pt precursor is anchored on graphene surface by electrostatic attraction due to electron transfer between C atoms and doped N, P atoms. During the high-temperature annealing process, some of the Pt complexes start to decompose and nucleate. Then the Pt cluster or Pt nanoparticles are formed taking the initially Pt nuclei as nuclei. The surface chemistry of the graphene supports significantly affect the deposition behavior of Pt atoms. As seen in figure 4.5 of RGO, its hydrophobicity and the defects-less surface are not conducive for the Pt deposition. The Pt atoms are prone to growth on the edges and few defects, causing a limited number of Pt nanoparticles.^{24, 30} Furthermore, the newly formed Pt nuclei tend to aggregates because of weak interaction between Pt and the un-doped graphene, which further diminish active sites. In contrast, the doped graphene is more hydrophilic and can provide enough anchoring sites to adsorb Pt complex ions homogeneously. The nitrogen, phosphorus and defective carbons may be ionically bonded or covalently bonded with platinum, thus ensuring uniform distribution of Pt nanoparticles. When it comes to N, P-graphene materials, they have a higher abundance of defects and edges and therefore additional nucleation sites.

Besides, their interaction with platinum can be enhanced because additional P-doping could enhance asymmetric charge density and increased charge delocalization.^{32, 33} This strong bond causes the uniform distribution of the Pt small clusters and hinder further growth of Pt nanoparticles. In summary, large Pt particles with a limited number are found in Pt/RGO, while small Pt particles are homogeneously dispersed on N-Graphene. For Pt N, P-Graphene, there are small clusters with efficient utilization. Furthermore, the doped atoms on the surface can also influence the valence electrons of Pt. Therefore, the supporting material will play a vital role in the activity and stability of Pt for ORR.

Conclusion

In summary, three different kinds of graphene were used as supporting material to anchor Pt by wet impregnation method. Then the support interaction effect on Pt supported by different graphene material was discussed. The surface properties can not only affect the Pt size and distribution on the surface but also affect the Pt electronic structure. The Pt/N, P-graphene showed high activity, low Tafel slope, 4-electron ORR pathway with low H₂O₂ yield and excellent durability because of its stronger interaction of the Pt atoms with the doped atoms. This study will supply a promising route for improving activity and durability, and also enrich the knowledge of support interaction effect in the catalyst field.

Experimental method

Doping heteroatoms into graphene

All the chemical are purchased from Sigma-Aldrich Company unless specified. GO was synthesized by an improved Hummers' method using natural graphite flake (325 mesh, metal basis). For N, P-graphene, GO was dispersed in DI water, followed by the addition of triphenylphosphine (Ph₃P) ether solution in a weight ratio of 1:5. Then the mixture was under ultra-sonication for 4h and stirred for another 4 h at room temperature. This precursor solution was vacuum dried on 60°C for at least 24 h. Subsequently, the powders were heated at 200 °C for 1 h under an argon atmosphere, and then the temperature was raised to 950 °C and kept for 15min while feeding Ar (100 sccm) and NH₃ (100 sccm) at room pressure. The preparation of N-Graphene follows similar procedures, without the Ph₃P mixing process. For RGO, similar annealing process was achieved under inert argon atmosphere.

Loading the Pt Catalyst on graphene Materials

Pt catalyst was loaded on graphene material (include RGO, N-Graphene and N, P-Graphene) by traditional wet impregnation method. First, graphene material was added into water and sonicated for 2h, followed by

adding an aqueous $\text{H}_2\text{PtCl}_6 \cdot 6\text{H}_2\text{O}$ solution in a weight ratio of 1:20. After 2 hours of violent magnetic stirring, the products were washed with water and freeze-dried for 12h. Then, the mild heat treatment of the powder was performed at 450°C for 2 h under inert argon atmosphere with a flow rate of 100 mL min^{-1} .

Physical Characterizations.

The morphology of all catalysts was characterized by a JEM-2200FS transmission electron microscope (TEM) operated at 200 kV. The sizes of the Pt nanoparticles were estimated by counting at least 100 nanoparticles with Nano measurer free software. The scanning electron microscope (SEM) images and energy dispersive spectroscopy (EDS) were achieved by Tescan Vega3 LMH. Inductively Coupled Plasma / Optical emission spectrometry (ICP-OES) are characterized by Agilent Technologie, 5100. Chemical analysis of the surface was characterized by X-ray photoelectron spectroscopy (XPS) with a VG Escalab 220i-XL using Mg $K\alpha$ line as an excitation source.

Electrochemical Characterizations.

Electrochemical measurements were performed in a three-electrode cell with a bipotentiostat (Pine, Model PGSTAT-72637) workstation at room temperature. A Pt wire was used as the counter electrode, and a saturated calomel electrode (SCE) was served as the reference electrode, which was calibrated by a reversible hydrogen electrode (RHE) before the test. The rotating ring-disk electrode (RRDE) (0.252 cm^2 , PINE Instrumentation) was used as the working electrode. The catalyst ink is prepared as follows, 5 mg of catalyst was mixed in a glass vial with $1650 \mu\text{l}$ of ethanol, $85 \mu\text{l}$ of water, $47.5 \mu\text{l}$ of 5 wt.% Nafion solution and five small glass beads, followed by sonication and agitation in a vortex mixer, alternatively, for three times. Then $18 \mu\text{l}$ of the catalyst suspension was dropped onto the GC electrode surface of RRDE (with the loading of $\sim 10 \mu\text{g Pt cm}^{-2}$). Before the electrochemical tests, the cycling voltammograms (CVs) between 0.03 and 1.20 V (vs. RHE) at 200 mV/s for 50 cycles were run in an N_2 -saturated 0.1 M HClO_4 to activate the electrocatalyst. The linear sweep voltammograms (LSV) were recorded at 10 mV s^{-1} , between 0.03-1.2 V (vs. RHE). The chronoamperometric (CA) measurement was achieved at a constant potential of 0.8v versus RHE using the carbon rod as a counter electrode. The kinetic currents were calculated using the Koutecky–Levich equation:

$$\frac{1}{J} = \frac{1}{J_k} + \frac{1}{J_L} \quad (1)$$

Where J , J_k , and J_L represent the measured, kinetic and diffusion-limited (Levich) current densities, respectively.

The peroxide yield ($\text{H}_2\text{O}_2\%$) and the electron transfer number (n) were calculated as equation (2) - (3):

$$H_2O_2\% = \frac{200I_R/N}{(I_R/N+I_D)} \quad (2)$$

$$n = \frac{4I_D}{(I_R/N+I_D)} \quad (3)$$

Where I_D is the disk current, I_R is the ring current, and N is the collection efficiency, equal to 0.37 for the present case.

References

- (1) Liu, M.; Zhao, Z.; Duan, X.; Huang, Y., Nanoscale Structure Design for High-Performance Pt-Based ORR Catalysts. *Adv Mater* **2019**, 31, e1802234.
- (2) Zhao, S.; Wang, D. W.; Amal, R.; Dai, L., Carbon-Based Metal-Free Catalysts for Key Reactions Involved in Energy Conversion and Storage. *Adv Mater* **2019**, 31, e1801526.
- (3) Dai, L.; Xue, Y.; Qu, L.; Choi, H. J.; Baek, J. B., Metal-free catalysts for oxygen reduction reaction. *Chem Rev* **2015**, 115, 4823-92.
- (4) Zhou, X. J.; Qiao, J. L.; Yang, L.; Zhang, J. J., A Review of Graphene-Based Nanostructural Materials for Both Catalyst Supports and Metal-Free Catalysts in PEM Fuel Cell Oxygen Reduction Reactions. *Advanced Energy Materials* **2014**, 4, 1301523.
- (5) Tong, X.; Wei, Q.; Zhan, X.; Zhang, G.; Sun, S., The New Graphene Family Materials: Synthesis and Applications in Oxygen Reduction Reaction. *Catalysts* **2017**, 7, 1.
- (6) Nie, Y.; Li, L.; Wei, Z., Recent advancements in Pt and Pt-free catalysts for oxygen reduction reaction. *Chem Soc Rev* **2015**, 44, 2168-201.
- (7) Adria Wilson, G. K., and Dimitrios Papageorgopoulos, Fuel Cell System Cost - 2017. *DOE Hydrogen and Fuel Cells Program Record* **2017**.
- (8) Sui, S.; Wang, X. Y.; Zhou, X. T.; Su, Y. H.; Riffatc, S.; Liu, C. J., A comprehensive review of Pt electrocatalysts for the oxygen reduction reaction: Nanostructure, activity, mechanism and carbon support in PEM fuel cells. *Journal of Materials Chemistry A* **2017**, 5, 1808-1825.
- (9) Li, T. F.; Liu, J. J.; Song, Y.; Wang, F., Photochemical Solid-Phase Synthesis of Platinum Single Atoms on Nitrogen-Doped Carbon with High Loading as Bifunctional Catalysts for Hydrogen Evolution and Oxygen Reduction Reactions. *Acs Catalysis* **2018**, 8, 8450-8458.
- (10) Zeng, X.; Shui, J.; Liu, X.; Liu, Q.; Li, Y.; Shang, J.; Zheng, L.; Yu, R., Single-Atom to Single-Atom Grafting of Pt onto FeN₄ Center: Pt₁@FeN₄C Multifunctional Electrocatalyst with Significantly Enhanced Properties. *Advanced Energy Materials* **2018**, 8, 1701345.
- (11) Liu, J.; Jiao, M.; Mei, B.; Tong, Y.; Li, Y.; Ruan, M.; Song, P.; Sun, G.; Jiang, L.; Wang, Y.; Jiang, Z.; Gu, L.; Zhou, Z.; Xu, W., Carbon-Supported Divacancy-Anchored Platinum Single-Atom Electrocatalysts with Superhigh Pt Utilization for the Oxygen Reduction Reaction. *Angew Chem Int Ed Engl* **2019**, 58, 1163-1167.
- (12) Yamamoto, K.; Imaoka, T.; Chun, W. J.; Enoki, O.; Katoh, H.; Takenaga, M.; Sonoi, A., Size-specific catalytic activity of platinum clusters enhances oxygen reduction reactions. *Nat Chem* **2009**, 1, 397-402.

- (13) Bu, L. Z.; Zhang, N.; Guo, S. J.; Zhang, X.; Li, J.; Yao, J. L.; Wu, T.; Lu, G.; Ma, J. Y.; Su, D.; Huang, X. Q., Biaxially strained PtPb/Pt core/shell nanoplate boosts oxygen reduction catalysis. *Science* **2016**, 354, 1410-1414.
- (14) Xia, B. Y.; Wu, H. B.; Li, N.; Yan, Y.; Lou, X. W.; Wang, X., One-pot synthesis of Pt-Co alloy nanowire assemblies with tunable composition and enhanced electrocatalytic properties. *Angew Chem Int Ed Engl* **2015**, 54, 3797-801.
- (15) Li, W.; Zou, S., PtNi nanoparticles encapsulated in few carbon layers as high-performance catalysts for oxygen reduction reaction. *ACS Applied Energy Materials* **2019**.
- (16) Chong, L.; Wen, J.; Kubal, J.; Sen, F. G.; Zou, J.; Greeley, J.; Chan, M.; Barkholtz, H.; Ding, W.; Liu, D. J., Ultralow-loading platinum-cobalt fuel cell catalysts derived from imidazolate frameworks. *Science* **2018**, 362, 1276-1281.
- (17) Tong, X.; Zhang, J.; Zhang, G.; Wei, Q.; Chenitz, R.; Claverie, J. P.; Sun, S., Ultrathin Carbon-Coated Pt/Carbon Nanotubes: A Highly Durable Electrocatalyst for Oxygen Reduction. *Chemistry of Materials* **2017**, 29, 9579-9587.
- (18) Alegre, C.; Galvez, M. E.; Moliner, R.; Baglio, V.; Arico, A. S.; Lazaro, M. J., Towards an optimal synthesis route for the preparation of highly mesoporous carbon xerogel-supported Pt catalysts for the oxygen reduction reaction. *Applied Catalysis B-Environmental* **2014**, 147, 947-957.
- (19) Sakthivel, M.; Drillet, J. F., An extensive study about influence of the carbon support morphology on Pt activity and stability for oxygen reduction reaction. *Applied Catalysis B-Environmental* **2018**, 231, 62-72.
- (20) Mirshekari, G. R.; Rice, C. A., Effects of support particle size and Pt content on catalytic activity and durability of Pt/TiO₂ catalyst for oxygen reduction reaction in proton exchange membrane fuel cells environment. *Journal of Power Sources* **2018**, 396, 606-614.
- (21) Yang, S.; Tak, Y. J.; Kim, J.; Soon, A.; Lee, H., Support Effects in Single-Atom Platinum Catalysts for Electrochemical Oxygen Reduction. *Acs Catalysis* **2017**, 7, 1301-1307.
- (22) Zhang, L.; Zhao, Y.; Banis, M. N.; Adair, K.; Song, Z.; Yang, L.; Markiewicz, M.; Li, J.; Wang, S.; Li, R.; Ye, S.; Sun, X., Rational design of porous structures via molecular layer deposition as an effective stabilizer for enhancing Pt ORR performance. *Nano Energy* **2019**, 60, 111-118.
- (23) Liu, J.; Jiao, M.; Lu, L.; Barkholtz, H. M.; Li, Y.; Wang, Y.; Jiang, L.; Wu, Z.; Liu, D.-j.; Zhuang, L.; Ma, C.; Zeng, J.; Zhang, B.; Su, D.; Song, P.; Xing, W.; Xu, W.; Wang, Y.; Jiang, Z.; Sun, G., High performance platinum single atom electrocatalyst for oxygen reduction reaction. *Nature Communications* **2017**, 8, 15938.
- (24) Xin, L.; Yang, F.; Rasouli, S.; Qiu, Y.; Li, Z.-F.; Uzunoglu, A.; Sun, C.-J.; Liu, Y.; Ferreira, P.; Li, W.; Ren, Y.; Stanciu, L. A.; Xie, J., Understanding Pt Nanoparticle Anchoring on Graphene Supports through Surface Functionalization. *ACS Catalysis* **2016**, 6, 2642-2653.
- (25) Tong, X.; Wang, H.; Wang, G.; Wan, L.; Ren, Z.; Bai, J.; Bai, J., *Controllable synthesis of graphene sheets with different numbers of layers and effect of the number of graphene layers on the specific capacity of anode material in lithium-ion batteries*. 2011; Vol. 184, p 982-989.
- (26) Wen, Y.; Wang, B.; Huang, C.; Wang, L.; Hulicova-Jurcakova, D., Synthesis of phosphorus-doped graphene and its wide potential window in aqueous supercapacitors. *Chemistry* **2015**, 21, 80-5.
- (27) Xiong, B.; Zhou, Y. K.; Zhao, Y. Y.; Wang, J.; Chen, X.; O'Hayre, R.; Shao, Z. P., The use of nitrogen-doped graphene supporting Pt nanoparticles as a catalyst for methanol electrocatalytic oxidation. *Carbon* **2013**, 52, 181-192.

- (28) Chai, G. L.; Qiu, K. P.; Qiao, M.; Titirici, M. M.; Shang, C. X.; Guo, Z. X., Active sites engineering leads to exceptional ORR and OER bifunctionality in P,N Co-doped graphene frameworks. *Energy & Environmental Science* **2017**, 10, 1186-1195.
- (29) Moulder, J. F.; Chastain, J., *Handbook of X-ray Photoelectron Spectroscopy: A Reference Book of Standard Spectra for Identification and Interpretation of XPS Data*. Physical Electronics Division, Perkin-Elmer Corporation: 1992.
- (30) Choi, C. H.; Kim, M.; Kwon, H. C.; Cho, S. J.; Yun, S.; Kim, H.-T.; Mayrhofer, K. J. J.; Kim, H.; Choi, M., Tuning selectivity of electrochemical reactions by atomically dispersed platinum catalyst. *Nature Communications* **2016**, 7, 10922.
- (31) Zhang, C.; Sha, J.; Fei, H.; Liu, M.; Yazdi, S.; Zhang, J.; Zhong, Q.; Zou, X.; Zhao, N.; Yu, H.; Jiang, Z.; Ringe, E.; Yakobson, B. I.; Dong, J.; Chen, D.; Tour, J. M., Single-Atomic Ruthenium Catalytic Sites on Nitrogen-Doped Graphene for Oxygen Reduction Reaction in Acidic Medium. *ACS Nano* **2017**, 11, 6930-6941.
- (32) Choi, C. H.; Park, S. H.; Woo, S. I., Phosphorus–nitrogen dual doped carbon as an effective catalyst for oxygen reduction reaction in acidic media: effects of the amount of P-doping on the physical and electrochemical properties of carbon. *Journal of Materials Chemistry* **2012**, 22, 12107-12115.
- (33) Paraknowitsch, J. P.; Thomas, A., Doping carbons beyond nitrogen: an overview of advanced heteroatom doped carbons with boron, sulphur and phosphorus for energy applications. *Energy & Environmental Science* **2013**, 6, 2839-2855.

Supporting information for
Support interaction effect of platinum clusters anchoring on
doped graphene supports for the oxygen reduction reaction

Xin Tong,^{†,‡} Gaixia Zhang,[†] Jerome P. Claverie^{§,*} and Shuhui Sun^{†,*}

[†] Institut National de la Recherche Scientifique-Énergie Matériaux et Télécommunications, Varennes, QC, Canada J3X 1S2.

[‡] School of Chemistry and Material Science, Guizhou Normal University, Guiyang, China, 550001.

[§] Department of Chemistry, Université de Sherbrooke, Sherbrooke, QC, Canada J1K 2R1.

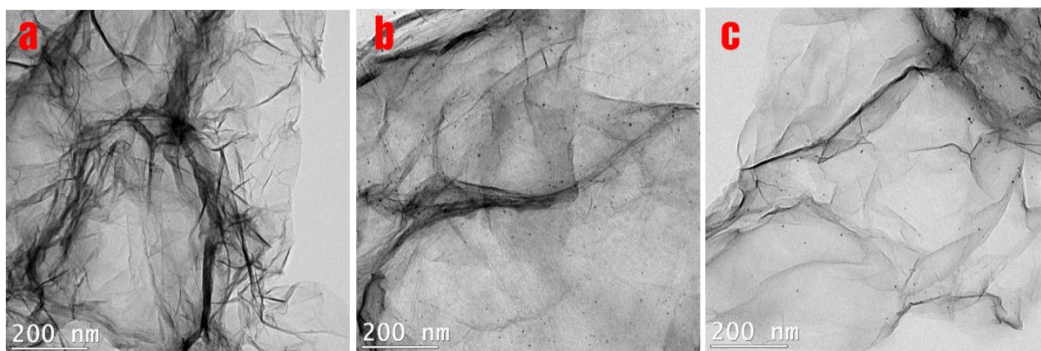


Figure S1. Low magnification TEM images of (a) Pt/N, P-Graphene, (b) Pt/N-Graphene and (c) Pt/RGO.

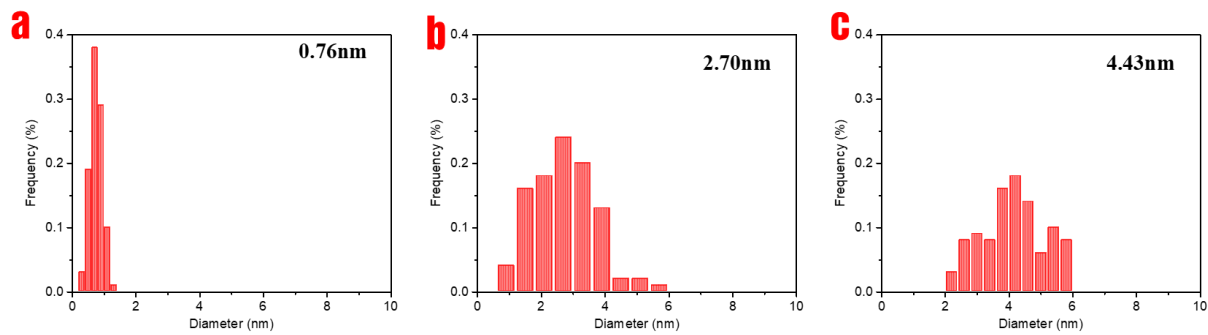


Figure S2. The size-distribution histogram of (a) Pt/N, P-Graphene, (b) Pt/N-Graphene and (c) Pt/RGO.

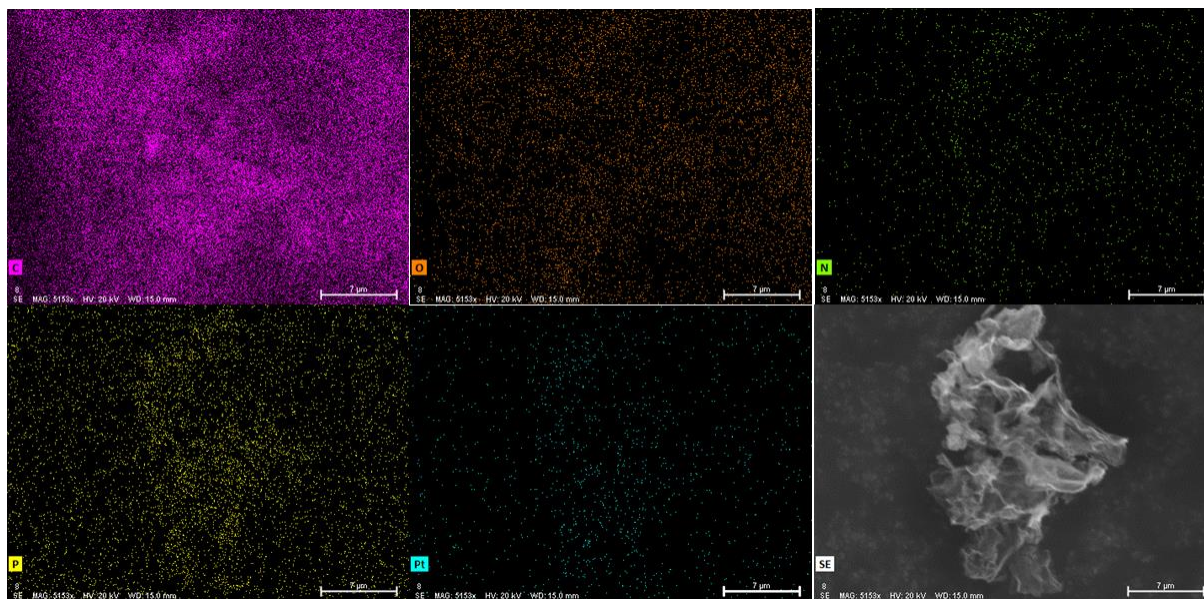
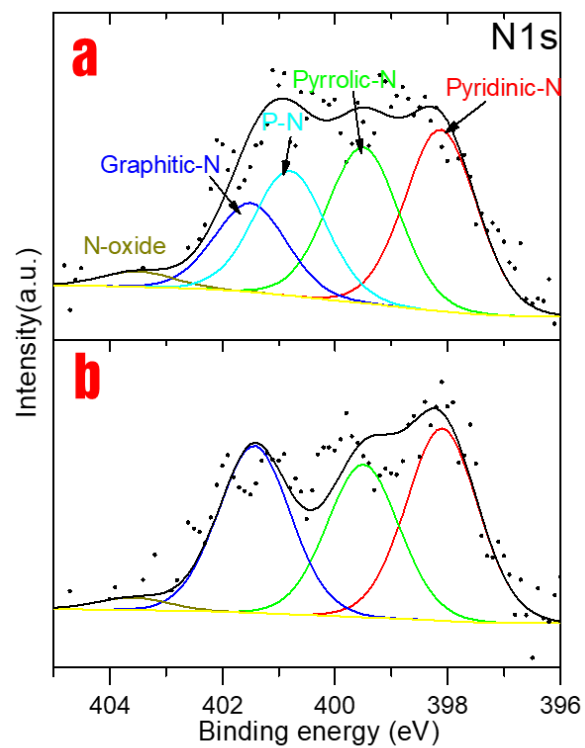
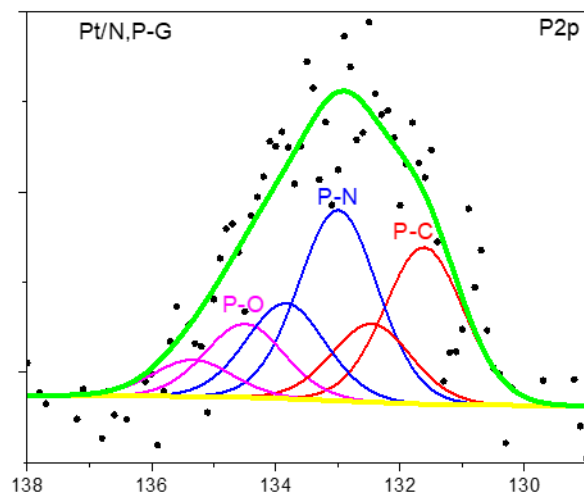


Figure S3. SEM Mapping of C, O, N, P, and Pt of Pt/N, P-Graphene.



FigureS4. High-resolution XPS spectra of N1s of (a) Pt/N, P-Graphene and (b) Pt/N-Graphene.



FigureS5. High-resolution XPS spectra of P2P of Pt/N, P-Graphene.

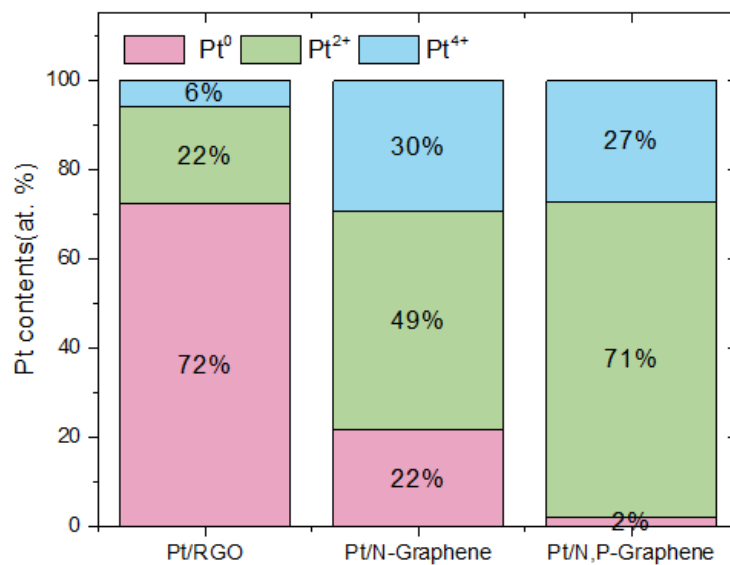


Figure S6. Normalized concentrations of Pt 4f binding configurations for Pt/RGO, Pt/N-Graphene and Pt/N, P-Graphene.

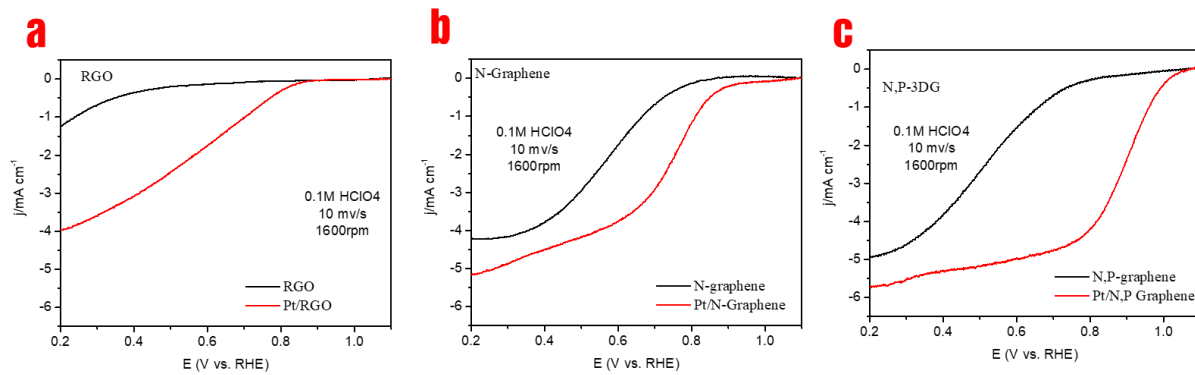


Figure S7. (a,b,c) LSV on RRDE of RGO and Pt/RGO, N-Graphene and Pt/N-Graphene, N,P-Graphene and Pt/N,P-Graphene in O_2 -saturated 0.1 M $HClO_4$ at a scan rate of 10 mV s^{-1} (rotation speed: 1600 rpm).

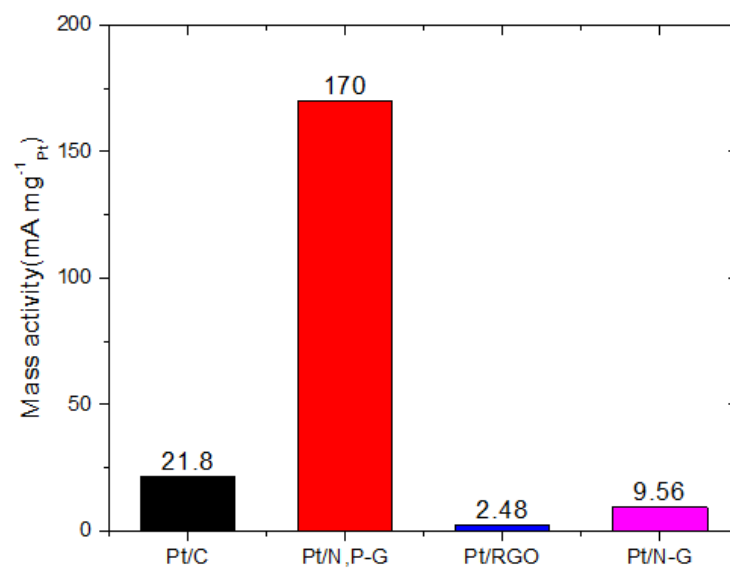


Figure S8. The mass activity of these four catalysts normalized by the weight of Pt at 0.9 V versus RHE.

Table S.1 Elemental quantification of Pt/N, P-Graphene, Pt/N-Graphene, and Pt/RGO obtained from XPS results.

Sample	Element content /at. %				
	C	O	N	P	Pt ¹
Pt/RGO	82.65	12.47	-	-	4.88
Pt/N-Graphene	85.27	6.39	3.13	-	5.03
Pt/N,P-Graphene	87.36	3.18	3.31	0.93	5.22

1. Pt content were derived from ICP-OES.

Table S.2 Curve fitting results of the XPS N1s spectrum.

	Peak assign									
	Pyridinic-N		Pyrolic-N		N-P		Graphitic-N		N-oxide	
	BE(eV)	%	BE(eV)	%	BE(eV)	%	BE(eV)	%	BE(eV)	%
Pt/N- Graphene	398.1	36.63	399.5	29.12	-	-	401.4	31.86	403.5	2.39
Pt/N-P Graphene	398.1	32.05	399.5	27.50	400.8	22.04	401.5	15.68	403.5	2.73

N, P co-doped graphene dots supported on N-doped 3D graphene as metal-free catalyst for oxygen reduction

Titre de l'article: N, P points de graphène co-dopée supportés sur N-dopée graphène 3D comme catalyseur exempt de métal pour la réduction de l'oxygène

Authors: Xin Tong, Mohamed Cherif, Gaixia Zhang, Jugang Ma, Ali Almesrati, Vidal François, Yujun Song, Jerome P. Claverie, and Shuhui Sun

Title of the journal: To be submitted

Link between the previous articles:

Based on previous research, the doped graphene cannot only be used as supporting material but also the metal-free catalysts for ORR. Therefore, we synthesized nitrogen and phosphorus co-doped graphene dots supported on nitrogen-doped three-dimensional graphene (N, P-GDs/N-3DG) by a facile freeze-annealing process.

The as-obtained N, P-GDs are uniformly dispersed on the surface of the interconnected 3D porous network. The metal-free N, P-GDs/N-3DG composite exhibits excellent electrocatalytic activity for the ORR comparable to the commercial Pt/C catalyst. Moreover, it shows a higher tolerance to methanol and better stability than the Pt/C. This enhanced electrocatalytic performance can be ascribed to the synergetic effect of abundant functional groups and the edge defects.

N, P co-doped graphene dots supported on N-doped 3D graphene as metal-free catalyst for oxygen reduction

Xin Tong,^{†, ‡} Mohamed Cherif,[†] Gaixia Zhang,^{†, *} Jugang Ma,[§] Ali Almesrati,[†] Vidal François,[†] Yujun Song,[§] Jerome P. Claverie^{‡, *} and Shuhui Sun^{†, *}

[†] Institut National de la Recherche Scientifique-Énergie Matériaux et Télécommunications, Varennes, QC, Canada J3X 1S2.

[‡] School of Chemistry and Material Science, Guizhou Normal University, Guiyang, China, 55000

[§] School of Mathematics and Physics, University of Science & Technology Beijing, Beijing, China, 10008

[‡] Department of Chemistry, Université de Sherbrooke, Sherbrooke, QC, Canada J1K 2R1

ABSTRACT: Nitrogen and phosphorus co-doped graphene dots supported on nitrogen-doped three-dimensional graphene (N, P-GDs/N-3DG) have been synthesized by a facile freeze-annealing process. The as-obtained N, P-GDs are uniformly dispersed on the surface of the interconnected 3D porous network. The metal-free N, P-GDs/N-3DG composite exhibits excellent electrocatalytic activity for the oxygen reduction reaction (ORR) comparable to commercial Pt/C catalyst. Moreover, it shows a higher tolerance to methanol and better stability than the Pt/C. This enhanced electrocatalytic performance can be ascribed to the synergetic effect of abundant functional groups and the edge defects. This study indicates that P-N bonded structures play an important role as active sites in ORR.

The exploitation of electrocatalytic reactions is one of the most up-and-coming strategies to convert chemical energy into electrical energy in an efficient and environment-friendly manner.¹⁻⁴ Among these reactions, the oxygen reduction reaction (ORR) is central for the efficient exploitation of renewable technologies such as fuel cells and metal-air batteries. The oxygen molecule is difficult to be reduced because of a strong oxygen double bond. The ORR can occur through two ways, (i) via a direct four-electron pathway where the oxygen is reduced directly to water, ($O_2 + 4H^+ + 4e^- \rightarrow 2H_2O$) and (ii) via a two-step two-electron pathway where the oxygen is first reduced to hydrogen peroxide as an intermediate ($O_2 + 2H^+ + 2e^- \rightarrow H_2O_2$). In fuel cells and metal-air batteries, the four-electron pathway must predominate in order to achieve a highly efficient catalytic process. Up to now, Pt-based material is the most efficient ORR catalyst with a 4e⁻ pathway.¹ However, the mass-deployment of Pt-based electrocatalysts is curtailed by its high cost, poor availability and poisoning by CO. Therefore, various strategies such as the development of non-precious metal catalysts or even metal-free catalysts have been explored for the ORR.^{1, 4-6}

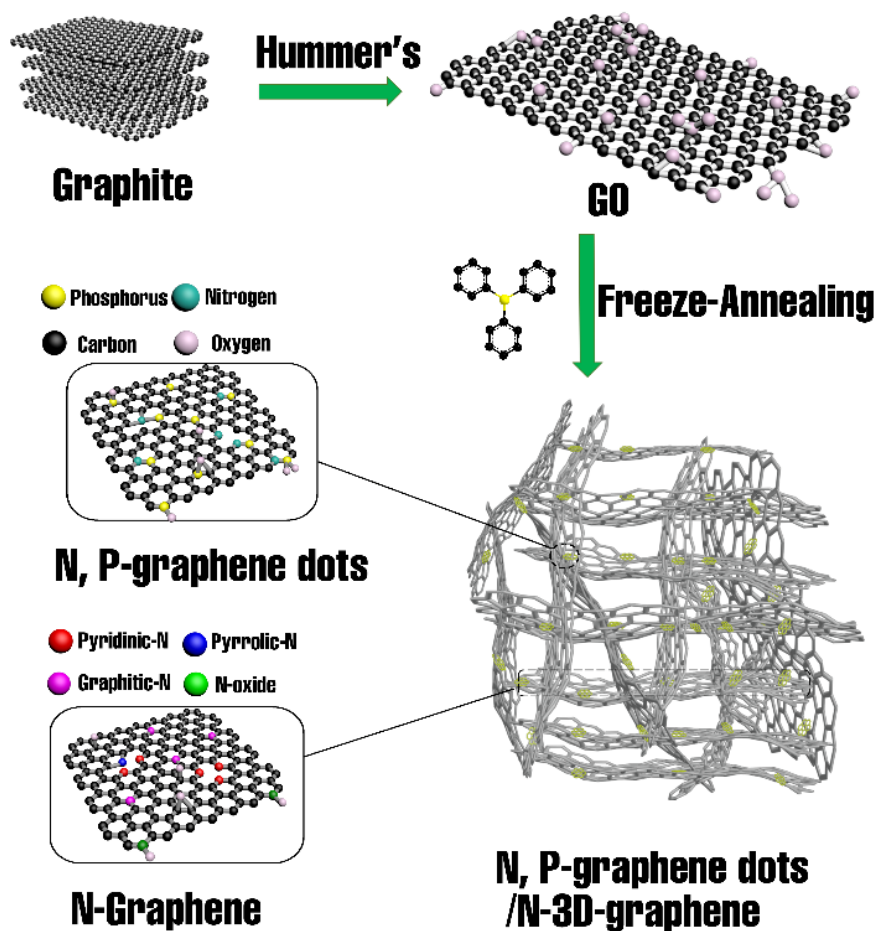
In the past decade, graphene is regarded as one of the most attractive candidates for catalysis, especially in energy applications, due to its high surface area, outstanding conductivity, high thermal/chemical stability

and excellent mechanical properties.⁷⁻¹² Because graphene has abundant free-flowing π electrons, it has the potential to catalyze the ORR. However, the π electrons of the pristine graphene are too inert to be active for ORR.¹³ It is therefore essential to tune the electrical properties of graphene. Doping graphene with heteroatoms such as N, B, O, P or S is an effective way to modulate the chemisorption energy of O₂, resulting in more catalytic sites, and consequently enhancing the ORR performance.^{2, 14} Among them, nitrogen is by far the most frequently investigated heteroatom as it has been proved to be able to enhance the electrochemical performance of the catalyst. When the carbon atoms bond with N dopants that have five valence electrons, more free π -electrons are available to participate in the catalytic process. Furthermore, the co-doping of graphene has recently been explored in recent years.^{15, 16} The dual-doped graphene is more catalytically active than singly-doped one because of the synergistic coupling effect between co-dopants. However, the synergy between these heteroatoms has not been fully understood yet.

The 2D graphene layers easily aggregate and restack because of the strong van der Waals interactions, which results in a significant decrease of surface area and of the number of active sites, therefore, consequently in a lowering of the catalytic performance.¹⁷ One of the most promising routes to solve this problem is the building of graphene-based nanostructures such as graphene dots (GDs), graphene nanoribbons (GNRs), and three-dimensional graphene (3DG), which can be called graphene derivatives.¹⁸ Graphene derivative materials can not only maintain the intrinsic properties of graphene, but also possess some unique properties such as abundant active sites and edge effects. Graphene dots (GDs), zero-dimensional (0D) graphene with a size below 100 nm, have attracted much interest for efficient metal-free catalysts for ORR.^{19, 20} Similarly, the heteroatom-doped graphene dots (X-GDs) have been demonstrated to be electrochemically active toward ORR because the chemically bonded heteroatoms could alter the electronic characteristics of graphene and offer more active sites.²¹

However, the low conductivity of the pristine GD electrode limits its ORR performance.²² Synergistic enhancement of the ORR activity is observed in composites of GDs supported on conductive substrates such as carbon nanotubes²³ and graphene.^{21, 24} GDs can at the same time render the graphene active in ORR and create active sites for oxygen adsorption. 3DG, a highly porous graphene material, combines a very high surface area with good conductivity. As both mass transfer and electron transport are enhanced, such material has drawn widespread interest for potential applications in fuel cells.²⁵⁻²⁷ In particular, GDs supported on conductive substrates are usually synthesized by two-step methods due to the difficulty in synthesizing GDs. Wang *et al.* first prepared GDs from carbon fiber and then embedded them in graphene hydrogel by hydrothermal method.²⁴ Tam *et al.* synthesized boron doped GDs by carbonization of glucose followed by a hydrothermal process which leads to GDs composites.²⁸

Herein, we propose a facile one-step and scalable freeze-annealing method for the synthesis of N, P-graphene dots supported on N-3D-graphene (N, P-GDs/N-3DG). Firstly, triphenylphosphine (TPP) molecules were adsorbed on the surface of GO. The adsorption is facilitated by the presence of acidic groups (carboxylic acid, inter alia) that can interact with the basic TPP. In this hydrogel, GO sheets are self-assembled to a network and TPP act as the cross-linking agent. By immersing the hydrogel into liquid nitrogen and followed by freeze-drying, the aggregation was prevented and the 3D network structure was maintained. The N, P-GDs synthesized *in situ* were uniformly distributed at the surface of N-3DG. The GDs in the composite can offer more catalytically active sites while the N-3DG not only acts as an excellent conductive substrate for electrons but also ensure the efficient mass transport of oxygen molecule and electrolyte during the ORR process. In addition, N, P-doping can effectively tailor their intrinsic electrical characteristics and surface properties.²⁹ So the obtained N, P-GDs/N-3DG with synergistic enhancement of the ORR activity could become a promising catalyst in alkaline fuel cells. Further, it can provide an effective platform for fundamental investigations on the role of GDs and on heteroatom doping.



Scheme 1. Schematic Illustration of the Fabrication Process and Structure of the N, P-Graphene Dots supporting on N-3D-graphene (N, P-GDs/N-3DG).

The N, P-GDs/N-3DG materials were synthesized by the following procedure described in Scheme 1. First, the GO was obtained by the modified Hummer's method.³⁰ Then, the TPP was added to the GO solution. The small TPP molecules are adsorbed at the surface of GO due to the development of acid-base interaction between surface acidic groups and the basic phosphine. Non-site-specific adsorption can also occur via hydrophobic interactions. Then the GO dispersion was dropped directly into liquid nitrogen through a spring pump with controlled speed (Scheme S1 in the Supporting Information (SI)). The as-prepared hydrogel was treated by the freeze-drying process to maintain the 3D monolithic architecture and then heated at 950 °C for 10 min under ammonia. During the annealing process, the labile oxygen functional groups on the GO were thermally removed, thus active sites were induced by both *in situ* N doping with ammonia treatment and by the growth of GDs, finally resulting in the compact packing of N, P-GDs on N-3DG by π - π stacking. Significantly, both the solution based freeze-drying process and template-free pyrolysis process is easy to scale up with low-cost mass production.

Transmission electron microscopy (TEM) images of the N, P-GDs/N-3DG are shown in Figure 5.1. It can be seen that uniform GDs with a diameter of \sim 8.8 nm are deposited on the graphene sheet surfaces. The low magnification TEM image in Figure 1. (a) exhibits a wrinkled morphology, which is mainly composed of multilayered graphene sheets. The GDs are homogeneously distributed at the surface of the 3D network formed by graphene sheets. The GDs show spherical morphology (Figure 5.1b) with an average diameter of \sim 8.8 nm and a narrow size distribution (4 to 20 nm, Figure 5.1b Inset). The scanning electron microscope (SEM) images of the 3DG, N-3DG, P-GDs/3DG and N, P-GDs/N-3DG are presented in Supporting Information (Figure S1). It can be seen that the as-prepared samples have a well-defined and interconnected 3D porous network. The lateral dimensions of the graphene sheets range from sub-micrometers to several micrometers. The photographs of the samples are shown in the inset of Figure S1. These four self-assembled samples display quasi-spherical morphology with black color. Elemental mapping analysis (Figure 5.1. (c)) of N, P-GDs/N-3DG suggest the presence of C, N, and O components in the substrate and in the GDs. The N atoms are distributed uniformly throughout the surfaces of the graphene layer and are enriched in the dots. Interestingly, the P atoms are mainly located in the GDs, indicating that the TPP molecules have mainly formed the doped GDs and have not been incorporated into the graphene lattice. In addition, the nitrogen and oxygen contents are slightly higher in the GD region than in the graphene layers. This phenomenon indicates that there may be a larger variety of functional groups on the GDs and thus we may expect more active sites.

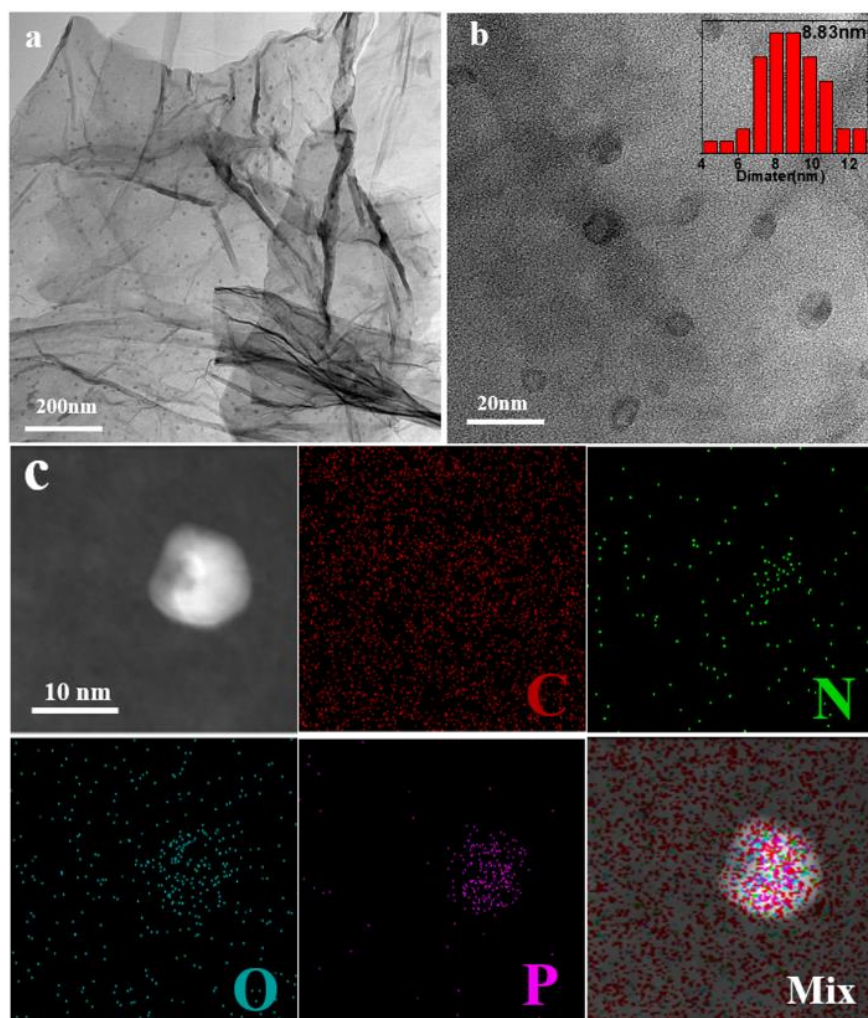


Figure 5.1. TEM images of N, P-GDs/N-3DG. (a, b) Inset: corresponding size distribution histogram of N, P-GDs/N-3DG. Elemental mapping images of N, P-GDs/N-3DG. (c) Dark-field TEM image, elemental mapping of C, N, O, P and the mixed elements with the dark-field image.

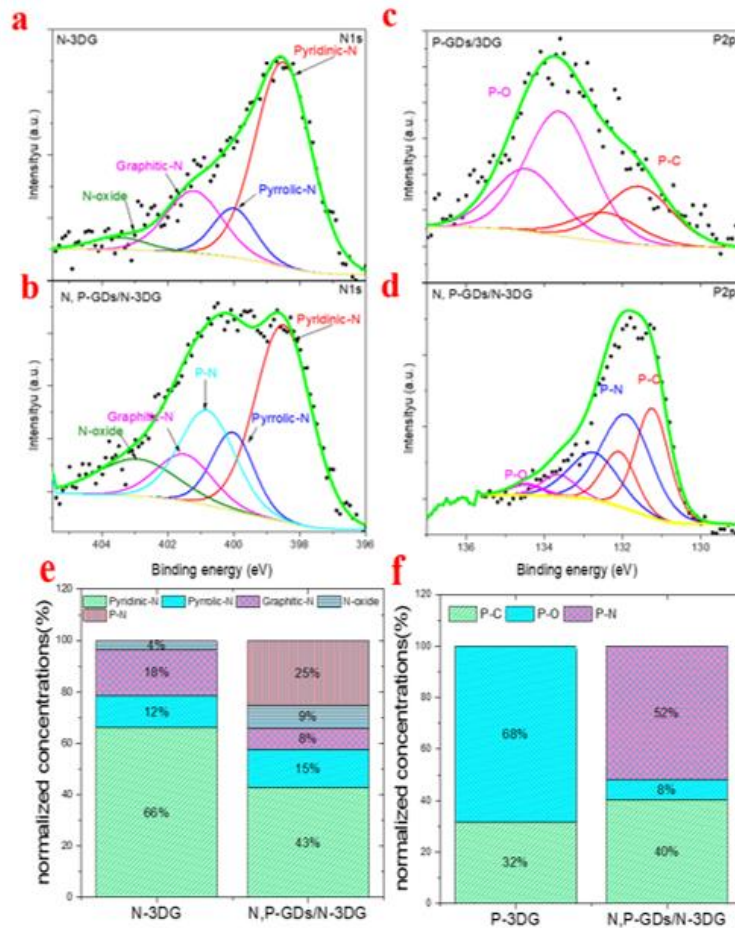


Figure 5.2. (a) High resolution N1s XPS spectra of N-3DG (a) and N, P-GDs/N-3DG (b). (b) High resolution P2p XPS spectra of P-GDs/3DG (c) and N, P-GDs/N-3DG (d). Normalized concentrations of (e) N1s binding configurations for N-3DG, N, P-GDs/N-3DG and (f) P2p binding configurations for P-3DG, N, P-GDs/N-3DG.

X-ray photoelectron spectroscopy (XPS) was conducted to reveal the chemical composition of each sample. XPS survey spectra of 3D graphene, N-3DG, P-3DG, N, P-GDs/N-3DG are shown in Figure S2 in the SI. The oxygen content of 3DG is 20.1%, which is as high as expected as the sintering temperature was low. The oxygen content has been significantly decreased after high-temperature annealing under ammonia, implying that GO can be effectively reduced through ammonia treatment under high temperature. The N-doping level in N-3DGs is 4.25% while it is 3.42% in the N, P-GDs/N-3DG. In addition, the P content in N, P-GDs/N-3DG is 1.45% while it is 0.82% in P-GDs/N-3DG. The high-resolution N 1s XPS spectra (Figure 5.2. a, b) of N-3DG and N, P-GDs/N-3DG reveal the presence of pyridinic, pyrrolic, and graphitic N as well as N–O species.³¹ The high proportion of pyridinic N can be observed in both N-3DG and N, P-GDs/N-3DG. Significantly, there is a new P-N structure which can be found in the N, P-GDs/N-3DG sample. Its peak position is between the position of pyrrolic, and graphitic N.²⁹ The normalized concentrations of P-N in N1s binding configurations is around 20% (Figure 5.2.e), implying that the main

component in N, P-GDs is P-N bonded structure. The presence of P-N bonding shows the successful doping of N atoms into P-GDs. In Figure 5.2. (c)(d), the P2p XPS spectra of P-GDs/3DG and N, P-GDs/N-3DG were deconvoluted into three doublet components ($2p_{1/2}$ and $2p_{3/2}$ $\Delta E=0.84$ eV). The three components located at 131.2, 132.1 and 133.7 eV in $2p_{3/2}$ can be assigned to P atoms bonded to C atoms (P-C bonding), to N atoms (P-N bonding) and to O atoms (P-O bonding), respectively.^{29, 32} Since the P element is mainly distributed on the GDs, the high-resolution P2p XPS spectrum only corresponds to GDs. Obviously, the C-O bonding content in P-GDs is comparatively high (68%) while that in N-P-GDs is relatively low (8%) in Figure 5.2.(f). Instead, the content of P-N bonding in N, P-GDs is very high (52%), further confirming that most of the N atoms are directly bonded to P atoms in N, P-GDs. It can be explained as follows. First, the basic TPP molecule interacts with surface COOH acid groups present at the GO surface (Figure S3). At high temperature, TPP is known to deoxygenate GO to lead to RGO and phosphine oxide, $\text{Ph}_3\text{P}=\text{O}$.³³ $\text{Ph}_3\text{P}=\text{O}$ is not stable under 950 °C and leads to the formation P-GDs in Ar atmosphere. As the ammonia annealing was conducted at 950 °C, the phosphine can react with ammonia to form a phosphinimine, $\text{Ph}_3\text{P}=\text{NH}$.³⁴ Such phosphinimine is highly reactive, in particular in the presence of OH groups.³⁵ Thus, at elevated temperatures, a mixture of $\text{Ph}_3\text{P}=\text{O}$ and $\text{Ph}_3\text{P}=\text{NH}$ molecules are formed, which decomposes into N, P-GDs at 950 °C.

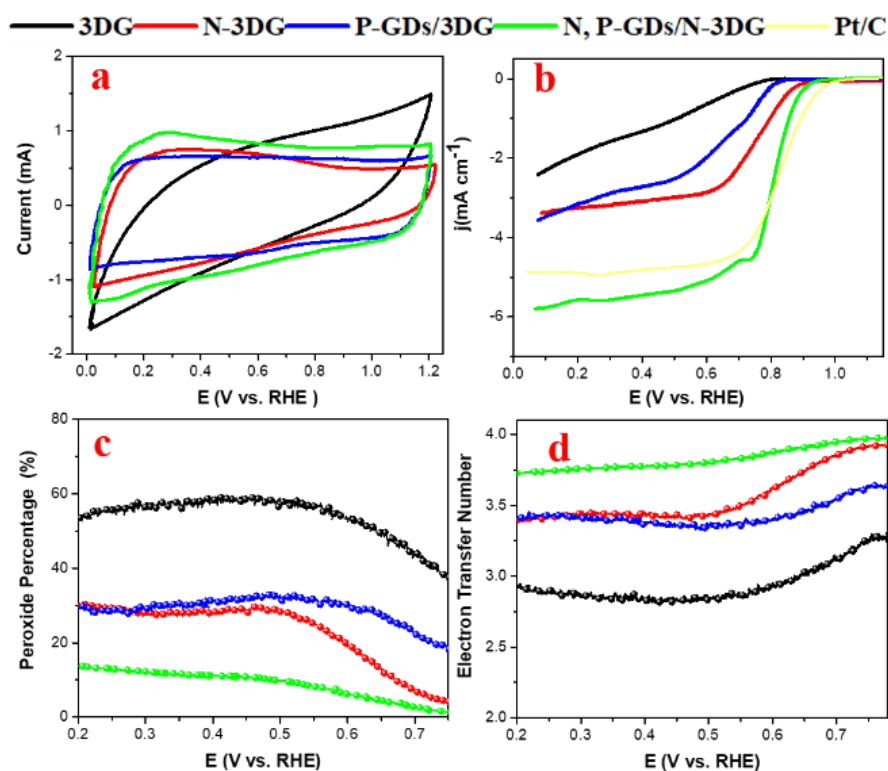


Figure 5.3. (a) CVs of four samples named as 3D graphene, N-3DG, P-GDs/3DG and N, P-GDs/N-3DG in N_2 -saturated 0.1 M KOH at a scan rate of 100 mV s^{-1} . (b) RDE polarization curves of the as-prepared materials and Pt/C 20% in O_2 -saturated 0.1 M KOH at a scan rate of 10 mV s^{-1} (rotation speed: 1600

rpm). (c) Hydrogen peroxide yields and (d) electron transfer numbers of 3D graphene, N-3DG, P-3DG and N, P-GDs/N-3DG as the function of the electrode potential.

The electrochemical performance of 3D graphene, N-3DG, P-3DG and N, P-GDs/N-3DG were studied in a three-electrode system in 0.1 M KOH electrolyte solution. Figure 3a shows the cyclic voltammetry (CV) curves of as-prepared catalysts within the potential range 0 to 1.2 V at a scan rate of 100 mV/s. All the 3DG materials exhibited quasi-rectangular CV curves as a result of the typical supercapacitance effect of graphene materials. As measured from the encircled area in CV curves, the electric double layer capacitance is larger in the N, P-GDs/N-3DG sample. The presence of a large quantity of N, P in N, P-GDs/N-3DG as well as graphene edges in this sample facilitates the adsorption of ions in the electrolyte, thus increasing the double-layer capacitance.^{36,37} Furthermore, the electrocatalytic activity of as-prepared catalysts toward ORR was investigated by linear sweep voltammetry (LSV) using a rotating ring disk electrode (RRDE). Figure 5.3. (b) shows the LSV curves of different catalysts at a rotational speed of 1600 rpm in an O₂-saturated 0.1 M KOH electrolyte at a scanning rate of 10 mV s⁻¹. The onset potential follows the order of 3DG (0.72 V) < P-GDs/3DG (0.80 V) < N-3DG (0.88 V) < N, P-GDs/N-3DG (0.94 V). In all the aforementioned metal-free catalysts, N, P-GDs/N-3DG composite shows highest electrocatalytic activity in terms of most positive half-wave potential (0.81 V) and highest limiting current density (5.6 mA cm⁻²), indicating a more efficient ORR performance. The ORR onset potential and half-wave potential for N, P-GDs/N-3DG are close to those of the state-of-the-art commercial Pt/C catalyst (1.0 V and 0.82 V, respectively). Moreover, the limiting current density of N, P-GDs/N-3DG composite is higher than that of the commercial Pt/C (4.9 mA cm⁻²) which is attributed to the high surface area of the N, P-GDs/N-3DG sample. In addition, Figure 5.3 (c) shows that the H₂O₂ yield of N, P-GDs/N-3DG is lower than the other composites at all potentials in 0.1 M KOH. The low H₂O₂ yield confirms the high selectivity of N, P-GDs/N-3DG. Among the various catalyst materials, N, P-GDs/N-3DG has the highest electron-transfer number (3.75 in Figure 5.3.d), revealing that the N, P-dots/N-3DG favors a direct 4e⁻ pathway. The methanol tolerance, which is a highly desirable feature of efficient electrocatalysts for the fuel cell application, was investigated for N, P-GDs/N-3DG and Pt/C samples, as presented in Figure S3 (a). After methanol was added to the electrolyte, the chronoamperometric response for the N, P-GDs/N-3DG remained stable, whereas the Pt/C catalyst showed a significant drop due to the methanol oxidation reaction on the Pt/C catalyst. The durability of the N, P-GDs/N-3DG and Pt/C catalysts was evaluated by carrying out chronoamperometric measurements in O₂-saturated 0.1 M KOH solution at 0.8 V (vs. the RHE) with a rotation speed of 1600 rpm (Figure S3 b). A slight current density loss (6.7%) was observed for the N, P-GDs/N-3DG after 30,000 s tests. This loss is clearly lower than that in commercial Pt/C catalyst (~35% after 20000 s) under the same conditions, indicating that our catalyst possesses a more stable electrocatalytic performance.

Based on the electrochemical analysis of as-prepared composites, the superior electrocatalytic activity of N, P-GDs/N-3DG is clear. The main reason is that the GDs can offer more catalytic active sites while the N-3DG acts as a conductive substrate.^{28, 38} DFT calculations were performed in order better understanding the electrocatalytic activity of N, P-GDs/N-3DG. Because the prerequisite step for the reduction of oxygen in fuel cells is the adsorption of O₂ molecules on the catalyst surface, the adsorption energies of oxygen (E_{ads}) on various bond structures were calculated to determine the active sites where O₂ could adsorb. The adsorption energy of molecular oxygen (O₂) was calculated by

$$E_{ads} = E_{P/N/C/O_2} - E_{P/N/C} - E_{O_2}$$

Where E_{P/N/C/O₂} is the energy of the adsorbate/graphene system and E_{P/N/C} is the energy of co-doped graphene and E_{O₂} is the energy of the free oxygen molecule.

First, the O₂ molecule was placed at different positions on the structure, taking into consideration the side-on (parallel to plane) and head-on (perpendicular to the plane) orientations. Then, the site with the strongest O₂ adsorption was determined by determining by DFT calculations the most negative adsorption energy. To consider the doping effect, the configurations of an initial oxygen position are constrained to the site near the doped atoms. Such sites are shown in Figure 4 for P-N bonded structure (P directly bonded with N) and P-C, N-C bonded structure (P bonded with C and N bonded with C separately). The calculated E_{ads} for the P-N bond structure are -3.994 eV and -3.998 eV, respectively, for side-on and head-on orientations whereas they are -2.81 eV and -2.97 eV, respectively, for the P-C, N-C bonded structure. Therefore, the adsorption of O₂ on the P-N bond structure is more favorable than on the P-C, N-C structure. Other calculated O₂ adsorption energies in different position are shown in Fig. S4–S6. In addition, the oxygen molecule adsorb by the P atom on side-on direction in any configurations of an initial O₂ position after simulation process (shown in figure S7). These theoretical investigations are consistent with the above XPS and electrochemical characterizations, suggesting the P-N bond structures present in the N, P-GDs/N-3DG structure are essential sites to enhance the electrocatalytic activity of ORR.

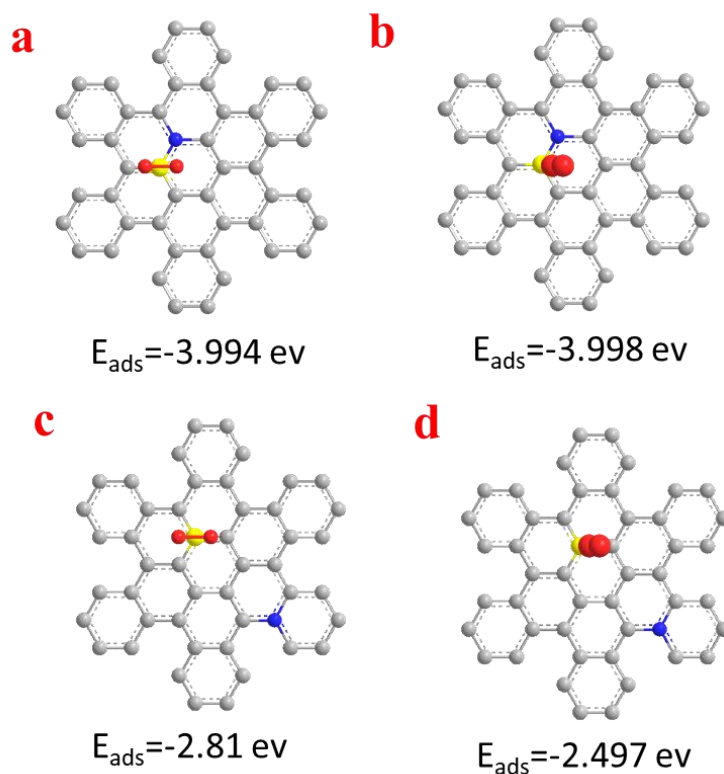


Figure 5.4. Optimized structures of the lowest O₂ adsorption energy configurations on different bond structures in N, P-GDs/N-3DG: (a, b) P-N bond structure, (c, d) P-C, N-C bond structure. (a, c) Side-on direction, (b, d) Head-on direction. The gray, yellow, blue and red colors represent carbon, phosphorus, nitrogen, and oxygen atom, respectively.

In summary, a facile and effective freeze-annealing strategy for *in situ* growth of GDs with N- and P-rich functional groups on N-3DG multidimensional architecture is reported. The obtained material shows an improved ORR performance in comparison to the samples with single-doping, without doping or even to the commercial Pt/C catalyst. Using DFT calculations as well as XPS measurements, P-N bonded structures were found to be of pivotal importance in ORR. Thus we have not only unraveled an excellent metal free ORR electrocatalyst for fuel cell and metal/air batteries but also an effective platform for fundamental investigations on the role of GDs and heteroatom doping.

ASSOCIATED CONTENT

Supporting Information

The Supporting Information is available free of charge on the ACS Publications website. Experimental details; Schematic illustration of equipment; XPS survey spectra, Normalized concentrations N_{1s} and P_{2p} binding configurations, Chronoamperometric responses curves and DFT calculations details.

AUTHOR INFORMATION

Corresponding Author

*E-mail: gaixia.zhang@emt.inrs.ca(G.Z.)

*E-mail: jerome.claverie@usherbrooke.ca (J.C.)

*E-mail: shuhui@emt.inrs.ca (S.S.)

Notes

The authors declare no competing financial interests.

ACKNOWLEDGMENT

The authors would like to acknowledge funding from the Natural Sciences and Engineering Research Council of Canada (NSERC), Fonds de la Recherche du Québec sur la Nature et les Technologies (FRQNT), Centre Québécois sur les Matériaux Fonctionnels (CQMF), and the Canada Research Chair program. S. Sun acknowledges the ECS-Toyota Young Investigator Fellowship. X.T. is grateful to the CSC scholarship.

REFERENCES

- (1) Dai, L.; Xue, Y.; Qu, L.; Choi, H. J.; Baek, J. B., Metal-free catalysts for oxygen reduction reaction. *Chem Rev* **2015**, 115, 4823-92.
- (2) Wang, D. W.; Su, D. S., Heterogeneous nanocarbon materials for oxygen reduction reaction. *Energy & Environmental Science* **2014**, 7, 576-591.
- (3) Wei, Q. L.; Tong, X.; Zhang, G. X.; Qiao, J. L.; Gong, Q. J.; Sun, S. H., Nitrogen-Doped Carbon Nanotube and Graphene Materials for Oxygen Reduction Reactions. *Catalysts* **2015**, 5, 1574-1602.
- (4) Wu, G.; Zelenay, P., Nanostructured nonprecious metal catalysts for oxygen reduction reaction. *Acc Chem Res* **2013**, 46, 1878-89.
- (5) Geng, D. S.; Ding, N.; Hor, T. S. A.; Liu, Z. L.; Sun, X. L.; Zong, Y., Potential of metal-free "graphene alloy" as electrocatalysts for oxygen reduction reaction. *Journal of Materials Chemistry A* **2015**, 3, 1795-1810.
- (6) Wang, J. M.; Hao, J.; Liu, D.; Qin, S.; Portehault, D.; Li, Y. W.; Chen, Y.; Lei, W. W., Porous Boron Carbon Nitride Nanosheets as Efficient Metal-Free Catalysts for the Oxygen Reduction Reaction in Both Alkaline and Acidic Solutions. *Acs Energy Letters* **2017**, 2, 306-312.
- (7) Pandey, R. P.; Shukla, G.; Manohar, M.; Shahi, V. K., Graphene oxide based nanohybrid proton exchange membranes for fuel cell applications: An overview. *Adv Colloid Interface Sci* **2017**, 240, 15-30.
- (8) Qiu, H. J.; Liu, L.; Wang, Y., Template-directed fabrication of 3D graphene-based composite and their electrochemical energy-related applications. *Science Bulletin* **2016**, 61, 443-450.
- (9) Choi, H. J.; Jung, S. M.; Seo, J. M.; Chang, D. W.; Dai, L. M.; Baek, J. B., Graphene for energy conversion and storage in fuel cells and supercapacitors. *Nano Energy* **2012**, 1, 534-551.

- (10) Zhou, X.; Qiao, J.; Yang, L.; Zhang, J., A Review of Graphene-Based Nanostructural Materials for Both Catalyst Supports and Metal-Free Catalysts in PEM Fuel Cell Oxygen Reduction Reactions. *Advanced Energy Materials* **2014**, *4*.
- (11) Xue, Y.; Wu, B.; Bao, Q.; Liu, Y., Controllable synthesis of doped graphene and its applications. *Small* **2014**, *10*, 2975-91.
- (12) Mao, J. J.; Iocozzia, J.; Huang, J. Y.; Meng, K.; Lai, Y. K.; Lin, Z. Q., Graphene aerogels for efficient energy storage and conversion. *Energy & Environmental Science* **2018**, *11*, 772-799.
- (13) Hu, H.; Xin, J. H.; Hu, H.; Wang, X.; Kong, Y., Metal-free graphene-based catalyst—Insight into the catalytic activity: A short review. *Applied Catalysis A: General* **2015**, *492*, 1-9.
- (14) Kong, X. K.; Chen, C. L.; Chen, Q. W., Doped graphene for metal-free catalysis. *Chem Soc Rev* **2014**, *43*, 2841-57.
- (15) Zhang, C.; Wang, X.; Liang, Q.; Liu, X.; Weng, Q.; Liu, J.; Yang, Y.; Dai, Z.; Ding, K.; Bando, Y.; Tang, J.; Golberg, D., Amorphous Phosphorus/Nitrogen-Doped Graphene Paper for Ultrastable Sodium-Ion Batteries. *Nano Lett* **2016**, *16*, 2054-60.
- (16) Lv, Y.; Wang, X.; Mei, T.; Li, J.; Wang, J., Single-Step Hydrothermal Synthesis of N, S-Dual-Doped Graphene Networks as Metal-Free Efficient Electrocatalysts for Oxygen Reduction Reaction. *ChemistrySelect* **2018**, *3*, 3241-3250.
- (17) Cong, H. P.; Chen, J. F.; Yu, S. H., Graphene-based macroscopic assemblies and architectures: an emerging material system. *Chem Soc Rev* **2014**, *43*, 7295-325.
- (18) Tong, X.; Wei, Q.; Zhan, X.; Zhang, G.; Sun, S., The New Graphene Family Materials: Synthesis and Applications in Oxygen Reduction Reaction. *Catalysts* **2017**, *7*, 1.
- (19) Li, X. M.; Rui, M. C.; Song, J. Z.; Shen, Z. H.; Zeng, H. B., Carbon and Graphene Quantum Dots for Optoelectronic and Energy Devices: A Review. *Advanced Functional Materials* **2015**, *25*, 4929-4947.
- (20) Zhang, Z. P.; Zhang, J.; Chen, N.; Qu, L. T., Graphene quantum dots: an emerging material for energy-related applications and beyond. *Energy & Environmental Science* **2012**, *5*, 8869-8890.
- (21) Fan, M. M.; Zhu, C. L.; Yang, J. Z.; Sun, D. P., Facile self-assembly N-doped graphene quantum dots/graphene for oxygen reduction reaction. *Electrochimica Acta* **2016**, *216*, 102-109.
- (22) Fei, H.; Ye, R.; Ye, G.; Gong, Y.; Peng, Z.; Fan, X.; Samuel, E. L.; Ajayan, P. M.; Tour, J. M., Boron- and nitrogen-doped graphene quantum dots/graphene hybrid nanoplatelets as efficient electrocatalysts for oxygen reduction. *ACS Nano* **2014**, *8*, 10837-43.
- (23) Zhou, X.; Tian, Z.; Li, J.; Ruan, H.; Ma, Y.; Yang, Z.; Qu, Y., Synergistically enhanced activity of graphene quantum dot/multi-walled carbon nanotube composites as metal-free catalysts for oxygen reduction reaction. *Nanoscale* **2014**, *6*, 2603-7.
- (24) Wang, M.; Fang, Z.; Zhang, K.; Fang, J.; Qin, F.; Zhang, Z.; Li, J.; Liu, Y.; Lai, Y., Synergistically enhanced activity of graphene quantum dots/graphene hydrogel composites: a novel all-carbon hybrid electrocatalyst for metal/air batteries. *Nanoscale* **2016**, *8*, 11398-402.
- (25) Jin, Z.; Nie, H.; Yang, Z.; Zhang, J.; Liu, Z.; Xu, X.; Huang, S., Metal-free selenium doped carbon nanotube/graphene networks as a synergistically improved cathode catalyst for oxygen reduction reaction. *Nanoscale* **2012**, *4*, 6455-60.
- (26) Wu, Z. S.; Yang, S.; Sun, Y.; Parvez, K.; Feng, X.; Mullen, K., 3D nitrogen-doped graphene aerogel-supported Fe₃O₄ nanoparticles as efficient electrocatalysts for the oxygen reduction reaction. *J Am Chem Soc* **2012**, *134*, 9082-5.

- (27) Fu, X. G.; Jin, J. T.; Liu, Y. R.; Liu, Q.; Niu, K. X.; Zhang, J. Y.; Cao, X. P., Graphene-xerogel-based non-precious metal catalyst for oxygen reduction reaction. *Electrochemistry Communications* **2013**, 28, 5-8.
- (28) Van Tam, T.; Kang, S. G.; Babu, K. F.; Oh, E.-S.; Lee, S. G.; Choi, W. M., Synthesis of B-doped graphene quantum dots as a metal-free electrocatalyst for the oxygen reduction reaction. *Journal of Materials Chemistry A* **2017**, 5, 10537-10543.
- (29) Chai, G. L.; Qiu, K. P.; Qiao, M.; Titirici, M. M.; Shang, C. X.; Guo, Z. X., Active sites engineering leads to exceptional ORR and OER bifunctionality in P,N Co-doped graphene frameworks. *Energy & Environmental Science* **2017**, 10, 1186-1195.
- (30) Tong, X.; Wang, H.; Wang, G.; Wan, L.; Ren, Z.; Bai, J.; Bai, J., Controllable synthesis of graphene sheets with different numbers of layers and effect of the number of graphene layers on the specific capacity of anode material in lithium-ion batteries. *Journal of Solid State Chemistry* **2011**, 184, 982-989.
- (31) Shao, Y.; Zhang, S.; Engelhard, M. H.; Li, G.; Shao, G.; Wang, Y.; Liu, J.; Aksay, I. A.; Lin, Y., Nitrogen-doped graphene and its electrochemical applications. *Journal of Materials Chemistry* **2010**, 20, 7491-7496.
- (32) Wen, Y.; Wang, B.; Huang, C.; Wang, L.; Hulicova-Jurcakova, D., Synthesis of phosphorus-doped graphene and its wide potential window in aqueous supercapacitors. *Chemistry* **2015**, 21, 80-5.
- (33) Shin, H.-S.; Kim, K. W.; Kang, Y.-g.; Myung, S.; Kim, J. S.; An, K.-S.; Lee, I. Y.; Lee, S. S., New approach for the reduction of graphene oxide with triphenylphosphine dihalide. *RSC Advances* **2016**, 6, 18809-18813.
- (34) Hendrickson, J.; Sommer, T.; Singer, M., *A Facile Approach to N-Unsubstituted Phosphinimines*. 1995; Vol. 1995, p 1496-1496.
- (35) Abel, E. W.; Mucklejohn, S. A., THE CHEMISTRY OF PHOSPHINIMINES. *Phosphorus and Sulfur and the Related Elements* **1981**, 9, 235-266.
- (36) Qu, D. Y., Studies of the activated carbons used in double-layer supercapacitors. *Journal of Power Sources* **2002**, 109, 403-411.
- (37) Zhu, Z. H.; Hatori, H.; Wang, S. B.; Lu, G. Q., Insights into hydrogen atom adsorption on and the electrochemical properties of nitrogen-substituted carbon materials. *J Phys Chem B* **2005**, 109, 16744-9.
- (38) Fu, G.; Yan, X.; Chen, Y.; Xu, L.; Sun, D.; Lee, J.-M.; Tang, Y., Boosting Bifunctional Oxygen Electrocatalysis with 3D Graphene Aerogel-Supported Ni/MnO Particles. *Advanced Materials* **2018**, 30, 1704609.

Supporting information for

N, P co-doped graphene dots on N-doped 3D graphene as metal free catalyst for oxygen reduction

Xin Tong,^{†,‡} Mohamed Cherif,[†] Gaixia Zhang^{†,*}, Jugang Ma,[§] Ali Almesrati,[†] Vidal François,[†] Yujun Song,[§] Jerome P. Claverie^{‡,*} and Shuhui Sun^{†,*}

[†] Institut National de la Recherche Scientifique-Énergie Matériaux et Télécommunications, Varennes, QC, Canada J3X 1S2.

[‡] School of Chemistry and Material Science, Guizhou Normal University, Guiyang, China, 55000

[§] School of Mathematics and Physics, University of Science & Technology Beijing, Beijing, China, 10008

[‡] Department of Chemistry, Université de Sherbrooke, Sherbrooke, QC, Canada J1K 2R1.

E-mail: gaixia.zhang@emt.inrs.ca (G.Z.) jerome.claverie@usherbrooke.ca (J.C.)
shuhui@emt.inrs.ca (S.S.)

Experimental

Preparation

GO sheets were prepared from natural graphite powder by a modified Hummers method. N, P-GDs/N-3DG was prepared by freeze-annealing approach. Briefly, 20 ml GO solution (10 mg/ml) was mixed with 1 g triphenylphosphine (Ph₃P)(dissolved in ether) by ultrasonic treatment for 2 h. The mixture was then transferred into syringe and was fixed to a syringe pump connected to the liquid nitrogen, which was stored in a thermal insulation container. Once the GO solution contacted with the liquid nitrogen, a small ball was formed and sink in the liquid nitrogen. The flow velocity was 1 ml min⁻¹. The GO balls were kept in the liquid nitrogen at least 30 min. The obtained composite hydrogel was freeze-dried for 1 day. After that, the hydrogel was annealed under ammonia at 950 °C for 10 min. For the production of 3DG, the GO balls without adding TPP were annealed under argon at 300 °C for 1 h. For the N-3DG, the GO balls without adding TPP were annealed ammonia at 950 °C for 10 min. For P-GDs/3DG, the GO balls with TPP were annealed under argon at 950 °C for 10 min.

Characterizations

The scanning electron microscope (SEM) images were determined by ULTRA 55 scanning electron microscope (SEM) at 200 K. Transmission electron microscopy (TEM) observations were conducted with JEM-2200FS, 200kV and Titan ETEM. X-ray photoelectron spectroscopy (XPS) was measured with a VG Escalab 220i-XL using Mg K α line as an excitation source. All the spectra were calibrated by placing C 1s principle peak at 284.6 eV.

Electrochemical characterizations

All electrochemical measurements were carried out in a three-electrode cell using a rotating disk electrode (RDE, PINE Research Instrumentation) with a bipotentiostat (Pine, Model PGSTAT-72637) workstation at room temperature. A Pt wire and a saturated calomel electrode (SCE) were used as the counter and reference electrodes, respectively. All potentials in this study refer to the reversible hydrogen electrode (RHE). A rotating ring-disk electrode (RRDE) with a Pt ring and a GC disk (5.61 mm diameter) were used as the substrates for the working electrodes. Before using, the tips of RRDE are polished using aqueous alumina suspension on felt polishing pads. The ink is prepared as follows, 10 mg of catalyst was mixed in a glass vial with 95 μl of 5 wt.% Nafion solution and 350 μl of ethanol, followed by sonication and agitation in a vortex mixer, alternatively, for 3 times. Then 9 μl of the catalyst suspension was dropped onto the GC electrode surface of RRDE (with loading of $\sim 800 \mu\text{g}/\text{cm}^2$).

In 0.1 M KOH, the cyclic voltammetry (CV) profiles were recorded at 50 mV s^{-1} and the linear sweep voltammograms (LSV) were recorded at 10 mV s^{-1} , between 0-1.2 V (vs. RHE). The peroxide yield ($\text{H}_2\text{O}_2\%$) and the electron transfer number (n) were calculated as Eqs (1) - (2):

$$\text{H}_2\text{O}_2\% = (200 \times I_r/N) / (I_d + I_r/N) \quad (1)$$

$$n = 4 \times I_d / (I_d + I_r/N) \quad (2)$$

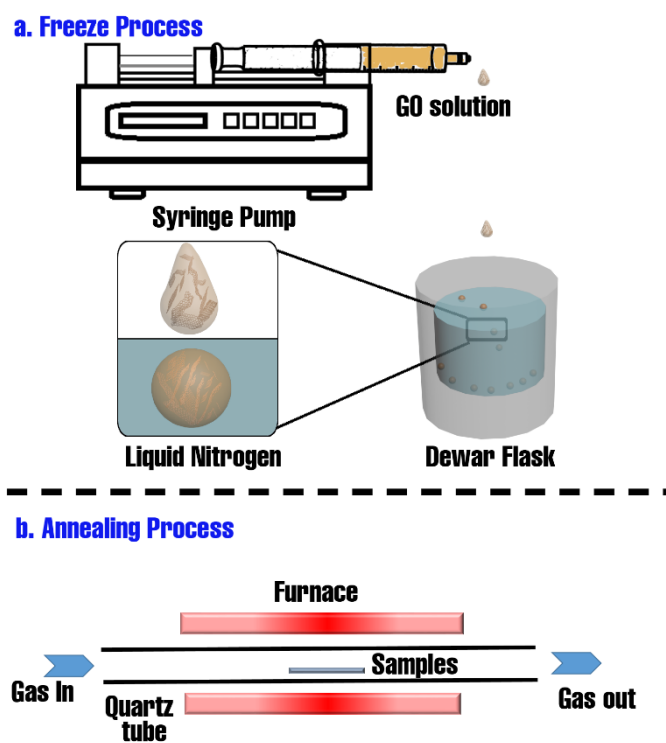
Where I_d is the disk current, I_r is the ring current, and N is the collection efficiency, equal to 0.37 for the present case.

Computational method

DFT calculations with periodic boundary conditions were performed by using VASP Software package and based on the Perdew-Burke-Ernzerhof (PBE) exchange-correlation functional within the generalized gradient approximation (GGA).

We start our DFT calculations by examining the stability of binary doping phosphorus and nitrogen into the graphene layer. Several configurations were chosen to check the possibility of adsorbing oxygen molecule. Head-on and side-on O_2 orientations take into account in this part of calculations. The binding energy was calculated for each selected position of O_2 .

Supplementary Figures



Scheme S1. Schematic Illustration of the Fabrication process and equipment of the N, P-graphene dots supporting on N-3D-graphene (N, P-GDs/N-3DG).

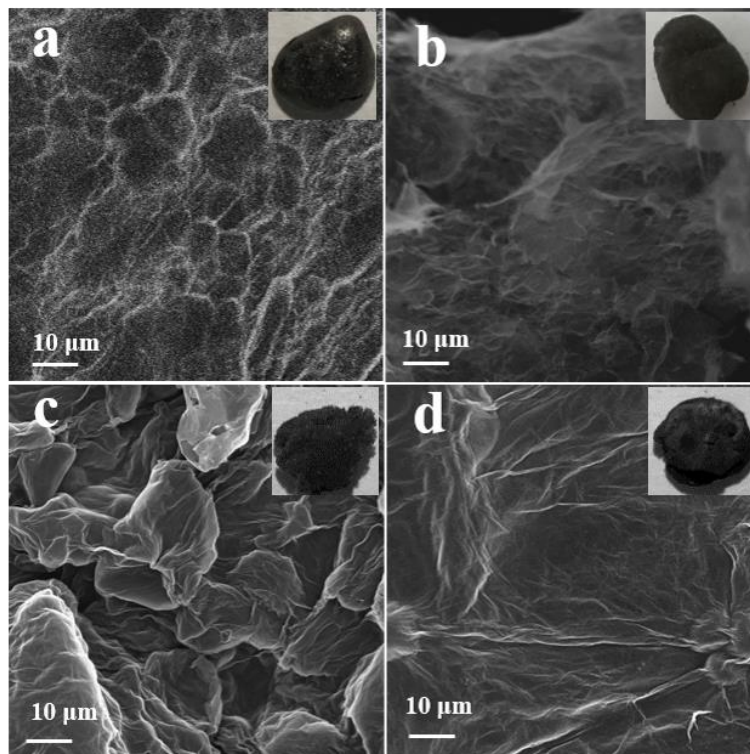


Figure S1. SEM images of (a) 3DG, (b) N-3DG, (c) P-GDs/3DG and (d) N, P-GDs/N-3DG. Inset: the corresponding photographs.

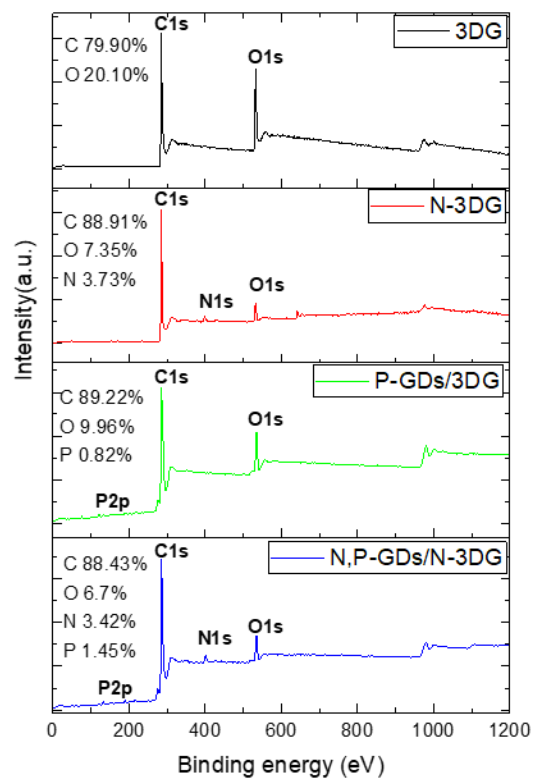


Figure S2. XPS survey spectra of 3D graphene, N-3DG, P-3DG, N, P-GDs/N-3DG.

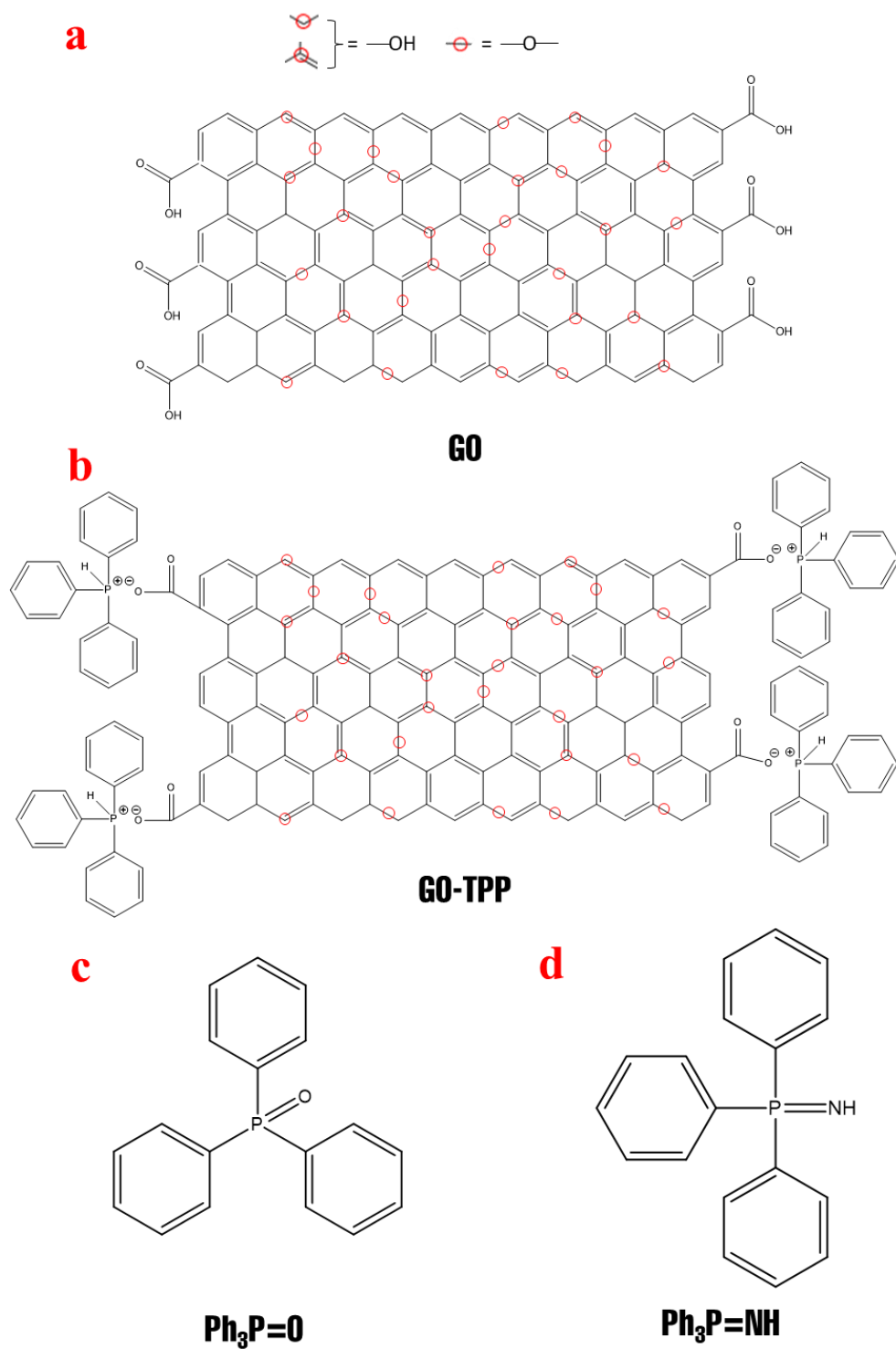


Figure S3. The molecular structure of (a)GO, (b)GO-TPP, (c)Ph₃P=O, and (d) Ph₃P=NH.

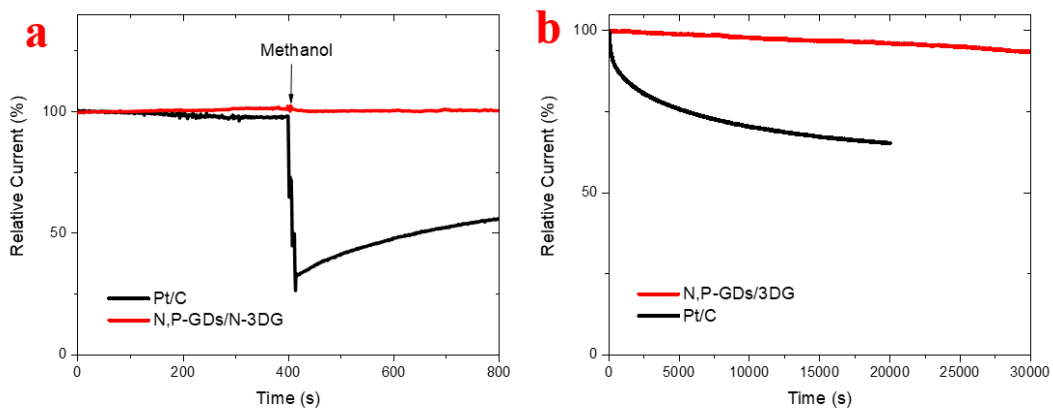


Figure S4. (a) Chronoamperometric responses of N, P-GDs/N-3DG and Pt/C in O₂-saturated 0.1 M KOH solution on addition of methanol to form 3 M methanol after 300 s at 0.8 V (vs.RHE) and a rotation speed of 1600 rpm. (b) Chronoamperometric curves of the N, P-GDs/N-3DG and Pt/C at 0.8v (vs. RHE) and a rotation speed of 1600 rpm.

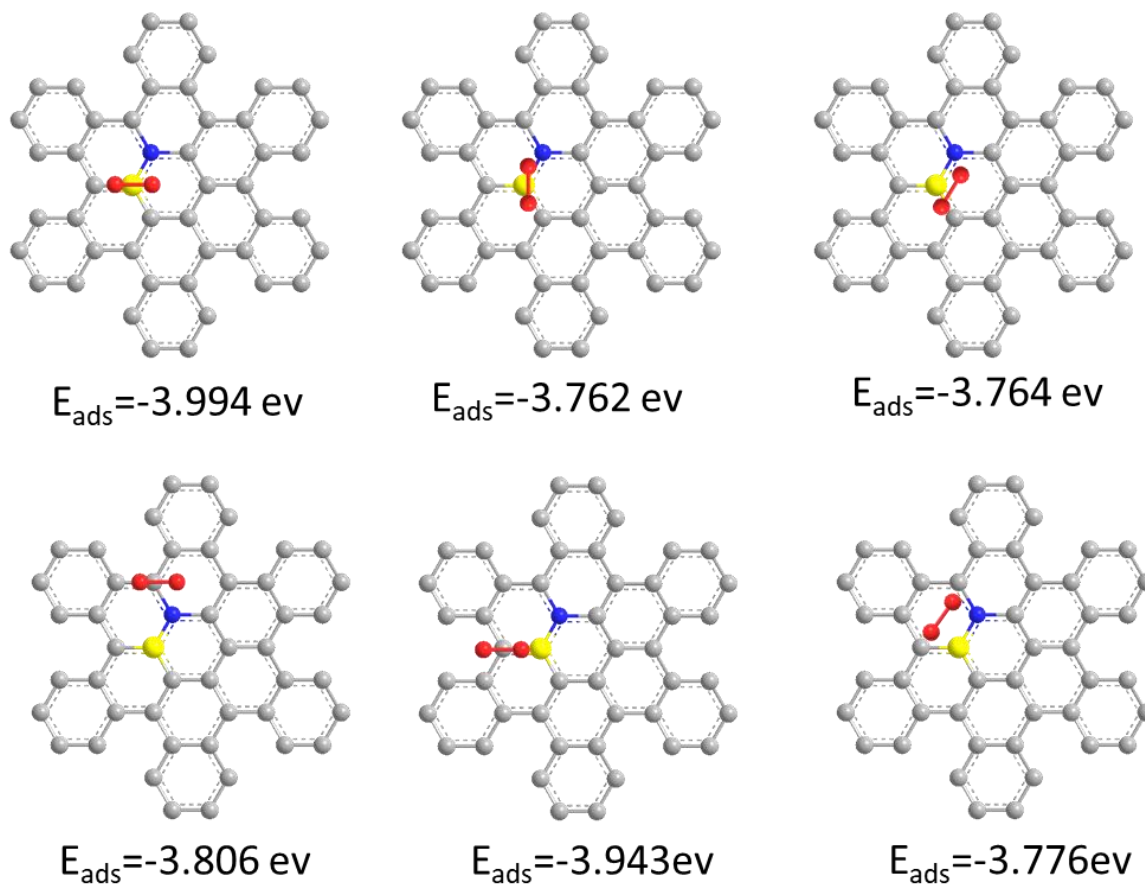


Figure S5. Different optimized structures of O₂ adsorption on P-N bond structure (side-on direction) in N, P-GDs/N-3DG.

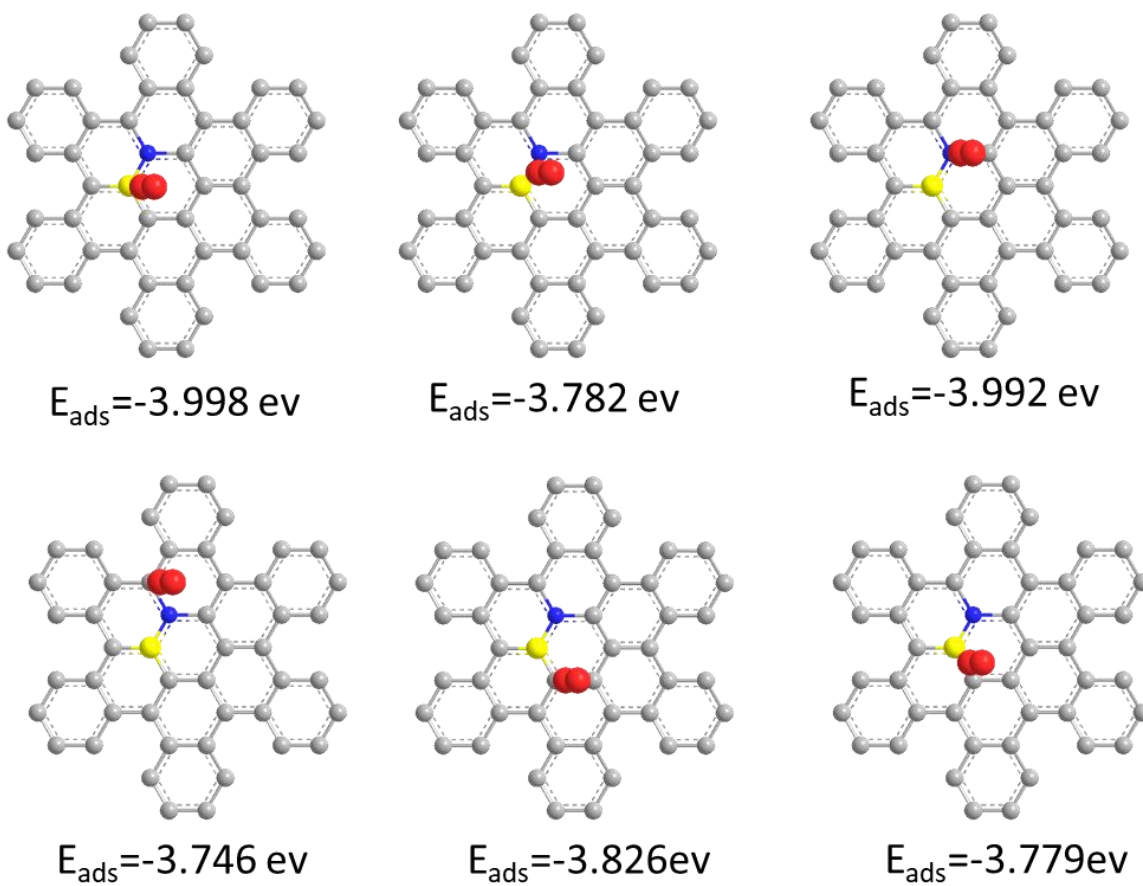


Figure S6. Different optimized structures of O₂ adsorption on P-N bond structure (head-on direction) in N, P-GDs/N-3DG.

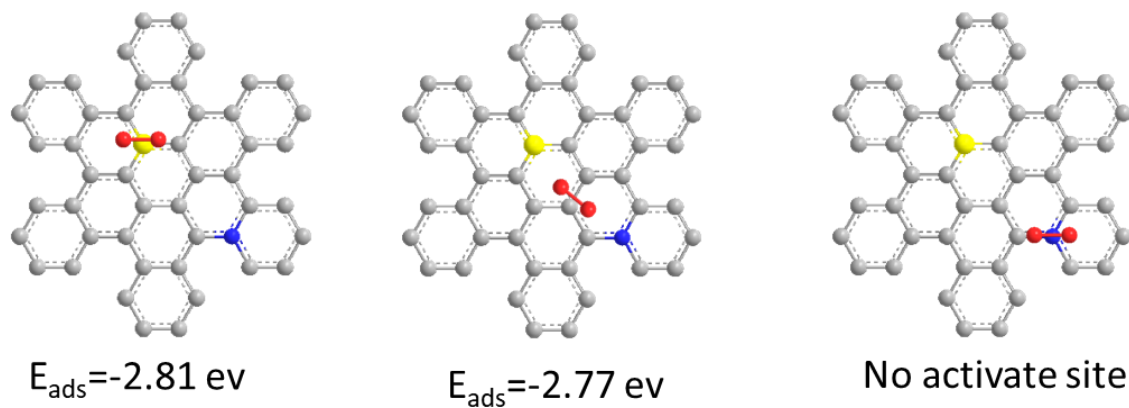


Figure S7. Different optimized structures of O_2 adsorption on P-C, N-C bond structure (side-on direction) in N, P-GDs/N-3DG.

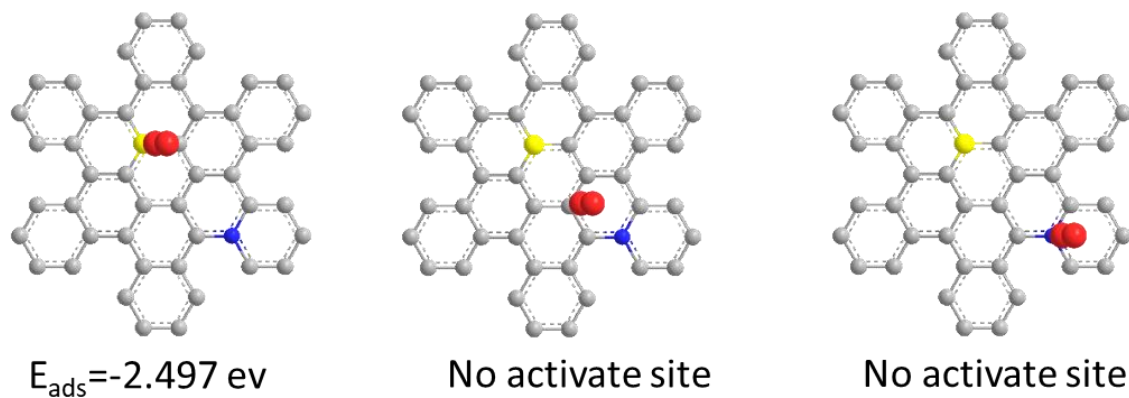


Figure S8. Different optimized structures of O_2 adsorption on P-C, N-C bond structure (head-on direction) in N, P-GDs/N-3DG.

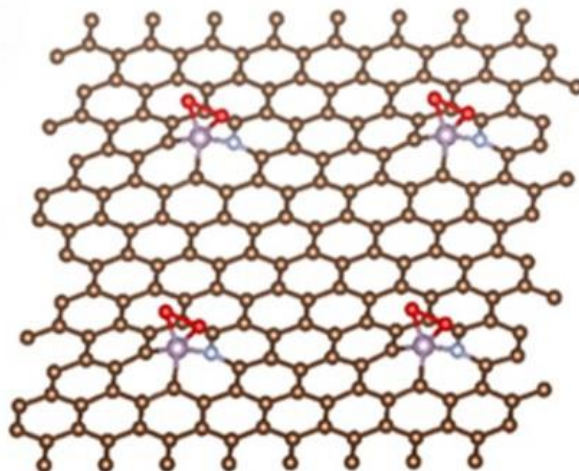


Figure S9. The most stable adsorption configurations of O₂ on P-N bond structure in N, P.

6 CONCLUSIONS AND PERSPECTIVES

6.1 Conclusions

Developing highly efficient electrocatalysts to facilitate the sluggish cathodic ORR is a key issue to commercial fuel cells. So far, Platinum (Pt) is still the most widely used ORR electrocatalysts. However, the high cost and inadequate long term operational stability of Pt/C catalysts inhibit most development of this technology. Therefore, the primary topic of this thesis is the development of Pt-based and graphene-based catalyst materials for oxygen reduction reaction (ORR). Three different materials including Pt/CNTs@C, Pt/doped graphene, and graphene-based metal-free catalyst are synthesized and investigated as ORR catalysts.

Firstly, the Pt/CNTs@C nanostructures were synthesized via an *in situ* polymer nano-encapsulation method, followed by a graphitization process. Pt NPs were first synthesized on the surface of the CNTs through the reduction of H_2PtCl_6 by HCOOH . After adsorption of the PABA RAFT dispersant via non-covalent interactions, an *in situ* growth of polymer chain occurs at the Pt/CNT surface via RAFT polymerization. Then the polymer layer was carbonized into a graphitic carbon shell by annealing at 550 °C under N_2 atmosphere. The thickness of the carbon coating shell can be precisely controlled by tuning the amount of added monomer. The thickness of the disordered graphitic carbon layer plays a key role to control the electrocatalytic performance. For too thick carbon shells, the oxygen molecules have to overcome a high barrier to reach the surface of the catalyst. In this case, the carbon layer mainly works as an obstacle for ORR, leading to a low activity of the catalyst. It is demonstrated that the carbon shells of ~0.8 nm in average thickness (Pt/CNTs@C-2) is permeable to oxygen molecules without hindering the mass transport of molecular oxygen and the contact between oxygen and the catalyst surface. In addition, such carbon coating is sufficiently thick to prevent Pt NP dissolution or detachment from the CNT surface. Remarkably, after 20000 cycles ADT, the remaining ECSA of the Pt/CNTs@C sample with 0.8 nm thick carbon shell is comparable to the initial Pt/CNTs before ADT cycling, demonstrating that proper carbon coating can significantly improve the stability of the Pt-based catalysts. Furthermore, the carbon shells can reduce the adsorption of methanol on the Pt surface, i.e. high methanol tolerance.

Compared with CNTs, the heteroatoms can be more easily introduced into the graphene due to the more open structure of graphene. Therefore, three different kinds of graphene were used as supporting material and the supporting effect is discussed. Firstly, GO was obtained through the modified Hummers' oxidation process. Then the doped graphene was got by a wet chemical method. Pt catalyst was then loaded on graphene material (include RGO, N-Graphene, and N, P-Graphene) by traditional wet impregnation method followed by annealing under 450 °C. it was revealed in this part that the surface chemistry of the graphene

supports significantly affect the deposition behavior of Pt atoms. A few large Pt are found in Pt/RGO, while small Pt particles are homogeneously dispersed on N-Graphene. For Pt N, P-Graphene, there are small clusters with enhanced utilization efficiency. Furthermore, the doped atoms on the surface can also influence the valence electrons of Pt. Accordingly, the supporting material will play a vital role in the activity and stability of Pt for ORR. The Pt/N, P-graphene showed high activity, low Tafel slope, dominant 4-electron ORR pathway with low H₂O₂ yield and excellent durability because of the stronger interaction of the Pt atoms with the doped atoms.

Based on that, the doped graphene was further developed as the metal-free catalyst. A facile one-step and scalable freeze-annealing method were used for the synthesis of N, P-graphene dots supported on N-3D-graphene (N, P-GDs/N-3DG). Firstly, triphenylphosphine (TPP) were mixed with GO to form graphene oxide hydrogel. By immersing the hydrogel into liquid nitrogen followed by freeze-drying, the aggregation was prevented and the 3D network structure was maintained. The *in situ* synthesized N, P-GDs were uniformly distributed on the surface of N-3DG. The GDs in the composite can offer more catalytically active sites while the N-3DG not only acts as an excellent conductive substrate for electrons but also ensure the efficient mass transport of oxygen molecule and electrolyte during the ORR process. In addition, N, P-doping can effectively tailor their intrinsic electrical characteristics and surface properties. The metal-free N, P-GDs/N-3DG composite exhibits an improved ORR performance in comparison to the samples with single-doping, without doping or even to the commercial Pt/C catalyst. This enhanced electrocatalytic performance can be ascribed to the synergetic effect of abundant functional groups and the edge defects. This study indicates that P-N bonded structures play an important role as active sites in ORR.

6.2 Perspectives

Based on the results achieved so far, the future work of ORR catalyst can be focused on:

(i) Metal-free heteroatoms doped 3DG catalyst

Based on our results, N, P-GDs/N-3DG shows enhanced synergistic activity towards ORR. The GDs can offer more catalytically active sites while the N-3DG acts as an excellent substrate ensuring the efficient electrons and mass transport. Therefore, we plan to co-dope 3DG with different heteroatoms, such as B or S, to further improve its catalytic activity. Based that, the role of heteroatoms-doping and the relationship between doping effects and active mechanism will be studied.

(ii) Pt alloy NPs supported on heteroatoms doped 3DG catalyst

The doped 3DG is an excellent supporting material allowing uniform and high loading of catalysts, not only providing a large supporting surface area but also alleviating the commonly encountered problem of

nanomaterial aggregation in nanoscience. Based on the above research, we plan to synthesize Pt alloy NPs supported on heteroatoms doped 3DG catalyst. The introduction of an additional transition metal into Pt-based alloys might produce a modification in the Pt electronic structure due to electron transfer from the transition metal to Pt and it likely causes lattice contraction. Then the effect of different metals in Pt-*M* alloys will be discussed in order to get insight of the mechanism of ORR on Pt alloy NPs.

(iii) Pt alloy NPs supported on heteroatoms doped 3DG catalyst encapsulated within carbon layers

The polymeric nanoencapsulation strategy is a promising and universal technique for the production of highly active and stable ORR catalysts for fuel cells and metal-air batteries. To enhance its durability and methanol tolerance performance, all the above optimized samples will be precisely covered with carbon layer. Then it will be employed as the cathode catalysts in the real membrane electrode assembly for PEM fuel cells. These studies are supposed to be useful in energy conversion/storage and many other related fields.

7 BIBLIOGRAPHY

- (1) Winter, M.; Brodd, R. J., What Are Batteries, Fuel Cells, and Supercapacitors? *Chemical Reviews* **2004**, 104, 4245-4270.
- (2) Debe, M. K., Electrocatalyst approaches and challenges for automotive fuel cells. *Nature* **2012**, 486, 43.
- (3) Wang, Y.-J.; Zhao, N.; Fang, B.; Li, H.; Bi, X. T.; Wang, H., Carbon-Supported Pt-Based Alloy Electrocatalysts for the Oxygen Reduction Reaction in Polymer Electrolyte Membrane Fuel Cells: Particle Size, Shape, and Composition Manipulation and Their Impact to Activity. *Chemical Reviews* **2015**, 115, 3433-3467.
- (4) Larminie, J.; Dicks, A.; McDonald, M. S., *Fuel cell systems explained*. J. Wiley Chichester, UK: 2003; Vol. 2.
- (5) Borup, R.; Meyers, J.; Pivovar, B.; Kim, Y. S.; Mukundan, R.; Garland, N.; Myers, D.; Wilson, M.; Garzon, F.; Wood, D.; Zelenay, P.; More, K.; Stroh, K.; Zawodzinski, T.; Boncella, J.; McGrath, J. E.; Inaba, M.; Miyatake, K.; Hori, M.; Ota, K.; Ogumi, Z.; Miyata, S.; Nishikata, A.; Siroma, Z.; Uchimoto, Y.; Yasuda, K.; Kimijima, K. I.; Iwashita, N., Scientific aspects of polymer electrolyte fuel cell durability and degradation. *Chemical Reviews* **2007**, 107, 3904-3951.
- (6) Wang, Y.; Chen, K. S.; Mishler, J.; Cho, S. C.; Adroher, X. C., A review of polymer electrolyte membrane fuel cells: Technology, applications, and needs on fundamental research. *Applied Energy* **2011**, 88, 981-1007.
- (7) Zhang, J.; Tang, Y.; Song, C.; Zhang, J.; Wang, H., PEM fuel cell open circuit voltage (OCV) in the temperature range of 23°C to 120°C. *Journal of Power Sources* **2006**, 163, 532-537.
- (8) Lefevre, M.; Proietti, E.; Jaouen, F.; Dodelet, J. P., Iron-based catalysts with improved oxygen reduction activity in polymer electrolyte fuel cells. *Science* **2009**, 324, 71-4.
- (9) Proietti, E.; Jaouen, F.; Lefevre, M.; Larouche, N.; Tian, J.; Herranz, J.; Dodelet, J. P., Iron-based cathode catalyst with enhanced power density in polymer electrolyte membrane fuel cells. *Nature Communications* **2011**, 2, 416.
- (10) Vaghari, H.; Jafarizadeh-Malmiri, H.; Berenjian, A.; Anarjan, N., Recent advances in application of chitosan in fuel cells. *Sustainable Chemical Processes* **2013**, 1, 16.
- (11) Gewirth, A. A.; Varnell, J. A.; DiAscro, A. M., Nonprecious Metal Catalysts for Oxygen Reduction in Heterogeneous Aqueous Systems. *Chemical Reviews* **2018**, 118, 2313-2339.
- (12) O'hayre, R.; Cha, S.-W.; Prinz, F. B.; Colella, W., *Fuel cell fundamentals*. John Wiley & Sons: 2016.
- (13) Xia, W.; Mahmood, A.; Liang, Z.; Zou, R.; Guo, S., Earth-Abundant Nanomaterials for Oxygen Reduction. *Angew Chem Int Ed Engl* **2016**, 55, 2650-76.
- (14) Kulkarni, A.; Siahrostami, S.; Patel, A.; Nørskov, J. K., Understanding Catalytic Activity Trends in the Oxygen Reduction Reaction. *Chemical Reviews* **2018**, 118, 2302-2312.
- (15) Zhou, R. F.; Zheng, Y.; Jaroniec, M.; Qiao, S. Z., Determination of the Electron Transfer Number for the Oxygen Reduction Reaction: From Theory to Experiment. *Acs Catalysis* **2016**, 6, 4720-4728.
- (16) Wroblowa, H. S.; Yen Chi, P.; Razumney, G., Electroreduction of oxygen: A new mechanistic criterion. *Journal of Electroanalytical Chemistry and Interfacial Electrochemistry* **1976**, 69, 195-201.

- (17) Chen, S.; Kucernak, A., Electrocatalysis under Conditions of High Mass Transport Rate: Oxygen Reduction on Single Submicrometer-Sized Pt Particles Supported on Carbon. *The Journal of Physical Chemistry B* **2004**, 108, 3262-3276.
- (18) Keith, J. A.; Jerkiewicz, G.; Jacob, T., Theoretical Investigations of the Oxygen Reduction Reaction on Pt(111) . *ChemPhysChem* **2010**, 11, 2779-2794.
- (19) He, Q.; Cairns, E. J., Review—Recent Progress in Electrocatalysts for Oxygen Reduction Suitable for Alkaline Anion Exchange Membrane Fuel Cells. *Journal of The Electrochemical Society* **2015**, 162, F1504-F1539.
- (20) Sui, S.; Wang, X. Y.; Zhou, X. T.; Su, Y. H.; Riffatc, S.; Liu, C. J., A comprehensive review of Pt electrocatalysts for the oxygen reduction reaction: Nanostructure, activity, mechanism and carbon support in PEM fuel cells. *Journal of Materials Chemistry A* **2017**, 5, 1808-1825.
- (21) Markiewicz, M.; Zalitis, C.; Kucernak, A., Performance measurements and modelling of the ORR on fuel cell electrocatalysts – the modified double trap model. *Electrochimica Acta* **2015**, 179, 126-136.
- (22) Nørskov, J. K.; Rossmeisl, J.; Logadottir, A.; Lindqvist, L.; Kitchin, J. R.; Bligaard, T.; Jónsson, H., Origin of the Overpotential for Oxygen Reduction at a Fuel-Cell Cathode. *The Journal of Physical Chemistry B* **2004**, 108, 17886-17892.
- (23) Greeley, J.; Markovic, N. M., The road from animal electricity to green energy: combining experiment and theory in electrocatalysis. *Energy & Environmental Science* **2012**, 5, 9246-9256.
- (24) Lim, D.-H.; Wilcox, J., Mechanisms of the Oxygen Reduction Reaction on Defective Graphene-Supported Pt Nanoparticles from First-Principles. *The Journal of Physical Chemistry C* **2012**, 116, 3653-3660.
- (25) Yu, L.; Pan, X.; Cao, X.; Hu, P.; Bao, X., Oxygen reduction reaction mechanism on nitrogen-doped graphene: A density functional theory study. *Journal of Catalysis* **2011**, 282, 183-190.
- (26) Cheng, F.; Chen, J., Metal–air batteries: from oxygen reduction electrochemistry to cathode catalysts. *Chemical Society Reviews* **2012**, 41, 2172-2192.
- (27) Ramaswamy, N.; Mukerjee, S., Fundamental mechanistic understanding of electrocatalysis of oxygen reduction on Pt and non-Pt surfaces: acid versus alkaline media. *Advances in Physical Chemistry* **2012**, 2012.
- (28) Ramaswamy, N.; Mukerjee, S., Influence of inner-and outer-sphere electron transfer mechanisms during electrocatalysis of oxygen reduction in alkaline media. *The Journal of Physical Chemistry C* **2011**, 115, 18015-18026.
- (29) Ramaswamy, N.; Tylus, U.; Jia, Q.; Mukerjee, S., Activity Descriptor Identification for Oxygen Reduction on Nonprecious Electrocatalysts: Linking Surface Science to Coordination Chemistry. *Journal of the American Chemical Society* **2013**, 135, 15443-15449.
- (30) Strmcnik, D.; Kodama, K.; van der Vliet, D.; Greeley, J.; Stamenkovic, V. R.; Marković, N. M., The role of non-covalent interactions in electrocatalytic fuel-cell reactions on platinum. *Nature Chemistry* **2009**, 1, 466.
- (31) Singh, S. K.; Takeyasu, K.; Nakamura, J., Active Sites and Mechanism of Oxygen Reduction Reaction Electrocatalysis on Nitrogen-Doped Carbon Materials. *Advanced Materials* **2019**, 31, 1804297.
- (32) Seh, Z. W.; Kibsgaard, J.; Dickens, C. F.; Chorkendorff, I.; Nørskov, J. K.; Jaramillo, T. F., Combining theory and experiment in electrocatalysis: Insights into materials design. *Science* **2017**, 355, eaad4998.

- (33) Wilson, M. S.; Gottesfeld, S., Thin-film catalyst layers for polymer electrolyte fuel cell electrodes. *Journal of applied electrochemistry* **1992**, *22*, 1-7.
- (34) Han, S.; Wu, D.; Li, S.; Zhang, F.; Feng, X., Porous graphene materials for advanced electrochemical energy storage and conversion devices. *Adv Mater* **2014**, *26*, 849-64.
- (35) Wang, X.; Sun, G.; Chen, P., Three-Dimensional Porous Architectures of Carbon Nanotubes and Graphene Sheets for Energy Applications. *Frontiers in Energy Research* **2014**, *2*.
- (36) Song, Z. X.; Cheng, N. C.; Lushington, A.; Sun, X. L., Recent Progress on MOF-Derived Nanomaterials as Advanced Electrocatalysts in Fuel Cells. *Catalysts* **2016**, *6*, 116.
- (37) Pandey, R. P.; Shukla, G.; Manohar, M.; Shahi, V. K., Graphene oxide based nanohybrid proton exchange membranes for fuel cell applications: An overview. *Adv Colloid Interface Sci* **2017**, *240*, 15-30.
- (38) Chen, Z.; Higgins, D.; Yu, A.; Zhang, L.; Zhang, J., A review on non-precious metal electrocatalysts for PEM fuel cells. *Energy & Environmental Science* **2011**, *4*, 3167-3192.
- (39) Stacy, J.; Regmi, Y. N.; Leonard, B.; Fan, M., The recent progress and future of oxygen reduction reaction catalysis: A review. *Renewable and Sustainable Energy Reviews* **2017**, *69*, 401-414.
- (40) Liu, D.; Tao, L.; Yan, D.; Zou, Y.; Wang, S., Recent Advances on Non-precious Metal Porous Carbon-based Electrocatalysts for Oxygen Reduction Reaction. *ChemElectroChem* **2018**, *5*, 1775-1785.
- (41) Xia, Z.; An, L.; Chen, P.; Xia, D., Non-Pt Nanostructured Catalysts for Oxygen Reduction Reaction: Synthesis, Catalytic Activity and its Key Factors. *Advanced Energy Materials* **2016**, *6*, 1600458.
- (42) Tse, E. C. M.; Varnell, J. A.; Hoang, T. T. H.; Gewirth, A. A., Elucidating Proton Involvement in the Rate-Determining Step for Pt/Pd-Based and Non-Precious-Metal Oxygen Reduction Reaction Catalysts Using the Kinetic Isotope Effect. *The Journal of Physical Chemistry Letters* **2016**, *7*, 3542-3547.
- (43) Liu, J.; Li, E.; Ruan, M.; Song, P.; Xu, W., Recent Progress on Fe/N/C Electrocatalysts for the Oxygen Reduction Reaction in Fuel Cells. *Catalysts* **2015**, *5*, 1167-1192.
- (44) Van Veen, J. A. R.; Colijn, H. A.; Van Baar, J. F., On the effect of a heat treatment on the structure of carbon-supported metalloporphyrins and phthalocyanines. *Electrochimica Acta* **1988**, *33*, 801-804.
- (45) Scherson, D. A.; Gupta, S. L.; Fierro, C.; Yeager, E. B.; Kordesch, M. E.; Eldridge, J.; Hoffman, R. W.; Blue, J., Cobalt tetramethoxyphenyl porphyrin—emission Mossbauer spectroscopy and O₂ reduction electrochemical studies. *Electrochimica Acta* **1983**, *28*, 1205-1209.
- (46) Scherson, D.; Tanaka, A. A.; Gupta, S. L.; Tryk, D.; Fierro, C.; Holze, R.; Yeager, E. B.; Lattimer, R. P., Transition metal macrocycles supported on high area carbon: Pyrolysis—mass spectrometry studies. *Electrochimica Acta* **1986**, *31*, 1247-1258.
- (47) Dodelet, J.-P., Oxygen reduction in PEM fuel cell conditions: heat-treated non-precious metal-N 4 macrocycles and beyond. In *N4-Macrocyclic Metal Complexes*, Springer: 2006; pp 83-147.
- (48) Dai, L., Carbon-based catalysts for metal-free electrocatalysis. *Current Opinion in Electrochemistry* **2017**, *4*, 18-25.
- (49) Gao, K.; Wang, B.; Tao, L.; Cunning, B. V.; Zhang, Z.; Wang, S.; Ruoff, R. S.; Qu, L., Efficient Metal-Free Electrocatalysts from N-Doped Carbon Nanomaterials: Mono-Doping and Co-Doping. *Advanced Materials* **2018**, *31*, 1805121.
- (50) Huang, C. C.; Li, C.; Shi, G. Q., Graphene based catalysts. *Energy & Environmental Science* **2012**, *5*, 8848-8868.

- (51) Paraknowitsch, J. P.; Thomas, A., Doping carbons beyond nitrogen: an overview of advanced heteroatom doped carbons with boron, sulphur and phosphorus for energy applications. *Energy & Environmental Science* **2013**, 6, 2839-2855.
- (52) Kong, X. K.; Chen, C. L.; Chen, Q. W., Doped graphene for metal-free catalysis. *Chem Soc Rev* **2014**, 43, 2841-57.
- (53) Rao, C. N. R.; Gopalakrishnan, K.; Govindaraj, A., Synthesis, properties and applications of graphene doped with boron, nitrogen and other elements. *Nano Today* **2014**, 9, 324-343.
- (54) Wang, D. W.; Su, D. S., Heterogeneous nanocarbon materials for oxygen reduction reaction. *Energy & Environmental Science* **2014**, 7, 576-591.
- (55) Liu, X.; Dai, L. M., Carbon-based metal-free catalysts. *Nature Reviews Materials* **2016**, 1, 16064.
- (56) Jin, H.; Guo, C.; Liu, X.; Liu, J.; Vasileff, A.; Jiao, Y.; Zheng, Y.; Qiao, S. Z., Emerging Two-Dimensional Nanomaterials for Electrocatalysis. *Chem Rev* **2018**, 118, 6337-6408.
- (57) Zhao, S.; Wang, D. W.; Amal, R.; Dai, L., Carbon-Based Metal-Free Catalysts for Key Reactions Involved in Energy Conversion and Storage. *Adv Mater* **2019**, 31, e1801526.
- (58) Hu, C.; Dai, L., Carbon-Based Metal-Free Catalysts for Electrocatalysis beyond the ORR. *Angewandte Chemie International Edition* **2016**, 55, 11736-11758.
- (59) Xiong, D.; Li, X.; Fan, L.; Bai, Z., Three-Dimensional Heteroatom-Doped Nanocarbon for Metal-Free Oxygen Reduction Electrocatalysis: A Review. *Catalysts* **2018**, 8, 301.
- (60) Wu, G.; Santandreu, A.; Kellogg, W.; Gupta, S.; Ogoke, O.; Zhang, H. G.; Wang, H. L.; Dai, L. M., Carbon nanocomposite catalysts for oxygen reduction and evolution reactions: From nitrogen doping to transition-metal addition. *Nano Energy* **2016**, 29, 83-110.
- (61) Shin, D.; Jeong, B.; Choun, M.; Ocon, J. D.; Lee, J., Diagnosis of the measurement inconsistencies of carbon-based electrocatalysts for the oxygen reduction reaction in alkaline media. *RSC Advances* **2015**, 5, 1571-1580.
- (62) Choi, H. J.; Jung, S. M.; Seo, J. M.; Chang, D. W.; Dai, L. M.; Baek, J. B., Graphene for energy conversion and storage in fuel cells and supercapacitors. *Nano Energy* **2012**, 1, 534-551.
- (63) Wang, S.; Iyyamperumal, E.; Roy, A.; Xue, Y.; Yu, D.; Dai, L., Vertically Aligned BCN Nanotubes as Efficient Metal-Free Electrocatalysts for the Oxygen Reduction Reaction: A Synergetic Effect by Co-Doping with Boron and Nitrogen. *Angewandte Chemie International Edition* **2011**, 50, 11756-11760.
- (64) Liang, J.; Jiao, Y.; Jaroniec, M.; Qiao, S. Z., Sulfur and nitrogen dual-doped mesoporous graphene electrocatalyst for oxygen reduction with synergistically enhanced performance. *Angew Chem Int Ed Engl* **2012**, 51, 11496-500.
- (65) Chai, G. L.; Qiu, K. P.; Qiao, M.; Titirici, M. M.; Shang, C. X.; Guo, Z. X., Active sites engineering leads to exceptional ORR and OER bifunctionality in P,N Co-doped graphene frameworks. *Energy & Environmental Science* **2017**, 10, 1186-1195.
- (66) Wang, S.; Yu, D.; Dai, L., Polyelectrolyte Functionalized Carbon Nanotubes as Efficient Metal-free Electrocatalysts for Oxygen Reduction. *Journal of the American Chemical Society* **2011**, 133, 5182-5185.
- (67) Gong, K.; Du, F.; Xia, Z.; Durstock, M.; Dai, L., Nitrogen-Doped Carbon Nanotube Arrays with High Electrocatalytic Activity for Oxygen Reduction. *Science* **2009**, 323, 760-764.
- (68) Shao, Y. Y.; Yin, G. P.; Gao, Y. Z., Understanding and approaches for the durability issues of Pt-based catalysts for PEM fuel cell. *Journal of Power Sources* **2007**, 171, 558-566.

- (69) Meier, J. C.; Galeano, C.; Katsounaros, I.; Witte, J.; Bongard, H. J.; Topalov, A. A.; Baldizzone, C.; Mezzavilla, S.; Schüth, F.; Mayrhofer, K. J., Design criteria for stable Pt/C fuel cell catalysts. *Beilstein journal of nanotechnology* **2014**, *5*, 44-67.
- (70) Asset, T.; Chattot, R.; Fontana, M.; Mercier-Guyon, B.; Job, N.; Dubau, L.; Maillard, F., A Review on Recent Developments and Prospects for the Oxygen Reduction Reaction on Hollow Pt-alloy Nanoparticles. *ChemPhysChem* **2018**, *19*, 1552-1567.
- (71) Zhu, C.; Fu, S.; Shi, Q.; Du, D.; Lin, Y., Single-Atom Electrocatalysts. *Angew Chem Int Ed Engl* **2017**, *56*, 13944-13960.
- (72) Chen, Y. J.; Ji, S. F.; Chen, C.; Peng, Q.; Wang, D. S.; Li, Y. D., Single-Atom Catalysts: Synthetic Strategies and Electrochemical Applications. *Joule* **2018**, *2*, 1242-1264.
- (73) Kim, J.; Kim, H.-E.; Lee, H., Single-Atom Catalysts of Precious Metals for Electrochemical Reactions. *ChemSusChem* **2018**, *11*, 104-113.
- (74) Kulkarni, A.; Siahrostami, S.; Patel, A.; Norskov, J. K., Understanding Catalytic Activity Trends in the Oxygen Reduction Reaction. *Chem Rev* **2018**, *118*, 2302-2312.
- (75) Nie, Y.; Li, L.; Wei, Z., Recent advancements in Pt and Pt-free catalysts for oxygen reduction reaction. *Chemical Society Reviews* **2015**, *44*, 2168-2201.
- (76) Zhang, C.; Shen, X.; Pan, Y.; Peng, Z., A review of Pt-based electrocatalysts for oxygen reduction reaction. *Frontiers in Energy* **2017**, *11*, 268-285.
- (77) Xia, W.; Mahmood, A.; Liang, Z.; Zou, R.; Guo, S., Earth-Abundant Nanomaterials for Oxygen Reduction. *Angewandte Chemie International Edition* **2016**, *55*, 2650-2676.
- (78) Tian, N.; Zhou, Z.-Y.; Sun, S.-G.; Ding, Y.; Wang, Z. L., Synthesis of tetrahedral platinum nanocrystals with high-index facets and high electro-oxidation activity. *Science* **2007**, *316*, 732-735.
- (79) Shao, M.; Chang, Q.; Dodelet, J. P.; Chenitz, R., Recent Advances in Electrocatalysts for Oxygen Reduction Reaction. *Chem Rev* **2016**, *116*, 3594-657.
- (80) Shao, M.; Peles, A.; Shoemaker, K., Electrocatalysis on Platinum Nanoparticles: Particle Size Effect on Oxygen Reduction Reaction Activity. *Nano Letters* **2011**, *11*, 3714-3719.
- (81) Kinoshita, K., Particle size effects for oxygen reduction on highly dispersed platinum in acid electrolytes. *Journal of The Electrochemical Society* **1990**, *137*, 845-848.
- (82) Stamenkovic, V.; Mun, B. S.; Mayrhofer, K. J.; Ross, P. N.; Markovic, N. M.; Rossmeisl, J.; Greeley, J.; Nørskov, J. K., Changing the activity of electrocatalysts for oxygen reduction by tuning the surface electronic structure. *Angewandte Chemie International Edition* **2006**, *45*, 2897-2901.
- (83) Yano, H.; Inukai, J.; Uchida, H.; Watanabe, M.; Babu, P. K.; Kobayashi, T.; Chung, J. H.; Oldfield, E.; Wieckowski, A., Particle-size effect of nanoscale platinum catalysts in oxygen reduction reaction: an electrochemical and 195 Pt EC-NMR study. *Physical Chemistry Chemical Physics* **2006**, *8*, 4932-4939.
- (84) Li, D.; Wang, C.; Strmcnik, D. S.; Tripkovic, D. V.; Sun, X.; Kang, Y.; Chi, M.; Snyder, J. D.; van der Vliet, D.; Tsai, Y., Functional links between Pt single crystal morphology and nanoparticles with different size and shape: the oxygen reduction reaction case. *Energy & Environmental Science* **2014**, *7*, 4061-4069.
- (85) Zhang, L.; Wang, Y.; Niu, Z.; Chen, J., Single Atoms on Graphene for Energy Storage and Conversion. *Small Methods* **0**, 1800443.
- (86) Kim, J.; Kim, H. E.; Lee, H., Single-Atom Catalysts of Precious Metals for Electrochemical Reactions. *ChemSusChem* **2018**, *11*, 104-113.

- (87) Peng, Y.; Lu, B.; Chen, S., Carbon-Supported Single Atom Catalysts for Electrochemical Energy Conversion and Storage. *Adv Mater* **2018**, 30, e1801995.
- (88) Su, J. W.; Ge, R. X.; Dong, Y.; Hao, F.; Chen, L., Recent progress in single-atom electrocatalysts: concept, synthesis, and applications in clean energy conversion. *Journal of Materials Chemistry A* **2018**, 6, 14025-14042.
- (89) Choi, C. H.; Kim, M.; Kwon, H. C.; Cho, S. J.; Yun, S.; Kim, H.-T.; Mayrhofer, K. J. J.; Kim, H.; Choi, M., Tuning selectivity of electrochemical reactions by atomically dispersed platinum catalyst. *Nature Communications* **2016**, 7, 10922.
- (90) Liu, J.; Jiao, M.; Lu, L.; Barkholtz, H. M.; Li, Y.; Wang, Y.; Jiang, L.; Wu, Z.; Liu, D.-j.; Zhuang, L.; Ma, C.; Zeng, J.; Zhang, B.; Su, D.; Song, P.; Xing, W.; Xu, W.; Wang, Y.; Jiang, Z.; Sun, G., High performance platinum single atom electrocatalyst for oxygen reduction reaction. *Nature Communications* **2017**, 8, 15938.
- (91) Yang, S.; Tak, Y. J.; Kim, J.; Soon, A.; Lee, H., Support Effects in Single-Atom Platinum Catalysts for Electrochemical Oxygen Reduction. *Acs Catalysis* **2017**, 7, 1301-1307.
- (92) Chong, L.; Wen, J.; Kubal, J.; Sen, F. G.; Zou, J.; Greeley, J.; Chan, M.; Barkholtz, H.; Ding, W.; Liu, D. J., Ultralow-loading platinum-cobalt fuel cell catalysts derived from imidazolate frameworks. *Science* **2018**, 362, 1276-1281.
- (93) Li, T. F.; Liu, J. J.; Song, Y.; Wang, F., Photochemical Solid-Phase Synthesis of Platinum Single Atoms on Nitrogen-Doped Carbon with High Loading as Bifunctional Catalysts for Hydrogen Evolution and Oxygen Reduction Reactions. *Acs Catalysis* **2018**, 8, 8450-8458.
- (94) Zeng, X.; Shui, J.; Liu, X.; Liu, Q.; Li, Y.; Shang, J.; Zheng, L.; Yu, R., Single-Atom to Single-Atom Grafting of Pt onto FeN₄ Center: Pt₁@FeN₄C Multifunctional Electrocatalyst with Significantly Enhanced Properties. *Advanced Energy Materials* **2018**, 8, 1701345.
- (95) Liu, J.; Jiao, M.; Mei, B.; Tong, Y.; Li, Y.; Ruan, M.; Song, P.; Sun, G.; Jiang, L.; Wang, Y.; Jiang, Z.; Gu, L.; Zhou, Z.; Xu, W., Carbon-Supported Divacancy-Anchored Platinum Single-Atom Electrocatalysts with Superhigh Pt Utilization for the Oxygen Reduction Reaction. *Angew Chem Int Ed Engl* **2019**, 58, 1163-1167.
- (96) Stamenkovic, V. R.; Fowler, B.; Mun, B. S.; Wang, G.; Ross, P. N.; Lucas, C. A.; Marković, N. M., Improved oxygen reduction activity on Pt₃Ni (111) via increased surface site availability. *Science* **2007**, 315, 493-497.
- (97) Gasteiger, H. A.; Kocha, S. S.; Sompalli, B.; Wagner, F. T., Activity benchmarks and requirements for Pt, Pt-alloy, and non-Pt oxygen reduction catalysts for PEMFCs. *Applied Catalysis B-Environmental* **2005**, 56, 9-35.
- (98) Xia, B. Y.; Wu, H. B.; Li, N.; Yan, Y.; Lou, X. W.; Wang, X., One-pot synthesis of Pt-Co alloy nanowire assemblies with tunable composition and enhanced electrocatalytic properties. *Angew Chem Int Ed Engl* **2015**, 54, 3797-801.
- (99) Bu, L. Z.; Zhang, N.; Guo, S. J.; Zhang, X.; Li, J.; Yao, J. L.; Wu, T.; Lu, G.; Ma, J. Y.; Su, D.; Huang, X. Q., Biaxially strained PtPb/Pt core/shell nanoplate boosts oxygen reduction catalysis. *Science* **2016**, 354, 1410-1414.
- (100) Colic, V.; Bandarenka, A. S., Pt Alloy Electrocatalysts for the Oxygen Reduction Reaction: From Model Surfaces to Nanostructured Systems. *Acs Catalysis* **2016**, 6, 5378-5385.
- (101) Li, W.; Zou, S., PtNi nanoparticles encapsulated in few carbon layers as high-performance catalysts for oxygen reduction reaction. *ACS Applied Energy Materials* **2019**.

- (102) Cleve, T. V.; Moniri, S.; Belok, G.; More, K. L.; Linic, S., Nanoscale Engineering of Efficient Oxygen Reduction Electrocatalysts by Tailoring the Local Chemical Environment of Pt Surface Sites. *ACS Catalysis* **2016**, *7*, 17-24.
- (103) Reddy, G. V.; Raghavendra, P.; Ankamwar, B.; Chandana, P. S.; Kumar, S. S.; Sarma, L. S., Ultrafine Pt–Ru bimetallic nanoparticles anchored on reduced graphene oxide sheets as highly active electrocatalysts for methanol oxidation. *Materials Chemistry Frontiers* **2017**, *1*, 757-766.
- (104) Greeley, J.; Stephens, I. E. L.; Bondarenko, A. S.; Johansson, T. P.; Hansen, H. A.; Jaramillo, T. F.; Rossmeisl, J.; Chorkendorff, I.; Nørskov, J. K., Alloys of platinum and early transition metals as oxygen reduction electrocatalysts. *Nat Chem* **2009**, *1*, 552-556.
- (105) Guo, S.; Li, D.; Zhu, H.; Zhang, S.; Markovic, N. M.; Stamenkovic, V. R.; Sun, S., FePt and CoPt nanowires as efficient catalysts for the oxygen reduction reaction. *Angewandte Chemie International Edition* **2013**, *52*, 3465-3468.
- (106) Wang, C.; Hou, Y.; Kim, J.; Sun, S., A general strategy for synthesizing FePt nanowires and nanorods. *Angewandte Chemie International Edition* **2007**, *46*, 6333-6335.
- (107) Bu, L.; Zhang, N.; Guo, S.; Zhang, X.; Li, J.; Yao, J.; Wu, T.; Lu, G.; Ma, J. Y.; Su, D.; Huang, X., Biaxially strained PtPb/Pt core/shell nanoplate boosts oxygen reduction catalysis. *Science* **2016**, *354*, 1410-1414.
- (108) Zhang, J.; Sasaki, K.; Sutter, E.; Adzic, R. R., Stabilization of platinum oxygen-reduction electrocatalysts using gold clusters. *Science* **2007**, *315*, 220-2.
- (109) Zhang, Y.; Huang, Q.; Zou, Z.; Yang, J.; Vogel, W.; Yang, H., Enhanced durability of Au cluster decorated Pt nanoparticles for the oxygen reduction reaction. *The Journal of Physical Chemistry C* **2010**, *114*, 6860-6868.
- (110) Choi, C. H.; Kwon, H. C.; Yook, S.; Shin, H.; Kim, H.; Choi, M., Hydrogen Peroxide Synthesis via Enhanced Two-Electron Oxygen Reduction Pathway on Carbon-Coated Pt Surface. *Journal of Physical Chemistry C* **2014**, *118*, 30063-30070.
- (111) Nie, Y.; Chen, S.; Ding, W.; Xie, X.; Zhang, Y.; Wei, Z., Pt/C trapped in activated graphitic carbon layers as a highly durable electrocatalyst for the oxygen reduction reaction. *Chem Commun (Camb)* **2014**, *50*, 15431-4.
- (112) Takenaka, S.; Miyamoto, H.; Utsunomiya, Y.; Matsune, H.; Kishida, M., Catalytic Activity of Highly Durable Pt/CNT Catalysts Covered with Hydrophobic Silica Layers for the Oxygen Reduction Reaction in PEFCs. *Journal of Physical Chemistry C* **2014**, *118*, 774-783.
- (113) Cheng, K.; Kou, Z. K.; Zhang, J.; Jiang, M.; Wu, H.; Hu, L.; Yang, X. Y.; Pan, M.; Mu, S., Ultrathin carbon layer stabilized metal catalysts towards oxygen reduction. *Journal of Materials Chemistry A* **2015**, *3*, 14007-14014.
- (114) Cheng, N.; Banis, M. N.; Liu, J.; Riese, A.; Li, X.; Li, R.; Ye, S.; Knights, S.; Sun, X., Extremely stable platinum nanoparticles encapsulated in a zirconia nanocage by area-selective atomic layer deposition for the oxygen reduction reaction. *Adv Mater* **2015**, *27*, 277-81.
- (115) Chung, D. Y.; Jun, S. W.; Yoon, G.; Kwon, S. G.; Shin, D. Y.; Seo, P.; Yoo, J. M.; Shin, H.; Chung, Y. H.; Kim, H.; Mun, B. S.; Lee, K. S.; Lee, N. S.; Yoo, S. J.; Lim, D. H.; Kang, K.; Sung, Y. E.; Hyeon, T., Highly Durable and Active PtFe Nanocatalyst for Electrochemical Oxygen Reduction Reaction. *J Am Chem Soc* **2015**, *137*, 15478-85.
- (116) Guo, L.; Jiang, W. J.; Zhang, Y.; Hu, J. S.; Wei, Z. D.; Wan, L. J., Embedding Pt Nanocrystals in N-Doped Porous Carbon/Carbon Nanotubes toward Highly Stable Electrocatalysts for the Oxygen Reduction Reaction. *Acs Catalysis* **2015**, *5*, 2903-2909.

- (117) Shen, L.; Sun, T.; Zhuo, O.; Che, R.; Li, D.; Ji, Y.; Bu, Y.; Wu, Q.; Yang, L.; Chen, Q.; Wang, X.; Hu, Z., Alcohol-Tolerant Platinum Electrocatalyst for Oxygen Reduction by Encapsulating Platinum Nanoparticles inside Nitrogen-Doped Carbon Nanocages. *ACS Appl Mater Interfaces* **2016**, *8*, 16664-9.
- (118) Chen, S.; Wei, Z.; Qi, X.; Dong, L.; Guo, Y. G.; Wan, L.; Shao, Z.; Li, L., Nanostructured polyaniline-decorated Pt/C@PANI core-shell catalyst with enhanced durability and activity. *J Am Chem Soc* **2012**, *134*, 13252-5.
- (119) Galeano, C.; Meier, J. C.; Peinecke, V.; Bongard, H.; Katsounaros, I.; Topalov, A. A.; Lu, A.; Mayrhofer, K. J.; Schuth, F., Toward highly stable electrocatalysts via nanoparticle pore confinement. *J Am Chem Soc* **2012**, *134*, 20457-65.
- (120) Wu, Z.; Lv, Y.; Xia, Y.; Webley, P. A.; Zhao, D., Ordered mesoporous platinum@graphitic carbon embedded nanophase as a highly active, stable, and methanol-tolerant oxygen reduction electrocatalyst. *J Am Chem Soc* **2012**, *134*, 2236-45.
- (121) Strmcnik, D.; Escudero-Escribano, M.; Kodama, K.; Stamenkovic, V. R.; Cuesta, A.; Marković, N. M., Enhanced electrocatalysis of the oxygen reduction reaction based on patterning of platinum surfaces with cyanide. *Nature Chemistry* **2010**, *2*, 880.
- (122) Miyabayashi, K.; Nishihara, H.; Miyake, M., Platinum Nanoparticles Modified with Alkylamine Derivatives as an Active and Stable Catalyst for Oxygen Reduction Reaction. *Langmuir* **2014**, *30*, 2936-2942.
- (123) Alegre, C.; Galvez, M. E.; Moliner, R.; Baglio, V.; Arico, A. S.; Lazaro, M. J., Towards an optimal synthesis route for the preparation of highly mesoporous carbon xerogel-supported Pt catalysts for the oxygen reduction reaction. *Applied Catalysis B-Environmental* **2014**, *147*, 947-957.
- (124) Sakthivel, M.; Drillet, J. F., An extensive study about influence of the carbon support morphology on Pt activity and stability for oxygen reduction reaction. *Applied Catalysis B-Environmental* **2018**, *231*, 62-72.
- (125) Chen, Y.; Wang, J.; Liu, H.; Banis, M. N.; Li, R.; Sun, X.; Sham, T.-K.; Ye, S.; Knights, S., Nitrogen Doping Effects on Carbon Nanotubes and the Origin of the Enhanced Electrocatalytic Activity of Supported Pt for Proton-Exchange Membrane Fuel Cells. *The Journal of Physical Chemistry C* **2011**, *115*, 3769-3776.
- (126) Saha, M. S.; Li, R.; Sun, X.; Ye, S., 3-D composite electrodes for high performance PEM fuel cells composed of Pt supported on nitrogen-doped carbon nanotubes grown on carbon paper. *Electrochemistry Communications* **2009**, *11*, 438-441.
- (127) Liu, Y.; Mustain, W. E., High Stability, High Activity Pt/ITO Oxygen Reduction Electrocatalysts. *Journal of the American Chemical Society* **2013**, *135*, 530-533.
- (128) Huang, S.-Y.; Ganesan, P.; Park, S.; Popov, B. N., Development of a Titanium Dioxide-Supported Platinum Catalyst with Ultrahigh Stability for Polymer Electrolyte Membrane Fuel Cell Applications. *Journal of the American Chemical Society* **2009**, *131*, 13898-13899.
- (129) Shen, Q.; Hou, M.; Liang, D.; Zhou, Z.; Li, X.; Shao, Z.; Yi, B., Study on the processes of start-up and shutdown in proton exchange membrane fuel cells. *Journal of Power Sources* **2009**, *189*, 1114-1119.
- (130) Jung, N.; Chung, D. Y.; Ryu, J.; Yoo, S. J.; Sung, Y.-E., Pt-based nanoarchitecture and catalyst design for fuel cell applications. *Nano Today* **2014**, *9*, 433-456.
- (131) Zhang, J.; Zhao, F.; Zhang, Z.; Chen, N.; Qu, L., Dimension-tailored functional graphene structures for energy conversion and storage. *Nanoscale* **2013**, *5*, 3112-26.

- (132) Wang, D.-W.; Su, D., Heterogeneous nanocarbon materials for oxygen reduction reaction. *Energy & Environmental Science* **2014**, *7*, 576-591.
- (133) Geng, D. S.; Ding, N.; Hor, T. S. A.; Liu, Z. L.; Sun, X. L.; Zong, Y., Potential of metal-free "graphene alloy" as electrocatalysts for oxygen reduction reaction. *Journal of Materials Chemistry A* **2015**, *3*, 1795-1810.
- (134) Chabot, V.; Higgins, D.; Yu, A. P.; Xiao, X. C.; Chen, Z. W.; Zhang, J. J., A review of graphene and graphene oxide sponge: material synthesis and applications to energy and the environment. *Energy & Environmental Science* **2014**, *7*, 1564-1596.
- (135) Holade, Y.; Sahin, N. E.; Servat, K.; Napporn, T. W.; Kokoh, K. B., Recent Advances in Carbon Supported Metal Nanoparticles Preparation for Oxygen Reduction Reaction in Low Temperature Fuel Cells. *Catalysts* **2015**, *5*, 310-348.
- (136) Wei, Q. L.; Tong, X.; Zhang, G. X.; Qiao, J. L.; Gong, Q. J.; Sun, S. H., Nitrogen-Doped Carbon Nanotube and Graphene Materials for Oxygen Reduction Reactions. *Catalysts* **2015**, *5*, 1574-1602.
- (137) Ni, J. F.; Li, Y., Carbon Nanomaterials in Different Dimensions for Electrochemical Energy Storage. *Advanced Energy Materials* **2016**, *6*, 1600278-n/a.
- (138) Agnoli, S.; Favaro, M., Doping graphene with boron: a review of synthesis methods, physicochemical characterization, and emerging applications. *Journal of Materials Chemistry A* **2016**, *4*, 5002-5025.
- (139) Wen, Y.; Wang, B.; Huang, C.; Wang, L.; Hulicova-Jurcakova, D., Synthesis of phosphorus-doped graphene and its wide potential window in aqueous supercapacitors. *Chemistry* **2015**, *21*, 80-5.
- (140) Lai, L. F.; Potts, J. R.; Zhan, D.; Wang, L.; Poh, C. K.; Tang, C. H.; Gong, H.; Shen, Z. X.; Jianyi, L. Y.; Ruoff, R. S., Exploration of the active center structure of nitrogen-doped graphene-based catalysts for oxygen reduction reaction. *Energy & Environmental Science* **2012**, *5*, 7936-7942.
- (141) Lin, Z. Y.; Waller, G.; Liu, Y.; Liu, M. L.; Wong, C. P., Facile Synthesis of Nitrogen-Doped Graphene via Pyrolysis of Graphene Oxide and Urea, and its Electrocatalytic Activity toward the Oxygen-Reduction Reaction. *Advanced Energy Materials* **2012**, *2*, 884-888.
- (142) Zhao, Y.; Hu, C.; Hu, Y.; Cheng, H.; Shi, G.; Qu, L., A versatile, ultralight, nitrogen-doped graphene framework. *Angew Chem Int Ed Engl* **2012**, *51*, 11371-5.
- (143) Ito, Y.; Qiu, H.-J.; Fujita, T.; Tanabe, Y.; Tanigaki, K.; Chen, M., Bicontinuous Nanoporous N-doped Graphene for the Oxygen Reduction Reaction. *Advanced Materials* **2014**, *26*, 4145-4150.
- (144) Vikkisk, M.; Kruusenberg, I.; Joost, U.; Shulga, E.; Kink, I.; Tammeveski, K., Electrocatalytic oxygen reduction on nitrogen-doped graphene in alkaline media. *Applied Catalysis B-Environmental* **2014**, *147*, 369-376.
- (145) Luo, E. G.; Xiao, M. L.; Ge, J. J.; Liu, C. P.; Xing, W., Selectively doping pyridinic and pyrrolic nitrogen into a 3D porous carbon matrix through template-induced edge engineering: enhanced catalytic activity towards the oxygen reduction reaction. *Journal of Materials Chemistry A* **2017**, *5*, 21709-21714.
- (146) Liu, H.; Liu, Y.; Zhu, D., Chemical doping of graphene. *Journal of materials chemistry* **2011**, *21*, 3335-3345.
- (147) Wei, D.; Liu, Y.; Wang, Y.; Zhang, H.; Huang, L.; Yu, G., Synthesis of N-doped graphene by chemical vapor deposition and its electrical properties. *Nano Lett* **2009**, *9*, 1752-8.
- (148) Li, C.; Chen, Z.; Kong, A.; Ni, Y.; Kong, F.; Shan, Y., High-rate oxygen electroreduction over metal-free graphene foams embedding P-N coupled moieties in acidic media. *Journal of Materials Chemistry A* **2018**, *6*, 4145-4151.

- (149) Lv, Y.; Wang, X.; Mei, T.; Li, J.; Wang, J., Single-Step Hydrothermal Synthesis of N, S-Dual-Doped Graphene Networks as Metal-Free Efficient Electrocatalysts for Oxygen Reduction Reaction. *ChemistrySelect* **2018**, *3*, 3241-3250.
- (150) Wang, S. Y.; Zhang, L. P.; Xia, Z. H.; Roy, A.; Chang, D. W.; Baek, J. B.; Dai, L. M., BCN Graphene as Efficient Metal-Free Electrocatalyst for the Oxygen Reduction Reaction. *Angewandte Chemie-International Edition* **2012**, *51*, 4209-4212.
- (151) Razmjooei, F.; Singh, K. P.; Song, M. Y.; Yu, J. S., Enhanced electrocatalytic activity due to additional phosphorous doping in nitrogen and sulfur-doped graphene: A comprehensive study. *Carbon* **2014**, *78*, 257-267.
- (152) Ye, R. Q.; Xiang, C. S.; Lin, J.; Peng, Z. W.; Huang, K. W.; Yan, Z.; Cook, N. P.; Samuel, E. L. G.; Hwang, C. C.; Ruan, G. D.; Ceriotti, G.; Raji, A. R. O.; Marti, A. A.; Tour, J. M., Coal as an abundant source of graphene quantum dots. *Nature Communications* **2013**, *4*, 2943.
- (153) Qiu, L.; Liu, J. Z.; Chang, S. L.; Wu, Y.; Li, D., Biomimetic superelastic graphene-based cellular monoliths. *Nat Commun* **2012**, *3*, 1241.
- (154) Cong, H. P.; Chen, J. F.; Yu, S. H., Graphene-based macroscopic assemblies and architectures: an emerging material system. *Chem Soc Rev* **2014**, *43*, 7295-325.
- (155) Li, X. M.; Rui, M. C.; Song, J. Z.; Shen, Z. H.; Zeng, H. B., Carbon and Graphene Quantum Dots for Optoelectronic and Energy Devices: A Review. *Advanced Functional Materials* **2015**, *25*, 4929-4947.
- (156) Zheng, X. T.; Ananthanarayanan, A.; Luo, K. Q.; Chen, P., Glowing graphene quantum dots and carbon dots: properties, syntheses, and biological applications. *Small* **2015**, *11*, 1620-36.
- (157) Zhu, S. J.; Song, Y. B.; Zhao, X. H.; Shao, J. R.; Zhang, J. H.; Yang, B., The photoluminescence mechanism in carbon dots (graphene quantum dots, carbon nanodots, and polymer dots) : current state and future perspective. *Nano Research* **2015**, *8*, 355-381.
- (158) Liu, Y.; Wu, P., Graphene quantum dot hybrids as efficient metal-free electrocatalyst for the oxygen reduction reaction. *ACS Appl Mater Interfaces* **2013**, *5*, 3362-9.
- (159) Saidi, W. A., Oxygen Reduction Electrocatalysis Using N-Doped Graphene Quantum-Dots. *Journal of Physical Chemistry Letters* **2013**, *4*, 4160-4165.
- (160) Fei, H.; Ye, R.; Ye, G.; Gong, Y.; Peng, Z.; Fan, X.; Samuel, E. L. G.; Ajayan, P. M.; Tour, J. M., Boron- and Nitrogen-Doped Graphene Quantum Dots/Graphene Hybrid Nanoplatelets as Efficient Electrocatalysts for Oxygen Reduction. *ACS Nano* **2014**, *8*, 10837-10843.
- (161) Favaro, M.; Ferrighi, L.; Fazio, G.; Colazzo, L.; Di Valentin, C.; Durante, C.; Sedona, F.; Gennaro, A.; Agnoli, S.; Granozzi, G., Single and Multiple Doping in Graphene Quantum Dots: Unraveling the Origin of Selectivity in the Oxygen Reduction Reaction. *ACS Catalysis* **2015**, *5*, 129-144.
- (162) Fan, M. M.; Zhu, C. L.; Yang, J. Z.; Sun, D. P., Facile self-assembly N-doped graphene quantum dots/graphene for oxygen reduction reaction. *Electrochimica Acta* **2016**, *216*, 102-109.
- (163) Wang, M.; Fang, Z.; Zhang, K.; Fang, J.; Qin, F.; Zhang, Z.; Li, J.; Liu, Y.; Lai, Y., Synergistically enhanced activity of graphene quantum dots/graphene hydrogel composites: a novel all-carbon hybrid electrocatalyst for metal/air batteries. *Nanoscale* **2016**, *8*, 11398-402.
- (164) Kim, H.; Lee, K.; Woo, S. I.; Jung, Y., On the mechanism of enhanced oxygen reduction reaction in nitrogen-doped graphene nanoribbons. *Physical Chemistry Chemical Physics* **2011**, *13*, 17505-17510.
- (165) Wang, C. N.; Li, H.; Zhao, J. H.; Zhu, Y.; Yuan, W. Z.; Zhang, Y. M., Graphene nanoribbons as a novel support material for high performance fuel cell electrocatalysts. *International Journal of Hydrogen Energy* **2013**, *38*, 13230-13237.

- (166) Davis, D. J.; Raji, A. R. O.; Lambert, T. N.; Vigil, J. A.; Li, L.; Nan, K. W.; Tour, J. M., Silver-Graphene Nanoribbon Composite Catalyst for the Oxygen Reduction Reaction in Alkaline Electrolyte. *Electroanalysis* **2014**, *26*, 164-170.
- (167) Liu, M.; Song, Y.; He, S.; Tjiu, W. W.; Pan, J.; Xia, Y. Y.; Liu, T., Nitrogen-doped graphene nanoribbons as efficient metal-free electrocatalysts for oxygen reduction. *ACS Appl Mater Interfaces* **2014**, *6*, 4214-22.
- (168) Xiao, B. B.; Lang, X. Y.; Jiang, Q., Pt monatomic wire supported on graphene nanoribbon for oxygen reduction reaction. *Rsc Advances* **2014**, *4*, 28400-28408.
- (169) Fan, X.; Peng, Z.; Ye, R.; Zhou, H.; Guo, X., M3C (M: Fe, Co, Ni) Nanocrystals Encased in Graphene Nanoribbons: An Active and Stable Bifunctional Electrocatalyst for Oxygen Reduction and Hydrogen Evolution Reactions. *ACS Nano* **2015**, *9*, 7407-18.
- (170) Gong, Y.; Fei, H.; Zou, X.; Zhou, W.; Yang, S.; Ye, G.; Liu, Z.; Peng, Z.; Lou, J.; Vajtai, R.; Yakobson, B. I.; Tour, J. M.; Ajayan, P. M., Boron- and Nitrogen-Substituted Graphene Nanoribbons as Efficient Catalysts for Oxygen Reduction Reaction. *Chemistry of Materials* **2015**, *27*, 1181-1186.
- (171) Jin, H.; Huang, H.; He, Y.; Feng, X.; Wang, S.; Dai, L.; Wang, J., Graphene Quantum Dots Supported by Graphene Nanoribbons with Ultrahigh Electrocatalytic Performance for Oxygen Reduction. *J Am Chem Soc* **2015**, *137*, 7588-91.
- (172) Lu, X. Y.; Chan, H. M.; Sun, C. L.; Tseng, C. M.; Zhao, C., Interconnected core-shell carbon nanotube-graphene nanoribbon scaffolds for anchoring cobalt oxides as bifunctional electrocatalysts for oxygen evolution and reduction. *Journal of Materials Chemistry A* **2015**, *3*, 13371-13376.
- (173) Chen, L.; Hernandez, Y.; Feng, X.; Mullen, K., From nanographene and graphene nanoribbons to graphene sheets: chemical synthesis. *Angew Chem Int Ed Engl* **2012**, *51*, 7640-54.
- (174) Yazyev, O. V., A guide to the design of electronic properties of graphene nanoribbons. *Acc Chem Res* **2013**, *46*, 2319-28.
- (175) Ma, L.; Wang, J.; Ding, F., Recent progress and challenges in graphene nanoribbon synthesis. *Chemphyschem* **2013**, *14*, 47-54.
- (176) Liang, J.; Jiao, Y.; Jaroniec, M.; Qiao, S. Z., Sulfur and Nitrogen Dual-Doped Mesoporous Graphene Electrocatalyst for Oxygen Reduction with Synergistically Enhanced Performance. *Angewandte Chemie International Edition* **2012**, *51*, 11496-11500.
- (177) Liang, J.; Du, X.; Gibson, C.; Du, X. W.; Qiao, S. Z., N-doped graphene natively grown on hierarchical ordered porous carbon for enhanced oxygen reduction. *Adv Mater* **2013**, *25*, 6226-31.
- (178) Lin, Z.; Waller, G. H.; Liu, Y.; Liu, M.; Wong, C.-p., 3D Nitrogen-doped graphene prepared by pyrolysis of graphene oxide with polypyrrole for electrocatalysis of oxygen reduction reaction. *Nano Energy* **2013**, *2*, 241-248.
- (179) Lin, Z. Y.; Waller, G. H.; Liu, Y.; Liu, M. L.; Wong, C. P., Simple preparation of nanoporous few-layer nitrogen-doped graphene for use as an efficient electrocatalyst for oxygen reduction and oxygen evolution reactions. *Carbon* **2013**, *53*, 130-136.
- (180) Xue, Y.; Yu, D.; Dai, L.; Wang, R.; Li, D.; Roy, A.; Lu, F.; Chen, H.; Liu, Y.; Qu, J., Three-dimensional B,N-doped graphene foam as a metal-free catalyst for oxygen reduction reaction. *Phys Chem Chem Phys* **2013**, *15*, 12220-6.
- (181) Chen, L.; Cui, X.; Wang, Y.; Wang, M.; Qiu, R.; Shu, Z.; Zhang, L.; Hua, Z.; Cui, F.; Wei, C.; Shi, J., One-step synthesis of sulfur doped graphene foam for oxygen reduction reactions. *Dalton Trans* **2014**, *43*, 3420-3.

- (182) Liu, J. F.; Takeshi, D.; Orejon, D.; Sasaki, K.; Lyth, S. M., Defective Nitrogen-Doped Graphene Foam: A Metal-Free, Non-Precious Electrocatalyst for the Oxygen Reduction Reaction in Acid. *Journal of the Electrochemical Society* **2014**, 161, F544-F550.
- (183) Wang, L.; Sofer, Z.; Ambrosi, A.; Simek, P.; Pumera, M., 3D-graphene for electrocatalysis of oxygen reduction reaction: Increasing number of layers increases the catalytic effect. *Electrochemistry Communications* **2014**, 46, 148-151.
- (184) Zhao, Y.; Hu, C. G.; Song, L.; Wang, L. X.; Shi, G. Q.; Dai, L. M.; Qu, L. T., Functional graphene nanomesh foam. *Energy & Environmental Science* **2014**, 7, 1913-1918.
- (185) Wang, M.; Wang, J.; Hou, Y.; Shi, D.; Wexler, D.; Poynton, S. D.; Slade, R. C.; Zhang, W.; Liu, H.; Chen, J., N-doped crumpled graphene derived from vapor phase deposition of PPy on graphene aerogel as an efficient oxygen reduction reaction electrocatalyst. *ACS Appl Mater Interfaces* **2015**, 7, 7066-72.
- (186) Wang, Z.; Cao, X.; Ping, J.; Wang, Y.; Lin, T.; Huang, X.; Ma, Q.; Wang, F.; He, C.; Zhang, H., Electrochemical doping of three-dimensional graphene networks used as efficient electrocatalysts for oxygen reduction reaction. *Nanoscale* **2015**, 7, 9394-8.
- (187) Xu, C.; Su, Y.; Liu, D.; He, X., Three-dimensional N,B-doped graphene aerogel as a synergistically enhanced metal-free catalyst for the oxygen reduction reaction. *Physical Chemistry Chemical Physics* **2015**, 17, 25440-25448.
- (188) Ye, D. X.; Wang, L.; Zhang, R.; Liu, B. H.; Wang, Y.; Kong, J. L., Facile preparation of N-doped mesocellular graphene foam from sludge flocs for highly efficient oxygen reduction reaction. *Journal of Materials Chemistry A* **2015**, 3, 15171-15176.
- (189) Zhou, X. J.; Bai, Z. Y.; Wu, M. J.; Qiao, J. L.; Chen, Z. W., 3-Dimensional porous N-doped graphene foam as a non-precious catalyst for the oxygen reduction reaction. *Journal of Materials Chemistry A* **2015**, 3, 3343-3350.
- (190) Zhou, Y.; Yen, C. H.; Fu, S.; Yang, G.; Zhu, C.; Du, D.; Wo, P. C.; Cheng, X.; Yang, J.; Wai, C. M.; Lin, Y., One-pot synthesis of B-doped three-dimensional reduced graphene oxide via supercritical fluid for oxygen reduction reaction. *Green Chemistry* **2015**, 17, 3552-3560.
- (191) Wu, M.; Dou, Z. Y.; Chang, J. J.; Cui, L. L., Nitrogen and sulfur co-doped graphene aerogels as an efficient metal-free catalyst for oxygen reduction reaction in an alkaline solution. *Rsc Advances* **2016**, 6, 22781-22790.
- (192) Zhao, L.; Sui, X.-L.; Li, J.-Z.; Zhang, J.-J.; Zhang, L.-M.; Huang, G.-S.; Wang, Z.-B., Supramolecular assembly promoted synthesis of three-dimensional nitrogen doped graphene frameworks as efficient electrocatalyst for oxygen reduction reaction and methanol electrooxidation. *Applied Catalysis B: Environmental* **2018**, 231, 224-233.
- (193) Han, J.; Huang, G.; Wang, Z.; Lu, Z.; Du, J.; Kashani, H.; Chen, M., Low-Temperature Carbide-Mediated Growth of Bicontinuous Nitrogen-Doped Mesoporous Graphene as an Efficient Oxygen Reduction Electrocatalyst. *Adv Mater* **2018**, 30, e1803588.
- (194) Xue, Q.; Ding, Y.; Xue, Y. Y.; Li, F.; Chen, P.; Chen, Y., 3D nitrogen-doped graphene aerogels as efficient electrocatalyst for the oxygen reduction reaction. *Carbon* **2018**, 139, 137-144.
- (195) Marinkas, A.; Arena, F.; Mitzel, J.; Prinz, G. M.; Heinzl, A.; Peinecke, V.; Natter, H., Graphene as catalyst support: The influences of carbon additives and catalyst preparation methods on the performance of PEM fuel cells. *Carbon* **2013**, 58, 139-150.

- (196) Imran Jafri, R.; Rajalakshmi, N.; Ramaprabhu, S., Nitrogen doped graphene nanoplatelets as catalyst support for oxygen reduction reaction in proton exchange membrane fuel cell. *Journal of Materials Chemistry* **2010**, *20*, 7114-7117.
- (197) Vinayan, B. P.; Nagar, R.; Rajalakshmi, N.; Ramaprabhu, S., Novel Platinum-Cobalt Alloy Nanoparticles Dispersed on Nitrogen-Doped Graphene as a Cathode Electrocatalyst for PEMFC Applications. *Advanced Functional Materials* **2012**, *22*, 3519-3526.
- (198) Xiong, B.; Zhou, Y.; Zhao, Y.; Wang, J.; Chen, X.; O'Hayre, R.; Shao, Z., The use of nitrogen-doped graphene supporting Pt nanoparticles as a catalyst for methanol electrocatalytic oxidation. *Carbon* **2013**, *52*, 181-192.
- (199) Liu, J.; Takeshi, D.; Sasaki, K.; Lyth, S. M., Platinum-Decorated Nitrogen-Doped Graphene Foam Electrocatalysts. *Fuel Cells* **2014**, *14*, 728-734.
- (200) Cheng, J. H.; Li, Y. Y.; Huang, X. D.; Wang, Q. Q.; Mei, A.; Shen, P. K., Highly stable electrocatalysts supported on nitrogen-self-doped three-dimensional graphene-like networks with hierarchical porous structures. *Journal of Materials Chemistry A* **2015**, *3*, 1492-1497.
- (201) Huang, Q.; Tao, F.; Zou, L.; Yuan, T.; Zou, Z.; Zhang, H.; Zhang, X.; Yang, H., One-step Synthesis of Pt Nanoparticles Highly Loaded on Graphene Aerogel as Durable Oxygen Reduction Electrocatalyst. *Electrochimica Acta* **2015**, *152*, 140-145.
- (202) Yang, S.; Verdager-Casadevall, A.; Arnarson, L.; Silvioli, L.; Čolić, V.; Frydendal, R.; Rossmeisl, J.; Chorkendorff, I.; Stephens, I. E. L., Toward the Decentralized Electrochemical Production of H₂O₂: A Focus on the Catalysis. *ACS Catalysis* **2018**, *8*, 4064-4081.

LIST OF PUBLICATIONS

1. **X. Tong**, G. Zhang, J. Claverie*, S. Sun*. Support interaction effect of platinum clusters anchoring on doped graphene supports for the oxygen reduction reaction. To be submitted.
2. **X. Tong**, M. Cherif, G. Zhang*, J. Ma, A. Almesrati, V. François, Y. Song, J. Claverie*, S. Sun*. N, P co-doped graphene dots supported on N-doped 3D graphene as metal-free catalyst for oxygen reduction. Submitted.
3. **X. Tong**, J. Zhang, G. Zhang, Q. Wei, R. Chenitz, J. Claverie*, S. Sun*. Ultra-thin carbon coated Pt/CNTs: a highly durable electro-catalyst for oxygen reduction. *Chem. Mater*, 2017, 29, 9579-9587.
4. **X. Tong**, Q. Wei, X. Zhan, G. Zhang, S. Sun*. The New Graphene Family Materials: Synthesis and Applications in Oxygen Reduction Reaction. *Catalysts*, 2017, 7, 1
5. J. Ma, **X. Tong (co-first author)**, J. Wang, G. Zhang, Y. Lv, Y. Zhu, S. Sun, Y. Yang, Y. Song. Rare-earth metal oxide hybridized PtFe nanocrystals synthesized via microfluidic process for enhanced electrochemical catalytic performance. *Electrochimica Acta*. 2019, 299, 80-88.
6. Q. Wei, **X. Tong (co-first author)**, G. Zhang, J. Qiao, Q. Gong, S. Sun. Nitrogen-doped carbon nanotube & graphene materials for oxygen reduction reactions. *Catalysis* 2015, 5 (3), 1574-1602
7. **X. Tong**, Q. Wei, G. Zhang, S. Sun*, New graphene family materials for Li-ion batteries, in the book of Carbon Nanomaterials for Electrochemical Energy Technologies – Fundamentals and Applications, CRC Press (Taylor & Francis Group), 2017. *Book chapter*
8. **X. Tong**, Q. Wei, G. Zhang, S. Sun*, New class of carbon materials for proton exchange membrane fuel cells, in the book of Carbon Nanomaterials for Electrochemical Energy Technologies – Fundamentals and Applications, CRC Press (Taylor & Francis Group), 2017. *Book chapter*
9. Q. Wei, **X. Tong**, G. Zhang, S. Sun*, N-doped carbon materials for oxygen reduction in PEM fuel cells, in the book of Carbon Nanomaterials for Electrochemical Energy Technologies – Fundamentals and Applications, CRC Press (Taylor & Francis Group), 2017. *Book chapter*
10. J. Prakash, **X. Tong**, G. Zhang, S. Sun*, 3D graphene and its nanocomposites: from Synthesis to multifunctional applications in the book of Graphene Functionalization Strategies: From Synthesis to Applications, Springer, 2019. *Book chapter*
11. F. Navarro-Pardo, **X. Tong**, X. Tong, G. S. Selopal, S. G. Cloutier, S. Sun, A. C. Tavares, H. Zhao, Z. M. Wang, F. Rosei. Graphene oxide/cobalt-based nanohybrid electrodes for robust hydrogen generation. *Applied Catalysis B: Environmental*. 2019, 245, 167-176.

12. Y. Fu, Q. Wei, G. Zhang, Y. Zhong, N. Moghimian, **X. Tong**, S. Sun. LiFePO₄-Graphene Composites as High-Performance Cathodes for Lithium-Ion Batteries: The Impact of Size and Morphology of Graphene. *Materials*, 2019, 12, 842.

SOMMAIRE RÉCAPITULATIF

1. L'introduction

1.1 Les Piles à Combustible à Membrane Échangeuse de Protons (PEMFC)

Les changements climatiques à cause de la consommation des combustibles fossiles sont actuellement un défi urgent dans le monde entier. Les sources d'énergie pratiques et écologiquement durables pour remplacer les combustibles fossiles traditionnels sont indispensables. La pile à combustible, en particulier la pile à combustible à membrane échangeuse de protons (en anglais: PEMFC), est considérée comme l'un des candidats les plus prometteurs, car elle pourrait convertir directement l'énergie chimique en énergie électrique utilisant par la méthode électrochimique.

La PEMFC est une cellule électrochimique qui convertit directement l'énergie chimique d'une cellule (généralement, hydrogène, méthanol, etc.) en énergie de l'électricité, de la chaleur et de l'eau. La structure des PEMFCs est présentée dans la Figure R1. Une membrane polymère électrolytique est sandwichée entre une cathode (ou électrode positive) et une anode (ou électrode négative). Les molécules d'hydrogène sur l'anode pourraient s'être séparées catalytiquement en protons et électrons par la réaction d'oxydation de l'hydrogène. Les électrons traversent un circuit externe du côté de la cathode en produisant de l'électricité en courant continu. Les protons sont tirés à traverser la membrane électrolytique polymère vers la cathode, en réaction avec une molécule d'oxygène et quatre électrons désirés pour former deux molécules d'eau dans un électrolyte acide. Cependant, l'hydrogène et l'oxygène gazeux sont cinétiquement stables dans les conditions opérationnelles. Les catalyseurs en deux côtés de l'électrode sont essentiels pour réduire l'énergie d'activation afin de garantir le déroulement de la réaction par des voies thermodynamiques alternatives.

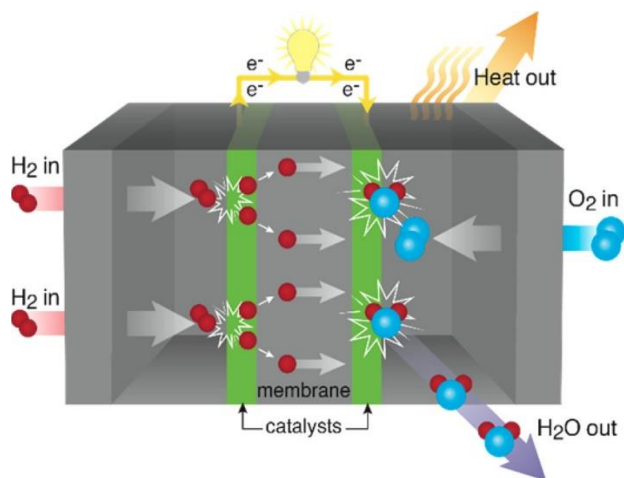


Figure R1. Le schéma de principe d'une PEMFC.

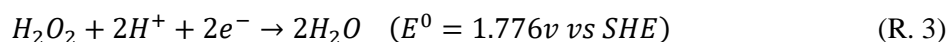
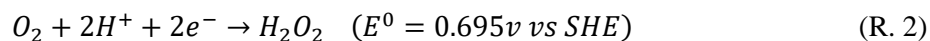
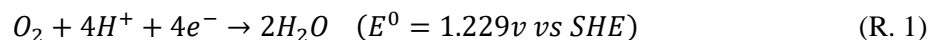
1.2 La Réaction de Réduction de l'Oxygène (l'ORR)

Théoriquement, les performances de sortie des piles à combustible sont déterminées par la cinétique de la réaction d'oxydation de l'hydrogène (en anglais: HOR) sur l'anode et par la réaction de réduction de l'oxygène (en anglais: ORR) sur la cathode. L'ORR est la réaction la plus lente en raison de la forte énergie de liaison de la molécule d'oxygène ($\Delta H = 498 \text{ kJ/mol}$). Pour les piles à combustible à la basse température, l'absence d'un catalyseur d'ORR efficace limite sérieusement l'efficacité globale de la cellule. Donc, les chercheurs déploient d'immenses efforts considérables pour découvrir et optimiser le catalyseur d'ORR.

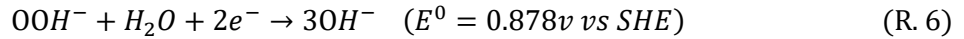
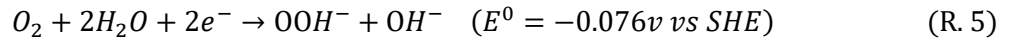
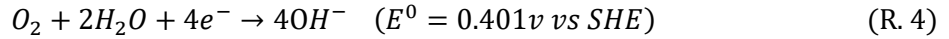
Il y a généralement deux voies différentes pour l'ORR:

- (i) la voie directe à quatre électrons;
- (ii) les processus indirects à deux électrons.

Dans le milieu acide, l'oxygène peut soit être réduit directement en molécules d'eau, soit réduit en peroxyde d'hydrogène (H_2O_2) en tant qu'espèce intermédiaire.



Dans le milieu alcalin, par rapport au H_2O_2 et à la formation d'eau lorsque les protons sont abondants, l'ORR génère un anion de peroxyde par la voie indirecte et un anion d'hydroxyde comme le produit final.



Dans les conditions de non-standard, le potentiel d'équilibre des réactions d'électrodes à oxygène est établi selon l'équation de Nernst:

$$E = E^0 - \frac{RT}{nF} \ln\left(\frac{a_{Ox}}{a_{Red}}\right) \quad (R.7)$$

où a est l'activité de l'espèce oxydée et réduite.

De toute évidence, la réaction à quatre électrons est la voie favorisée pour assurer des potentiels opérationnels et l'efficacité de courant plus élevés. En revanche, la formation du produit de réduction à deux électrons réduira le nombre de transfert d'électrons effectif de l'ORR en conduisant aux conversions à basse énergie. De plus, les espèces intermédiaires réactives peuvent former des espèces de radicaux libres nocives induisant à la dégradation de la membrane.

1.3 Les Catalyseurs pour l'ORR

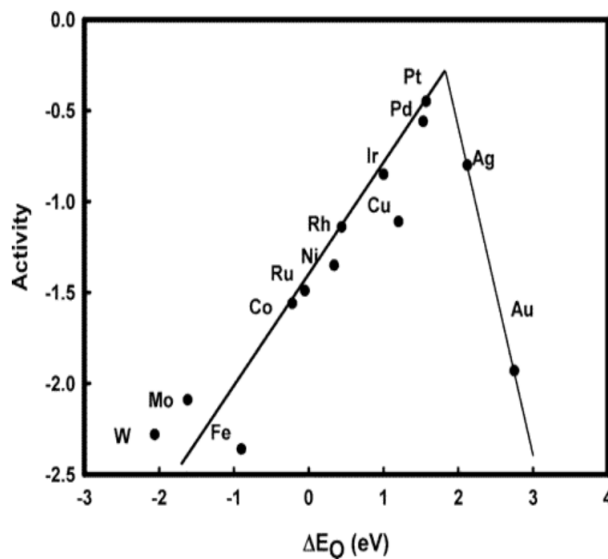


Figure R2. Les tendances de l'activité de réduction de l'oxygène tracées en fonction de l'énergie de liaison à l'oxygène.

Actuellement, il est prouvé que les catalyseurs à base de platine sont les catalyseurs plus avancés pour l'ORR dans le milieu acide. Théoriquement, l'activité d'ORR est déterminée par l'énergie de liaison de surface du catalyseur. Dans la Figure R2, les relations en forme de volcan entre l'activité d'ORR et l'énergie de liaison de l'oxygène ont été identifiées en montrant que le Pt est le meilleur catalyseur pour l'ORR. Pratiquement, le Pt supporté de noir de carbone a été largement utilisé et considéré comme le meilleur des catalyseurs depuis l'année 1992 où la première découverte par Wilson *et al.*

Toutefois, il y a de nombreux problèmes qui doivent encore être résolus avant la mise en œuvre commerciale à grande échelle. Tout d'abord, le Pt est un métal rare et noble. Le prix très élevé du Pt représente environ de 56% du coût d'une boîte de pile à combustible. De plus, la faible stabilité à long terme de ce catalyseur au Pt réduit la durée de vie et la durabilité des piles à combustible de PEM. La durée de vie du catalyseur à la base de Pt le plus avancé avec la performance de pile à combustible élevée est bien inférieure aux 5000 heures ayant l'objectif pour l'année de 2017 par le Département d'Energy (en anglais : DOE) aux États-Unis.

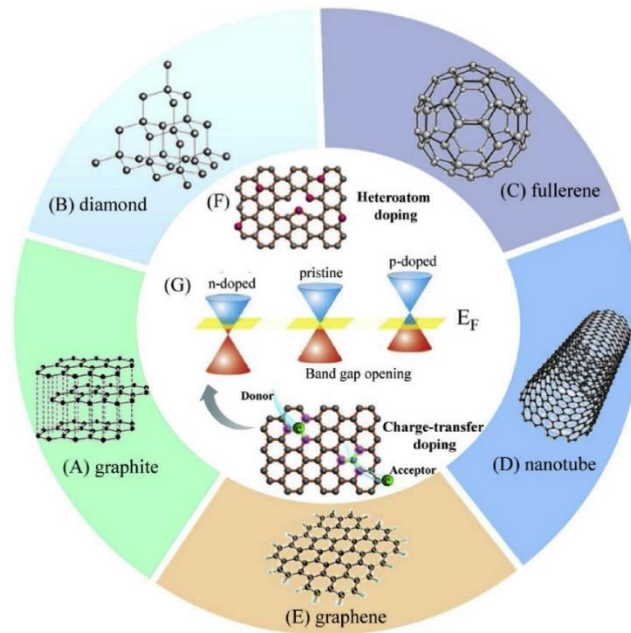


Figure R3. Les différents catalyseurs de l'absence du métal.

En conséquence, la manière de réduire les coûts en réduisant l'utilisation de Pt sans perte de l'activité et de la durabilité est un souci principal dans la recherche sur les catalyseurs d'ORR.

Jusqu'à présent, un grand nombre de recherches ont été effectuées pour résoudre les problèmes susmentionnés, et ces stratégies peuvent composer en deux catégories principales:

(i) l'amélioration de catalyseur de Pt/C soit par la méthode de modification de particules Pt remplaçant le support conventionnel, soit par l'ingénierie de surface en modifiant le revêtement de la nanoparticule Pt;

(ii) le remplacement des catalyseurs à base de Pt par des catalyseurs à base de métaux non-précieux et des catalyseurs de non-métaux (voir sur la Figure R3).

1.4 Les Catalyseurs à base de Pt pour l'ORR

Dans les piles à combustible, le catalyseur d'ORR fonctionne dans les conditions dures (les potentiels fortement positifs et les milieux fortement acides) et la région de surface électrochimique (en anglais : ECSA) de Pt est rapidement perdue au cours de cycles. Alors, les différents mécanismes de dégradation du Pt/C sont résumés dans la Figure R4.

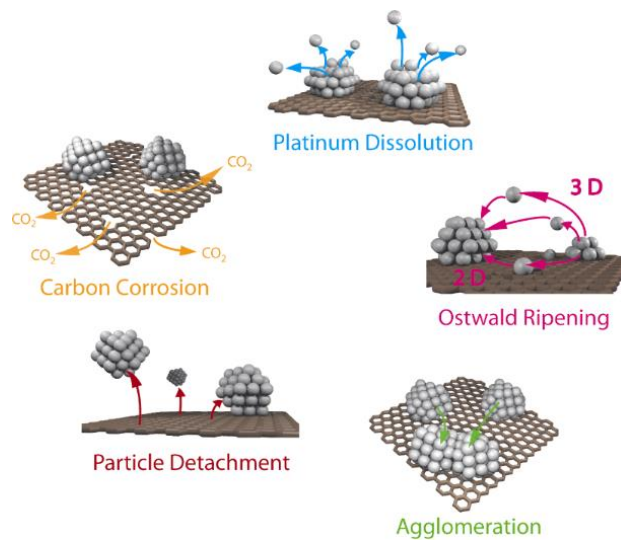


Figure R4. La représentation simplifiée des mécanismes de dégradation suggérés pour les particules de Pt sur un support en carbone dans des piles à combustible.

Maintenant, un grand nombre de recherches ont été effectuées pour résoudre les problèmes susmentionnés, et ces stratégies peuvent composer en trois catégories principales:

(i) la modification de particules Pt lui-même avec le contrôle précis sur la taille, la forme, la composition, la structure et l'architecture;

(ii) l'ingénierie de surface en modifiant le revêtement de la nanoparticule Pt (voir la Figure R5);

(iii) le remplacement de support conventionnel par les autres supports de catalyseurs appropriés avec la résistance élevée à la corrosion et les fortes interactions avec Pt.



Figure R5. Les avancées importantes récentes dans les nouvelles nanostructures actives et durables à base de Pt pour une meilleure catalyse d'ORR.

1.5 Les Catalyseurs à base de Graphène et Sans Métal

Dans les dernières années, les matériaux à base de graphène 2D ont été appliqués comme les catalyseurs électrochimiques en raison de leur conductivité excellente, de leur surface spécifique (en anglais: SSA) élevée et de leur chimie de surface ajustée, voyant sur les révisions précédentes. Bien que les grandes SSA et la haute conductivité électrique du graphène à l'état vierge soient supposées être utiles au processus d'électrocatalyse, pratiquement, avec les fortes interactions de Van Der Waals et l'empilement $\pi - \pi$ entre les couches de graphène, les nanofeuilles de graphène 2D pourraient facilement être empilées et agrégées, ce qui diminue considérablement la SSA et gêne le transport des électrons rapide limité son utilisation.

De plus, un nombre limité de sites réactifs sur les bords du graphène à l'état vierge est inacceptable pour les déployer dans la pratique. Par conséquent, le centre et l'avant-garde de ce domaine de recherche s'est tourné vers l'exploration du graphène modifié chimiquement, tel que le graphène fonctionnalisé ou dopé par hétéroatomes, et la nanostructure de graphène aux dimensions ajustées.

1.6 Les Matériaux du Support à base de Graphène

Quoique la plupart des graphènes dopé aux hétéroatomes, les catalyseurs sans nanostructure de graphène avec la dimension ajustée montrent des activités électrocatalytiques très prometteuses comparables au Pt/C dans le milieu alcalin. Les PEMFCs fonctionnant avec des électrolytes acides sont encore beaucoup plus viables commercialement et reposent sur une infrastructure plus mature. Jusqu'à maintenant, il y a des électrocatalyseurs à base de graphène rares rapportés pour l'ORR acide. Heureusement, grâce à sa conductivité élevée, sa très grande surface, sa variété structurelle abondante et sa chimie de surface ajustée, le graphène est un excellent matériau de support pour permettre l'utilisation des caractéristiques uniques dans le milieu d'acide.

1.7 Les Objectifs de la Recherche

Ce projet de la thèse est pour concevoir et réaliser un catalyseur d'ORR à base de Pt et des catalyseurs d'ORR à base de graphène avec les hautes performances, la durabilité extrême et le faible coût pour l'application de piles à combustible.

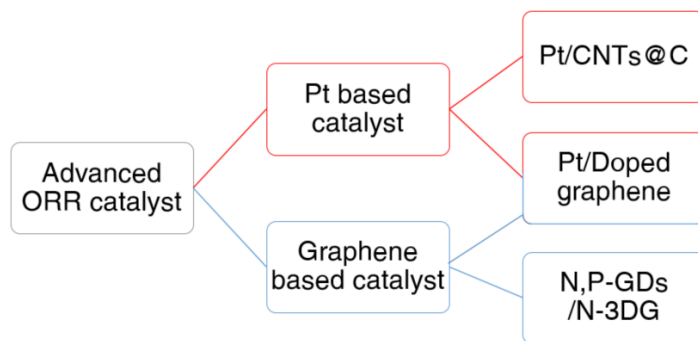


Figure R6. Le guide illustrant la disposition de cette thèse.

Montrant dans la Figure R6, les objectifs principaux de cette thèse présentent dans les suivants:

I. Pour construire des nanoparticules (NPs) de Pt encapsulées dans des couches de carbone supportant sur des nanotubes de carbone (en anglais : CNTs, Pt/CNTs@C) avec une structure d'épaisseur contrôlable avec précision.

II. Pour synthétiser des amas de Pt s'ancrant sur des supports en graphène dopé (la graphène dopée à Pt) et discuter de l'effet d'interaction entre supports.

III. Pour préparer des points de graphène co-dopés à l'azote et au phosphore supportant sur un catalyseur sans métal et dopé à l'azote tridimensionnel (N, P-GDs/N-3DG) avec une performance améliorée vers l'ORR.

2. Les Résultats

(1). Les Pt/CNTs revêtus par carbone ultra-minces: un électrocatalyseur très durable pour l'ORR

Dans cet article, nous avons synthétisé l'électrocatalyseur composé des NPs de Pt supportés sur des CNTs et recouverts d'une couche ultra-mince de carbone graphitique. Ces catalyseurs d'ORR hybrides ont été obtenus par la méthode d'encapsulation-graphitisation de polymère *in situ* interfacial, où un polymère contenant du glucose était développé directement à la surface de Pt/CNTs montrant dans la Figure R7. L'épaisseur de la couche de revêtement de carbone peut être réglée avec précision d'entre 0,5 et plusieurs nanomètres par simplement programmer la croissance du polymère sur Pt/CNTs.

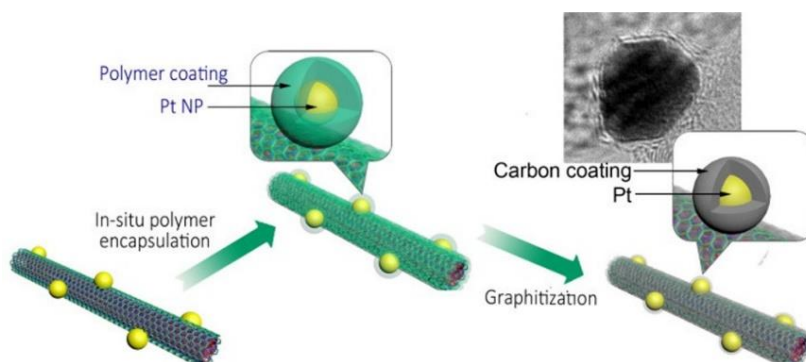


Figure R7. Le processus synthétique de Pt/CNTs@C.

Le Pt/CNTs@C obtenue avec une épaisseur de couche de carbone d'environ 0,8 nm (correspondant à environ 2 à 3 couches de graphène) a montré une activité élevée et une excellente durabilité sans perte d'activité notable.

Dans la Figure R8, même si l'après des cycles aux 20000, l'ECSA est toujours d'environ 64 m²/g, ce qui est proche de l'ECSA initiale et ne représente qu'une perte de 25% par rapport à la valeur du plateau. Ce revêtement de carbone ultra-mince s'agit non seulement comme une couche protectrice pour empêcher l'agrégation des NPs de Pt, mais de conduire également à une meilleure dispersion de l'échantillon dans un solvant dépourvu d'agrégats, ce qui permet d'une meilleure utilisation de Pt.

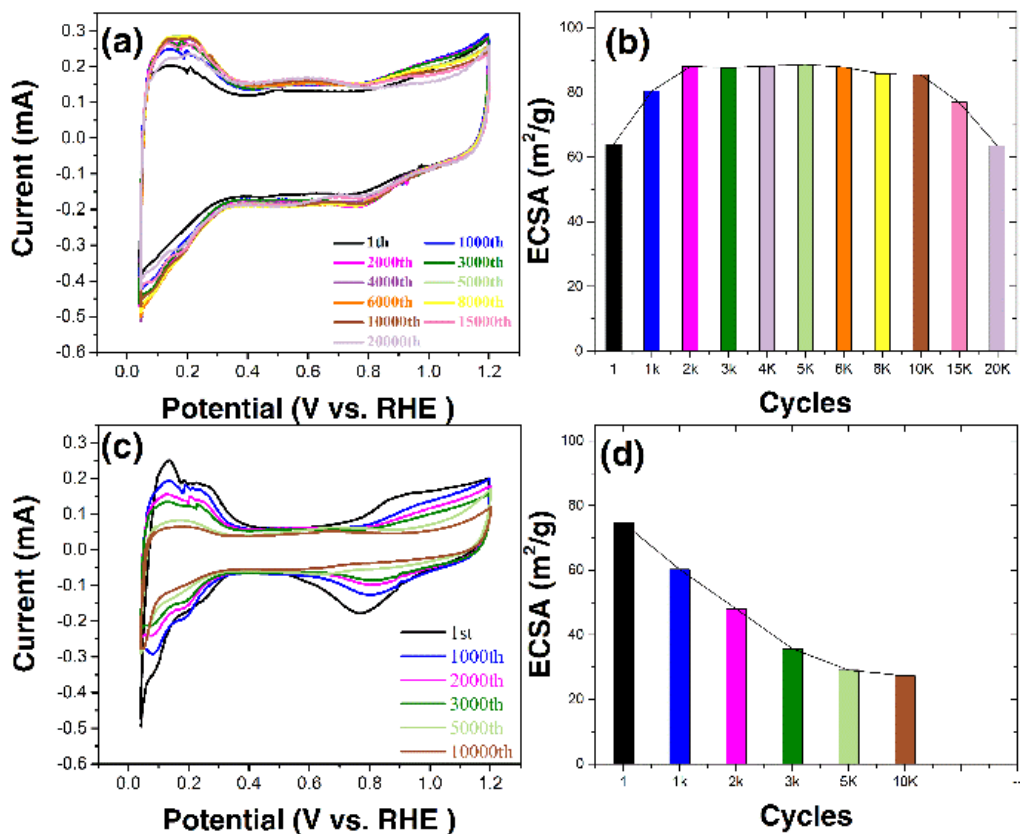


Figure R8. Le rendement à long terme sur les courbes CV de Pt/CNTs@C-2 (a) et Pt/CNTs (c). L'ECSA en fonction des cycles de réaction du Pt/CNTs@C-2 (b) et du Pt/CNTs (d). Les CVs ont été enregistrés dans HClO₄ saturé de N₂ en concentration d'environ 0,1 M.

(2). L'effet d'interaction de support des amas de Pt ancré sur le support de graphène dopé pour l'ORR

Dans cet article, tout à bord, nous avons utilisé trois types de matériaux de graphène différents: le graphène non modifié, le graphène dopé à l'azote (N-graphène) et le graphène co-dopé au phosphore d'azote (N, P-graphène) comme les matériaux de support pour ancrer des amas de Pt, montrant dans la Figure R9.

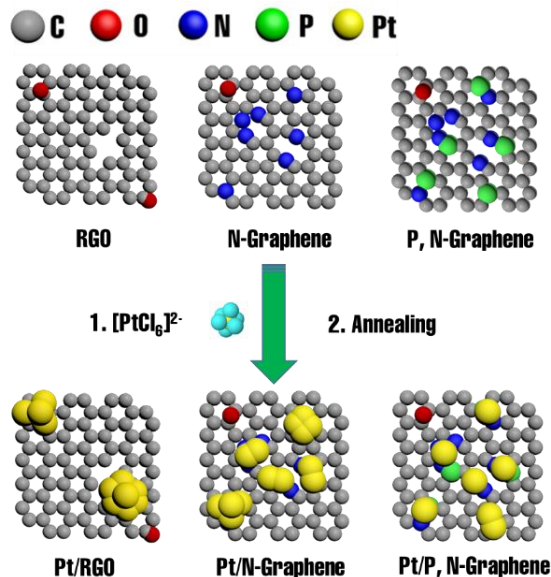


Figure R9. L'illustration schématique du mécanisme d'assemblage du Pt supporté sur graphène dopé.

Ensuite, une étude complète de l'effet d'interaction de support sur les amas de Pt a été discutée. Le N, P-graphène réduit non seulement la taille du Pt et facilite la distribution homogène à la surface, mais affecte également la structure électronique du Pt qui favorise l'activité d'ORR. Dans la Figure R10, le Pt/N, P-graphène montre non seulement une activité d'ORR élevée, une pente de Tafel faible et une voie d'ORR à 4 électrons avec un rendement en H₂O₂ faible, mais également une excellente durabilité en raison de sa plus forte interaction des atomes de Pt avec les atomes dopés.

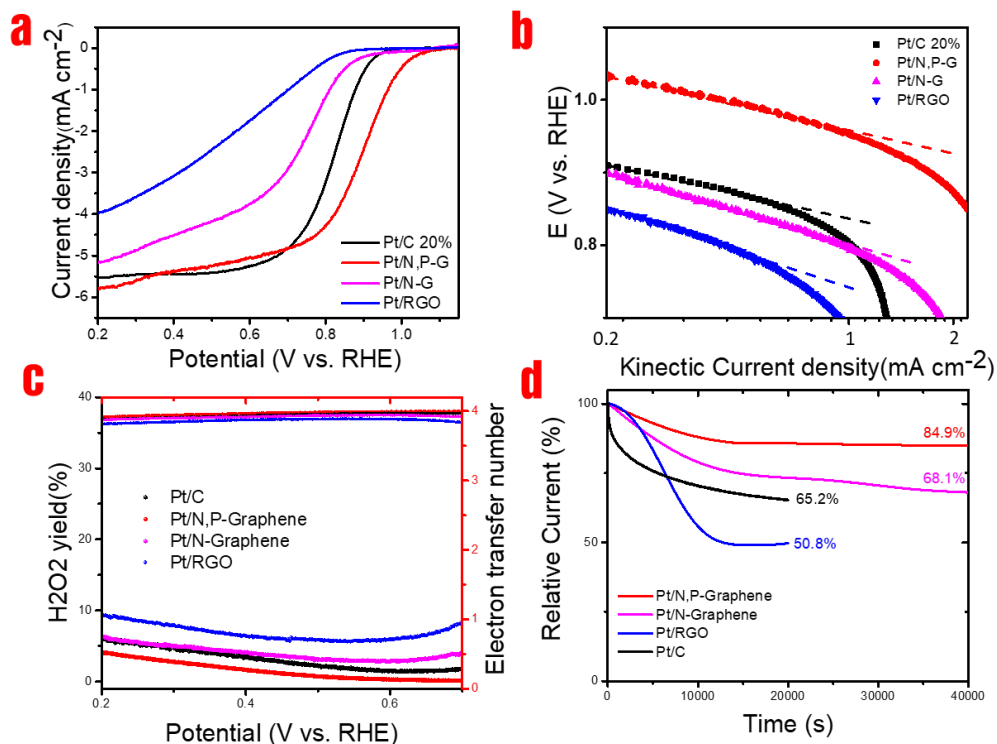


Figure R10. La caractérisation électrochimique de Pt/C commercial (20%), de Pt/N, P-graphène, de Pt/N-graphène et de Pt/RGO.

(3). Les points de graphène co-dopés N, P supporté sur du graphène 3D dopé au N comme le catalyseur sans métal pour l'ORR

À la base de la recherche précédente, le graphène dopé peut être utilisé non seulement comme le matériau de support, mais également comme le catalyseur sans métal pour l'ORR. En conséquence, nous avons synthétisé des points de graphène co-dopés à l'azote et au phosphore supporté sur du graphène dopé à l'azote 3D (N, P-GDs/N-3DG) par un processus de recuit refroidi facile. Montrant dans la Figure R11, les N, P-GDs obtenus sont uniformément dispersés à la surface du réseau poreux 3D interconnecté.

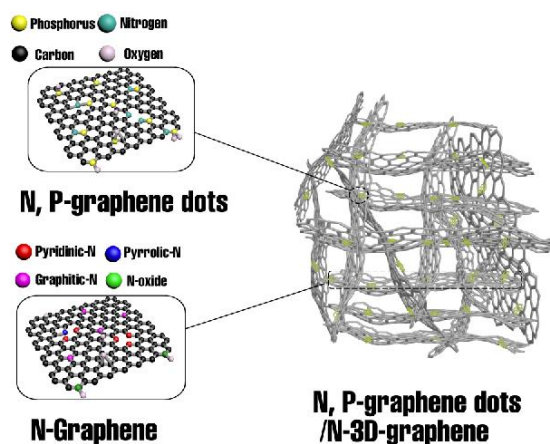


Figure R11. La structure des points de N, P-graphène supporté sur le graphène N-3D (N, P-GDs/N-3DG).

Montrant dans la Figure R12, le composite sans métal de N, P-GDs/N-3DG se présente une excellente activité électrocatalytique pour l'ORR, par exemple, le potentiel de départ positif et le potentiel de demi-vague positif, la voie à 4 électrons, le faible rendement en H_2O_2 par rapport du catalyseur commercial de Pt/C dans un milieu alcalin. Cette performance électrocatalytique améliorée peut être attribuée à l'effet synergique entre les abondants groupes fonctionnels et les défauts de bord.

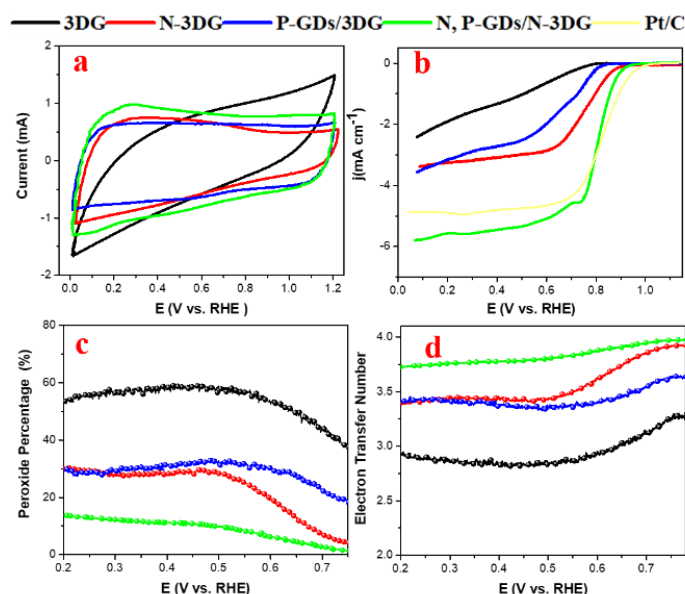


Figure R12. La caractérisation électrochimique de Pt/C (20%), graphène 3D, N-3DG, P-GDs/3DG et N, P-GDs/N-3DG commerciaux.